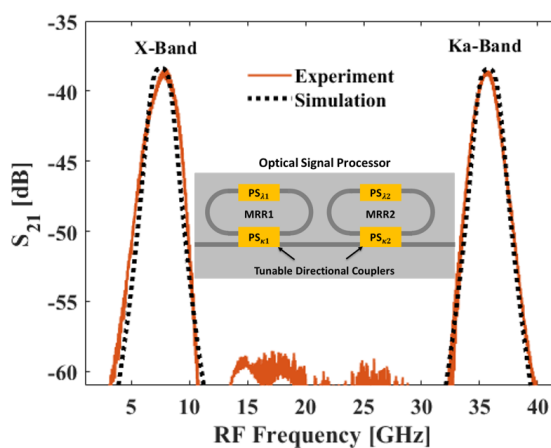


DEPARTMENT OF ELECTRICAL ENGINEERING  
INDIAN INSTITUTE OF TECHNOLOGY MADRAS  
CHENNAI – 600036

# Programmable Silicon Photonic Microwave Filters using Microring Resonators



*A Thesis*

*Submitted by*

**ASHITOSH VELAMURI**

*For the award of the degree*

*Of*

**DOCTOR OF PHILOSOPHY**

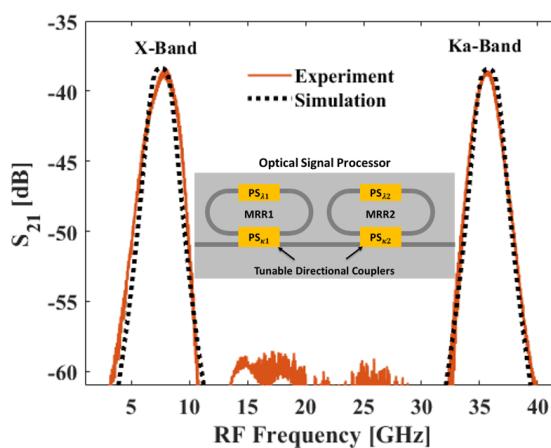
May 2025





DEPARTMENT OF ELECTRICAL ENGINEERING  
INDIAN INSTITUTE OF TECHNOLOGY MADRAS  
CHENNAI – 600036

# Programmable Silicon Photonic Microwave Filters using Microring Resonators



*A Thesis*

*Submitted by*

**ASHITOSH VELAMURI**

*For the award of the degree*

*Of*

**DOCTOR OF PHILOSOPHY**

May 2025





*Life is not a race. But you still have to run  
at your own pace to stay relevant.*



# THESIS CERTIFICATE

This is to undertake that the Thesis titled **PROGRAMMABLE SILICON PHOTONIC MICROWAVE FILTERS USING MICRORING RESONATORS**, submitted by me to the Indian Institute of Technology Madras, for the award of **Doctor of Philosophy**, is a bona fide record of the research work done by me under the supervision of **Prof. Bijoy Krishna Das**. The contents of this Thesis, in full or in parts, have not been submitted to any other Institute or University for the award of any degree or diploma.

**Chennai 600036**

**Ashitosh Velamuri**

**Date: May 2025**

**Dr. Bijoy Krishna Das**

Research advisor

Professor

Department of Electrical Engineering

IIT Madras



# LIST OF PUBLICATIONS

## I. REFEREED JOURNALS (BASED ON THESIS)

- **Ashitosh Velamuri** and Bijoy Krishna Das, “Programmable Silicon Photonic RF Filters With Symmetric Out-of-Band Rejection,” IEEE Journal of Lightwave Technology, vol. 42, no. 5 , pp. 1586-1596, 2024.

## II. REFEREED JOURNALS (OTHERS)

- Pratyasha Priyadarshini, Arnab Goswami, **Ashitosh Velamuri**, and Das, B. K. “Compact Tunable Resonance Filters with Ultra-Broad Rejection for Silicon Photonics”, Optics Express, vol. 32, no. 16, pp. 27409-27430, 2024
- Anushka Tiwari, **Ashitosh Velamuri**, Ram Mohan Rao Boyapati, Arnab Goswami, Enakshi Bhattacharya and Bijoy Krishna Das. “Widely Tunable Microwave Photonic Oscillator with a High-Q Silicon Nitride Microring Resonator,” *Accepted for Publication*, IEEE Journal of Lightwave Technology

## III. REFEREED JOURNALS (UNDER REVIEW)

- **Ashitosh Velamuri**, Kumar Piyush, Yash Raj, Arnab Goswami, Anandha Padmanabhan, Nitin Ghodgaonkar, Dinanath Soni, Janakiraman Viraraghavan and Bijoy Krishna Das, “Free Spectral Range Reconfigurable Multiband Silicon Photonic Microwave Filters,” Optica Photonics Research.

## IV. PUBLICATIONS IN CONFERENCE PROCEEDINGS (BASED ON THESIS)

- **Ashitosh Velamuri**, Anandha Padmanabhan, Nitin Ghodgaonkar, Dinanath Soni, Arnab Goswami and Bijoy Krishna Das, “Chip-Scale Demonstration of Tunable Two-Band Microwave Photonic Filter using Cascaded Microring Resonators,” 16th International Conference on Fiber Optics and Photonics, IIT Kharagpur, December 2024.
- **Ashitosh Velamuri** and Bijoy Krishna Das. “Integrated Photonic Microring Resonators for FSR Dependent Microwave Bandpass Filters”, Optical Fiber Communication Conference (OFC), San Diego, USA, March 2024.
- **Ashitosh Velamuri** and Bijoy Krishna Das. “Integrated Programmable Microwave Photonic Bandpass Filter with Symmetric Rejection.” Conference on Lasers and Electro-Optics (CLEO), San Jose, USA, May 2023.
- **Ashitosh Velamuri**, and Bijoy Krishna Das. “Accurate Measurement of Optical Delay in a Programmable Microring Resonator.” Frontiers in Optics

(FiO), Rochester, USA, October 2022.

## V. PUBLICATIONS IN CONFERENCE PROCEEDINGS (OTHERS)

- Kumar Piyush, Pawan Kumar Pandit, **Ashitosh Velamuri**, Arnab Goswami, Anandha Padmanabhan, Nitin Ghodgaonkar, Dinanath Soni, Janakiraman Viraraghavan and Bijoy Krishna Das. “Efficient Tuning of Silicon Photonic Power Splitters using Diode Integrated Microheaters.” 16th International Conference on Fiber Optics and Photonics, IIT Kharagpur, December 2024.
- Shruti Pandey, Tarun Arumugham, Anjana James, **Ashitosh Velamuri**, Arnab Goswami, Gan Yih Loong, Ng Chew Yan, Deleep R. Nair, Anjan Chakravorty, and Bijoy Krishna Das. “Extraction of Silicon Photonic Wafer-Scale Process Variability using ML-Enhanced Algorithm.” Conference on Lasers and Electro-Optics-PacificRim (CLEO-PR), Incheon, Korea, August 2024.
- Kumar Piyush, Yash Raj, Akash Shekhar, **Ashitosh Velamuri**, Arnab Goswami, Naveen Raj Murugesan, Anandha Padmanabhan, Dinanath Soni, Janakiraman Viraraghavan and Bijoy Krishna Das. “Extraction of Phase Errors in Photonic ICs from Passive Transmission Characteristics.” Conference on Lasers and Electro-Optics-PacificRim (CLEO-PR), Incheon, Korea, August 2024.
- Anushka Tiwari, **Ashitosh Velamuri**, Arnab Goswami, Deepa Venkitesh, Enakshi Bhattacharya and Bijoy Krishna Das. “A Compact and High-Q value SiN Microring Resonator for Microwave Photonic Applications,” IEEE Silicon Photonics Conference (SiPhotonics), Tokyo, Japan, April 2024.
- Pratyasha Priyadarshini, Arnab Goswami, **Ashitosh Velamuri**, and Das, B. K. “Thermo-optically Tunable DBR Resonator with Ultra-broad Rejection Band for Silicon Photonic Applications”, European Conference on Integrated-Optics (ECIO), University of Twente, Netherlands, April 2023.



# ACKNOWLEDGMENTS

No one's PhD journey is simple, and I am no exception. My journey started with my decision to pursue the path of PhD in the preplacement presentation of a multi-national company at IIT Kanpur in 2017. Since then, it has been a roller-coaster ride filled with several moments of extreme emotions. It would not have been possible without the personal and professional help of people around me.

First, I would like to thank my PhD supervisor, Prof. Bijoy Krishna Das, for his constant guidance and technical expertise, which helped me shape my work in the best presentable way possible. His way of organizing our Saturday group meetings, where we can ask questions without inhibitions, has thoroughly helped me get my fundamentals right. Also, his patience with me during the days I made mistakes has been helpful to come back the next day and try not to repeat them. This thesis is one of the outcomes of his vision for developing the Silicon Photonics ecosystem in India. I only tried to fit into that vision to the best of my abilities.

I am thankful for all the mistakes that I have made in my master's which have shaped my attitude in the PhD. I will perpetually be grateful to Prof. Pradeep Kumar K, my M.S(R) thesis supervisor, Prof. Ishan Sharma and Prof. Shakti Gupta from the mechanical department at IIT Kanpur for guiding me on the right path during my amateur research days.

I want to thank Prof. Anjan Chakravorthy, Prof. Deleep R. Nair, Prof. Janakiraman Viraraghavan, Prof. Sudharsanan Srinivasan and Prof. Deepa Venkitesh for their valuable suggestions in the meetings carried out for collaborative work.

I thank my Doctoral Committee, Prof. Shanti Bhattacharya, Prof. Deleep R. Nair, Prof. S. Christopher and Prof. Madhu Mutyam, for their comments and suggestions during the review meetings during my PhD.



I want to acknowledge Mr Dinanath Soni, Executive Director of iZMO Microsystems and Mr Nitin Ghodgaonkar, Chief Technology Officer of iZMO Microsystems, for the collaborative efforts towards the development of silicon photonic packaging solutions in India, and also for giving direct access to their facilities in Bengaluru to the research scholars of our lab. I would also like to thank Mr. Anandha Padmanabhan and Mr. Naveen Raj for their work on designing the photonic packaging modules. Experiments with the packaged photonic chips reported in this thesis were possible because of the collaborative work with the team at iZMO Microsystems.

I am grateful for the opportunity to get hands-on experience in in-house fabrication facilities at the Center for NEMS and Nanophotonics (CNNP). I acknowledge the technicians and staff members of CNNP for their help in various stages of the device fabrication, equipment maintenance and troubleshooting.

I would like to especially acknowledge Dr. KV Reddy, Founder of Pritel Inc., for sponsoring my trip to attend one of the prestigious events in the photonics community, the Optical Fiber Communications (OFC) conference held in San Diego, USA. I am also thankful to him for hosting his famous IITM Alumni dinners during my CLEO and OFC conferences visit.

I gratefully acknowledge Ministry of Electronic and Information Technology (MeitY), Govt. of India for sponsoring NNetRA project for Centre for NEMS and Nanophotonics (CNNP) and the establishment of Centre for Programmable Photonic Integrated Circuits and Systems (CoE-CPPICS), at IIT Madras. I am also grateful to Ministry of Education, Govt. of India for sponsoring the PhD research grant during the initial years of my PhD

I would also like to thank Dr. Arnab Goswami, Chief Technology Officer for our Silicon Photonic CoE-CPPICS IIT Madras, for his exceptional dedication and work towards developing the experimental lab and for coordinating several lab events since he has taken up the mantle.

I am grateful to my seniors, Dr Riddhi Nandi and Dr Sumi Radhakrishnan, for their guidance during the initial days in device simulations and fabrication and characterization in the lab. I am also thankful to all the alumni of our research lab for their efforts towards developing in-house fabrication and characterization facilities at IIT Madras during their tenure.

I thank my lab mates Kumar Piyush and Yash Raj for their help in designing and performing experiments with the programmable mesh architectures. I am also grateful to Riddhi Goswami and Shruti Pandey for their help in some of the long and brutal experiments that continued for days. I want to thank Dr Goutham Ezhilsarasu and Akash Shekhar for their work in the RF PCB design and Ankan Gayen, Dr Nagarajan Nallusamy, Dr Shamsul Hassan and Vinoth S for their work towards the development of the in-house optical packaging facilities. I am also thankful to my fellow lab mates Pawan Kumar Pandit, Anjana James, Pranita Kumari Swain, Sarad Subhra Bhakat, Dibyanchal Sahu, Mayukh Mandal, Rahul Krishna, Manu Maxim, Siddhartha Chaganti and Vardaan Mongia for their wishes. I wish them all the best in their future endeavours. I would like to thank the present and past members of the administrative staff of CoE-CPPICS for their help in the procurement related process.

I would like to especially thank my friends in the lab, Ram, Anushka, Suvarna, Pratyasha and Arnab, for all the technical and non-technical discussions during the tea, snack, lunch and dinner breaks. Their input during experimental troubleshooting was invaluable and often resulted in fruitful results. Special thanks to Aggraj, my badminton partner during my stay in the hostel, for knocking at my door every morning during COVID-19 days to ask “Bhai!! Chalega?”

I want to thank my friends from masters Bhanu, Parneeth, Dheeraj and Anil for some of the great moments even during my PhD. In many ways, their friendship was one of the reasons for my decision to pursue the PhD.

Being a Telugu speaker, I am heavily influenced by the movies made in our language, known for over-the-top action sequences. Even though I realize the fictional elements of the movie making, the lead characters' never-dying attitude has often inspired me to stay aggressive in pursuing my PhD. Jai Mahishmathi and Salaam Rocky Bhai.

Finally, I would like to give special mention to my parents, who, from childhood, have always prioritized my education and that of my sister. They would be happy today as we both have pursued PhDs in our individual streams. To my sister, who has always given me a phone call from time to time and asked, "How are you?". To my wife, who was always waiting at home to ask, "How was your day?" and was patient enough to listen to me answer it.

Thank you all.

# ABSTRACT

**KEYWORDS** Microwave photonics, silicon photonics, programmable photonics, RF filter, microring resonator, optical signal processor, programmable square mesh, radio over fiber.

The futuristic 5G/6G communication and RADAR signal processing systems operating beyond X-band ( $> 10$  GHz) demand scalable microwave photonic integrated circuits for re-configurable operations. CMOS-compatible silicon photonics technology is being studied intensively for programmable optical signal processors (OSP) for high-frequency microwave to mm-wave applications. The bandpass filter is an essential microwave receiver architecture block to separate the signal of interest from the noise and eliminate cross-talks. The microring resonator is a popular device for designing an efficient optical signal processor for RF photonic filters. One significant challenge is implementing bandpass programmable microwave photonic filters with symmetrical out-of-band rejection around the central carrier frequency. In this thesis, we will discuss the proof-of-concept experimental results of the microwave photonic filter with the novel OSP design (based on cascaded microring resonators) fabricated in-house, along with its limitations and improvement scopes. The central frequency and bandwidth of the RF bandpass filter could be tuned up to 8 GHz (theoretical limit: 60 GHz) and 0.84 - 1.8 GHz in our experimental setup with a symmetric out-of-band rejection  $> 20$  dB.

Next, we have investigated the programmable photonic integrated circuit comprising 14 tunable balanced Mach-Zehnder interferometers designed into a square mesh architecture to demonstrate a silicon photonic multi-band microwave filter with tunable bandwidths and re-configurable number of passbands. The mesh architecture is programmed into three different microring resonator configurations to realize microwave filters with two, three and four bands within the modulator bandwidth used in the experiments. Among these, the two-band filter realized for X- and Ka-band was thoroughly investigated, and

the bandwidth of both the filter bands was tuned over the extensive range of 1.6 GHz to 12.7 GHz by controlling the MRR Q-factor and the resonance spacing from the carrier. Following, an X-band receiver link was set up to test the performance of the programmable microwave filter module in a radio-over-fiber communication network. With an optimized set of operating parameters of the programmable microwave filter, we could achieve a bit-error-rate as low as  $\sim 10^{-20}$  (mathematically calculated using the Q-function) for a fiber-optic link length of 400 m (@ 100 Mbps).

Finally, the proposed OSP design of cascaded microring resonators was extended to realize an integrated two-band microwave photonic filter with an on-chip modulator and detector. We have first individually characterized the phase modulator (BW  $\sim 39.7$  GHz), photodetector (BW  $\sim 40$  GHz, responsivity  $\sim 0.75$  A/W) and ring resonators of the OSP ( $Q \sim 0.8 \times 10^5$ , FSR  $\sim 43.5$  GHz). Owing to the heavy crosstalk between the RF input-output ports, we have verified the realization of the filter functionality with the on-chip modulator and on-chip detector separately. In the experiments, both passbands' central frequency could be tuned in the 5 - 18 GHz range and 38.5 - 25.5 GHz, respectively, with a symmetric out-of-band rejection  $> 20$  dB. For the tuned frequency range, the bandwidth of the microwave filter could be tuned from 1 - 6 GHz in our experimental setup.

# CONTENTS

	Page
<b>ACKNOWLEDGMENTS</b>	<b>i</b>
<b>ABSTRACT</b>	<b>v</b>
<b>LIST OF TABLES</b>	<b>ix</b>
<b>LIST OF FIGURES</b>	<b>xi</b>
<b>ABBREVIATIONS</b>	<b>xxv</b>
<b>NOTATION</b>	<b>xxix</b>
 <b>CHAPTER 1      INTRODUCTION</b>	 <b>1</b>
1.1      Background and Motivation . . . . .	1
1.2      Research Objective . . . . .	9
1.3      Thesis Organization . . . . .	10
 <b>CHAPTER 2      OSP WITH SINGLE MRR</b>	 <b>13</b>
2.1      Operation Scheme . . . . .	13
2.2      MRR Design . . . . .	15
2.3      Microwave Photonic Filter Function . . . . .	26
2.3.1      Simulation Results . . . . .	26
2.3.2      OSP Fabrication and Characterization . . . . .	32
2.3.3      MRR Delay Measurements . . . . .	44
2.3.4      RF Filter Experiments . . . . .	45
2.4      Summary . . . . .	49
 <b>CHAPTER 3      OSP WITH CASCADED MRRS</b>	 <b>51</b>
3.1      Operation Scheme . . . . .	51
3.2      Design and Simulation Results . . . . .	53
3.3      Fabrication and Characterization . . . . .	63
3.3.1      Passive Transmission Characteristics . . . . .	68
3.3.2      Thermo-Optic Characteristics . . . . .	69
3.4      RF Filter Experiments . . . . .	72
3.5      Summary . . . . .	76
 <b>CHAPTER 4      OSP WITH PROGRAMMABLE MESH ARCHITECTURE</b>	 <b>79</b>
4.1      Design and Working Principle . . . . .	79
4.2      Fabrication and Testing . . . . .	88
4.2.1      Calibration of Tunable MZIs (TBUs) . . . . .	91

4.2.2	Characterizations of Programmable Ring Resonators . . . . .	95
4.3	Demonstration of Multi-Band Filters . . . . .	98
4.4	Link Performance Evaluation . . . . .	105
4.5	Summary . . . . .	114
<b>CHAPTER 5</b>	<b>INTEGRATED MICROWAVE PHOTONIC FILTER</b>	<b>117</b>
5.1	Operation Scheme and Chip Layout . . . . .	117
5.2	Packaging and Components Testing . . . . .	123
5.2.1	Phase Modulator . . . . .	125
5.2.2	Photodetector . . . . .	126
5.2.3	Optical Signal Processor . . . . .	131
5.3	Microwave Filter Experiment . . . . .	133
5.4	Summary . . . . .	140
<b>CHAPTER 6</b>	<b>CONCLUSIONS</b>	<b>143</b>
6.1	Thesis Summary . . . . .	143
6.2	Future Outlook . . . . .	145
<b>APPENDIX A</b>	<b>MICROWAVE PHOTONIC FILTER: THEORETICAL FORMULATION</b>	<b>149</b>
<b>APPENDIX B</b>	<b>OPTIMIZED RECIPES AND PROCESS FLOW FOR IN-HOUSE FABRICATED STRUCTURES</b>	<b>153</b>
B.1	SOI Wafer Specifications (SOITEC) . . . . .	153
B.2	Silicon Wafer Cleaning Steps . . . . .	153
B.3	Spin Coating Procedure . . . . .	154
B.4	Electron-Beam Lithography: Writing Strategies . . . . .	155
B.4.1	Conventional Patterning . . . . .	155
B.4.2	Fixed Beam Moving Stage . . . . .	155
B.5	Dry Etching Parameters . . . . .	156
B.6	Thermo-Optic Phase Shifter Patterning . . . . .	156
B.6.1	Aluminum Contact Pads and Metal Routing Integration . . . . .	157
B.6.2	Titanium Microheater Integration . . . . .	158
B.7	Process Flow . . . . .	158
<b>APPENDIX C</b>	<b>OSP WITH CASCADED MRR USING MZI AS TUNABLE COUPLER</b>	<b>163</b>
<b>APPENDIX D</b>	<b>CALIBRATION OF PROGRAMMABLE MESH ARCHITECTURE</b>	<b>165</b>
<b>BIBLIOGRAPHY</b>		<b>169</b>
<b>CURRICULUM VITAE</b>		<b>181</b>
<b>DOCTORAL COMMITTEE</b>		<b>183</b>

# LIST OF TABLES

Table	Caption	Page
1.1	List of commercially available passive microwave electronic filter for different RF bands and their specifications. Source: Mini-Circuits . . . .	4
2.1	Chosen design parameters of the integration platform and the waveguide geometry for the reported MRR simulations. . . . .	17
2.2	The parameters for the laser source, modulator, microring resonator, and detection circuit used for simulation results shown in Fig. 2.11. . . . .	27
2.3	Design parameters chosen for the in-house fabrication of the MRR. . . .	36
3.1	The calculated values for the directional coupler of effective length $L = 9.75 \mu\text{m}$ used in MRR design of waveguide bend radius $R = 100 \mu\text{m}$ , $W_1 = 0.5 \mu\text{m}$ , $W_2 = 1 \mu\text{m}$ , $g = 250 \text{ nm}$ . . . . .	58
3.2	Simulation parameter values for calculating RF filter output of the proposed OSP described in Fig. 3.1a. . . . .	59
3.3	Design parameters chosen for the fabrication of the OSP. . . . .	63
3.4	Extracted coefficients of the fabricated devices. FSR: free spectral range, $\lambda_r$ : resonant wavelength, $n_g$ : group index, $r$ : self-coupling coefficient, $a$ : round trip loss factor, $Q$ : quality factor $\alpha$ : waveguide loss and ER: extinction ratio . . . . .	70
3.5	Comparison of the measured RF filter responses with the proposed OSP and the state-of-the-art demonstrations. . . . .	76
4.1	A set of programming schemes for the 14 TBUs to reconfigure the PMA into three different MRRs in all-pass configurations. . . . .	81
4.2	The parameters for the laser source, modulator, PMA based MRR configuration-1, and detection circuit used for simulation results shown in Fig. 4.4. . . . .	85
4.3	The extracted thermal switching powers for each tunable basic unit (TBU) to operate in cross and bar state along with the operated phase shifters, and the cross and bar state extinctions. The phase shifter notation used here is as per the convention given in Fig. 4.1b. $\text{PS}_{mX}$ , $\text{PS}_{mY}$ corresponds to the integrated phase shifter to both the arms of the $m$ -th TBU, where $\{X, Y\} = \{L, R\}$ (left and right) for the vertical TBUs (3, 6, 9 and 12), $\{X, Y\} = \{T, B\}$ (top and bottom) for the remaining horizontal TBUs. . . . .	94
4.4	Experimentally observed important figure of merits of three configurations of the PMA (given in Fig. 4.2). . . . .	98
4.5	Extracted figure of merits of the measured filter responses marked as #1, #2, #3 and #4 in Fig. 4.14a. Shape Factor = (10-dB bandwidth)/(3-dB bandwidth) . . . . .	101
4.6	Comparison of the measured multi-band RF filter responses with the programmable square mesh and the state-of-the-art demonstrations. . .	105



4.7	Extracted metrics of the two-tone test for the X-band filter responses given in Fig. 4.14a and Fig. 4.15. G - RF link gain; IIP - input intercept point; OIP - output intercept point; SFDR - spurious free dynamic range; NF - noise figure. The subscript three correspond to the third order inter-modulation terms. . . . .	107
4.8	Calculated BER for the change in the fiber length between the equivalent RRH and BBU sections (as marked in Fig. 4.18) and the transmitted data rate. Zero fiber length: back-to-back fiber connections between the equivalent RRH and BBU sections. . . . .	113
5.1	Comparison of the measured multi-band RF filter responses with the proposed OSP and the state-of-the-art demonstrations. . . . .	140
6.1	Extracted metrics of the two-tone test for the filter response at $f_{c1}$ with on-chip detector given in Fig. 5.13d. G - RF link gain; IIP - input intercept point; OIP - output intercept point; SFDR - spurious free dynamic range; NF - noise figure; OA - optical amplifier (after off-chip modulator, 10 dB gain); EA - electrical amplifier (after on-chip PD, 35 dB gain). The subscript three correspond to the third order inter-modulation terms. . . . .	146
B.1	Specifications of silicon-on-insulator wafer used in the fabrication. . . .	153
B.2	Spin coating parameters for negative tone Hydrogen silsesquioxane (HSQ) resist used for waveguide patterning . . . . .	154
B.3	Optimized EBL parameters for patterning and developing the windows for the waveguides . . . . .	156
B.4	Optimized recipe for the dry etching of silicon using ICP-RIE . . . . .	156
B.5	Spin coating parameters for PMMA-A8 resist (positive tone) used for the contact pads and heater (thermo-optic phase shifters) patterning . .	157
B.6	Optimized EBL parameters for patterning and developing the windows for the contact pads and metal routing lines . . . . .	157
B.7	Optimized EBL parameters for patterning and developing the windows for the metal heaters . . . . .	158

# LIST OF FIGURES

Figure	Caption	Page
1.1	Schematic representation of a microwave photonic processor module. E/O: electrical-to-optical, O/E: optical-to-electrical. . . . .	2
2.1	(a) The schematic of the microwave photonic bandpass filter with single microring resonator as the OSP, (b) phase modulated spectrum of the optical carrier around $\nu_0$ with sidebands having $\pi$ phase difference, (c) the phase modulated optical spectrum aligned with the resonance of a microring resonator with resonant frequency $\nu_r$ , such that $f_{rf} =  \nu_0 - \nu_r $ , and (d) the expected microwave bandpass filter response at the photodetector output with $f_{rf}$ as the central frequency. . . . .	14
2.2	(a) Schematic top-view of an typical MRR design in all-pass configuration with passive directional coupler in SOI platform; $L_{dc}$ is the length of the parallel section of the directional coupler, $R$ is the bend radius of the ring waveguide, and $r, t$ are the self and cross coupling coefficients of the directional coupler, and (b) schematic cross-sectional view of the passive directional coupler annotated with important design parameters; $W$ : waveguide width, $H$ : device layer thickness, $h$ : slab height, $g$ : directional coupler gap, $t_{BOX}$ : buried oxide thickness (bottom cladding), $t_{TOX}$ : top oxide thickness (top cladding). . . . .	16
2.3	The (a) symmetric and (b) anti-symmetric mode solutions of the directional coupler for the design parameters listed in Table. 2.1 at $\lambda = 1550$ nm, and gap $g = 200$ nm. . . . .	18
2.4	The variation of the coupling coefficient $\kappa$ for chosen waveguide dimensions (listed in Table. 2.1) with three different slab heights $h = 0, 90$ nm and $150$ nm with (a) directional coupler gap $g$ at wavelength $\lambda = 1550$ nm, and (b) wavelength $\lambda$ at gap $g = 200$ nm. . . . .	19
2.5	(a) The variation of the self coupling coefficient $r$ of the directional coupler ( $g = 400$ nm, coupler length $L_{dc} = 10 \mu\text{m}$ , and bend radius $R = 50 \mu\text{m}$ ) with wavelength and also marked are the loss factor $a$ ( $\sim 0.9923$ ; considered wavelength-independent) and different coupling conditions of the MRR, and (b) the corresponding MRR characteristics plotted using equation (2.3), also indicating the coupling conditions; the simulation results in both the figures are for the waveguide geometry given in Table. 2.1. . . . .	20

2.6	(a) The zoomed-in characteristics of the MRR to two resonances to indicate the free spectral range (full-spectrum shown in Fig. 2.5b), (b) the zoomed-in characteristics of the MRR to one resonance (left-resonance of Fig. 2.6a) to indicate the resonance wavelength $\lambda_r$ , extinction, full-width at half maximum and quality-factor, and (c) the extracted Q-factor and extinction from the MRR spectral characteristics shown in Fig. 2.5b, over the range of resonance wavelengths. UC: under-coupled, CC: critically-coupled, OC: over-coupled. . . . .	21
2.7	The power transmission ( $ T_r ^2$ ), phase ( $\phi_r$ ) and the delay ( $\tau_r$ ) response of the MRR with same extinction along with the figures of merit values (Q-factor, FWHM, extinction and resonant wavelength); (a) $ T_r ^2$ and $\phi_r$ for ring operating in under-coupled condition ( $r > a$ ), (b) $\tau_r$ for ring operating in under-coupled condition, (c) $ T_r ^2$ and $\phi_r$ for ring operating in over-coupled condition ( $r < a$ ), and (d) $\tau_r$ for ring operating in over-coupled condition. . . . .	22
2.8	(a) Schematic top-view of a tunable microring resonator with two phase shifters $PS_\kappa$ and $PS_\lambda$ integrated to tune the coupling coefficient and the resonant wavelength, respectively, and (b) schematic top-view of the conventional tunable coupler based on Mach-Zehnder interferometer (MZI) integrated with phase shifter $PS_\kappa$ in one arm. . . . .	23
2.9	(a) The variation of the self coupling coefficient $r$ of the MZI-based tunable directional coupler (see Fig. 2.8b) with thermal power applied to the phase shifter $PS_\kappa$ , and also marked is the loss factor $a$ and different coupling conditions of the MRR, (b) the MRR characteristics around 1550 nm plotted over the tuned values of $r$ , and (c) the extracted Q-factor and extinction from the MRR responses over the tuned values of $r$ . . . .	24
2.10	(a) MRR characteristics plotted by tuning the thermal power applied to the phase shifter $PS_\lambda$ of the tunable coupler ring (see Fig. 2.8a), for a given value of $r = 0.932$ , (b) the extracted Q-factor, and (c) extinction of the simulated MRR transmission by tuning the thermal power $PS_\lambda$ for different values of $r$ (set by tuning $PS_\kappa$ ). . . . .	25
2.11	(a) Optical power transmission characteristics of the modulated laser light aligned with the MRR resonance, and also indicating the separation $f_{rf}$ ( $= 10$ GHz) between the resonant frequency $\nu_r$ and the laser carrier frequency $\nu_0$ , and (b) calculated $S_{21}$ ( $= P_{RF,out}/P_{RF,in}$ ) of the microwave photonic link (see Fig. 2.1a), exhibiting bandpass filter response at 10 GHz central frequency with asymmetric out-of-band rejection. The simulation results are for the parameter values given in Table. 2.2. . . .	28

2.12	(a) Normalized optical power transmission and phase associated with its electric field of the MRR around the carrier frequency $\nu_0$ , (b) spectral response of the amplitude terms $A_+$ , $A_-$ (defined in Eq. (2.6)) which are proportional to the beat currents $i_+$ and $i_-$ , (c) spectral response of the phase terms $\phi_{r,+}$ , $\phi_{r,-}$ (defined in Eq. (2.7)) indicating the phase added by the MRR to the beat currents $i_+$ and $i_-$ , and (d) spectral response of $\Delta\phi = \Delta\phi_r + \pi$ (defined in Eq. (2.8)) indicating the phase difference between the beat currents $i_+$ and $i_-$ . The simulation results are for the parameter values given in Table. 2.2. . . . .	30
2.13	(a) Calculated $S_{21}$ ( $= P_{RF,out}/P_{RF,in}$ ) of the microwave photonic filter with 10 GHz central frequency for three different values of $r$ : {0.958, 0.939, 0.906} corresponding to UC, CC and OC resonances, respectively, (b) extracted 3-dB bandwidth of the filter responses obtained by tuning the MRRs coupling coefficient, (c) extracted link gain of the filter responses ( $= P_{RF,out}/P_{RF,in}$ at central frequency $f_{rf}$ ) obtained by tuning the MRRs coupling coefficient, and (d) the variation of the link gain with the bandwidth of the simulated filter responses over the full-range of coupling coefficients covering OC, CC and UC resonances. The simulation results are for the parameter values given in Table. 2.2. . . .	31
2.14	(a) Optical spectrum of the phase modulated optical carrier $\nu_0$ indicating the equal amplitude and $\pi$ phase shift between 1 <sup>st</sup> order USB and LSB, (b) transmission and phase characteristics of the MRR for an under-coupled (UC) resonance, (c) transmission and phase characteristics of the MRR for an over-coupled (OC) resonance, (d) optical spectrum of the phase modulated optical carrier after transmission through the UC-resonance of the MRR, (e) optical spectrum of the phase modulated optical carrier after transmission through the OC-resonance of the MRR, (f) electrical spectrum of the RF signal after the photodetector for filter achieved with UC-resonance, and (g) electrical spectrum of the RF signal after the photodetector for filter achieved with OC-resonance. . . . .	33
2.15	(a) Mask layout of the fabricated structures comprising of reference waveguide and MRR with different lengths of directional couplers $L_{dc}$ (0 to 5 $\mu\text{m}$ ) along with grating couplers, contact pads and test heater elements, (b) zoomed-in mask layout indicating the grating coupler and an extra polygon added to avoid to the stitching error in e-beam lithography, (c) mask layout of the MRR ( $L_{dc} = 5 \mu\text{m}$ ) along with the phase shifter $\text{PS}_\lambda$ , and (d) microscope image of the fabricated passive structures corresponding to the mask layout given in Fig. 2.15a. . . . .	35

2.16	Microscope images of the fabricated MRRs ( $L_{dc}$ : 4, 5 $\mu\text{m}$ ) devices during different stages of the active fabrication process: (a) after the contact pads patterning and PMMA-A8 resist development of MRR with partial window openings due to low EBL dose, (b) after the contact pads patterning and PMMA-A8 resist development with optimized EBL dose, (c) post Aluminium metal (thermal) deposition and lift-off, (d) after microheater patterning and development, (e) after microheater patterning and development zoomed-in to single MRR ( $L_{dc}$ : 5 $\mu\text{m}$ ), and (f) post Titanium (e-beam) deposition and lift-off zoomed-in to single MRR ( $L_{dc}$ : 5 $\mu\text{m}$ ). . . . .	37
2.17	Experimental setup for passive and thermo-optic characterization of the fabricated OSP. PC: polarization controller . . . . .	38
2.18	(a) Transmission characteristics of the in-house fabricated microring resonator ( $L_{dc}$ : 4, 5 $\mu\text{m}$ ) and its comparison with reference waveguide response, (b) transmission characteristics of the in-house fabricated microring resonator ( $L_{dc}$ : 0 – 3 $\mu\text{m}$ ), and (c) the least square fit of the critically coupled resonance around 1541 nm in Fig. 2.18a (using Eq. (2.3)) to extract coupling coefficient $r$ and loss factor $a$ . . . . .	39
2.19	Microscope image of the foundry-fabricated microring resonators indicating the integrated phase shifters; (a) passive directional coupler ring with phase shifter $\text{PS}_\lambda$ to tune the resonant wavelength, and (b) Mach-Zehnder interferometer based tunable directional coupler ring integrated with phase shifters $\text{PS}_\kappa$ and $\text{PS}_\lambda$ to tune the coupling coefficient and resonant wavelength, respectively. . . . .	41
2.20	(a) Experimentally measured transmission characteristics of the reference waveguide and the passive directional coupler microring resonator, (b) the least square fit of the measured data (resonance around 1554 nm in Fig. 2.20a) using Eq. (2.3) to extract coupling coefficient $r$ and loss factor $a$ , (c) thermo-optic tuning characteristics of the ring for different values of applied thermal powers $\text{PS}_\lambda$ , and (d) the extracted coefficients $\{r, a\}$ for different values of $\text{PS}_\lambda$ . . . . .	42
2.21	(a) Experimentally measured transmission characteristics of the tunable coupler ring by tuning $\text{PS}_\kappa$ with $\text{PS}_\lambda = 0$ mW, (b) transmission characteristics of the tunable coupler ring by tuning $\text{PS}_\lambda$ with $\text{PS}_\kappa = 10$ mW, (c) calculated Q-factor and extinction of the characteristics shown in Fig. 2.21a, (d) calculated Q-factor and extinction of the characteristics shown in Fig. 2.21b, (e) extracted coefficients $r, a$ using the least square fit for the characteristics shown in Fig. 2.21a, and (f) extracted coefficients $r, a$ using the least square fit for the characteristics shown in Fig. 2.21b . . . . .	43
2.22	(a) Delay characteristics of the tunable coupler ring and its fit with the theoretical model for over-coupled (OC) and under-coupled (UC) region with similar extinction ( $\sim 10$ dB), and (b) comparison of measured peak time delay at the resonant wavelength with the theoretical delay, for different thermal power applied to the phase shifter $\text{PS}_\kappa$ . . . . .	45

2.23	The experimental setup to characterize the RF photonic bandpass filter with symmetric rejection. EDFA: erbium doped fiber amplifier, PC: polarization controller, FOC: fiber-optic coupler. . . . .	46
2.24	(a) Measured $S_{21}$ of the microwave photonic filter centered at 10 GHz with the in-house fabricated microring resonator (see Fig. 2.16), (b) measured $S_{21}$ of the microwave photonic filter centered at 10 GHz with the foundry-fabricated passive directional coupler ring (see Fig. 2.19), (c) microwave photonic filter response using the foundry-fabricated MRR with frequency tuned from 2 GHz to 14 GHz, using the thermo-optic phase shifter $PS_\lambda$ , and (d) extracted 3-dB bandwidths of the filter responses shown in the Fig. 2.24c. . . . .	48
2.25	(a) Measured $S_{21}$ of the microwave photonic filter centered at 10 GHz by tuning the coupling coefficient of the tunable directional coupler ring (see Fig. 2.19) using the phase shifters $PS_\kappa$ and $PS_\lambda$ , and (b) the link gain of the filter responses variation with the filter bandwidth, obtained by tuning the coupling coefficient of the tunable directional coupler ring. . . . .	49
3.1	(a) The schematic of the proposed OSP chip along with its operational scheme for the RF photonic bandpass filter functions with symmetric out-of-band rejection; (b) top-left: schematic representation of the phase modulated optical spectrum with RF frequency band centering around $f_m$ . Top-right: optical transmission characteristics of the modulated laser light along with the transmission and phase spectrum of the OSP, $f_1, f_2$ correspond to the resonance spacings with respect to the laser carrier frequency $\nu_0$ . Bottom-left: the phase spectrum of the beat signal corresponding to carrier and USB (top), and carrier and LSB (bottom). Bottom-right: schematic representation of the phase deviation $\Delta\phi$ (from $\pi$ ) between beat photocurrents $i_+$ and $i_-$ at the photodetector as a function of RF frequency (top), and the RF filter response corresponding to the superposition of $i_+$ and $i_-$ at the photodetector output. . . . .	52
3.2	Left: schematic top view of an MRR design in SOI platform for which the ring waveguide is relatively wider than the bus waveguide; the design is to facilitate desired value of $r$ and resonance wavelength setting using thermo-optic phase-shifters $PS_\lambda$ and $PS_\kappa$ ; $L_{dc}$ is the length of the parallel section of the directional coupler, $R$ is the bend radius of the ring waveguide. Right: schematic cross-sectional view of the the coupler annotated with important design parameters. . . . .	54
3.3	Transmission characteristics of the MRR exhibiting resonances corresponding to fundamental ( $TE_0$ ) and first-order ( $TE_1$ ) guided modes at $\lambda_{r0} \sim 1549.792$ nm and $\lambda_{r1} \sim 1549.3$ nm, for the parameter values given in Table 3.1. . . . .	55

3.4	Simulation results of a MRRs for the parameter values given in Table 3.1: (a) the self-coupling coefficient $ r_0 $ as a function of the effective phase mismatch $\Delta\beta_0$ (between the fundamental modes in bus and ring waveguides): the values corresponding to bus and ring waveguides dimensions $\{W_1 = W_2 = 0.5 \mu\text{m}\}$ and $\{W_1 = 0.5 \mu\text{m}, W_2 = 1 \mu\text{m}\}$ are annotated; (b) the self-coupling coefficient $ r_0 $ as a function of the differential temperature $\Delta T$ between the bus and ring waveguides in the coupler region for $\{W_1 = W_2 = 0.5 \mu\text{m}\}$ and $\{W_1 = 0.5 \mu\text{m}, W_2 = 1 \mu\text{m}\}$ ; (c) the MRR extinction ratio as a function of $\Delta T$ between the bus and ring waveguides in the coupler region for $\{W_1 = W_2 = 0.5 \mu\text{m}\}$ and $\{W_1 = 0.5 \mu\text{m}, W_2 = 1 \mu\text{m}\}$ . . . . .	57
3.5	Phase and amplitude spectrum for single MRR and cascaded double MRRs: (a) Calculated phase difference (deviation from $\pi$ ) between the LSB and USB beat signals at the photodetector as function of frequency; and (b) the simulated RF filter response for single ring and cascaded ring configuration with 600 MHz bandwidth. Calculations are carried out for $f = 10$ GHz (laser wavelength position with respect to a resonant frequency of the MRR) for the single ring and $f_1 = 9.9375$ GHz, $f_2 = 10.0625$ GHz for cascaded ring. . . . .	59
3.6	(a) The RF filter response with tunable bandwidth by detuning $\Delta f =  f_2 - f_1 $ , (b) the change in MRR Q-factor and extinction ratio with the coupling coefficient $ t_0 ^2$ with under-coupled (UC), over-coupled (OC) and critically coupled (CC) regions marked, (c) the plot of change in tunable bandwidth range of the RF filter and the corresponding change in RF link gain for different coupling coefficients (Q-factor) of the MRR, and (d) the tuning of RF central frequency by detuning the resonance spacing $f_1 + f_2$ and maintaining constant $\Delta f =  f_2 - f_1  = 125$ MHz and MRR coupling coefficient $ t_0 ^2 = 2.7$ %. . . . .	61
3.7	(a) Mask layout of the fabricated structure comprising of two cascaded OSP MRRs (D1 and D2), reference asymmetric directional coupler (D3), reference single microring resonator (D4) along with grating couplers, metal routing, contact pads and test heater elements, (b) zoomed-in mask layout indicating the grating coupler and an extra polygon added to avoid to the stitching error in e-beam lithography, (c) mask layout of the rib waveguide based OSP MRR (D2) along with the phase shifters and (d) contact pads for the probing of the fabricated structures along with its dimensions. . . . .	65
3.8	Microscope images of the fabricated structures during different stages of the active fabrication process: (a) after the contact patterning and development, (b) post Aluminium metal deposition and lift-off, (c) after microheater patterning and development, and (d) post Titanium deposition and lift-off. . . . .	66

3.9	Scanning electron microscope (SEM) images of the fabricated structures: (a) grating coupler, (b) zoomed image of the grating coupler with 49.5 % duty cycle, (c) asymmetric directional coupler of the fabricated ring (device D2) indicating the integrated microheater $PS_{\kappa 2}$ and the device dimensions, and (d) ring waveguide integrated microheater $PS_{\lambda 2}$ . . . . .	67
3.10	Microscope image of the fabricated OSP (a) with asymmetric DC as the tunable coupler (design #1), and (b) with MZI as the tunable coupler (design #2), along with a reference tunable coupler, a reference MRR and test microheater structures. . . . .	68
3.11	Transmission characteristics of the fabricated (a) single MRR; and (b) cascaded MRR devices around $\lambda \sim 1540$ nm. . . . .	69
3.12	The thermo-optic tuning characteristics of: (a) resonance wavelength; and (b) extinction ratio of MRR2 using the phase shifters $PS_{\lambda 2}$ and $PS_{\kappa 2}$ , respectively, for the different settings of the thermal power level $P_{th}$ . . . . .	71
3.13	The transmission characteristics of the fabricated OSP designs (1 % tapped from $FOC_2$ shown in Fig. 2.23) for a programmed setting of thermo-optic phase shifters, along with the launched optical carrier for a RF photonic bandpass filter with symmetric out-of-band rejection: (a) for OSP design #1, $\lambda_0 = 1540.032$ nm, $PS_{\kappa 1} - 83.7$ mW, $PS_{\lambda 1} - 10.8$ mW, $PS_{\kappa 2} - 0$ mW, $PS_{\lambda 2} - 0$ mW, central frequency $\sim 8$ GHz, and (b) for OSP design #2, $\lambda_0 = 1542.625$ nm, $PS_{\kappa 1} - 0$ mW, $PS_{\lambda 1} - 0$ mW, $PS_{\kappa 2} - 21.8$ mW, $PS_{\lambda 2} - 0$ mW, central frequency $\sim 7$ GHz. . . . .	72
3.14	(a) Measured RF filter response with single ring and cascaded ring configuration, and (b) measured RF filter response at 8 GHz central frequency with tunable bandwidth of 0.84 GHz - 1.8 GHz. The given results correspond to OSP design #1. . . . .	73
3.15	(a) Measured RF filter response with single ring and cascaded ring configuration, and (b) measured RF filter response with tunable bandwidth of 3.2 GHz - 5.8 GHz. The given results correspond to OSP design #2. . . . .	74
3.16	(a) Measured RF filter response with central frequency tuned from 2 GHz - 8 GHz and fixed 3-dB bandwidth close to 1 GHz, and (b) the 3-dB bandwidths of the measured filter responses at different central frequencies. . . . .	75
4.1	(a) Schematic representation of the PMA design based on 14 thermo-optically tunable MZIs with four input ports (I1, I2, I3 and I4) and four output ports (O1, O2, O3 and O4); and (b) schematic top view of an MZI used as the tunable basic unit (TBU) in the mesh architecture annotated with its physical design parameters and their values: two phase shifters ( $PS_{mX}$ , $PS_{mY}$ ) on both the arms and indicating the dimensions of the individual components of the TBU. MMI: multimode interferometers, $PS_{mX}$ , $PS_{mY}$ corresponds to the integrated phase shifter to both the arms of the $m$ -th TBU, where $\{X, Y\} = \{L, R\}$ (left and right) for the vertical TBUs (3, 6, 9 and 12), $\{X, Y\} = \{T, B\}$ (top and bottom) for the remaining horizontal TBUs and $R$ is the waveguide bend radius. . . . .	80



4.2	Schematic representation of the PMA to operate in three different MRRs in all-pass configurations with 3-mm (configuration-1), 6-mm (configuration-2), and 8-mm (configuration-3) cavity lengths, respectively. Inset: color-codes to indicate functions of TBUs. . . . .	82
4.3	Component level schematic representation for the realization of microwave photonic bandpass filter using PMA-based OSP: $P_{RF,in}$ : input RF signal power (frequency tunable), $PS_k$ : MZI based tunable phase shifter to tune the MRR coupling coefficient, $PS_\lambda$ : MZI based tunable phase shifter to tune the MRR resonant wavelength, $i_{PD}$ : photocurrent generated at the detector, $R_S$ : internal resistance of the detector, $R_L$ : load resistor, $R_{mat}$ : resistor to match the detector and the load such that $R_S    R_{mat} = R_L$ , $i_{RF}$ : photocurrent through the load resistor, $P_{RF,out}$ : average output RF power. . . . .	83
4.4	Theoretical demonstration of multiband microwave photonic filter using PMA based OSP: (a) Normalized optical power transmission and phase associated with its electric field of the MRR in configuration-1 around the carrier frequency $\nu_0$ ( $\pm 45$ GHz); (b) optical power transmission characteristics of the modulated laser light aligned with the four resonances of the equivalent MRR, indicating the resonance positions at $f_1, f_2, f_3, f_4$ with respect to the laser carrier frequency $\nu_0$ , such that $f_1 + f_2 = \text{FSR}$ and $f_3 + f_4 = 3\text{FSR}$ ; (c) the difference in phase of the detected ac beat signals corresponding to optical carrier and USB ( $i_+$ ), and the optical carrier and LSB ( $i_-$ ); and (d) calculated $S_{21}$ ( $= P_{RF,out}/P_{RF,in}$ ) exhibiting pass-bands around microwave X- and Ka-bands: The simulation results are for the parameter values given in Table. 4.2 and $\Delta f_{12} = \Delta f_{34} = 1$ GHz. . . . .	84
4.5	Simulation of $S_{21} = P_{RF,out}/P_{RF,in}$ exhibiting multi-band microwave photonic filter using PMA based OSP and the parameter values given in Table-2: (a) PMA configuration-2 (see Fig. 4.2) gives simultaneous bandpass filter response around C-, K- and Ka-bands by setting $r = 0.83$ , $a = 0.75$ ; and (b) PMA configuration-3 (see Fig. 4.2) gives simultaneous bandpass filter response around C-, Ku-, K- and Ka-bands by setting $r = 0.49$ , $a = 0.54$ . . . . .	86
4.6	(a) Microscope image of the fabricated PMA structure along with a few test structures; and (b) PMA mounted on a Aluminum housing and electrically packaged with necessary DC printed circuit boards (PCB), thermistor and thermo-electric cooler (TEC). . . . .	89
4.7	Experimental setup for the demonstration of multiband microwave photonic bandpass filter functions: Opt. Amp. - optical amplifier; EDFA - erbium doped fiber amplifier; PC - polarization controller; FOC - fiber-optic coupler; PMA - programmable mesh architecture; TEC - thermo-electric cooler; $P_{in}$ - input optical power ( $= -5.6$ dBm) from OSSA; and $P_{out}$ - output optical power from PMA package. . . . .	91

4.8	(a) Schematic representation of the programmable square mesh indicating an all-cross path from input I1 to output O2 (I1→O2); (b) measured optical power spectrum transmitted at the output ports before phase error corrections, indicating the highest-case crosstalk of 8 dB between O2 and other output ports; and (c) measured optical power spectrum for the selected path at all the output ports after phase error corrections (total thermal power burnt = 11.34 mW) indicating the highest-case crosstalk improved to 21.2 dB between O2 and other output ports. . . . .	93
4.9	(a) Measured MRR response by programming the mesh network to configuration-1 (see Fig. 4.2) exhibiting two resonances around $\lambda = 1550$ nm with an FSR = 186 pm (23.25 GHz); and (b) the least square fit of the measured data (first resonance in Fig. 4.9a around 1545.06 nm) using Eq. (2.3) to extract coupling coefficient $r$ and loss factor $a$ . . . . .	95
4.10	Thermo-optic resonance tuning of MRR in configuration-1 for a given coupling condition ( $PS_k = 18.15$ mW): (a) Wavelength dependent transmission characteristics for different micro-heater power delivered by $PS_\lambda$ ; (b) extracted values of $r$ and $a$ for the ring responses as a function of microheater power delivered by $PS_\lambda$ . . . . .	96
4.11	(a) Measured characteristics of the PMA programmed to MRR in configuration-1 by tuning $PS_k$ in the range of 18.15 - 23.46 mW; and (b) extracted values of $r$ and $a$ for the ring responses at different $PS_k$ . . . . .	97
4.12	Experimental observation of resonance extinction and Q-values as a function of through-put coupling coefficient $r$ (obtained by powering $PS_k$ ) for the three configurations of the electrically packaged PMA: (a) extinction ratio; and (b) the Q-value. The subscripts 1, 2 and 3 indicated in the figure for CC, $r$ , $a$ and $Q$ correspond to the MRR configuration. . . . .	99
4.13	Demonstration of X- and Ka-band filter using the MRR configuration-1 of the PMA: (a) The transmission characteristics of the MRR along with the positioning of optical carrier ( $\lambda_0 = 1545.625$ nm) indicating the operating condition to realize a two-band microwave photonic filter, with a band spacing of $\sim 23.25$ GHz; and (b) Experimental RF filter response exhibiting passbands around X-band and Ka-band closely matching with simulation results. The MRR configuration-1 was tuned such that the resonance extinction = 10 dB, Q-value = $1.2 \times 10^5$ with $f_1 = 11.37$ GHz, $f_2 = 12.19$ GHz, $f_3 = 34.47$ GHz, $f_4 = 35.59$ GHz . . . . .	100
4.14	(a) Measured two-band microwave filter response with tunable bandwidth for 3-mm cavity length MRR configured in under-coupled region with extinction = 10 dB, $Q = 1.2 \times 10^5$ ; and (b) the corresponding variation of the RF link gain with the filter bandwidth. . . . .	101

4.15	(a) Measured two-band microwave filter response with tunable bandwidth using configuration-1 MRR programmed to operate in over-coupled region with extinction = 10 dB, $Q = 0.75 \times 10^5$ ; (b) calculated $\Delta\phi$ variation of two-band microwave filter for MRR operating in over-coupled (OC) and under-coupled (UC) region with 10 dB extinction and (c) measured two-band microwave filter response with tunable bandwidth using configuration-1 MRR programmed to operate in over-coupled region with extinction = 5 dB, $Q = 0.6 \times 10^5$ . . . . .	103
4.16	(a) Measured three-band microwave filter response with tunable bandwidth (2 GHz - 6 GHz) using configuration-2 MRR operating in under-coupled region with extinction = 10 dB, $Q = 1.2 \times 10^5$ , and (b) Measured four-band microwave filter response with tunable bandwidth using configuration-3 MRR operating in under-coupled region with extinction = 10 dB, $Q = 0.8 \times 10^5$ . . . . .	104
4.17	Output RF power variation for fundamental tone $f_{rf1}$ and IMD3 tone $2f_{rf1} - f_{rf2}$ with the input RF power along with the linear fits and indicating the link gain $G = (-33.04 \text{ dB} ; P_{RF,out} \text{ for } P_{RF,in} = 0 \text{ dBm})$ , input intercept point $IIP_3$ and output intercept point $OIP_3$ . The subscript three correspond to the third order inter-modulation terms and $p_{N,out}$ - output noise power spectral density. . . . .	107
4.18	Experimental setup for the demonstration of X-band radio over fiber receiver link. BBU - baseband unit; RRH - remote radio head; Opt. Amp. - optical amplifier; EDFA - erbium doped fiber amplifier; PC - polarization controller; FOC - fiber-optic coupler; PMA - programmable mesh architecture; TEC - thermo-electric cooler; $P_{in}$ - input optical power (= -5.6 dBm) from OSSA; $P_{out}$ - output optical power from PMA package; AWG - arbitrary waveform generator; PRBS - pseudo-random binary sequence; EA - electrical amplifier; LO - local oscillator; LPF - low-pass filter; BB - baseband; ESA - electrical spectrum analyzer; and RTO - real-time oscilloscope. . . . .	109
4.19	Eye diagram of the received PRBS data with the PMA programmed to configuration-1 with 10 dB resonance extinction in over-coupled state and the data transferred with a carrier frequency of (a) 11 GHz; (b) 15 GHz; (c) calculated BER of the receiver link with the carrier frequency of the PRBS data, and (d) Calculated BER of the receiver link with the change in the extinction (coupling condition) of the ring resonator. OC - over-coupled; CC - critically-coupled; and UC - under-coupled. . . . .	111

5.1	(a) The schematic of the proposed OSP chip along with its operational scheme for the RF photonic bandpass filter functions with symmetric out-of-band rejection; (b) schematic representation of the fabricated ring resonator of the OSP indicating the critical dimensions, (c) optical transmission characteristics of the modulated laser light along with the transmission and phase spectrum of the OSP, $f_1, f_2, f_3, f_4$ correspond to the resonance spacings with respect to the laser carrier frequency $\nu_0$ , and (d) schematic representation of the phase deviation $\Delta\phi$ (from $\pi$ ) between beat photocurrents $i_+$ and $i_-$ at the photodetector as a function of RF frequency (top) and microwave filter response corresponding to the superposition of $i_+$ and $i_-$ at the photodetector output. . . . .	118
5.2	(a) Cross-sectional view of the PN doped silicon waveguide for phase modulator, and (b) cross-sectional view of the vertical Ge-PIN photodetector. . . . .	121
5.3	Schematic representation of the designed PIC for microwave photonic filter with on-chip modulator, detector and single/cascaded ring resonator along with the necessary 90:10 taps. . . . .	122
5.4	Microscope image of the fabricated PIC along with the zoomed images of input grating coupler array, ring resonator, multi-mode interferometer, 90:10 tap and photodetector. . . . .	122
5.5	(a) Electrically packaged PIC with necessary housing, DC printed circuit boards (PCB), thermistor and thermo-electric cooler (TEC), (b) zoomed-in microscope image of the packaged module showing the wirebonds between the PIC and the DC PCB, and (c) snapshot of the PIC package probed with the necessary optical and electrical connections (DC: wirebonded to PCB, RF: using GSG infinity probe), also indicating the contact substrate and ISS card for planarization and probe calibration. . . . .	124
5.6	Schematic of the experimental setup used to characterize the on-chip phase modulator. OSA: optical spectrum analyzer, PNA: performance network analyzer, PD: photodetector, LCA: lightwave component analyzer, and SMU: source meter unit. . . . .	125
5.7	(a) Optical spectrum of the phase-modulated optical carrier ( $\lambda_0 \sim 1550$ nm) for different RF frequencies, (b) measured $S_{21}$ characteristics of the single sideband suppressed on-chip phase modulator for different values of reverse bias voltage, and indicating the 3-dB bandwidth of the measured $S_{21}$ at -2 V, and (c) extracted 3-dB bandwidth of the on-chip phase modulator for different values of reverse bias voltages. . . . .	127
5.8	Schematic of the experimental setup used to characterize the on-chip photodetector. PNA: performance network analyzer, PD: photodetector, LCA: lightwave component analyzer, and SMU: source meter unit. . . .	128

5.9	(a) Measured dark current of the PD for different values of reverse bias voltage, (b) measured photocurrent of the PD for different values of reverse bias voltage for different optical powers launched on to the PD, (c) measured photocurrent of the PD for different launched optical powers for $V_{\text{bias}}$ of -2 V and the linear fit for responsivity extraction, and (d) extracted responsivity of the PD for different values of applied reverse bias voltage. . . . .	130
5.10	(a) $S_{21}$ characteristics of the photodetector for different values of reverse bias voltage, (b) extracted 3-dB bandwidth of the photodetector for different values of reverse bias voltage. . . . .	131
5.11	(a) Normalized transmission characteristics of MRR1 of device D3 for $PS_{\kappa 1} = 18.4$ mW, (b) normalized transmission characteristics of MRR1 of device D3 by tuning $PS_{\kappa 1}$ in the range of 18.4 mW - 22.1 mW, (c) extracted Q-factor and extinction of the ring responses given in Fig. 5.11b, and (d) measured optical spectrum along with the optical carrier for the set values of $PS_{\kappa 1} = 18.4$ mW, $PS_{\kappa 2} = 23.2$ mW, $PS_{\lambda 1} = 5$ mW, $PS_{\lambda 2} = 0$ mW, such that $f_{c1} = 8$ GHz and $f_{c2} = 35.5$ GHz. . . . .	132
5.12	(a) Schematic of the experimental setup used to measure the microwave photonic filter response with the on-chip modulator and photodetector, (b) snapshot of the PIC package probed with the necessary optical and electrical connections (DC: wirebonded to PCB, RF: using GSGSG probe), and (c) measured $S_{21}$ of the microwave photonic link with OSP turned on (filter response) and off (crosstalk between RF IO). PNA: performance network analyzer, PD: photodetector, OSSA: optical source and spectrum analyzer and SMU: source meter unit. . . . .	134
5.13	(a) Schematic of the experimental setup used to measure the microwave photonic filter response with the on-chip modulator and an external photodetector, (b) schematic of the experimental setup used to measure the microwave photonic filter response with the off-chip modulator and on-chip photodetector, (c) measured two-band microwave photonic filter response with on-chip modulator, and (d) measured two-band microwave photonic filter response with on-chip photodetector. . . . .	136
5.14	(a) Measured two-band microwave photonic filter response with tunable bandwidth (1.5 - 3.8 GHz) at $f_{c1} = 8$ GHz and $f_{c2} = 35.5$ GHz, (b) measured two-band microwave photonic filter response with tunable frequency ( $f_{c1}$ : 5 to 18 GHz, $f_{c2}$ : 38.5 to 25.5 GHz), with a bandwidth of $\sim 2$ GHz, and (c) the 3-dB bandwidths of the measured filter responses over the range of tuned central frequencies. . . . .	138
6.1	(a) Schematic representation of the microwave photonic filter looped back to realize an optoelectronic oscillator using SiN-MRR, (b) experimentally measured tunable (up to 40 GHz) narrowband ( $\sim 290$ MHz) filter response using SiN-based high-Q MRR ( $\sim 2.5 \times 10^6$ ), and (c) experimentally measured tunable (up to 20 GHz) optoelectronic oscillator response with side mode suppression ratio $\geq 60$ dB. . . . .	147

A.1	Component level schematic representation for the realization of microwave photonic bandpass filter in simulations: $P_{RF,in}$ : input RF signal power (frequency tunable), $H$ is the transfer function of the optical signal processor, $i_{PD}$ : photocurrent generated at the detector, $R_S$ : internal resistance of the detector, $R_L$ : load resistor, $R_{mat}$ : resistor to match the detector and the load such that $R_S    R_{mat} = R_L$ , $i_{RF}$ : photocurrent through the load resistor, $P_{RF,out}$ : average output RF power.	149
B.1	Schematic cross-section depicting the process steps for the in-house fabrication of SOI waveguides: (a) cleaned SOI substrate, (b) HSQ resist coating on the surface, (c) electron beam lithography for patterning of the rib waveguide, and (d) dry etching (ICPRIE) of the rib waveguide	159
B.2	Schematic cross-section depicting the process steps for the integration of the contact pads, metal routing lines and microheaters, (a) SOI substrate patterned with the rib waveguide, (b) PMMA resist coating on the surface, (c) window opening for Aluminium contact pads and metal routing lines, (d) thermal deposition of Aluminium, (e) Aluminium lift-off using acetone, (f) PMMA resist coating on the surface, (g) window opening for Titanium microheaters, (h) e-beam deposition of the Titanium, (i) Titanium lift-off using acetone.	160
C.1	(a) Normalized transmission characteristics of the in-house fabricated microring resonator with MZI as the tunable coupler indicating its FSR ( $= 0.348$ nm), and (b) the least square fit of the left resonance in Fig. C.1a around 1542.2 nm (using Eq. (2.3)) to extract coupling coefficient $r$ and loss factor $a$ .	163
C.2	The thermo-optic tuning characteristics of fabricated OSP shown in Fig. 3.10b: (a) by tuning the phase shifter $PS_{\kappa 1}$ of MRR1, with $PS_{\kappa 2}$ set to 0 mW, and (b) by tuning the phase shifter $PS_{\kappa 2}$ of MRR2, with $PS_{\kappa 1}$ set to 0 mW.	164
D.1	(a) Schematic representation of the programmable square mesh from input I1 to output O2 with all TBUs in the path operating as a cross-switch, and (b) schematic representation of the programmable square mesh from input I1 to output O1 with TBU 1 operating as a bar-switch and remaining TBUs in the path operating as a cross-switch.	165
D.2	(a) Measured optical power spectrum transmitted at the output ports by sweeping the thermal power applied to the phase shifter $PS_{1B}$ , indicating thermal powers for TBU 1 to operate as cross- and bar-switch, and (b) measured optical power spectrum transmitted at the output ports by sweeping the thermal power applied to the phase shifter $PS_{1T}$ , indicating thermal powers for TBU 1 to operate as bar-switch.	166



# ABBREVIATIONS

<b>Al</b>	Aluminium.
<b>AMF</b>	Advanced Micro Foundry.
<b>AWG</b>	Arbitrary waveform generator.
<b>BBU</b>	Baseband unit.
<b>BOX</b>	Buried Oxide.
<b>BW</b>	Bandwidth.
<b>C-Band</b>	Conventional wavelength band ( $\lambda \sim 1527 - 1567$ nm).
<b>CMOS</b>	Complimentary metal oxide semiconductor.
<b>DC</b>	Directional coupler.
<b>DI</b>	De-ionized (water).
<b>DSO</b>	Digital storage oscilloscope.
<b>DUT</b>	Device under test.
<b>EBL</b>	Electron beam lithography.
<b>ExR</b>	Extinction ratio.
<b>FBMS</b>	Fixed beam moving stage.
<b>FSR</b>	Free spectral range.
<b>FWHM</b>	Full-width at half maximum.
<b>GC</b>	Grating coupler.
<b>GDS-II</b>	Graphinc database system-II (mask file format).
<b>HSiQ</b>	Hydrogen silsesquioxane.
<b>ICPRIE</b>	Inductively coupled plasma reactive ion etching.



<b>IF</b>	Intermediate frequency.
<b>IL</b>	Insertion loss.
<b>IM</b>	Intensity modulator.
<b>IMEC</b>	Interuniversity Microelectronics Centre.
<b>IMWPF</b>	Integrated microwave photonic filter.
<b>L-Band</b>	Long wavelength band ( $\lambda \sim 1567 - 1607$ nm).
<b>LCA</b>	Lightwave component analyzer.
<b>LO</b>	Local oscillator.
<b>MMI</b>	Multi-mode interferometers.
<b>MRR</b>	Microring resonator.
<b>MWP</b>	Microwave Photonics.
<b>MZI</b>	Mach-Zehnder interferometer.
<b>OSA</b>	Optical spectrum analyzer.
<b>PD</b>	Photodetector.
<b>PIC</b>	Photonic integrated circuit.
<b>PM</b>	Phase modulator.
<b>PMF</b>	Polarization maintaining fiber.
<b>PMMA</b>	poly methyl methacrylate.
<b>PNA</b>	Performance network analyzer.
<b>PPIC</b>	Programmable photonic integrated circuit.
<b>RF</b>	Radio frequency.
<b>RoF</b>	Radio over fiber.
<b>RRH</b>	Remote radio head.
<b>SEM</b>	Scanning electron microscope.

<b>Si</b>	Silicon.
<b>SiO<sub>2</sub></b>	Silicon di-oxide.
<b>SMF</b>	single mode fiber.
<b>SOI</b>	Silicon-on-insulator.
<b>TE</b>	Transverse-electric (polarization).
<b>Ti</b>	Titanium.
<b>TiN</b>	Titanium Nitride.
<b>TM</b>	Transverse-magnetic (polarization).
<b>W</b>	Tungsten.



## NOTATION

$\alpha$	waveguide loss
$\beta$	propagation constant
$\epsilon_0$	the dielectric constant of free space
$\kappa$	coupling per unit length in directional coupler
$\lambda$	optical wavelength
$\lambda_0$	laser carrier wavelength
$\lambda_r$	resonant wavelength of microring resonator
$\nu$	optical frequency
$\nu_0$	laser carrier frequency
$\nu_r$	resonant frequency of microring resonator
$a$	waveguide loss factor
$c$	the speed of light in vacuum
$f_{c,RF}$	central frequency of the single band microwave filter
$f_{cn}$	$n$ -th central frequency of the multiband microwave filter
$n_{eff}$	mode effective index
$n_g$	mode group index
$Q$	quality factor of a ring resonance
$r$	self-coupling coefficient in directional coupler
$t$	cross-coupling coefficient in directional coupler



# CHAPTER 1

## INTRODUCTION

This thesis comprehensively studies microwave photonic bandpass filters with silicon microring resonators acting as optical signal processors. The main objective of the thesis is for it to work as the stepping stone towards the demonstration of a microwave photonic filter module with wideband operation, reconfigurable characteristics, monolithic integration of modulator, detector, and required driver electronics and hybrid integration of the laser module. The designs and operation schemes proposed in the thesis are CMOS-compatible and adhere to the industry-standard fabrication design rules, with an option to perform the optical and electrical packaging of the chip. The mentioned traits are critical to extending the carried-out work towards low-cost and large-scale production of the envisioned programmable filter module. The motivation for the research performed, along with the overview of the relevant literature, are discussed in this chapter. Next, the research objectives for the thesis are defined, followed by the outline of the thesis and the individual chapter's organization.

### 1.1 BACKGROUND AND MOTIVATION

Silicon photonics was first envisioned as a solution to overcome the inevitable interconnect bottleneck of the ever-scaling electronic integrated circuits (EIC) [1, 2, 3, 4, 5, 6]. Owing to the complementary metal-oxide semiconductor (CMOS) fabrication compatibility of the silicon-on-insulator (SOI) platform, silicon photonics has seen an exponential rise in the investments and R&D activities over the last three decades [7]. The successful commercialization of high-speed silicon photonic transceivers by companies such as Intel and Luxtera (acquired by Cisco) has boosted the viability of the silicon photonic products [8]. As a result, other applications such as microwave photonics [9], quantum photonics

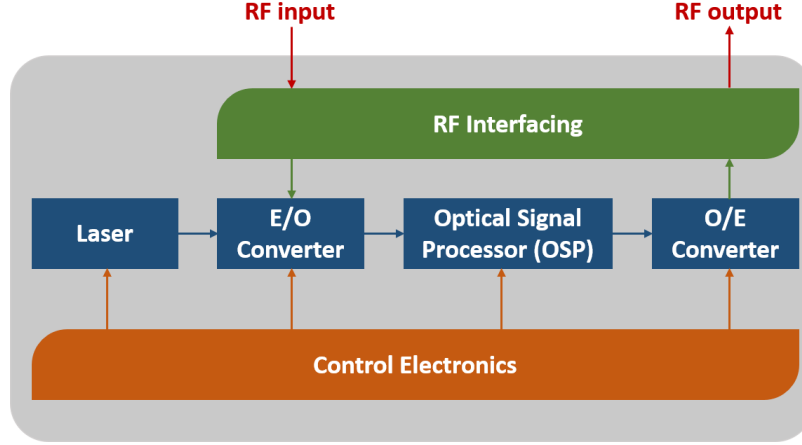


Figure 1.1: Schematic representation of a microwave photonic processor module. E/O: electrical-to-optical, O/E: optical-to-electrical.

[10], neuromorphic computing [11], and lab-on-chip sensors [12] have emerged. Among these, the thesis mainly focuses on microwave photonics, especially for RADAR and satellite communication systems.

Over the years there have been efforts to realize a microwave photonic processor module, similar to the one shown schematically in Fig. 1.1, and demonstrate various functional blocks such as microwave bandpass and bandstop filters [13], up-conversion and down-conversion mixers [14], photonic analog to digital converters (P-ADC) [15] and photonic digital to analog converters (P-DAC) [16]. The mentioned components are an integral part of a wireless communication transceiver [17]. The significant advantage of realizing such components in the photonic domain is the tunable functionalities and wideband operation [18]. The opto-electronic oscillators [19] and arbitrary waveform generators [20] for wireless communication networks, photonic beam-forming networks for multiple-input multiple-output (MIMO) systems [21, 22] and the microwave frequency measurement modules [23] are the other popular microwave photonic processors demonstrated in the literature.

At the core, the processor module comprises the optical laser carrier, electrical-to-optical (E/O) converter or modulator for up-conversion (GHz to THz), optical signal

processor (OSP) block and optical-to-electrical (O/E) converter or photodetector for down-conversion (THz to GHz). The OSP block is the critical component where the up-converted signal is optically manipulated through one or more integrated photonic devices, followed by the down-conversion to achieve the desired microwave functionalities, thus resulting in the processing of the input RF signal. In addition, all the above components require a control electronics block to provide the required bias and control signals. An RF interfacing block is present to transfer the signal of interest into and from the chip.

Even though the concept of a microwave photonic module is very attractive in terms of its advantages, such as tunable functionalities and wideband operation, several challenges are involved in realizing such a processor on par with its electronic counterparts, starting with the choice of material platform, efficiency of modulator and detector, design of the optical signal processor, interfacing of the required control electronics with the photonic chip and the design of a wideband RF interfacing. This thesis focuses on realizing such microwave photonic processor module to perform bandpass filter operation with reconfigurable features for wireless communication networks, focusing mainly on the design aspects of the OSP block. For most of the thesis, the other peripheral components depicted in Fig. 1.1 are considered off-chip. However, the last chapter discusses experimental results with on-chip modulators and detectors, and high-speed RF probes acting as the mentioned RF interfacing unit.

The bandpass filter is an essential radio frequency (RF) receiver architecture block to suppress the noise and eliminate cross-talks [13]. Passive electrical filters are commonly used in the current operating RF architectures because of their robustness and cost-effectiveness. However, filter design for the RF receivers operating at higher frequencies (mm-Wave) is more complex [18]. Moreover, these filters are typically designed to operate at a desired frequency band and are not tunable (as listed in Table. 1.1). Therefore, RF photonic filters have recently been explored as an alternative [13, 24, 25]. For such filters, the choice of material platform determines the scope and complexity involved



Table 1.1: List of commercially available passive microwave electronic filter for different RF bands and their specifications. Source: Mini-Circuits

Model	RF Band	Frequency [GHz]	Bandwidth [GHz]	Insertion Loss [dB]	Rejection [dB]
ZFBP-2400-S+	S	2.4	0.2	2.2	20
ZVBP-5800-S+	C	5.8	0.15	0.8	35
ZVBP-10R5G-S+	X	10.5	1.5	1.5	35
ZVBP-16R3G-S+	Ku	16.3	0.8	1	40
ZVBP-K26R25G+	K	26	1.75	2	63
ZVBP-K34R5G+	Ka	34	3	2	36

in integrating all the necessary components. Among the diverse list of the possible material platforms, indium phosphide (InP), silicon on insulator (SOI) and silicon nitride on insulator (SNOI) are the matured platforms viable to implement monolithic/hybrid integrated microwave photonic filters (IMWPF) [26]. In addition, chalcogenide ( $\text{As}_2\text{S}_3$ ) and lithium niobate on insulator (LNOI) are the two other popular platforms in this area.

The chalcogenide platform is favored for the ultra-narrow band filters (as low as 30 MHz in [27], 25 MHz in [28], and 7.8 MHz in [29]) using on-chip stimulated Brillouin scattering (SBS) process. However, integrating other peripheral components, including the modulators and detectors, is challenging and high production cost limits the scope of the chalcogenide platform [30]. LNOI has recently become popular owing to the platform's high electro-optic coefficient enabling the high-speed (up to 100 GHz) modulators [31]. Owing to this advantage, some LNOI-based proof-of-concept microwave filter demonstrations are available in the literature [32, 33]. Despite its advantage, the non-CMOS-compatible nature of the material hinders the demonstration of large-scale circuits. However, efforts are ongoing towards developing LNOI-based microwave photonic processors with external drivers and photodetectors [34].

On the other hand, InP is popular as it is the only technology capable of monolithic integration of all the active (including lasers and amplifiers) and passive photonic devices [35]. As a result, Fandino et al. [36] have demonstrated a fully integrated InP chip with on-chip laser (output power = -8 dBm; wavelength  $\sim$  1550 nm; SMSR > 40 dB),

modulator (3-dB BW  $\sim 10$  GHz) and photodetector (responsivity = 0.85 A/W, 3-dB BW  $\sim 10$  GHz) for microwave photonic low-pass filter (3-dB BW = 3 GHz; with external photodetector and optical amplifier). Other efforts are also ongoing to mainstream the InP platform to realize monolithic photonic integrated circuits (PIC) [37, 38, 39]. In addition, people have also tried to develop a silicon photonic chip with hybrid/heterogeneous integration of InP laser chip using butt-coupling ( $\sim 2$  dB loss/coupler) [40], micro-lens ( $\sim 3.36$  dB loss/coupler) [41], wafer-scale micro-transfer printing [42] and photonic wire-bonds ( $\sim 0.4$  dB loss/coupler) [43]. Very recently, Tao et al. [44] and Li et al. [45] have demonstrated a hybrid integrated (SOI/InP) microwave photonic processor module using micro-lenses to couple light from InP to Si chip with a coupling loss of 12.3 dB and 3.5 dB, respectively.

The silicon nitride has been a very efficient platform, second only to SOI, for the demonstration of microwave photonic processors because of ultra low-loss TriPlex waveguides ( $< 0.1$  dB/cm) [46, 47] with negligible fiber-to-chip coupling loss ( $< 1$  dB) [35]. However, despite their excellent features, poor electro-optic and thermo-optic properties of silicon nitride and non-CMOS compatible fabrication process of the TriPlex waveguides limit the integration of phase shifters, modulators and detector [35]. Other than, TriPlex waveguides, Ji et al. [48] have demonstrated a stoichiometric deposition of silicon nitride waveguides using low-pressure chemical vapour deposition (LPCVD) with a waveguide loss of 1.4 dB/m, and Pfeiffer et al. [49] have shown the waveguide fabrication using the damascene process with waveguide loss less than 1 dB/m, thus enabling the realization of high-Q microring resonators and low-loss spiral waveguides. In addition, works are also ongoing towards developing low-loss passive SiN devices integrated with active Si devices to compensate for the disadvantages of each platform [50].

Finally, owing to its CMOS compatibility (large-scale production at a low cost), the silicon-on-insulator (SOI) platform, over the years, has been the front-runner choice for

several microwave photonic processor demonstrations. As a result of the decades of R&D innovations in electronic industry, SOI currently is the matured photonic platform with a scope of the monolithic integration of the modulators [51, 52, 53], photodetector [54, 55] and the required electronic driver circuits [8, 56]. Currently, all the commercial silicon photonic foundries offer process design kits (PDK) for high-speed modulators ( $> 30$  GHz) and high-speed detectors ( $> 40$  GHz) [7]. Very recently, global foundries have come up with an optimized process flow enabling the electronic and photonic co-integration on SOI platform with a device layer thickness of 160 nm for photonics and 90 nm for electronics [57]. In addition, the hybrid integration of InP laser and low-loss SiN passive to silicon chips are also currently viable options offered by IMEC and AMF in their PDK libraries [58, 7]. Taking note of all the global technological advancements, in our work reported in the thesis, we set our focus on the novel designs of SOI-based OSPs for developing microwave photonic filters.

In theory, the RF photonic filters are very promising in terms of size, weight and power (SWaP), wide-band tunability, scalability, immunity to electromagnetic interference and programmable filter functions. In practice, there are plenty of scopes for improvement in filter characteristics such as shape factor, out-of-band rejection, link gain, noise figure and spurious free dynamic range to replace its electronic counterparts for mass manufacturing and deployment. Nevertheless, the research progress in integrated RF photonic filters are phenomenal. For example, RF photonic filters demonstrated based on stimulated Brillouin scattering (SBS) [28, 29], comb sources [59], photonic crystal cavity (PhC) [60, 61], distributed Bragg gratings (DBR) [62], micro disk resonators [63, 64], microring resonators (MRR) [44, 65, 66, 67, 68, 69, 70, 71, 72, 73], coupled resonator optical waveguides (CROWs) [74, 75, 76] and ring-assisted Mach-Zehnder interferometers (RAMZIs) [36] are found to be very promising. Especially, the MRR based photonic filters are attractive owing to its lower footprint, higher tunability through electro-optic and/or thermo-optic phase shifters and thereby better bandwidth control.

As already mentioned, the silicon nitride (SiN) on insulator (SNOI) and SOI are two widely used CMOS compatible technology platforms for the demonstration of RF photonic filters, especially for MRR based OSPs. The SiN waveguides in SNOI platform offers low waveguide loss in order to achieve high Q-value of the MRR and to realize filter response with sub-GHz bandwidth [65, 66, 67, 68, 77]. Zhu et al [66], Yang et al [68] and Wang et al [77] have reported a tunable filter response with a bandwidth of 260 MHz, 100 MHz and 63 MHz respectively. However, the thermo-optic/electro-optic tuning for SiN microring resonators are either inefficient or extremely difficult to fabricate; need hybrid integration [35].

Though the silicon waveguides are relatively lossier, they offer a compact design of microring resonators, and losses can be optimized by a better design of waveguide geometry. Moreover, both thermo-optic and electro-optic detuning can be achieved to reconfigure the MRR response. To achieve the sub-GHz bandwidth in SOI platform Qiu et al [70] and Tao et al [44] have used adiabatically tapered low-loss waveguide sections in the ring to improve the Q-factor ( $\sim 10^6$ ). They have reported a RF filter bandwidth of 170 MHz and 100 MHz, respectively. These filters could be detuned to a frequency range up to 18 GHz. The out-of-band rejections are reported as 27 dB. These designs are relatively higher footprints and bandwidth detuning options are not included, which is essential for high-speed data transmission at higher operating frequency range. Also, the filter response exhibits asymmetric out-of-band rejection in reported literature, which is attributed to the phase change in carrier frequency along with the modulated sidebands [65]. This in turn effects the shape factor of the RF photonic bandpass filter limiting its applications. The issue of shape factor degradation due to asymmetric rejection has been addressed recently by considering certain design aspects and operating conditions. Li, et al [65] has used wavelength division multiplexing of two optical carriers before launching into the phase modulator and positioned their wavelengths on the lower and upper sides of the two resonances (with frequency separation greater than the photodetector bandwidth). Song, S., et al [71] has designed a non-identical cascaded ring structure on two different

chips, whereas Yang, Wenjian, et al [69] has used an external phase compensator after the microring resonator. However, all the mentioned methods involve the introduction of additional components into the setup, with no scope for on-chip integration or altering the fabrication process altogether. In this thesis, we propose a novel OSP design on a CMOS-compatible SOI platform to overcome the problem of asymmetric out-of-band rejection.

In addition, even though ring-based OSPs are in-principle easily extendable to realize multiband filter response, due to their periodic notch filter response, we find only a few attempts demonstrating such MRR-based multiband microwave filters. Z. Zhu et al. [66] have used two cascaded ring resonators to realize a two-band microwave bandpass filter. In this case, the spacing between the two bands was adjusted by tuning the individual resonant wavelengths of the MRR. H. Yang et al. [68] have used a multimode ring resonator structure to realize a two-band microwave filter with the resonances corresponding to two modes of the multimode ring. Both cases, the MRR based OSPs were designed with silicon nitride ( $\text{Si}_3\text{N}_4$ ) waveguides and fabricated using low-loss TripleX technology. Though these works are very attractive, the individual passband response exhibits asymmetric out-of-band rejection which we will address in the thesis by a design modification and experimental demonstration.

Very recently, Y. Chen et al. [78] realized a three-band microwave bandpass filter, where the filter band spacing is limited by the MRR's free spectral range (FSR). Moreover, the authors have designed a conventional racetrack resonator in an all-pass configuration with silica waveguides for a fixed radius of 9 mm. Thus, the scope of programmability of the MRR characteristics and the corresponding multiband filter response are limited in the reported experimental demonstration. As the tuning of FSR was not possible for the designed conventional MRR, the number of realizable filter passbands was fixed in the experiments, establishing the requirement of superior programmable photonic integrated circuit (PPIC) design with a scope of tuning the FSR of the ring and correspondingly the

number of filter passbands in the experiments.

The programmable mesh architectures (PMA), as the mentioned PPIC design, have already been tried earlier for single-band microwave photonic filter functions using low-loss  $\text{Si}_3\text{N}_4$  TripleX waveguide technology [79]. Though it was very attractive but the footprint of the device is relatively large ( $3.5 \times 8.5 \text{ mm}^2$ ) as well as it consumes very high electrical power for thermo-optic programming (250 mW per tunable basic building blocks). Moreover, futuristic co-integration of modulator, detectors and electronic driver circuits using CMOS fabrication process is challenging for a low-loss  $\text{Si}_3\text{N}_4$  TripleX technology [35]. On the other hand, SOI-based PMAs have been demonstrated in recent years [80, 81, 82]. However, we do not find any reports to the best of our knowledge which rigorously investigated for multiband microwave filter demonstrations targeting application specific RF bands (e.g., C-band, X-band, Ku-band, and so on).

In addition, we also do not find thorough evaluations of the performance of microwave photonic filters in wireless communication systems; which is critical in realizing the next-generation communication networks with programmable microwave photonic processing blocks. Very recently, Garrett et al. [83] and Tao et al. [84], in their respective works, have demonstrated successful data retrieval in the presence of a jamming signal using bandstop filters and analyzed the quality of the retrieved data. Even though the results are attractive, studying the performance of such communication links with the programmable features of the ring resonators still needs to be fully explored to understand the optimal operating point for the efficient link performance.

## 1.2 RESEARCH OBJECTIVE

As outlined in the previous section, significant efforts are underway to realize microwave photonic filter modules. However, several challenges must be addressed to obtain the filter response and metrics on par with the electronic counterparts. This thesis focuses on designing and demonstrating MRR-based OSPs to realize silicon photonic foundry-

compatible microwave photonic filters. We aim to address the limitation of asymmetric out-of-band rejection of the filter response in single-band and multiband filters and propose novel OSPs to overcome the limitation. For the proposed OSP architectures, we study the effect of the programmable features of the MRR on the filter characteristics and its tuning range. We also investigate the feasibility of integrating such microwave photonic filters in the equivalent radio over fiber receiver link, and study the effect of ring operating conditions on data transmission efficiency. Finally, we provide the experimental results of the microwave photonic filter module with an on-chip modulator and photodetector. The laser sources and control electronics were considered off-chip in the filter module, and the modulator and detector were chosen from the foundry's process design kit. The OSP structures were fabricated using the in-house facilities at the Centre for NEMS and Nanophotonics (CNNP), IIT Madras for the proof-of-concept demonstrations. The PICs were taped out through the silicon photonics foundry for the programmable mesh circuit and module demonstration. The electrical packaging of the PICs reported in the thesis was done at iZMO Microsystems, Bengaluru.

### **1.3 THESIS ORGANIZATION**

To address the objective of the thesis, we begin by understanding the fundamental bottleneck of the microwave photonic bandpass filters with single MRR as the OSP, through numerical simulations, followed by the experimental validations. Subsequently, we propose a novel OSP design and an operation scheme based on cascaded MRRs to overcome the mentioned bottleneck, and validate the same in experiments. Next, we investigate programmable mesh architectures to demonstrate the MRRs free spectral range dependent multiband microwave bandpass filter with reconfigurable filter passbands. Finally, we extend the proposed OSP design of cascaded MRR structure to experimentally demonstrate an integrated microwave photonic filter module with an on-chip modulator and photodetector. The entire work is divided into four main chapters as follows:

**Chapter-2** discusses the operation scheme of the microwave photonic filter based on single ring as the OSP. The theory and the design parameters of the microring resonator with passive and tunable directional coupler and the mentioned operation scheme are thoroughly studied through the numerical simulations to outline its fundamental bottlenecks. The obtained findings in the simulations are validated through the proof-of-concept experiments using both in-house fabricated and foundry fabricated MRR structures. The limitations in the ring response and the corresponding filter response using in-house device has also been outlined.

**Chapter-3** proposes an operation scheme based on a novel OSP design of cascaded MRRs with four thermo-optic phase shifters integrated for the independent control the Q-factor and the resonant wavelength of both the rings. The proposed OSP structure and the operation scheme is thoroughly investigated to realize a tunable frequency and tunable bandwidth filter, in the simulations for different Q-values of the MRR. Next, the OSP was designed using a asymmetric directional coupler to improve the achievable Q-factor using the in-house fabrication and also to tune the coupling coefficient. The OSP design with asymmetric directional coupler and the conventional MZI-based tunable coupler were fabricated at IIT Madras. Next, proof-of-concept experiments with both the fabricated structures were performed to validate the proposed scheme with in the limitations of the experimental setup.

**Chapter-4** investigates the programmable mesh architecture based OSP comprising of fourteen Mach-Zehnder interferometers acting as tunable basic units (TBU). The mesh architecture was experimentally programmed to obtain ring resonator response with three different cavity lengths, and realize multiband microwave photonic filter response with tunable bandwidth and reconfigurable number of passbands (two-, three- and four-band). Here the central frequencies of the filter passbands are dependent on the free spectral range of the microring resonator. For the realization of appropriate ring responses, the mesh architecture was carefully calibrated to estimate the thermal powers required for



individual TBU to operate in the desired state. After the mesh calibration, the two-band filter response (at X-band and Ka-band) was extensively studied to understand the effect of ring coupling coefficient on the link gain, bandwidth tuning range and the spurious free dynamic range (SFDR). For the realized filter response at X-band, a radio over fiber receiver link was established and its performance with operating frequency, ring resonator's coupling coefficient, fiber transmission length and data rate was evaluated by estimating the bit-error rate (BER) of the received data.

**Chapter-5** focuses on the experiments performed towards the realization of a integrated microwave photonic bandpass filter with on-chip modulator, OSP and photodetector. First, the integrated functional blocks were individually tested. Followed by the discussion on the problems faced to measure the filter response with simultaneous probing of modulator and detector due to heavy crosstalk between the input and output RF ports. Finally, the filter responses with tunable frequency and bandwidth are reported with the individual probing of on-chip modulator and on-chip detector.

**Chapter-6** highlights the summary of the research conducted in this thesis, and presents a detailed conclusion and the prospects for future developments.

## CHAPTER 2

### OSP WITH SINGLE MRR

As mentioned in Chapter 1, microring resonators (MRR) are very popular OSPs to realize microwave photonic filters, owing to their simple structure, low footprint and ease of tunability. In this Chapter, we will discuss the operation scheme of the microwave photonic bandpass filter with a single microring resonator as the OSP. To perform the theoretical analysis of the mentioned scheme, we will first discuss the microring resonator's working principle and design aspects. Next, we will provide a thorough simulation results indicating the impact of the microring resonator characteristics on the microwave filter response and the operation scheme's bottlenecks. Finally, we validate the simulated observations with the experimental results using the extensively characterized in-house and foundry-fabricated structures.

#### 2.1 OPERATION SCHEME

The operation scheme comprising a phase modulator (for up-conversion), a microring resonator (as OSP) and a photodetector (for down-conversion) to realize a microwave photonic bandpass filter is given in Fig. 2.1a. A representative RF band is upconverted into an optical frequency range centering around  $\nu_0$  via a phase modulator. The phase modulation of the optical carrier results in an upper sideband (USB) and lower sideband (LSB) with  $\pi$  phase difference, as shown in Fig. 2.1b. The microring resonator breaks the out-of-phase symmetry of the phase-modulated signal, as shown in Fig. 2.1c. Here, the bandstop response of the MRR with resonant frequency  $\nu_r$  ( $= c/\lambda_r$ , where  $c$  is the speed of light) is shown to be aligned with a separation of  $f_{rf}$  from the carrier frequency. The ac component of the output photocurrent across the matched load  $R_L$  is the result of superposition between two beat current signals: (i) the beat current component between

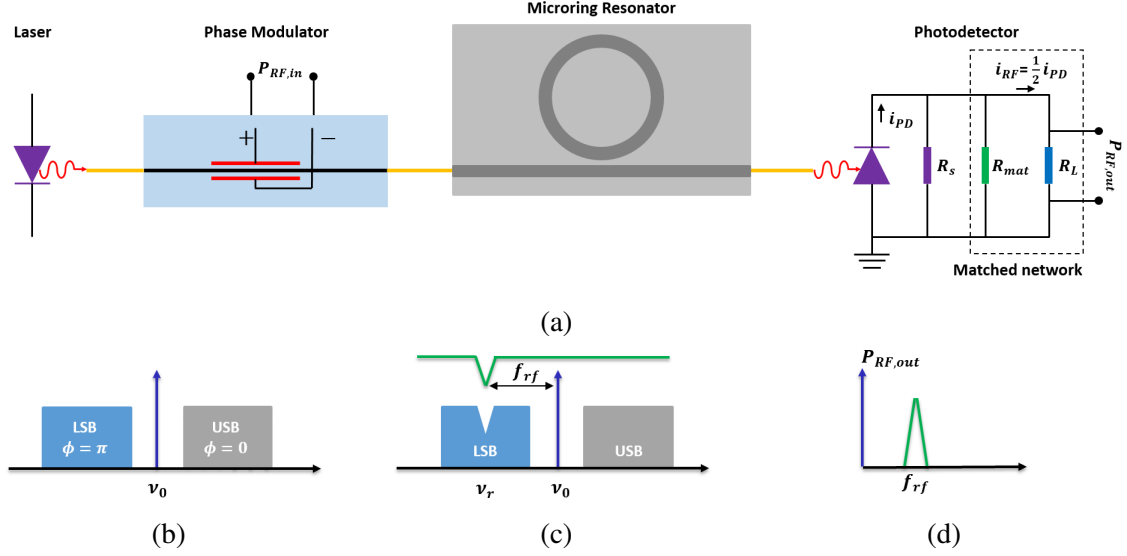


Figure 2.1: (a) The schematic of the microwave photonic bandpass filter with single microring resonator as the OSP, (b) phase modulated spectrum of the optical carrier around  $\nu_0$  with sidebands having  $\pi$  phase difference, (c) the phase modulated optical spectrum aligned with the resonance of a microring resonator with resonant frequency  $\nu_r$ , such that  $f_{rf} = |\nu_0 - \nu_r|$ , and (d) the expected microwave bandpass filter response at the photodetector output with  $f_{rf}$  as the central frequency.

the carrier and the USB,  $i_+$ , and (ii) the beat current component between the carrier and LSB,  $i_-$ . For the phase-modulated optical carrier directly transmitted into the photodetector (in the absence of MRR, i.e.,  $T_r = 1$ ), the phase difference between the beat components  $\Delta\phi = \angle i_+ - \angle i_- = \pi$  for all the frequencies, and thus resulting in the destructive interference of the beat signals for the entire frequency band. Hence, no RF signal is detected at the photodetector output. However, in the presence of the ring due to the inherent  $\pi$  phase shift between the sidebands, a complimentary bandpass response with central frequency  $f_{rf}$  ( $= |\nu_0 - \nu_r|$ ) reflects at the output of the detector, as shown in Fig. 2.1d. However, to completely understand the performance and the bottlenecks of the given operation scheme, we must know the design aspects and the characteristics (both passive and phase tuning) of the microring resonator device. Therefore, in the next section, we will perform a thorough device analysis of the MRR, which is followed the microwave filter performance analysis.

## 2.2 MRR DESIGN

The theory and design aspects of the microring resonators have been widely studied in the literature [85, 86]. However, for completion, we will cover the required fundamentals of the MRR and its influence on the filter response. The top-view schematic of the racetrack MRR in all-pass configuration is shown in Fig. 2.2a. An MRR consists of two waveguides (bus and ring waveguides) placed nearby, forming a cavity by looping back the ring waveguide. The length of the cavity  $L$ , a critical design parameter, is given by the directional coupler length  $L_{dc}$  and the bend radius  $R$  of the ring waveguide ( $L = 2\pi R + 2L_{dc}$ ). The self and cross-coupling coefficients ( $r, t$ ) are crucial design variables to quantify the percentage of light coupled into the ring waveguide from the bus waveguide and vice-versa. For a lossless directional coupler (DC):

$$r^2 + t^2 = 1 \quad (2.1)$$

The coupled light into the ring travels through the ring waveguide experiencing loss and accumulating the phase  $\phi$  ( $= \beta L = \frac{2\pi}{\lambda} n_{eff} L$ ;  $\beta$  and  $n_{eff}$  are the propagation constant and effective index of the mode, respectively). The round-trip survival factor or the loss-factor of electric-field in a ring resonator is denoted by  $a$ , and its expression is given by:

$$a = e^{-\alpha L/2} \quad (2.2)$$

where  $\alpha$  is the waveguide loss. The coupled light into the ring after the round trip interferes with the input light from the bus waveguide. The field intensity builds inside the ring when the accumulated round trip phase  $\phi$  equals the integer multiples of  $2\pi$ . The wavelength for which  $\phi = 2m\pi$  (resonance condition) is the resonant wavelength  $\lambda_r$ , where  $m$  ( $= 1, 2, 3$  and so on) is the resonance order. Following the multiple round trips, the analytical expression for the steady-state transfer function of the MRR is given by:

$$T_r = \frac{E_{out}}{E_{in}} = \frac{r - ae^{-j\phi}}{1 - ar^*e^{-j\phi}} \quad (2.3)$$

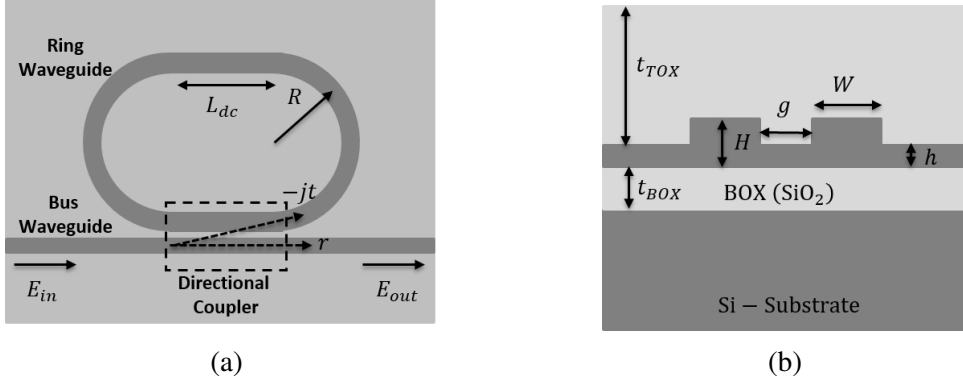


Figure 2.2: (a) Schematic top-view of an typical MRR design in all-pass configuration with passive directional coupler in SOI platform;  $L_{dc}$  is the length of the parallel section of the directional coupler,  $R$  is the bend radius of the ring waveguide, and  $r, t$  are the self and cross coupling coefficients of the directional coupler, and (b) schematic cross-sectional view of the passive directional coupler annotated with important design parameters;  $W$ : waveguide width,  $H$ : device layer thickness,  $h$ : slab height,  $g$ : directional coupler gap,  $t_{BOX}$ : buried oxide thickness (bottom cladding),  $t_{TOX}$ : top oxide thickness (top cladding).

From our earlier discussion and Eq. (2.3), we can infer that: (i) the resonant wavelength and its periodicity is dependent on the waveguide effective index  $n_{eff}$  and its dispersion, and (ii) at resonant wavelength the output field-intensity  $E_{out}$  (and also the field intensity stored inside the ring) are only dependent on the parameters  $r$  and  $a$ . Usually, the effective index and dispersion are fixed with the waveguide geometry for a passive MRR (without any doping in the cavity). The loss is also a predetermined value dependent on the fabrication process. Therefore, the directional coupler is the critical component in the design of microring resonators. The design of the directional coupler is a fundamental yet complex task as it involves various design parameters as marked in Fig. 2.2. Here, to understand the functionality of the directional coupler, we have fixed a few design parameters to the values given in Table 2.1. The parameter values are chosen based on the process design kit (PDK) of the Advanced Micro Foundry (AMF), Singapore.

Using the weak perturbation approximation of the coupled mode theory [87], the self-coupling coefficient  $r$  and cross-coupling coefficient  $t$  of a lossless directional coupler is

Table 2.1: Chosen design parameters of the integration platform and the waveguide geometry for the reported MRR simulations.

	Parameter	Symbol	Values
Wafer	Integration platform	–	SOI
	Device layer thickness	$H$	220 nm
	BOX thickness	$t_{BOX}$	2 $\mu\text{m}$
Waveguide	Waveguide width	$W$	500 nm
	Slab height	$h$	0 nm
	Top cladding material	–	SiO <sub>2</sub>
	Top cladding thickness	$t_{TOX}$	3 $\mu\text{m}$
	Waveguide Loss	$\alpha$	2 dB/cm
	Bend radius	$R$	50 $\mu\text{m}$

given by:

$$r = \cos(\kappa L_{dc}^{eff}); t = \sin(\kappa L_{dc}^{eff}) \quad (2.4)$$

where  $\kappa$  is the field coupling coefficient per unit length,  $L_{dc}^{eff}(= L_{dc} + 2\Delta L_b)$  is the effective coupling length considering the length of the straight section of the directional coupler i.e.,  $L_{dc}$  and the equivalent length due to the close proximity of the bent ring waveguide to the bus waveguide near the DC region i.e.,  $\Delta L_b$  [88]. The multiplication factor 2 is to consider the bent section on both the sides of the DC. Further using the super mode theory [87], the analytical expression for the  $\kappa$  can be expressed as:

$$\kappa = \frac{\pi \Delta n_{eff}}{\lambda} \quad (2.5)$$

where  $\Delta n_{eff}$  is the effective index difference between the symmetric and anti-symmetric modes of the directional coupler and  $\lambda$  is the wavelength of operation. Fig. 2.3 shows the symmetric and anti-symmetric mode profile solutions of the directional coupler indicating the effective indices for  $\lambda = 1550$  nm,  $h = 0$  nm, and gap  $g = 200$  nm.

Fig. 2.4a, shows the variation of the coupling coefficient  $\kappa$  with the DC gap  $g$  at wavelength  $\lambda = 1550$  nm and for the slab heights  $h = 0, 90$  nm and  $150$  nm. The coupling coefficient decreases exponentially with the increase in coupler gap  $g$ , i.e., the farther the waveguide, the lesser the coupling. Fig. 2.4b, shows the variation of the coupling

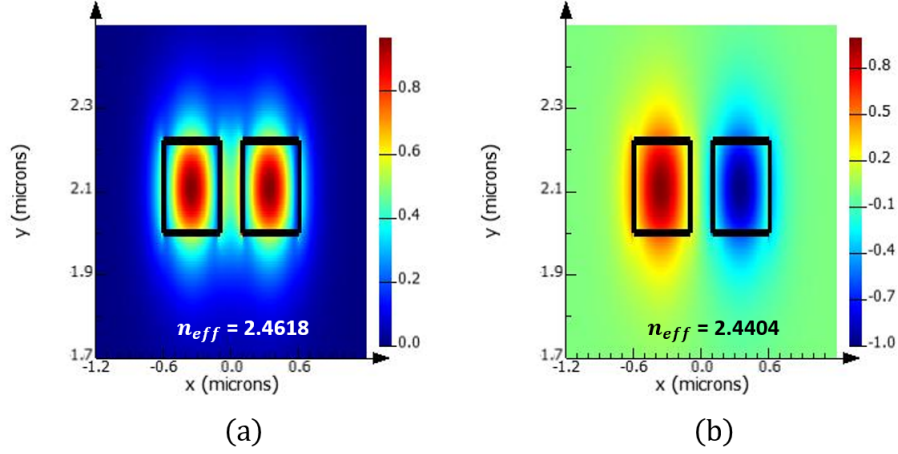


Figure 2.3: The (a) symmetric and (b) anti-symmetric mode solutions of the directional coupler for the design parameters listed in Table. 2.1 at  $\lambda = 1550$  nm, and gap  $g = 200$  nm.

coefficient  $\kappa$  with wavelength  $\lambda$  at gap  $g = 200$  nm for the slab heights  $h = 0, 90$  nm and  $150$  nm. Here, the slope  $d\kappa/d\lambda$  indicates the directional coupler's dispersion, which can be engineered with the waveguide dimensions [89]. In both the figures, it is evident that  $\kappa$  is strong for the waveguides with higher slab heights due to strong evanescent tails in the slab region, which can leak easily to the second waveguide.

Next, the self-coupling coefficient's variation by substituting  $\kappa$  for the chosen waveguide dimensions (listed in Table. 2.1) with the coupler gap  $g = 400$  nm and coupler length  $L_{dc} = 10 \mu\text{m}$ , in equation (2.4), is given in Fig. 2.5a ( $\Delta L_b$  estimated using the method discussed in [88]). In the same figure, the loss factor  $a \sim 0.9923$  calculated using Eq. (2.2), for the waveguide loss of  $2 \text{ dB/cm}$ , ring radius  $R = 50 \mu\text{m}$  and coupler length  $L_{dc} = 10 \mu\text{m}$  is also marked. Based on our experimental observations, we have considered the waveguide loss to be wavelength-independent. Also, in the calculations, we have not considered the waveguide bend loss and coupler loss. Depending on the values of  $r$  and  $a$ , the MRR operation can be divided into three conditions: (i) under-coupled ( $r > a$ ; UC), (ii) over-coupled ( $r < a$ ; OC) and (iii) critically coupled ( $r = a$ ; CC). Here, the coupler gap  $g$  and coupler length  $L_{dc}$  were chosen so the critically coupled condition occurs

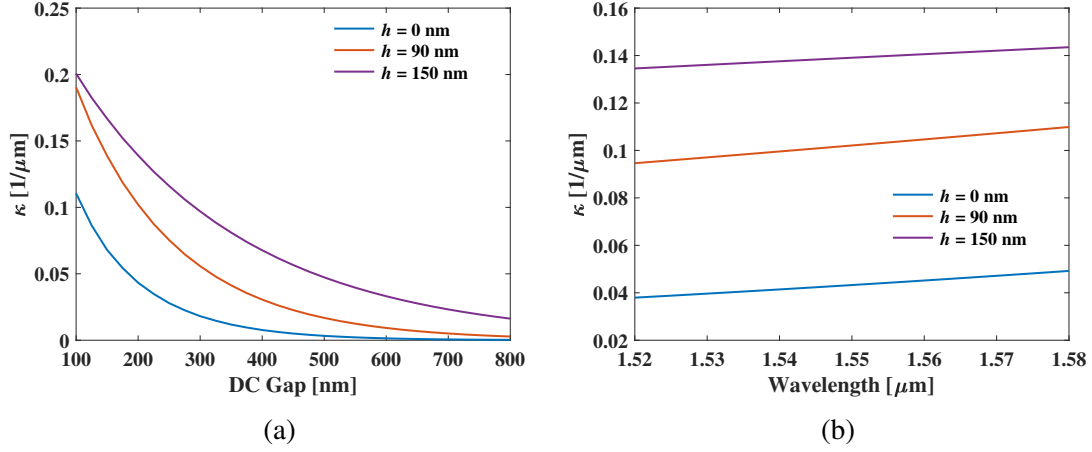


Figure 2.4: The variation of the coupling coefficient  $\kappa$  for chosen waveguide dimensions (listed in Table. 2.1) with three different slab heights  $h = 0, 90$  nm and  $150$  nm with (a) directional coupler gap  $g$  at wavelength  $\lambda = 1550$  nm, and (b) wavelength  $\lambda$  at gap  $g = 200$  nm.

around  $1550$  nm wavelength for the chosen waveguide dimensions. The corresponding MRR characteristics (using equation (2.3)) marked with different coupling conditions is given in Fig. 2.5b.

To understand the periodic notch filter response of the MRR, one must define its figure of merits as shown in Fig. 2.6a and Fig. 2.6b. The free spectral range (FSR) is the spacing between the two successive resonances, and the extinction is the output power difference between the on-resonant and off-resonant wavelengths. The quality factor (Q), which is the ratio of the amount of energy stored in the ring to the energy lost per unit cycle, can be given as  $\lambda_r/\text{FWHM}$ , where FWHM is the full-width at half maximum of the MRR resonance spectrum. Fig. 2.6c shows the extracted Q-factor and the extinction ratio from the MRR characteristics. The figure shows that the MRR's Q-factor is dependent on the operating coupling condition despite having the same extinction ratio.

In addition to coupling coefficient dependent amplitude response (shown in Fig. 2.5b), the MRR is also associated with the coupling coefficient dependent phase ( $\phi_r$ ) and delay ( $\tau_r = -d\phi_r/d\omega$ ) response, which are given in Fig. 2.7. For the same extinction ( $\sim 15$



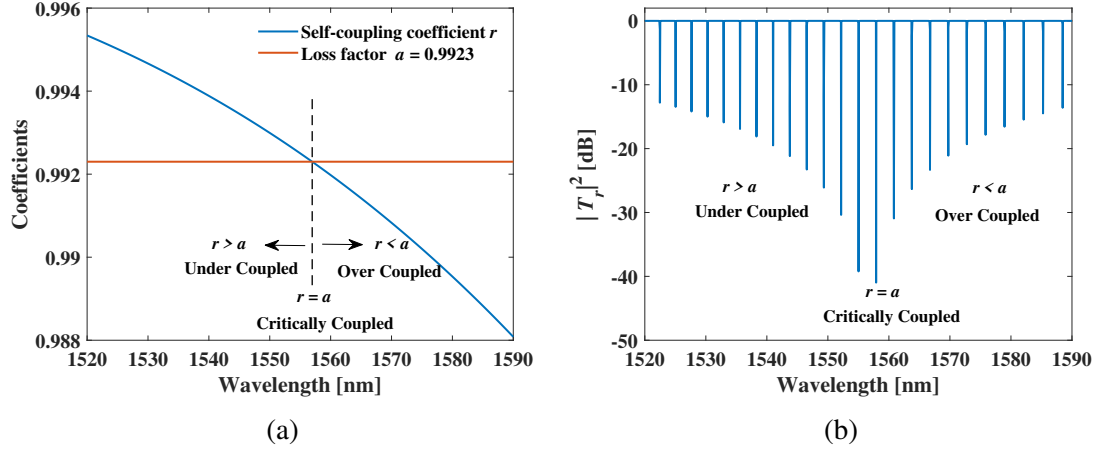


Figure 2.5: (a) The variation of the self coupling coefficient  $r$  of the directional coupler ( $g = 400$  nm, coupler length  $L_{dc} = 10$   $\mu\text{m}$ , and bend radius  $R = 50$   $\mu\text{m}$ ) with wavelength and also marked are the loss factor  $a$  ( $\sim 0.9923$ ; considered wavelength-independent) and different coupling conditions of the MRR, and (b) the corresponding MRR characteristics plotted using equation (2.3), also indicating the coupling conditions; the simulation results in both the figures are for the waveguide geometry given in Table. 2.1.

dB), the MRR has a higher Q-factor ( $\sim 1.4 \times 10^5$ ), adds no phase (see Fig. 2.7a) and a negative delay (see Fig. 2.7b) at resonant wavelength, while operating in undercoupled condition. Whereas, the Q-factor drops ( $\sim 0.85 \times 10^5$ ),  $\pi$  phase (see Fig. 2.7c) and a positive delay (see Fig. 2.7d) is added to the resonant wavelength, for over-coupled condition. Here, the addition of the negative and positive delay correspond to the time delay and advance. As we will see in the next section, the phase response of the MRR is very critical in determining the corresponding filter characteristics. Also, the MRR delay tuning is a very key figure of metric for its use in applications such as quantum information processing [90] and microwave photonic beam-forming networks [91].

Owing to the factors mentioned, a microring resonator integrated with phase shifters to facilitate the independent tuning of the coupling coefficient and the resonant wavelength is highly beneficial in controlling the MRR characteristics and, correspondingly, the response of the microwave photonic filter. In this thesis, we have carried out the phase tuning using thermo-optic mechanism owing to its near zero insertion loss and the

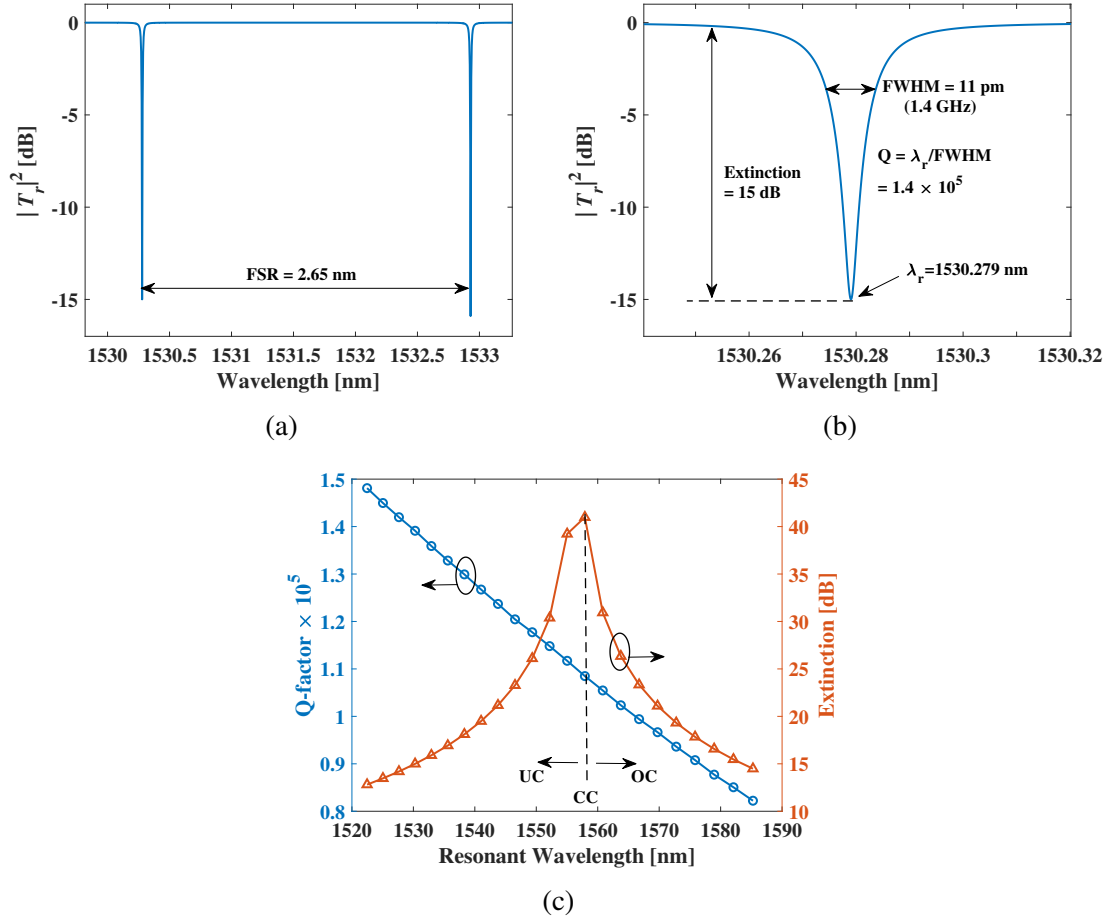


Figure 2.6: (a) The zoomed-in characteristics of the MRR to two resonances to indicate the free spectral range (full-spectrum shown in Fig. 2.5b), (b) the zoomed-in characteristics of the MRR to one resonance (left-resonance of Fig. 2.6a) to indicate the resonance wavelength  $\lambda_r$ , extinction, full-width at half maximum and quality-factor, and (c) the extracted Q-factor and extinction from the MRR spectral characteristics shown in Fig. 2.5b, over the range of resonant wavelengths. UC: under-coupled, CC: critically-coupled, OC: over-coupled.

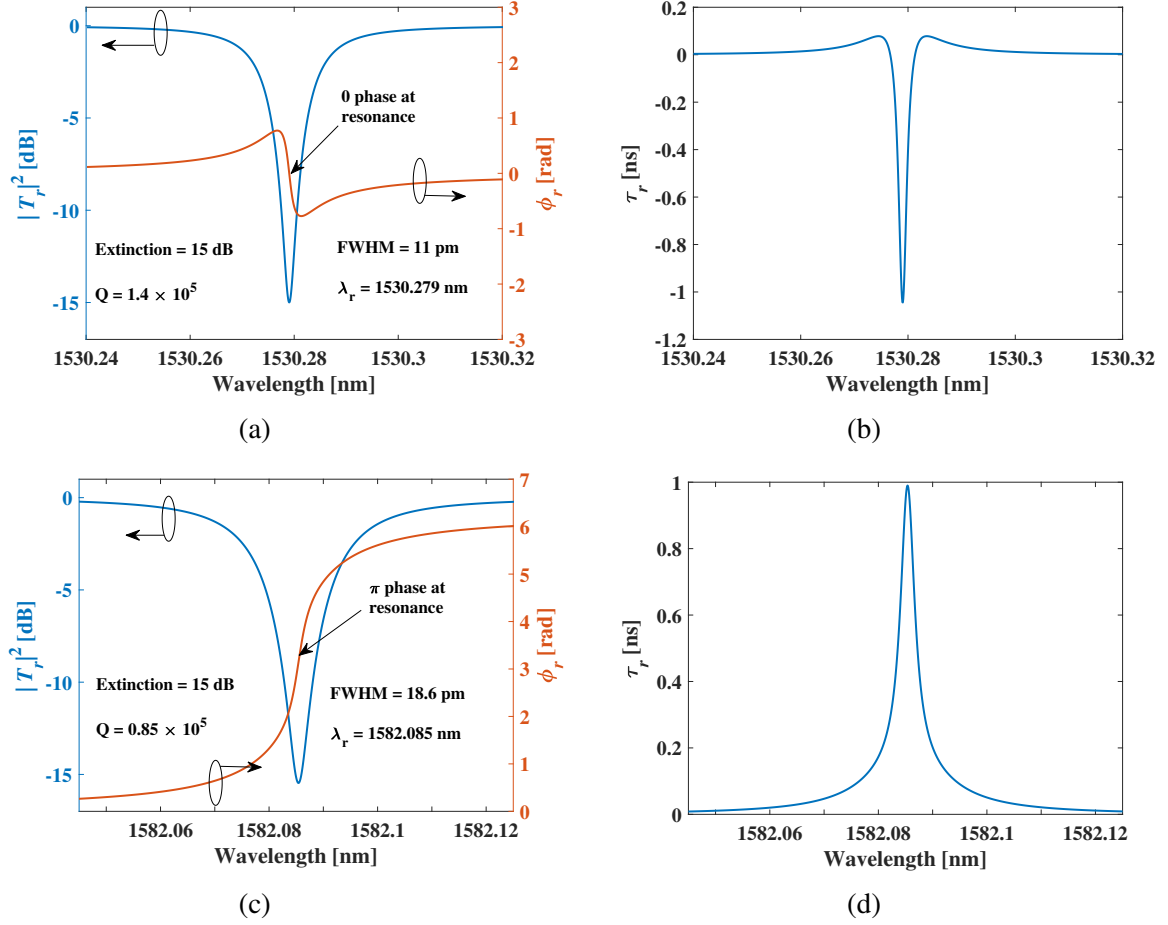


Figure 2.7: The power transmission ( $|T_r|^2$ ), phase ( $\phi_r$ ) and the delay ( $\tau_r$ ) response of the MRR with same extinction along with the figures of merit values (Q-factor, FWHM, extinction and resonant wavelength); (a)  $|T_r|^2$  and  $\phi_r$  for ring operating in under-coupled condition ( $r > a$ ), (b)  $\tau_r$  for ring operating in under-coupled condition, (c)  $|T_r|^2$  and  $\phi_r$  for ring operating in over-coupled condition ( $r < a$ ), and (d)  $\tau_r$  for ring operating in over-coupled condition.

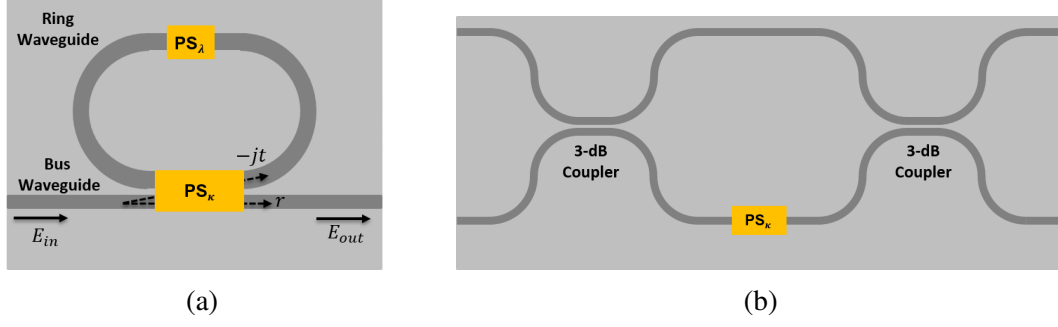


Figure 2.8: (a) Schematic top-view of a tunable microring resonator with two phase shifters  $PS_k$  and  $PS_\lambda$  integrated to tune the coupling coefficient and the resonant wavelength, respectively, and (b) schematic top-view of the conventional tunable coupler based on Mach-Zehnder interferometer (MZI) integrated with phase shifter  $PS_k$  in one arm.

ease of its integration using the in-house and foundry facilities. Hence all the phase shifters are addressed as the thermo-optic phase shifters. Other phase tuning mechanisms includes MEMS-based, free-carrier dispersion based, liquid crystal-based and phase change materials [92]; with each mechanism having its own merits.

The schematic top view of a tunable microring resonator with two thermo-optic phase shifters  $PS_k$  and  $PS_\lambda$  integrated to tune the coupling coefficient and the resonant wavelength, respectively, is shown in Fig. 2.8a. The Mach-Zehnder interferometer (MZI) is the widely reported tunable coupler in the literature, and its schematic is shown in Fig. 2.8b. However, in Chapter 3 we discuss a modified design for the tunable coupler based on asymmetric waveguides to overcome some of the limitations in the MZI-coupler ring with a compromise in the tuning range of the coupling coefficient. The MZI, in simpler words, can be described as two 3-dB directional couplers cascaded back-to-back. It is already established that the coupling coefficient tuning range of the MZI is maximum when the directional coupler splitting ratio is 50:50 (3-dB coupler). To ensure the directional coupler's 3-dB power splitting, we have considered the coupler gap  $g = 150$  nm and coupler length  $L_{dc} = 8 \mu\text{m}$  in the simulations. For the considered geometry (see Table. 2.1), the tuning of self-coupling coefficient with the thermal power dissipated

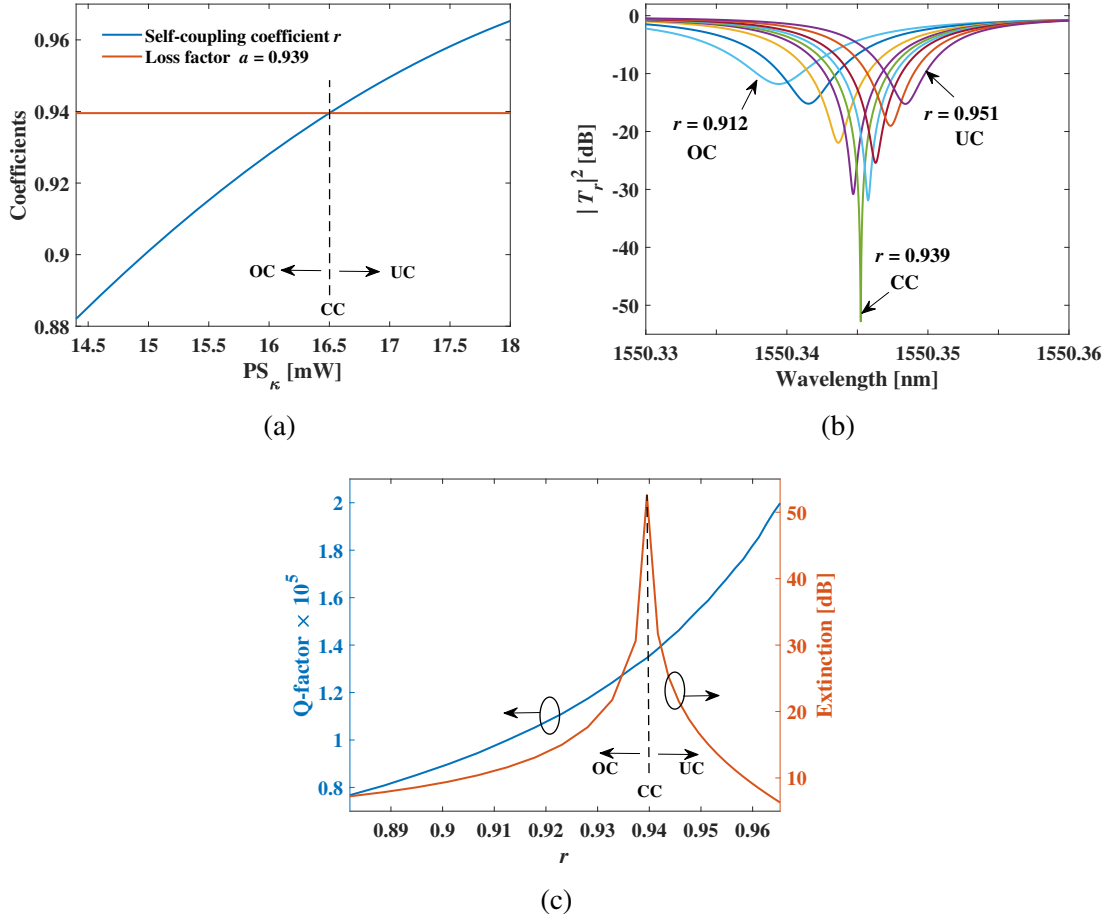


Figure 2.9: (a) The variation of the self coupling coefficient  $r$  of the MZI-based tunable directional coupler (see Fig. 2.8b) with thermal power applied to the phase shifter  $PS_\kappa$ , and also marked is the loss factor  $a$  and different coupling conditions of the MRR, (b) the MRR characteristics around 1550 nm plotted over the tuned values of  $r$ , and (c) the extracted Q-factor and extinction from the MRR responses over the tuned values of  $r$ .

across the phase shifter  $PS_\kappa$  around 1550 nm wavelength is given in Fig. 2.9a. The thermo-optic phase shifters are designed according to the process design kit (PDK) of AMF, Singapore. The loss factor  $a$  ( $= 0.939$ ) and the corresponding coupling conditions are marked in the same figure. Here, for the same waveguide loss, the change in the value of  $a$  when compared with the passive MRR (see Fig. 2.5a) is due to the increase in the cavity length of the ring.

Next, for the tuned self-coupling coefficient  $r$  of the ring, the MRR characteristics and

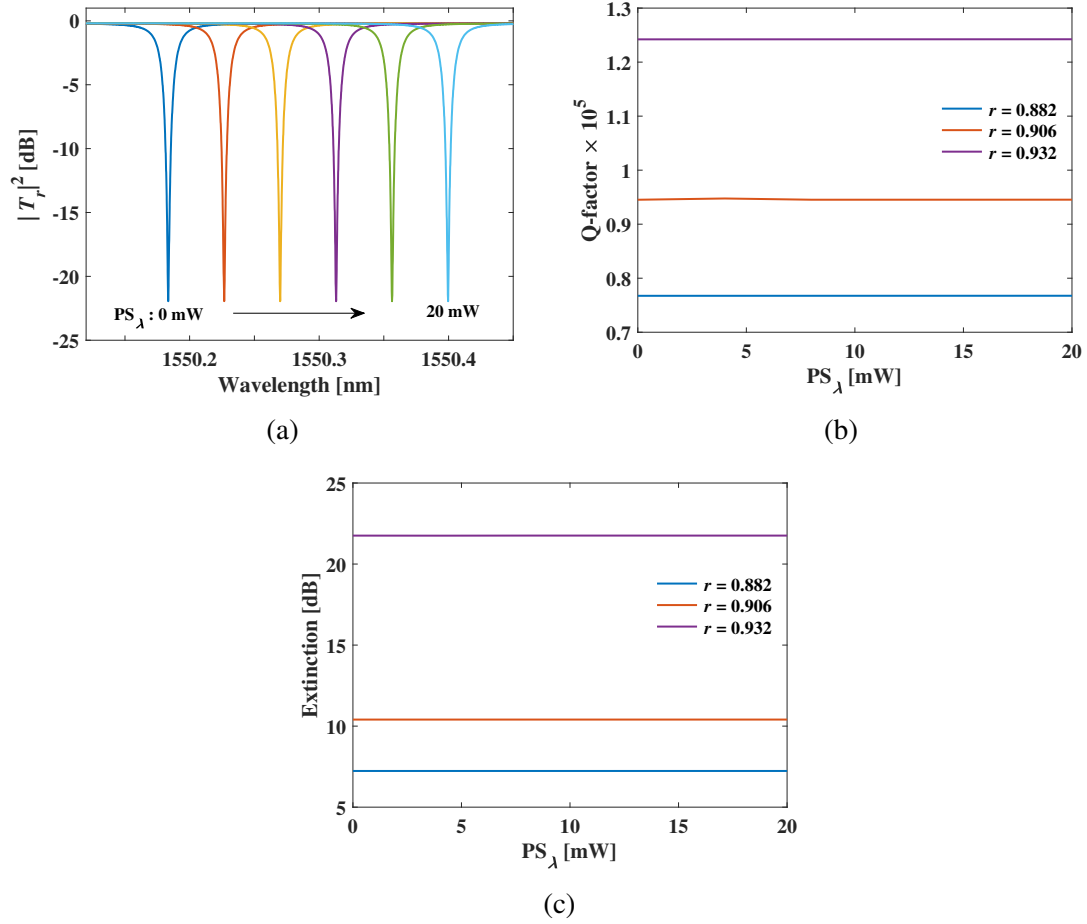


Figure 2.10: (a) MRR characteristics plotted by tuning the thermal power applied to the phase shifter  $PS_\lambda$  of the tunable coupler ring (see Fig. 2.8a), for a given value of  $r = 0.932$ , (b) the extracted Q-factor, and (c) extinction of the simulated MRR transmission by tuning the thermal power  $PS_\lambda$  for different values of  $r$  (set by tuning  $PS_\kappa$ ).

the extracted extinction ratio and Q-factor around 1550 nm wavelength are given in Fig. 2.9b and 2.9c, respectively. As expected, we can obtain the full range of the coupling conditions by tuning the phase shifter  $PS_\kappa$ . In the characteristics, the slight red-shift in the resonance wavelength is due to the amplitude and the phase tuning of the coupling coefficient with  $PS_\kappa$ , thus making it complex. In Fig. 2.9a, only the amplitude part of the coupling coefficient  $r$ , i.e.,  $|r|$  is given. However, we can adjust for the mentioned wavelength shift with the help of the second phase shifter  $PS_\lambda$ .

Fig. 2.10a shows the tuning of the MRR characteristics with the second phase shifter

$PS_\lambda$  at a given coupling coefficient  $r$  ( $= 0.932$ ). In addition, the extracted extinction ratio and Q-factor for three different values of  $r$  are given in Fig. 2.10b and 2.10c, respectively. As expected, the phase shifter  $PS_\lambda$  has minimal, if not zero, influence on the extinction ratio and Q-factor. However, we will see in the experiments that this is not true for a real-world fabricated structure due to the thermal crosstalk and/or the dispersion of the tunable coupler. As we have established the design aspects and the tuning characteristics of a microring resonator, we will discuss the realization of a microwave photonic filter based on the designed tunable directional coupler ring.

## 2.3 MICROWAVE PHOTONIC FILTER FUNCTION

After the extensive device analysis of the MRR, we have carried out the numerical analysis of the operation scheme given in Fig. 2.1, to understand the scheme performance and its bottlenecks in this section, which is followed by the experimental validations.

### 2.3.1 Simulation Results

The theoretical formulations followed for all the microwave filter simulations given in the thesis are discussed in detail in Appendix A. As MRR is the designated OSP in the current operation scheme, we have implemented the equations given in Appendix A by replacing the OSPs transfer function  $H(\omega)$  with the MRRs transfer function  $T_r(\omega)$  (see Eq. (2.3)), for the simulations discussed in this chapter. Using the simulation parameters listed in Table. 2.2, we have plotted the optical carrier at  $\nu_0$  ( $\sim 193.515$  THz) modulated with a broadband RF signal and transmitted through the designed MRR and received at the detector in Fig. 2.11a. In the simulations, the RF frequency band is visualized by sweeping the frequency of the input sinusoidal RF signal to the modulator (1 - 20 GHz) in the steps of 100 MHz. In the figure, the attenuation of the selected frequencies of the lower sideband (LSB) due to MRR and no attenuation of the frequencies of the upper sideband (USB) is visible. It must be noted that the carrier frequency  $\nu_0$  has been selected such that resonant frequency  $\nu_r$  is positioned at  $f_{rf}$ , with respect to the carrier

Table 2.2: The parameters for the laser source, modulator, microring resonator, and detection circuit used for simulation results shown in Fig. 2.11.

Component	Parameter		
	Description	Symbol	Value
Laser source	Input power	$p_{in}$	13.5 dBm
	Carrier wavelength	$\lambda_0$	$\sim 1550$ nm
	Carrier frequency	$\nu_0$	$\sim 193.548$ THz
Phase modulator (Lithium Niobate)	Optical insertion loss	$\alpha_m$	4 dB
	Input RF signal	–	sinusoidal
	Modulation index	$\delta = V_{in}/V_\pi$	0.014
	RF frequency band	$f_m$	1 - 20 GHz
	RF band step size	–	100 MHz
Microring Resonator	Fiber-to-chip coupling loss	$\eta_L$	5 dB/coupler
	Bend radius	$R$	50 $\mu$ m
	Self-coupling coefficient	$r$	0.958
	Loss factor	$a$	0.939
	Estimated Q-value	$Q$	$1.76 \times 10^5$
	Extinction	–	10 dB
Photodetector	FWHM	–	8.8 pm ( $\sim 1.1$ GHz)
	Responsivity	$R_d$	0.45 A/W
	Matched load	$R_L$	50 $\Omega$

frequency, such that  $f_{rf} = |\nu_0 - \nu_r| = 10$  GHz. The corresponding  $S_{21}$  ( $= P_{RF,out}/P_{RF,in}$ ) of the filter response centered at 10 GHz is given in Fig. 2.11b. The calculated filter response's 3-dB bandwidth and RF link gain are 1.2 GHz and -47.52 dB, respectively. The filter bandwidth is very close to the FWHM of the designed MRR ( $\sim 1.1$  GHz) at the operated value of  $r$  ( $= 0.958$ ). At the same time, the poor RF link gain is largely attributed to the fiber-to-chip coupling loss and modulator and detector efficiency, which can be improved by efficient device designs and optical/RF amplification. However, the key takeaway from the calculated response is the difference in the filter roll-off on either side of the central frequency resulting in asymmetric out-of-band rejection (17.6 dB and 10.4 dB, at the offset of  $\pm 2.5$  GHz) and degrading the filter performance. The asymmetric rejection indicates the difference in the degree of destructive interference on either side of the central frequency due to the influence of the MRR (aligned with the LSB) phase on the carrier and the USB.



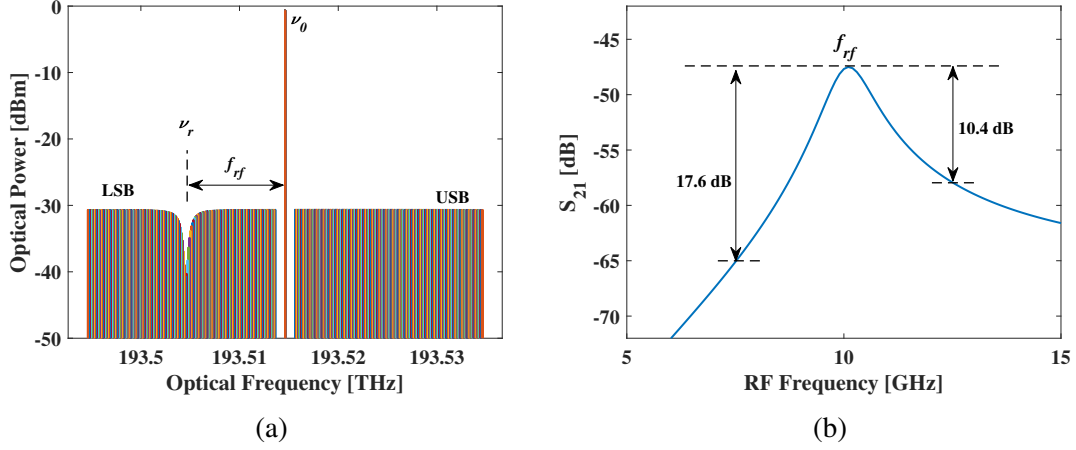


Figure 2.11: (a) Optical power transmission characteristics of the modulated laser light aligned with the MRR resonance, and also indicating the separation  $f_{rf}$  ( $= 10$  GHz) between the resonant frequency  $\nu_r$  and the laser carrier frequency  $\nu_0$ , and (b) calculated  $S_{21}$  ( $= P_{RF,out}/P_{RF,in}$ ) of the microwave photonic link (see Fig. 2.1a), exhibiting bandpass filter response at 10 GHz central frequency with asymmetric out-of-band rejection. The simulation results are for the parameter values given in Table. 2.2.

To understand the anomaly of the asymmetric out-of-band rejection and the effect of the MRR characteristics on the filter response, first, we have given the transfer characteristics of the MRR (transmission and phase) around the chosen carrier frequency  $\nu_0$  in Fig. 2.12a. In the figure, we can observe that even though the MRR transmission is 1 ( $\sim 0$  dB) for the carrier and all the frequencies corresponding to the USB, a frequency-dependent non-zero phase is added to the carrier and the USB by the MRR. To investigate the MRR role in the asymmetric rejection of the filter further, we have defined amplitude terms  $A_+$ ,  $A_-$  and phase terms  $\phi_{r,+}$ ,  $\phi_{r,-}$  as:

$$A_+ = |T_r(\omega_0 + \omega_{rf}) \times T_r(\omega_0)|^2; A_- = |T_r(\omega_0 - \omega_{rf}) \times T_r(\omega_0)|^2 \quad (2.6)$$

$$\phi_{r,+} = \phi_r(\omega_0 + \omega_{rf}) - \phi_r(\omega_0); \phi_{r,-} = \phi_r(\omega_0) - \phi_r(\omega_0 - \omega_{rf}) \quad (2.7)$$

$$\Delta\phi_r = \phi_{r,+} - \phi_{r,-} = \phi_r(\omega_0 + \omega_{rf}) + \phi_r(\omega_0 - \omega_{rf}) - 2\phi_r(\omega_0) \quad (2.8)$$

where the amplitudes  $A_+$ ,  $A_-$  are proportional to the beat currents  $i_+$  and  $i_-$ , the phases  $\phi_{r,+}$  and  $\phi_{r,-}$  indicate the phase added by the microring resonator to the beat currents  $i_+$

and  $i_-$ ,  $\Delta\phi_r$  is their phase difference and  $\phi_r$  at any given frequency is the phase response of the microring resonator. By comparing equations Eq. (2.7) and Eq. (2.8) with Eq. (A.6) and Eq. (A.7) of Appendix. A, we can conclude  $\phi_{r,+} = \phi_+$ ,  $\phi_{r,-} = \phi_- - \pi$  and  $\Delta\phi = \Delta\phi_r + \pi$ , where  $\phi_+$  and  $\phi_-$  are the phases of the beat currents  $i_+$  and  $i_-$ , respectively, and  $\Delta\phi$  is their phase difference.

The spectral response of the amplitude and phase terms, defined in Eq. (2.6) and Eq. (2.7), are given in Fig. 2.12b and Fig. 2.12c, respectively. For better understanding, the frequency range is divided into three regimes based on the expected central frequency of the filter and its bandwidth: (i) low-frequency region (up to 7.5 GHz), (ii) passband (7.5 - 12.5 GHz) and (iii) high-frequency region ( $> 12.5$  GHz). As the MRR is aligned with the LSB of the phase-modulated optical spectrum,  $A_-$  is frequency sensitive in the passband and constant in low and high-frequency regions, whereas  $A_+$  is flat throughout the RF frequency range. However, the non-zero phase of MRR at carrier and USB results in the frequency-dependent  $\phi_{r,+}$  and  $\phi_{r,-}$  as shown in Fig. 2.12c. Correspondingly the phase difference between the two beat signals  $\Delta\phi (= \Delta\phi_r + \pi)$  is given in Fig. 2.12d. The figure shows the phase difference  $\Delta\phi \neq \pi$  in the passband, which results in the filter response. However,  $\Delta\phi \rightarrow \pi$  only for the low-frequency region and does not converge to  $\pi$  in the high-frequency region. Therefore, despite having equal amplitude  $A_+$  and  $A_-$  values in both low and high-frequency regions, the degree of destructive interference is less for high-frequency regions, which results in the undesired asymmetric out-of-band rejection.

Next, we have estimated the filter response (with central frequency at 10 GHz) by tuning the MRRs self-coupling coefficient  $r$  using the phase shifter  $PS_k$  in the range of 0.88 - 0.97 to cover the entire coupling condition range of deep over-coupled to deep under coupled resonance. The filter response comparison for three values of  $r$  is given in Fig. 2.13a, and the extracted filter 3-dB bandwidth (and its comparison with MRR FWHM) is given in Fig. 2.13b. From the results, we can conclude that the filter bandwidth is very close to the MRRs FWHM, and the issue of asymmetric out-of-band rejection is inherent

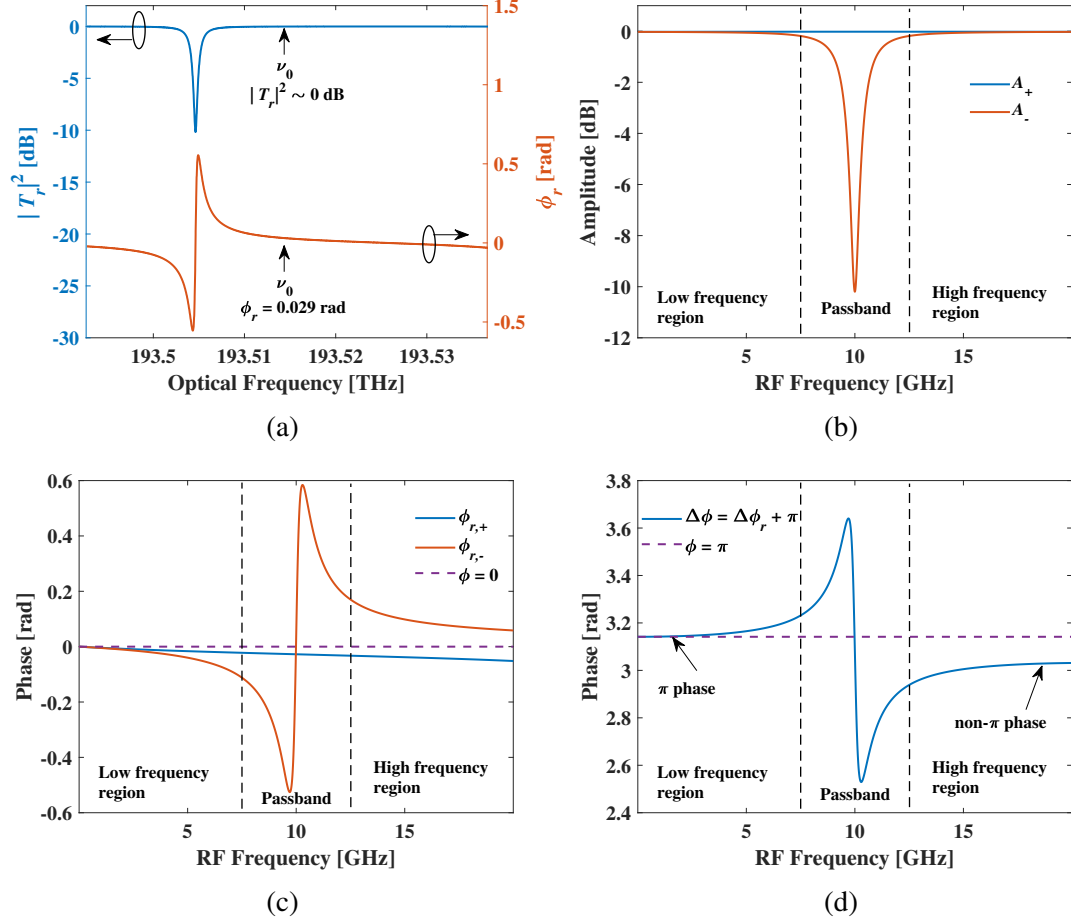


Figure 2.12: (a) Normalized optical power transmission and phase associated with its electric field of the MRR around the carrier frequency  $\nu_0$ , (b) spectral response of the amplitude terms  $A_+$ ,  $A_-$  (defined in Eq. (2.6)) which are proportional to the beat currents  $i_+$  and  $i_-$ , (c) spectral response of the phase terms  $\phi_{r,+}$ ,  $\phi_{r,-}$  (defined in Eq. (2.7)) indicating the phase added by the MRR to the beat currents  $i_+$  and  $i_-$ , and (d) spectral response of  $\Delta\phi = \Delta\phi_r + \pi$  (defined in Eq. (2.8)) indicating the phase difference between the beat currents  $i_+$  and  $i_-$ . The simulation results are for the parameter values given in Table. 2.2.

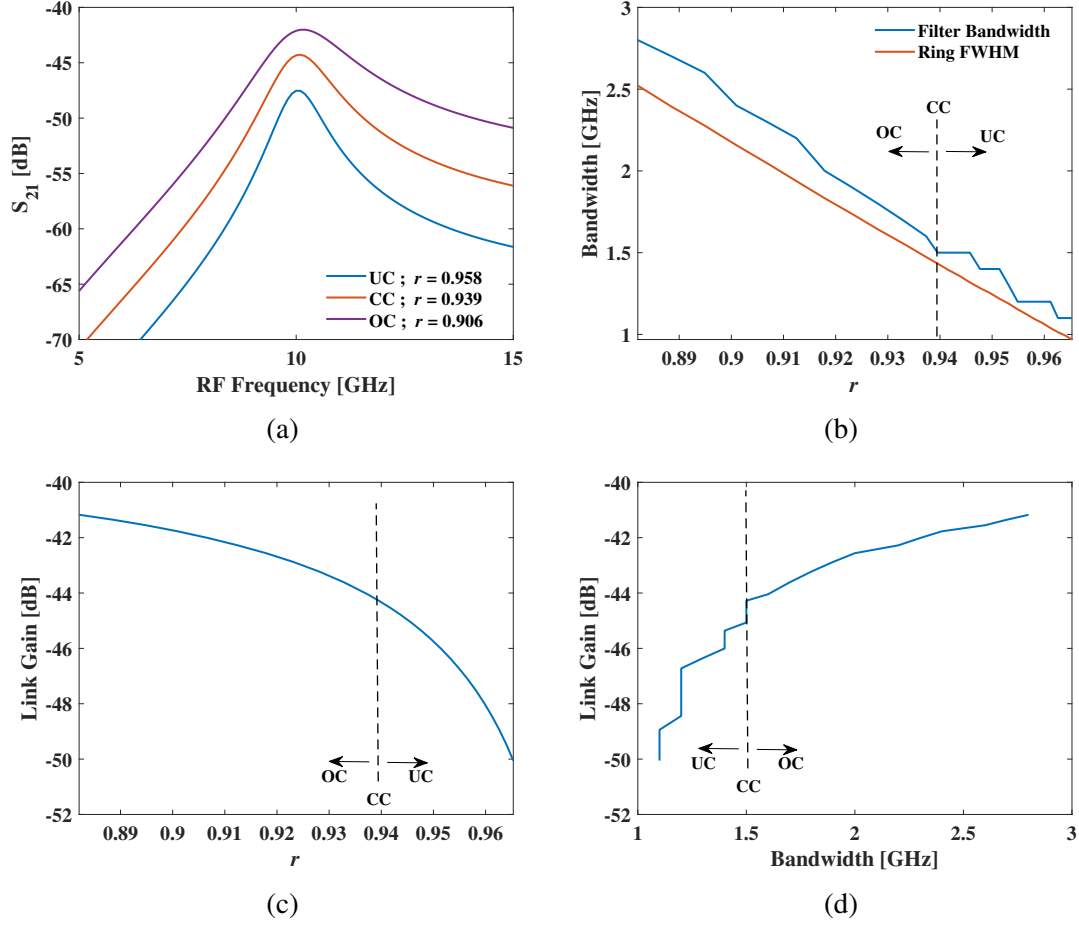


Figure 2.13: (a) Calculated  $S_{21}$  ( $= P_{RF,out}/P_{RF,in}$ ) of the microwave photonic filter with 10 GHz central frequency for three different values of  $r$ :  $\{0.958, 0.939, 0.906\}$  corresponding to UC, CC and OC resonances, respectively, (b) extracted 3-dB bandwidth of the filter responses obtained by tuning the MRRs coupling coefficient, (c) extracted link gain of the filter responses ( $= P_{RF,out}/P_{RF,in}$  at central frequency  $f_{rf}$ ) obtained by tuning the MRRs coupling coefficient, and (d) the variation of the link gain with the bandwidth of the simulated filter responses over the full-range of coupling coefficients covering OC, CC and UC resonances. The simulation results are for the parameter values given in Table. 2.2.

to the operation scheme and is present for all the values of  $r$ . However, to understand the variation of the RF link gain with  $r$ , which is depicted in Fig. 2.13c, we must again look into the phase response of the MRR, which is explained in Fig. 2.14.

As already mentioned, the optical spectrum of a phase-modulated optical carrier comprises two sidebands (USB and LSB) with two equal power amplitudes (say  $A$ ) and a phase difference of  $\pi$  (see Fig. 2.14a). The MRR optical bandstop filter response helps break the out-of-phase symmetry and realize a bandpass filter response. However, as shown in Fig. 2.13c, the filter link gain highly depends on the MRR coupling condition. Suppose the ring is operated in an under-coupled (UC) or an over-coupled (OC) condition with the same extinction value such that the power at the resonant frequency  $\nu_r$  gets attenuated to  $B$  in both cases. However, owing to the difference in the phase response, no phase is added at  $\nu_r$  while operating with UC-resonance (see Fig. 2.14b) and  $\pi$  phase is added at  $\nu_r$  while operating with OC-resonance (see Fig. 2.14c). As a result, for the filter responses with UC and OC resonances, at the central frequency  $f_{rf} (= |\nu_0 - \nu_r|)$ , we will have two beat components with unequal amplitudes ( $A$  &  $B$ ) and the phase difference of  $\pi$  and 0, as shown in Fig. 2.14d and Fig. 2.14e, respectively. Therefore, the RF power at the output of the photodetector proportional to  $(A - B)^2$  for UC resonance (see Fig. 2.14f) and  $(A + B)^2$  for OC resonance (see Fig. 2.14g), respectively. Thus resulting in the improved link gain for the filter realized with OC-resonance with a compromise in the filter bandwidth, as shown in Fig. 2.13d. Therefore, an over-coupled resonance with improved Q-factor would be a desired feature of the MRR for the realization of the microwave bandpass filter, which is not trivial, especially for in the silicon-on-insulator platform (limited by the sidewall roughness induced waveguide loss). Otherwise, critically coupled resonance can be termed the optimal operating point regarding the link gain and bandwidth trade-offs.

### 2.3.2 OSP Fabrication and Characterization

To experimentally validate the observed consequence of asymmetric out-of-band rejection for microwave photonic filters realized using the single ring as the OSP, we have fabricated

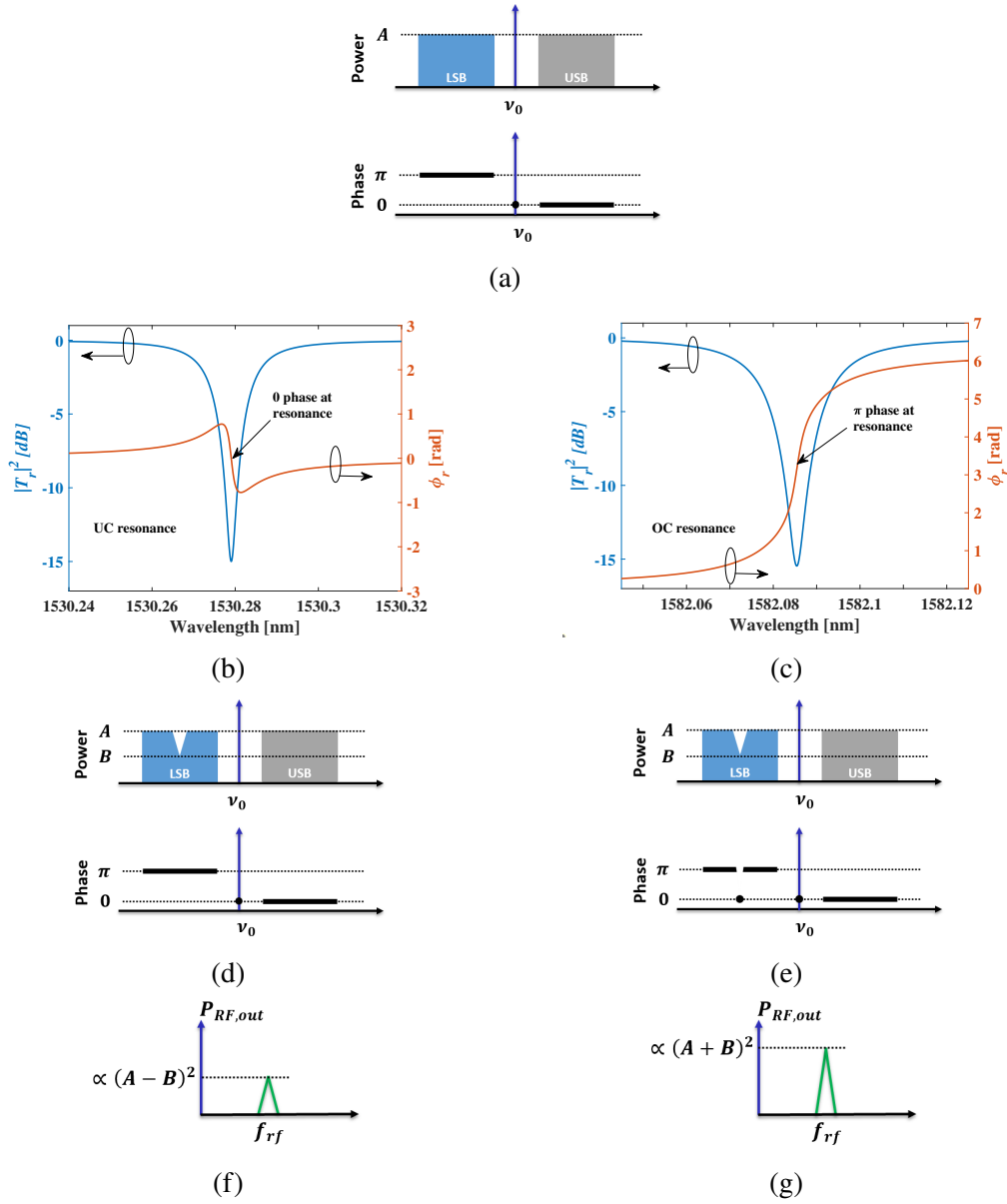


Figure 2.14: (a) Optical spectrum of the phase modulated optical carrier  $\nu_0$  indicating the equal amplitude and  $\pi$  phase shift between 1<sup>st</sup> order USB and LSB, (b) transmission and phase characteristics of the MRR for an under-coupled (UC) resonance, (c) transmission and phase characteristics of the MRR for an over-coupled (OC) resonance, (d) optical spectrum of the phase modulated optical carrier after transmission through the UC-resonance of the MRR, (e) optical spectrum of the phase modulated optical carrier after transmission through the OC-resonance of the MRR, (f) electrical spectrum of the RF signal after the photodetector for filter achieved with UC-resonance, and (g) electrical spectrum of the RF signal after the photodetector for filter achieved with OC-resonance.

the microring resonator structure using the in-house process facilities at the Centre for NEMS and Nanophotonics (CNNP), IIT Madras, as well as the foundry facilities at Advanced Micro Foundry (AMF), Singapore. The in-house designs were opted for the proof-of-concept demonstrations and the foundry designs are opted for their scalability. In this section, the fabrication details, characteristics of the in-house and foundry-fabricated devices are discussed.

### ***In-House Fabricated MRR***

In the in-house fabrication of the ring, we have focused only the MRR structure with passive directional coupler. The various design parameter values chosen for the in-house fabrication of the MRR are based on the optimized recipes for the in-house facilities and they are listed in Table 2.3. The mask layout comprising of reference waveguide and MRR structures with different directional coupler length  $L_{dc}$ , along with the required contact pads and test heater elements is given in Fig. 2.15a. The input/output waveguides are terminated with grating couplers for fiber-chip-fiber coupling (see Fig. 2.15b). An additional polygon structure is added to the grating couplers (also marked in Fig. 2.15b), to avoid the stitching error between the two write fields while using the e-beam lithography. The Titanium micro-heaters ( $PS_{\lambda}$ ) are integrated on the silicon slab within a close proximity of the rib waveguide structures as per requirements of the thermo-optic phase detuning (see Fig. 2.15c). The micro-heater design parameters (width  $W_H = 2 \mu\text{m}$ , thickness  $t_H = 100 \text{ nm}$ , distance from the waveguide  $g_H = 2 \mu\text{m}$ ) were chosen based on the previously studied experimental results [89]. Each microheater is associated with a pair of Aluminium contact pads (signal and ground), with the dimensions of  $100 \mu\text{m} \times 200 \mu\text{m}$ , to facilitate individual electrical probing in the experiments. The optimized recipes and the complete process flow followed for the in-house fabrication of different structures in the thesis are discussed in detail in Appendix. B. The microscope image of the MRR structures (as per the layout given in Fig. 2.15a), after following the process flow for passive waveguide fabrication (see Fig. B.1) is given in Fig. 2.15d.

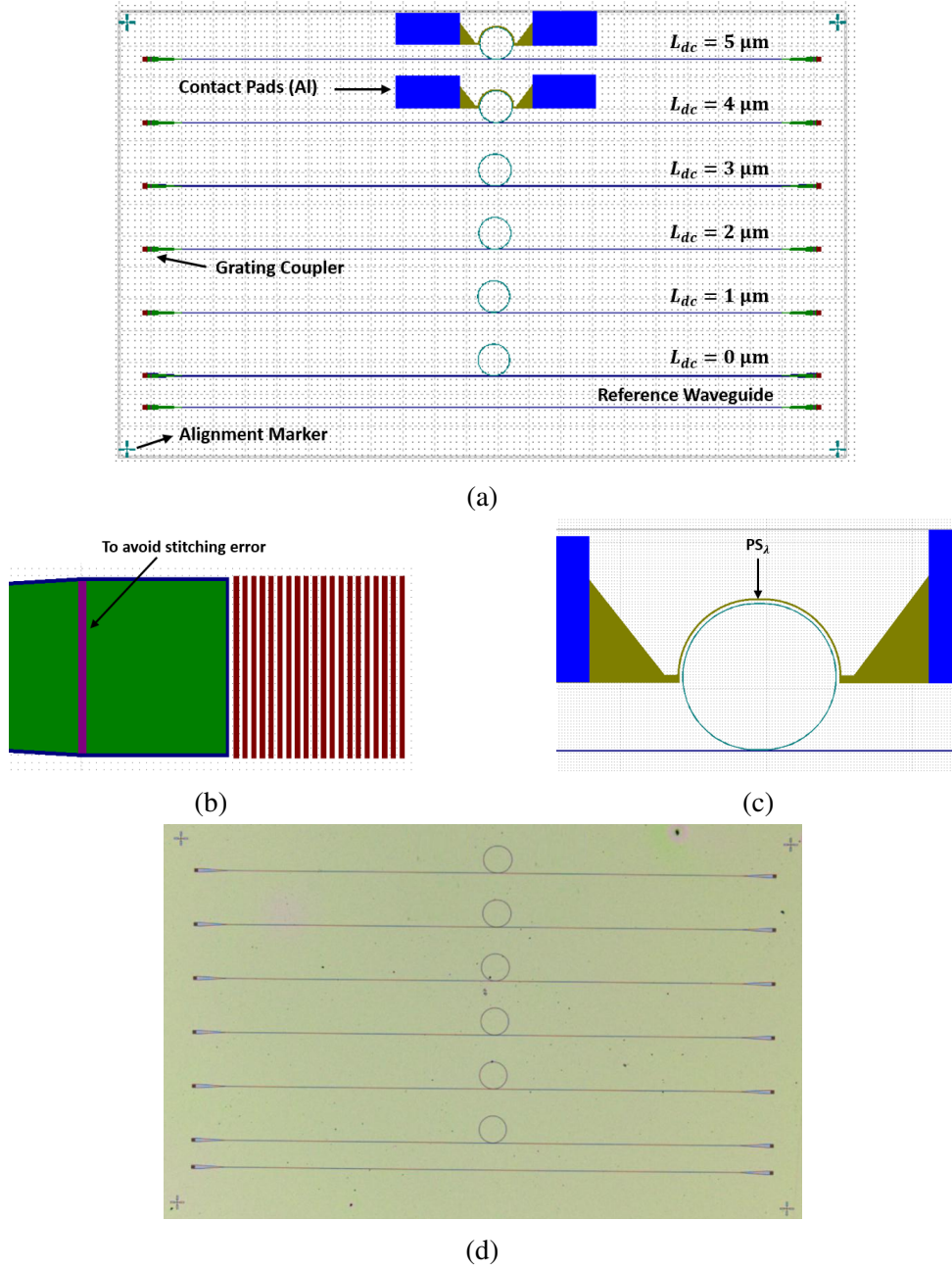


Figure 2.15: (a) Mask layout of the fabricated structures comprising of reference waveguide and MRR with different lengths of directional couplers  $L_{dc}$  (0 to  $5 \mu\text{m}$ ) along with grating couplers, contact pads and test heater elements, (b) zoomed-in mask layout indicating the grating coupler and an extra polygon added to avoid to the stitching error in e-beam lithography, (c) mask layout of the MRR ( $L_{dc} = 5 \mu\text{m}$ ) along with the phase shifter  $PS_\lambda$ , and (d) microscope image of the fabricated passive structures corresponding to the mask layout given in Fig. 2.15a.



Table 2.3: Design parameters chosen for the in-house fabrication of the MRR.

Description	Symbol	Value
Device layer thickness	$H$	220 nm
Slab height	$h$	150 nm
Ring radius	$R$	50 $\mu\text{m}$
Directional coupler gap	$g$	70 nm
Bus and ring waveguide width	$W$	0.5 $\mu\text{m}$
Directional coupler length	$L_{dc}$	0 to 5 $\mu\text{m}$
Heater width	$W_H$	2 $\mu\text{m}$
Heater thickness	$t_H$	100 nm
Waveguide to heater gap	$g_H$	2 $\mu\text{m}$

After the passive device fabrication, we have performed the phase shifter integration (using the process flow given in Fig. B.2). The corresponding microscope images are shown in Fig. 2.16. Among these, Fig. 2.16a shows the microscope image of the MRR structures (zoomed-into the devices with  $L_{dc}$ : 4, 5  $\mu\text{m}$ ), with partial opening of the contact pads region due to under-exposure during the e-beam lithography. Whereas, Fig. 2.16b - Fig. 2.16f shows microscope images at different stages of the phase shifter integration with optimized patterning parameters (see Section B.6 of Appendix B). In the fabricated structure integrated with the phase shifter, we observe a shift in the heater position relative to the MRR position. The offset is due to the occurrence of alignment error during the heater patterning. Despite the shift in heater position, as the heater is sufficiently spaced from the waveguide, we didn't notice any observable difference in the device characteristics.

After the fabrication, the passive transmission characteristics of the fabricated MRRs were experimentally investigated using the setup as shown schematically in Fig. 2.17. The in-built tunable laser source (TLS) of the optical source/spectrum analyzer (APEX 2043B) was used to sweep the laser wavelength, and the transmitted output was measured in the optical spectrum analyzer (OSA). In the current experiments for passive transmission measurements, the 8-channel programmable DC power supply (nicslab XDAC-8MUB-R4G8) depicted in the schematic is not activated. As mentioned earlier, the microring

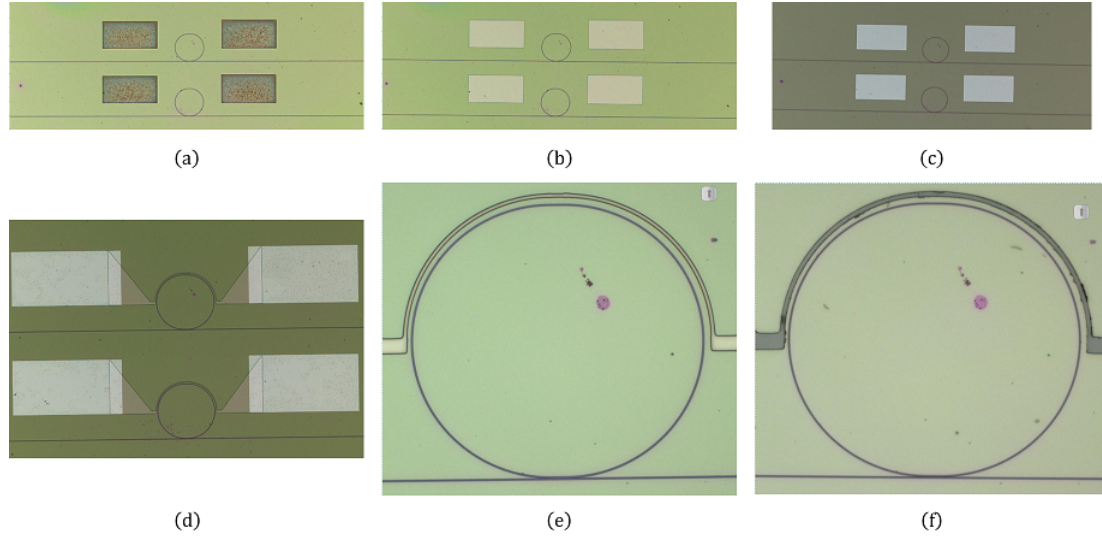


Figure 2.16: Microscope images of the fabricated MRRs ( $L_{dc}$ : 4, 5  $\mu\text{m}$ ) devices during different stages of the active fabrication process: (a) after the contact pads patterning and PMMA-A8 resist development of MRR with partial window openings due to low EBL dose, (b) after the contact pads patterning and PMMA-A8 resist development with optimized EBL dose, (c) post Aluminium metal (thermal) deposition and lift-off, (d) after microheater patterning and development, (e) after microheater patterning and development zoomed-in to single MRR ( $L_{dc}$ : 5  $\mu\text{m}$ ), and (f) post Titanium (e-beam) deposition and lift-off zoomed-in to single MRR ( $L_{dc}$ : 5  $\mu\text{m}$ ).

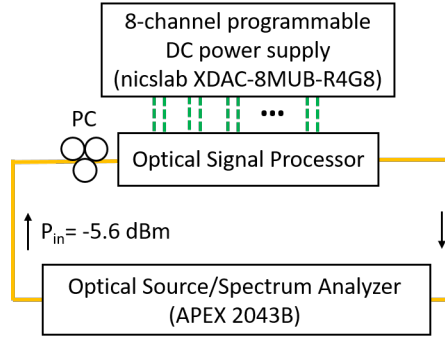


Figure 2.17: Experimental setup for passive and thermo-optic characterization of the fabricated OSP. PC: polarization controller

resonator is the optical signal processor in the current configuration. The experimental results are discussed below.

Fig. 2.18a shows the in-house fabricated microring resonator's transmission characteristics (for  $L_{dc} = 4, 5 \mu\text{m}$ ) and the reference waveguide's characteristics for the wavelength range of 1520 - 1560 nm. The other devices ( $L_{dc}$ : 0 to 3  $\mu\text{m}$ ) have resulted in very weak resonances, as shown in Fig. 2.18b, hence are not considered for further analysis. Owing to the improved range of extinction values over the measured wavelength span, we have considered the MRR response with  $L_{dc}$ : 5  $\mu\text{m}$  for filter experiments. The grating coupler performs with the peak efficiency of  $\sim 8.85$  dB/coupler around 1520 nm. The mismatch between reference waveguide response and the upper envelope of the MRR transmission indicate the device insertion loss ( $\sim 1$  dB around 1530 nm).

Next, the transmission characteristics of the MRR with  $L_{dc}$ : 5  $\mu\text{m}$ , zoomed-in to the critically coupled resonance (around 1541 nm) and its least-square fit using the ring transfer function (see Eq. (2.3)) is given in Fig. 2.18c. The coupling coefficient  $r$  and loss factor  $a$  of the critically coupled resonance extracted from the fit are equal, and the value is  $\sim 0.985$ . Based on the value of  $r$ ,  $a$  and the ring perimeter, the Q-factor of the ring and the waveguide loss are calculated to be  $0.87 \times 10^5$  and 4 dB/cm, respectively.

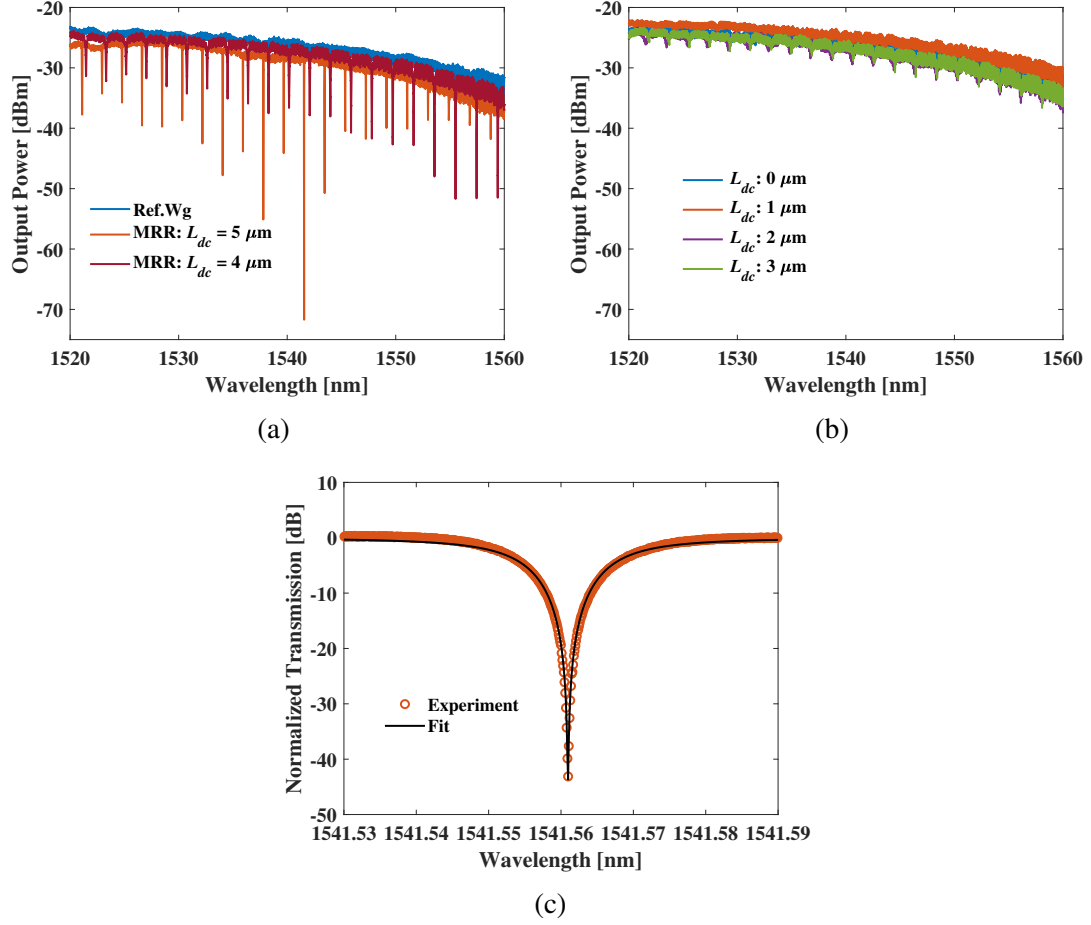


Figure 2.18: (a) Transmission characteristics of the in-house fabricated microring resonator ( $L_{dc}$ : 4, 5  $\mu\text{m}$ ) and its comparison with reference waveguide response, (b) transmission characteristics of the in-house fabricated microring resonator ( $L_{dc}$ : 0 – 3  $\mu\text{m}$ ), and (c) the least square fit of the critically coupled resonance around 1541 nm in Fig. 2.18a (using Eq. (2.3)) to extract coupling coefficient  $r$  and loss factor  $a$ .

Even though, the in-house fabricated devices are integrated with the phase shifters, we have not performed any tuning of the device characteristics, owing to the limitations in the obtained filter response (discussed in the next section).

### ***Foundry-Fabricated MRR***

After the discussion of in-house fabricated devices, next, we will discuss the results corresponding to the foundry-fabricated devices. In the foundry process, we have fabricated the designed microring resonator structure with passive and MZI-based tunable directional coupler, discussed in Section 2.2. The structures and the necessary thermo-optic phase shifters were fabricated at Advanced Micro Foundry (AMF), Singapore. The geometrical parameters for both structures were considered the same as discussed in the Section 2.2. However, in the case of the 3-dB coupler required for the MZI-based tunable directional coupler, instead of the standard DC, we have used the multi-mode interferometer (MMI) block from the process design kit (PDK) of AMF foundry, owing to its fabrication tolerance and wideband operation. The microscopic images of both the structures indicating the integrated phase shifters are given in Fig. 2.19a and Fig. 2.19b, respectively. Both devices' optical and thermo-optic tuning characteristics were measured first, followed by the RF filter experiments.

The passive transmission characteristics, thermo-optic detuning of the resonance wavelengths, and coupling coefficients were experimentally investigated using the same setup as shown schematically in Fig. 2.17. For thermo-optic tuning of foundry-fabricated devices, an 8-channel programmable DC power supply (nicslab XDAC-8MUB-R4G8) was used with a DC probe card. Both fiber-optic coupling and electrical probing were facilitated using a FormFactor silicon photonic probe station (MPS-150). The experimental results are discussed below.

Fig. 2.20a shows the microring resonator's transmission characteristics and the reference waveguide's characteristics for the 1520 - 1600 nm broad wavelength range. The grating

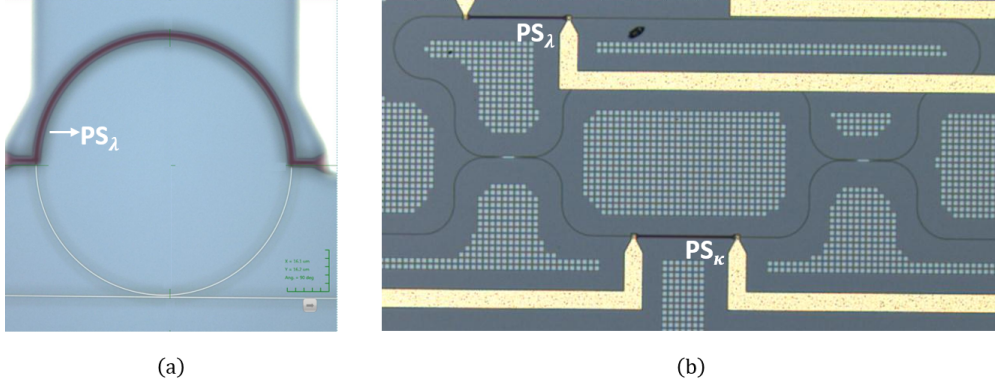


Figure 2.19: Microscope image of the foundry-fabricated microring resonators indicating the integrated phase shifters; (a) passive directional coupler ring with phase shifter  $PS_\lambda$  to tune the resonant wavelength, and (b) Mach-Zehnder interferometer based tunable directional coupler ring integrated with phase shifters  $PS_\kappa$  and  $PS_\lambda$  to tune the coupling coefficient and resonant wavelength, respectively.

coupler performs with the peak efficiency of  $\sim 6.5$  dB/coupler around 1570 nm. The upper envelope of the MRR response, which overlaps with the reference waveguide response, indicates that the insertion loss of the microring resonator structure is practically zero. Next, the transmission characteristics of the MRR zoomed-in to show one resonance (around 1550 nm) and its least-square fit using the ring transfer function (see Eq. (2.3)) is given in Fig. 2.20b. The coupling coefficient  $r$  and loss factor  $a$  were extracted from the fit to be  $\{0.99, 0.995\}$ , indicating the resonance to be over-coupled. Based on the value of  $r, a$  and the ring perimeter, the Q-factor of the ring and the waveguide loss are calculated to be  $1.91 \times 10^5$  and 1.35 dB/cm, respectively. These metrics clearly suggest the improvement when compared with the in-house fabricated device (loss: 4 dB/cm, Q:  $0.87 \times 10^5$ ), because of the superior process control in the foundries. Next, the thermo-optic phase shifter  $PS_\lambda$  was activated to tune the resonant wavelength of the ring resonator and the corresponding results are shown in Fig. 2.20c. For all the applied thermal powers,  $\{r, a\}$  were extracted and are given in Fig. 2.20d. As expected, we observe a minimal change in the values of  $\{r, a\}$  with  $PS_\lambda$ . The observed small changes can be associated with the directional coupler's dispersion and the wavelength-dependent waveguide loss (which was not considered in the simulations).

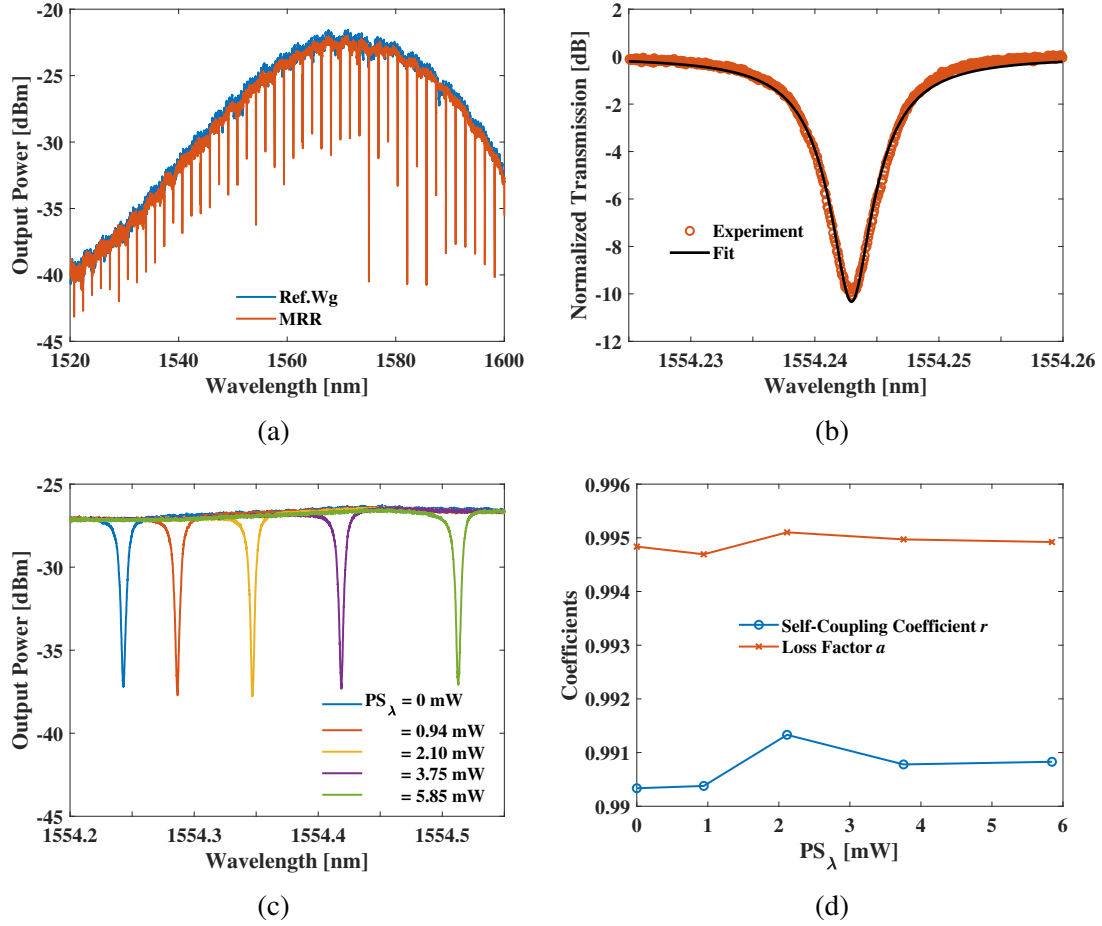


Figure 2.20: (a) Experimentally measured transmission characteristics of the reference waveguide and the passive directional coupler microring resonator, (b) the least square fit of the measured data (resonance around 1554 nm in Fig. 2.20a) using Eq. (2.3) to extract coupling coefficient  $r$  and loss factor  $a$ , (c) thermo-optic tuning characteristics of the ring for different values of applied thermal powers  $PS_\lambda$ , and (d) the extracted coefficients  $\{r, a\}$  for different values of  $PS_\lambda$ .

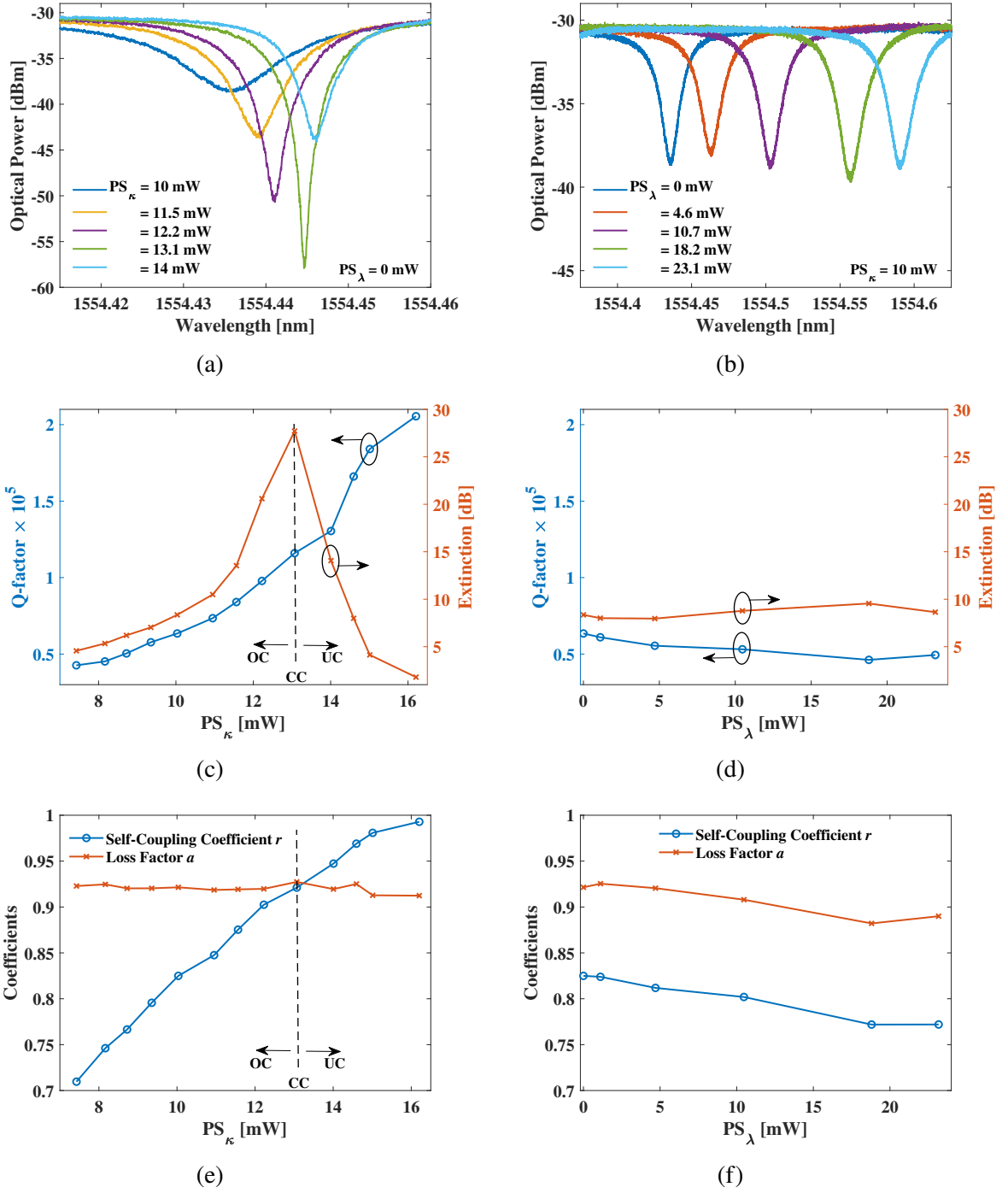


Figure 2.21: (a) Experimentally measured transmission characteristics of the tunable coupler ring by tuning  $PS_{\kappa}$  with  $PS_{\lambda} = 0$  mW, (b) transmission characteristics of the tunable coupler ring by tuning  $PS_{\lambda}$  with  $PS_{\kappa} = 10$  mW, (c) calculated Q-factor and extinction of the characteristics shown in Fig. 2.21a, (d) calculated Q-factor and extinction of the characteristics shown in Fig. 2.21b, (e) extracted coefficients  $r, a$  using the least square fit for the characteristics shown in Fig. 2.21a, and (f) extracted coefficients  $r, a$  using the least square fit for the characteristics shown in Fig. 2.21b



Next, we have characterized the MZI-based tunable coupler ring by adjusting both the phase shifters  $PS_{\kappa}$  and  $PS_{\lambda}$  individually to tune the coupling coefficient (Q-factor and extinction) and the resonant wavelength, respectively. The spectral characteristics of the device by tuning  $PS_{\kappa}$  ( $PS_{\lambda}$ ) are given in Fig. 2.21a (Fig. 2.21b). The corresponding variation Q-factor and extinction and the extracted coupling coefficient  $r$  and loss factor  $a$  with  $PS_{\kappa}$  ( $PS_{\lambda}$ ) are given in Fig. 2.21c and Fig. 2.21e (Fig. 2.21d and Fig. 2.21f), respectively. As expected, we can tune the ring characteristics from the deep over-coupled to the deep under-coupled region using  $PS_{\kappa}$ . At the same time, we observe a minimal change in the ring characteristics (and extracted Q-factor, extinction and  $r$ ,  $a$ ) while tuning the phase shifter  $PS_{\lambda}$ , which can be associated with the dispersion of the directional coupler.

### 2.3.3 MRR Delay Measurements

As mentioned earlier, the MRR is associated with a delay response (see Fig. 2.7), which can be tuned by the coupling coefficient  $r$ . Therefore, for completion, we have measured the delay characteristics for the fabricated tunable coupler MRR by controlling the phase shifter  $PS_{\kappa}$ . The delay measurements followed the working principle of the photodetector output of a single sideband (SSB) spectrum aligned with the MRR, resulting in the RF response proportional to the MRR characteristics [93]. Therefore, to generate an SSB spectrum in the experiments, we used the in-built intensity modulator of the lightwave component analyzer (LCA) followed by an optical bandpass filter (OBPF) to filter out one of the modulated sidebands. We have measured the RF delay response in the performance network analyzer (PNA) for different set values of  $PS_{\kappa}$  and also tracked the corresponding optical spectrum in OSA, using a 99:1 coupler at the output, to extract the values of  $r$ ,  $a$ .

Next, we calculated the theoretical delay from the extracted coupling coefficient and loss factor and compared the results with the measured RF delay mapped back into the optical domain. From Fig. 2.22a, we can see that the two results are in excellent agreement, which confirms that the measured RF delay based on SSB modulation and

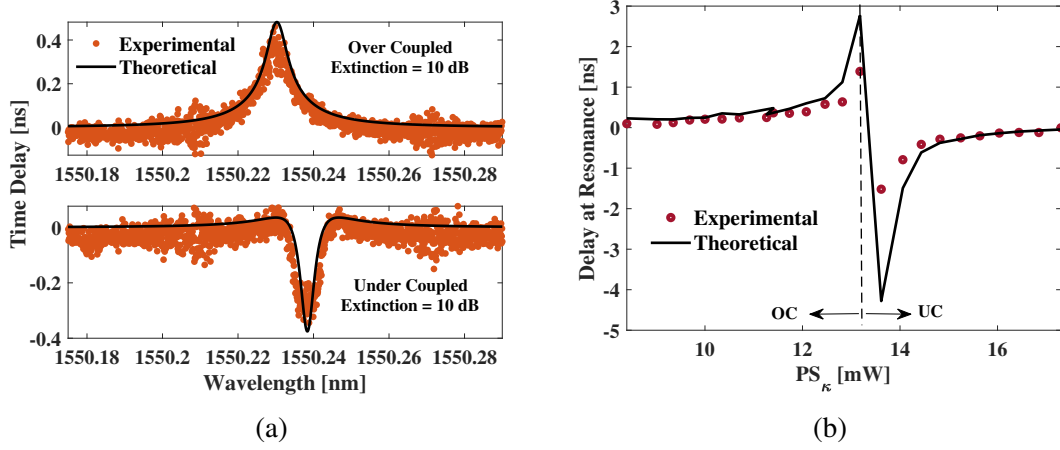


Figure 2.22: (a) Delay characteristics of the tunable coupler ring and its fit with the theoretical model for over-coupled (OC) and under-coupled (UC) region with similar extinction ( $\sim 10$  dB), and (b) comparison of measured peak time delay at the resonant wavelength with the theoretical delay, for different thermal power applied to the phase shifter  $PS_k$ .

high-speed PNA is the same as the MRR delay response. We repeated the same procedure for different coupling conditions and compared the theoretical and experimental data. From Fig. 2.22b, we observe that the two curves deviate near the critical coupling condition. As we feed only 1% of optical power to OSA, the measured results in OSA for critically coupled resonances are in the instrument's noise levels, resulting in the inaccurate estimation of  $r, a$ . The deviations can be reduced by tapping more optical power into OSA and compensating for the additional loss using EDFA. In the mentioned case, one needs to consider the effect of noise power added to the experiments through EDFA. However, these proof-of-concept delay measurements validate the potential of the MRR as the tunable delay lines.

### 2.3.4 RF Filter Experiments

After the thorough characterization of both in-house and foundry-fabricated structures, we went ahead to test their performance in the realization of the RF photonic filter, and validate our simulation prediction of asymmetric out-of-band rejection. For this purpose, we have modified the experimental setup shown in Fig. 2.17 by connecting Lightwave

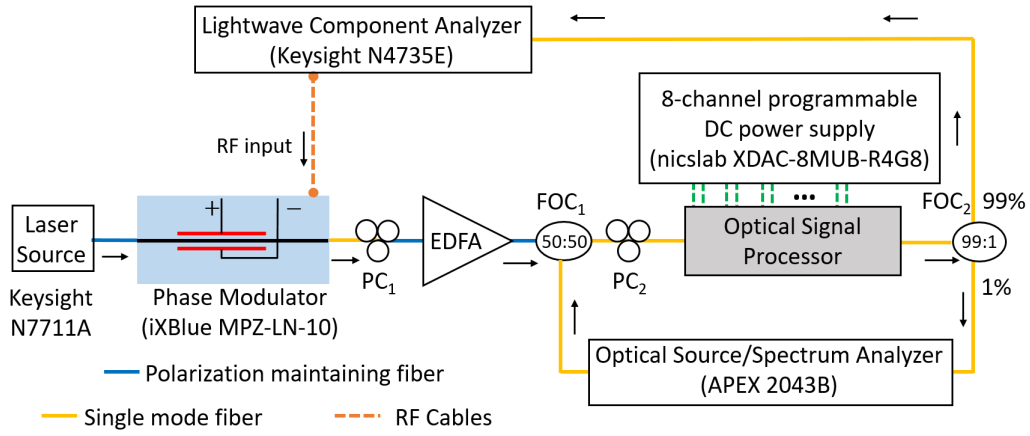


Figure 2.23: The experimental setup to characterize the RF photonic bandpass filter with symmetric rejection. EDFA: erbium doped fiber amplifier, PC: polarization controller, FOC: fiber-optic coupler.

Component Analyzer (Keysight N4735E), carrier laser light source (Keysight N7711A), phase modulator (iXBlue MPZ-LN-10), erbium-doped fiber amplifier (EDFA), as shown in Fig. 2.23. The carrier laser light source ( $\lambda_0 \sim 1550$  nm,  $p_{in} = 15$  dBm) was launched into the phase modulator ( $V_\pi = 6$  V, 3-dB BW = 10 GHz, insertion loss = 2.7 dB) through a polarization maintaining fiber. The Lightwave Component Analyzer (LCA) was used to drive the phase modulator, and the RF signals were swept from 1 GHz to 16 GHz ( $P_{in,RF} = -10$  dBm), with frequency steps of 10 MHz. The erbium-doped fiber amplifier (EDFA) was used to amplify the modulated laser light up to 20 dBm and subsequently launched into the OSP input grating coupler via 50:50 fiber-optic coupler (FOC<sub>1</sub>) and polarization controller (PC<sub>2</sub>). The output from the OSP is collected through the grating coupler, and 1% of it was tapped into the optical source/spectrum analyzer, and the remaining 99% was fed into the LCA using (FOC<sub>2</sub>). In the setup, the optical source/spectrum analyzer was used for in-situ tracking of the resonant wavelengths.

For the filter response, the laser carrier wavelength  $\lambda_0$  was placed at an offset of 80 pm with the ring's resonant wavelength  $\lambda_r$  ( $\sim 1541$  nm for the in-house device and  $\sim 1554$  nm for foundry-fabricated device). The corresponding filter responses with in-house and foundry-fabricated devices are shown in Fig. 2.24a and Fig. 2.24b, respectively. Even

though in both the cases we see a filter responses at the expected central frequency of 10 GHz, with asymmetric out-of-band rejection (similar to the calculated filter response in Fig. 2.11b), the filter shape and the rejection (9.4 dB and 2.2 dB, at the offset of  $\pm 2.5$  GHz with the central frequency) with the in-house device are limited by the poor Q-factor of the MRR. Whereas, owing to the enhancement in the waveguide loss and the Q-factor of the foundry-fabricated MRR, we see an improved filter shape, with an asymmetric out-of-band rejections of 16.3 dB and 8.3 dB, at the offset of  $\pm 2.5$  GHz with the central frequency.

Because of the improved filter shape, the foundry-fabricated devices were tested for the further analysis. For this purpose, the resonant wavelength of the foundry-fabricated MRR was tuned using the phase shifter  $PS_\lambda$  to realize the filter response from 2 - 14 GHz, as shown in Fig. 2.24c. Here, the tuning range is limited by the modulator bandwidth ( $\sim 15$  GHz) used in the experiments. The theoretical limit of the filter tuning range is 110 GHz ( $\sim FSR/2$ ). However, in the last chapter of the thesis, we will see that the mentioned theoretical limit is valid under the condition  $FSR/2 \gg FWHM$ . The drop in the filter link gain for increased frequency can be associated with the frequency response of the RF cables, modulator and photodetector used in the experiments. Also, the increase in the filter bandwidth for lower values of central frequency (as shown in Fig. 2.24d) is due to the increased value of the MRR residual phase on the carrier and hence the increased asymmetry in the filter response, when the ring is close to the carrier.

Next, the light was coupled in to tunable coupler ring and filter response for different values of self-coupling coefficient  $r$  from over-coupled to under-coupled region by tuning the thermal powers sourced to the phase shifter  $PS_\kappa$  was measured. For these measurements, the second phase shifter  $PS_\lambda$  was also activated to maintain the resonance spacing from the carrier to 10 GHz for all the values of  $PS_\kappa$  (or  $r$ ). The corresponding results are shown in Fig. 2.25a. As expected, the asymmetric out-of-band rejection is present for all values of  $r$  (similar to the results shown in 2.13a). From the measured

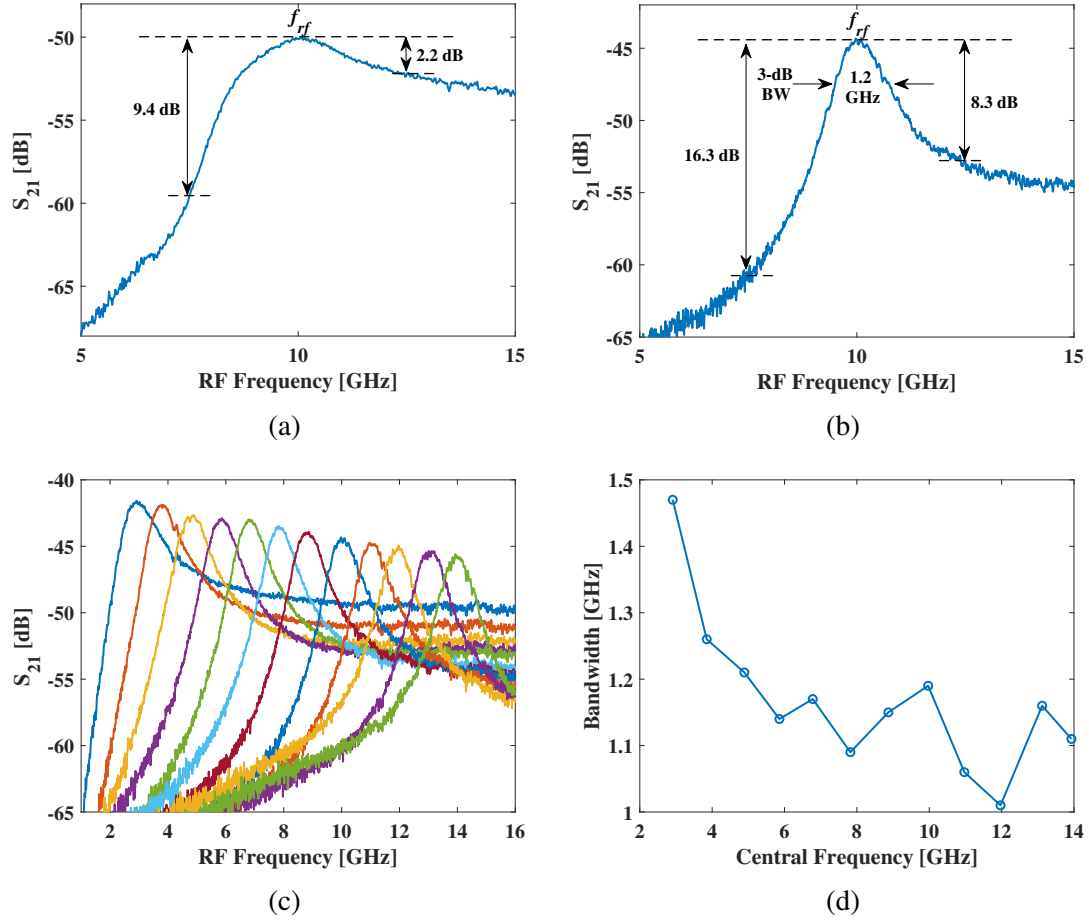


Figure 2.24: (a) Measured  $S_{21}$  of the microwave photonic filter centered at 10 GHz with the in-house fabricated microring resonator (see Fig. 2.16), (b) measured  $S_{21}$  of the microwave photonic filter centered at 10 GHz with the foundry-fabricated passive directional coupler ring (see Fig. 2.19), (c) microwave photonic filter response using the foundry-fabricated MRR with frequency tuned from 2 GHz to 14 GHz, using the thermo-optic phase shifter  $PS_{\lambda}$ , and (d) extracted 3-dB bandwidths of the filter responses shown in the Fig. 2.24c.

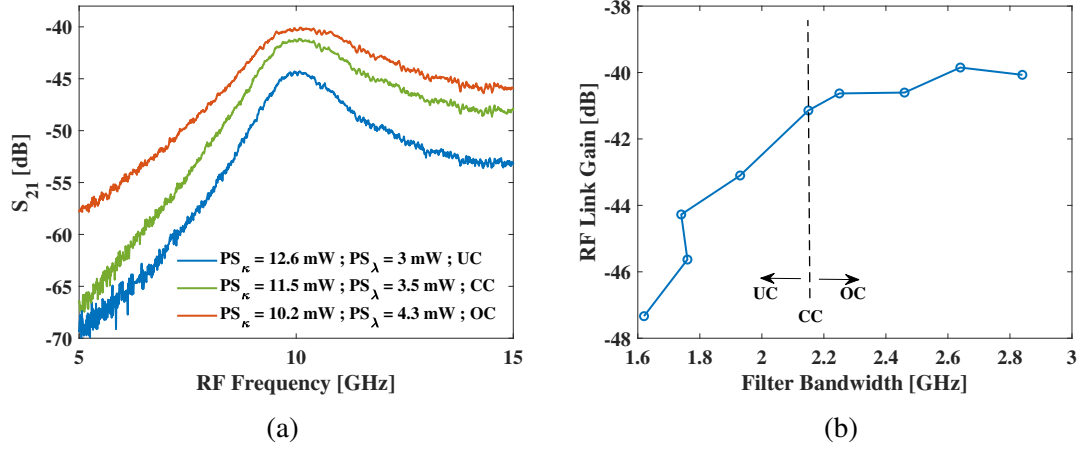


Figure 2.25: (a) Measured  $S_{21}$  of the microwave photonic filter centered at 10 GHz by tuning the coupling coefficient of the tunable directional coupler ring (see Fig. 2.19) using the phase shifters  $PS_{\kappa}$  and  $PS_{\lambda}$ , and (b) the link gain of the filter responses variation with the filter bandwidth, obtained by tuning the coupling coefficient of the tunable directional coupler ring.

results, we have extracted the filter bandwidth and link gain for different tuned values of  $PS_{\kappa}$ , and the results are given in Fig. 2.25b. The bandwidth and the link gain of the filter response are higher for over-coupled resonances due to increased MRR FWHM and phase response of the ring (similar to the results shown in 2.13d), respectively. These proof-of-concept experiments validate our simulation model and the problem of asymmetric out-of-band rejection for the microwave filter.

## 2.4 SUMMARY

In this chapter, we have also discussed the operation scheme of the microwave photonic bandpass filter using a single MRR as the OSP. To understand the bottlenecks of the mentioned scheme, we have discussed the microring resonator's working principle and design parameters with a passive directional coupler (two closely spaced identical waveguides) and an MZI-based tunable coupler. We have seen the tuning characteristics of the MRR by appropriately tuning the thermo-optic phase shifters  $PS_{\kappa}$  (for Q-factor and extinction tuning) and  $PS_{\lambda}$  (for resonant wavelength tuning) in both numerical

simulations and experimentally fabricated devices. In the theoretical calculations of the filter response, we observed that the filter bandwidth is approximately equal to the MRR FWHM, and the filter has an improved link gain with the ring operating in an over-coupled region (due to the addition of the  $\pi$  phase at the resonance). Even though the scheme is relatively simple, we observed that the filter response is limited by the asymmetric out-of-band rejection for all the values of coupling coefficients due to the residual MRR phase on the laser carrier. We have also validated the findings in simulations with the experimental measurements. For the experimental validation, we have opted for two fabrication routes using in-house and foundry facilities. The structures fabricated from both processes were thoroughly characterized and tested to obtain the RF filter responses. As expected, we observed the problem of asymmetric out-of-band rejection of the filter using both devices. However, the filter shape obtained using the in-house device was limited by poor Q-factor, resulting from high waveguide scattering loss ( $\sim 4$  dB/cm). We observed the enhancement in the extracted waveguide loss ( $\sim 1.35$  dB/cm) and filter shape using foundry-fabricated MRR.

Nevertheless, the simulation and experimental study reported in this chapter confirm the problem of asymmetric out-of-band rejection for the filter response using a single MRR as the OSP. The topic of interest for the next chapter is mitigating the asymmetrical nature of filter rejection by proposing a novel OSP structure.

## CHAPTER 3

### OSP WITH CASCADED MRRS

As discussed in the previous chapters, the MRR-based RF photonic filters in the SOI platform are attractive in compactness, broadband tunability, CMOS compatibility and scalability. However, the residual phase of MRR on the carrier results in asymmetric out-of-band rejection, limiting the filter response. To overcome this limitation and to achieve an RF photonic bandpass filter with symmetric out-of-band rejection, in this chapter, we propose a novel design of the OSP chip comprised of two cascaded microring resonators (MRR1, MRR2) in an all-pass configuration. We extensively study the effect of the ring characteristics on the filter response in simulations. Followed by the design and in-house fabrication of the MRRs based on the asymmetric directional coupler. Finally, we discuss the proof-of-concept microwave filter experiments performed on the in-house fabricated OSP.

#### 3.1 OPERATION SCHEME

As mentioned the proposed optical signal processor comprised of two identical MRRs and is integrated with four phase shifters to reconfigure the ring characteristics, as shown schematically in Fig. 3.1a along with its operational scheme. A representative RF band with center frequency at  $f_m$  is upconverted into optical frequency range centering around  $\nu_0$  via a phase modulator and subsequently launched into the proposed OSP chip. The phase modulation of the optical carrier results in an upper sideband (USB) and lower sideband (LSB) with  $\pi$  phase difference, as shown in top-left section of Fig. 3.1b. The two cascaded MRRs are configured with identical coupling conditions as well as identical Q-values. Since both the MRRs are identical they resonate at same wavelengths. A desired order of their resonant wavelength ( $\lambda_r \sim 1550$  nm) can be made non-degenerate by



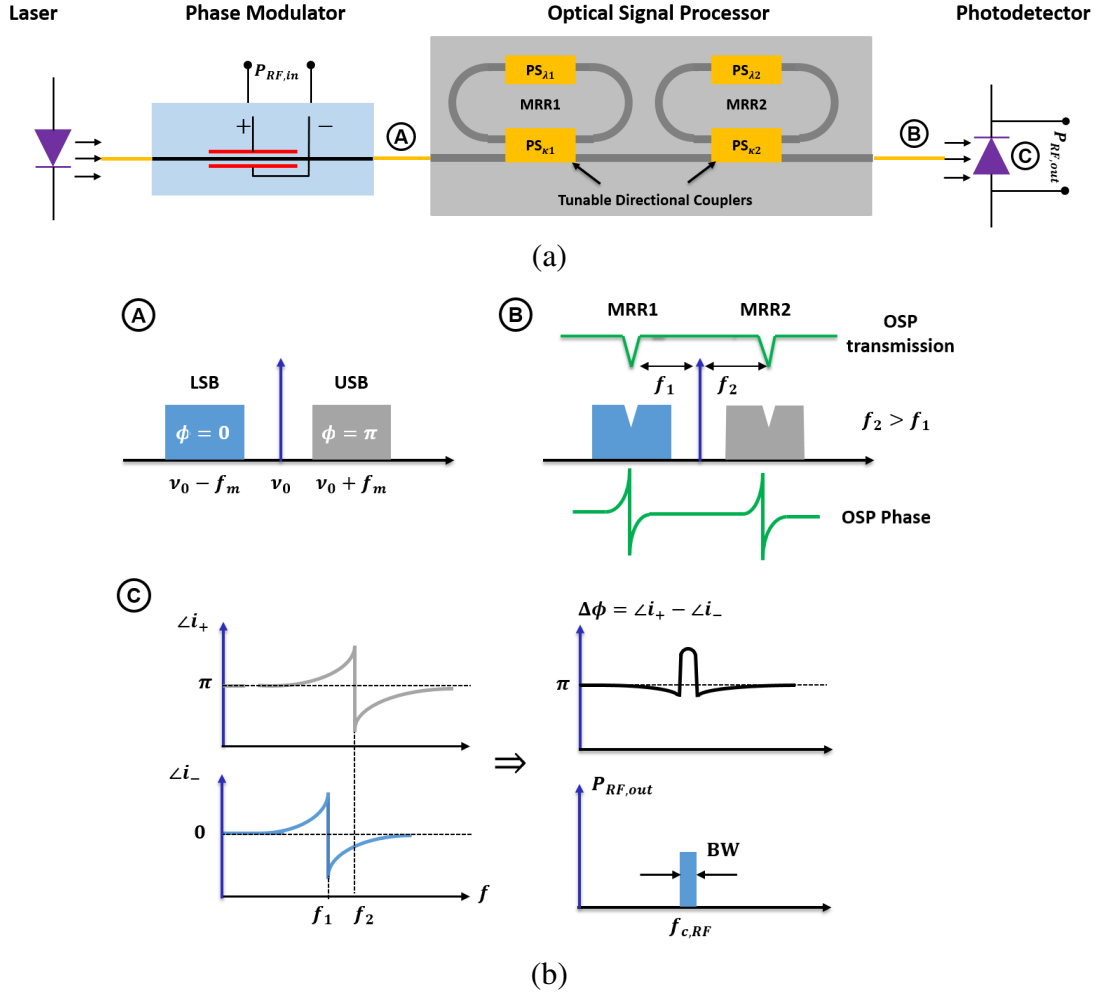


Figure 3.1: (a) The schematic of the proposed OSP chip along with its operational scheme for the RF photonic bandpass filter functions with symmetric out-of-band rejection; (b) top-left: schematic representation of the phase modulated optical spectrum with RF frequency band centering around  $f_m$ . Top-right: optical transmission characteristics of the modulated laser light along with the transmission and phase spectrum of the OSP,  $f_1, f_2$  correspond to the resonance spacings with respect to the laser carrier frequency  $\nu_0$ . Bottom-left: the phase spectrum of the beat signal corresponding to carrier and USB (top), and carrier and LSB (bottom). Bottom-right: schematic representation of the phase deviation  $\Delta\phi$  (from  $\pi$ ) between beat photocurrents  $i_+$  and  $i_-$  at the photodetector as a function of RF frequency (top), and the RF filter response corresponding to the superposition of  $i_+$  and  $i_-$  at the photodetector output.

detuning one of the microring resonators. However, the degeneracy can be easily broken in any fabricated device due to process induced variations in waveguide dimensions. The optical carrier frequency  $\nu_0$  needs to be positioned between these two non-degenerate resonances such that two resonance frequencies are at  $\nu_0 - f_1$  and  $\nu_0 + f_2$ , respectively. To achieve a symmetric out-of-band rejection the condition for the resonance offsets with the carrier is  $0 < |f_1 - f_2| \leq \text{FWHM}$ , where FWHM stands for the full-width at half maxima of the MRR resonances. The RF photonic bandpass filter response at the photodetector output is achieved by the phase readjustment in the USB and LSB induced by the microring resonators, as depicted in Fig. 3.1b. The resultant photocurrent at the detector output is the sum of two components: (i) beat current of carrier with the LSB ( $i_-$ ) and (ii) beat current of carrier with the USB ( $i_+$ ). Because of the asymmetric spacing of the resonances from the carrier, the resultant phase  $\Delta\phi = \angle i_+ - \angle i_-$  results in a non- $\pi$  from  $f_1$  to  $f_2$  and therefore, a passband is obtained with a central frequency  $f_{c,RF}$  around  $\frac{1}{2}(f_1 + f_2)$  with a symmetric out-of-band rejection. To summarize, the relative phase of the optical carrier frequency due to the resonance responses corresponding MRR1 and MRR2 are affecting the identical out-of-band rejections on the either sides of the RF passband (also see Fig. 3.1). Therefore, a careful design of the OSP comprised of two identical MRRs cascaded in all-pass configuration is very crucial which is discussed in the next section.

### 3.2 DESIGN AND SIMULATION RESULTS

The performance figure of merits (FOMs) e.g., bandwidth, out-of-band rejection, central frequency, link gain, etc. of the RF filters depend on the resonant wavelength, extinctions and the Q-values of microring resonators (MRR1 and MRR2). Therefore, we need to design our OSP such that Q-values and extinctions of each MRRs could be tuned via thermo-optic/electro-optic effect. The Q-value and extinction of a microring resonator in

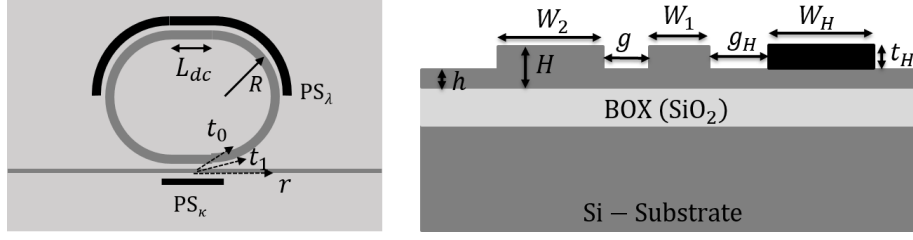


Figure 3.2: Left: schematic top view of an MRR design in SOI platform for which the ring waveguide is relatively wider than the bus waveguide; the design is to facilitate desired value of  $r$  and resonance wavelength setting using thermo-optic phase-shifters  $PS_\lambda$  and  $PS_\kappa$ ;  $L_{dc}$  is the length of the parallel section of the directional coupler,  $R$  is the bend radius of the ring waveguide. Right: schematic cross-sectional view of the the coupler annotated with important design parameters.

all-pass configuration is given by [85]:

$$Q = \frac{\pi n_g L_r \sqrt{ra}}{\lambda_r (1 - ra)} \quad (3.1)$$

$$\text{Extinction} = \left[ \frac{(r + a)(1 - ra)}{(1 + ra)(r - a)} \right]^2 \quad (3.2)$$

where  $n_g$  is the group index of guided mode,  $L_r$  is the perimeter length,  $\lambda_r$  is the resonance wavelength,  $r$  is the self-coupling coefficient and  $a$  is round trip loss factor ( $e^{-\alpha L_r}$ ;  $\alpha$  is the waveguide loss coefficient) of the MRR. From Eq. (3.1), (3.2), it is evident that both the FOMs are dependent on the coupling coefficient  $r$  of the coupler and the loss factor  $a$  inside the ring. Usually, the waveguide loss in a silicon waveguide is mainly attributed to the sidewall roughness, and the value is fixed for a given waveguide dimension; we have assumed the coupler itself is lossless. Nevertheless, designing a nearly lossless tunable coupler is critical to controlling the MRR extinction and its Q-value. In practice, the Mach-Zehnder interferometer (MZI) is the popular choice for a tunable coupler. However, the MZI-based design increases the device footprint and the perimeter of the ring  $L_r$ . The increase in perimeter eventually results in: (i) the drop of the Q-factor [85], which increases the resultant bandwidth of the filter, and (ii) the decrease in FSR, which affects the tuning range of the filter response ( $\sim \text{FSR}/2$ ) [65].

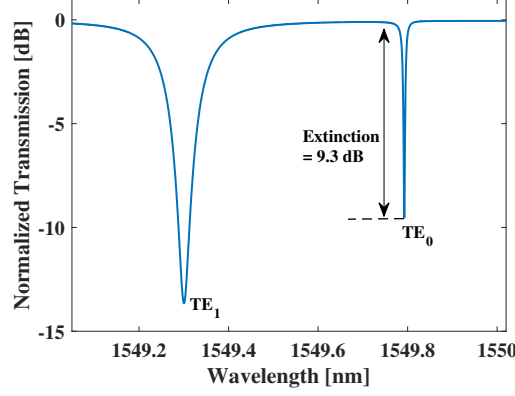


Figure 3.3: Transmission characteristics of the MRR exhibiting resonances corresponding to fundamental ( $TE_0$ ) and first-order ( $TE_1$ ) guided modes at  $\lambda_{r0} \sim 1549.792$  nm and  $\lambda_{r1} \sim 1549.3$  nm, for the parameter values given in Table 3.1.

To overcome the above mentioned challenges, we have designed an asymmetric directional coupler with a width  $W_1 = 0.5 \mu\text{m}$  for the bus waveguide and width  $W_2 = 1 \mu\text{m}$  for the ring waveguide, as shown in Fig. 3.2. The phase shifters  $PS_k$  and  $PS_\lambda$  tune the ring coupling coefficient and the resonant wavelength, respectively. However, we must note that for the slab height  $h = 150$  nm, the waveguide with width  $1 \mu\text{m}$  supports two TE-like modes ( $TE_0$  and  $TE_1$ ). Hence, there is a high chance that near the directional coupler, the input power from the bus waveguides gets coupled into the fundamental and first-order mode of the ring waveguide. In the case of higher order modes getting coupled into the ring, the conventional transfer function of the microring resonator given in Eq. 2.3 is not valid. The modified transfer function can be derived as:

$$T_R = r - \left[ \sum_{m=0}^n \frac{t_m^2 a_m e^{-j\delta_m}}{1 - a_m r_m e^{-j\delta_m}} \right] = |T_R| e^{j\phi_R} \quad (3.3)$$

where,  $m$  is the mode number,  $n$  is the number of modes coupled into the ring ( $= 2$ , in our case),  $r$  is the self coupling coefficient,  $t_m$ ,  $a_m$ ,  $\delta_m$  are the cross coupling coefficient, loss factor and phase accumulated inside the ring for  $m^{\text{th}}$ -order mode, respectively, and  $r_m = \sqrt{1 - t_m^2}$ ,  $\phi_R$  is the phase response of the MRR. For the lossless directional coupler,  $r^2 + \sum_{m=0}^n t_m^2 = 1$ .

From the coupled mode theory, the expression for the cross coupling coefficient  $t_m$  for a  $m^{\text{th}}$ -order mode, is given by [87]:

$$t_m = e^{i(\Delta\beta_m/2)L} \left[ -i\kappa_m^* \frac{\sin(s_m L)}{s_m} \right] \quad (3.4)$$

where

$$s_m = \frac{1}{2} \sqrt{4|\kappa_m|^2 + (\Delta\beta_m)^2} \quad (3.5)$$

$\Delta\beta_m$ ,  $\kappa_m$  are the effective phase mismatch and the coupling exchange between the fundamental mode of bus waveguide and the  $m^{\text{th}}$ -order mode of the ring waveguide, and  $L$  is the effective directional coupler length, which is not equal to the  $L_{dc}$ , due to the bend induced coupling [88]. Fig. 3.3 shows the simulated transmission characteristics of the proposed design of the MRR with a set of optimized parameter values given in Table 3.1. The values of  $\kappa_0$ ,  $\kappa_1$  were calculated using super-mode theory as discussed in [87] and the values  $a_0$ ,  $a_1$  are chosen based on our prior experimental observations. As the higher order modes tend to leak more due to the longer evanescent tail, the resonance of the  $\text{TE}_1$  mode in Fig. 3.3 is broader than the resonance of the  $\text{TE}_0$  mode.

The design parameters of the MRR has been optimized such that the Q-value and extinction can be tuned efficiently using the thermo-optic phase shifter ( $\text{PS}_\kappa$ ). Fig. 3.4a shows the  $r_0$  as a function of  $\Delta\beta_0$ , for the given length of the directional coupler and the gap between coupled waveguides as given in Table 3.1. For our chosen waveguide dimensions the value of  $\Delta\beta_0 \approx 0.43 [1/\mu\text{m}]$  and the corresponding  $r_0 = 0.995 (> a_0 = 0.99)$ , which is the undercoupled condition of the MRR resonance. Now, with the differential increment in temperature of the bus waveguide the values of  $\Delta\beta_m$  and  $\kappa_m$  will be changed and hence the values of  $r_m$  too. That means, the integrated thermo-optic phase shifter ( $\text{PS}_\kappa$ ) will be able to tune the value of  $r_0$  such that the resonance can be tuned from undercoupled toward critically coupled condition ( $r_0 = a_0$ ), and thus the Q-value can also be tuned. Higher Q-value is desired for a narrowband RF filter. It is important to note that in

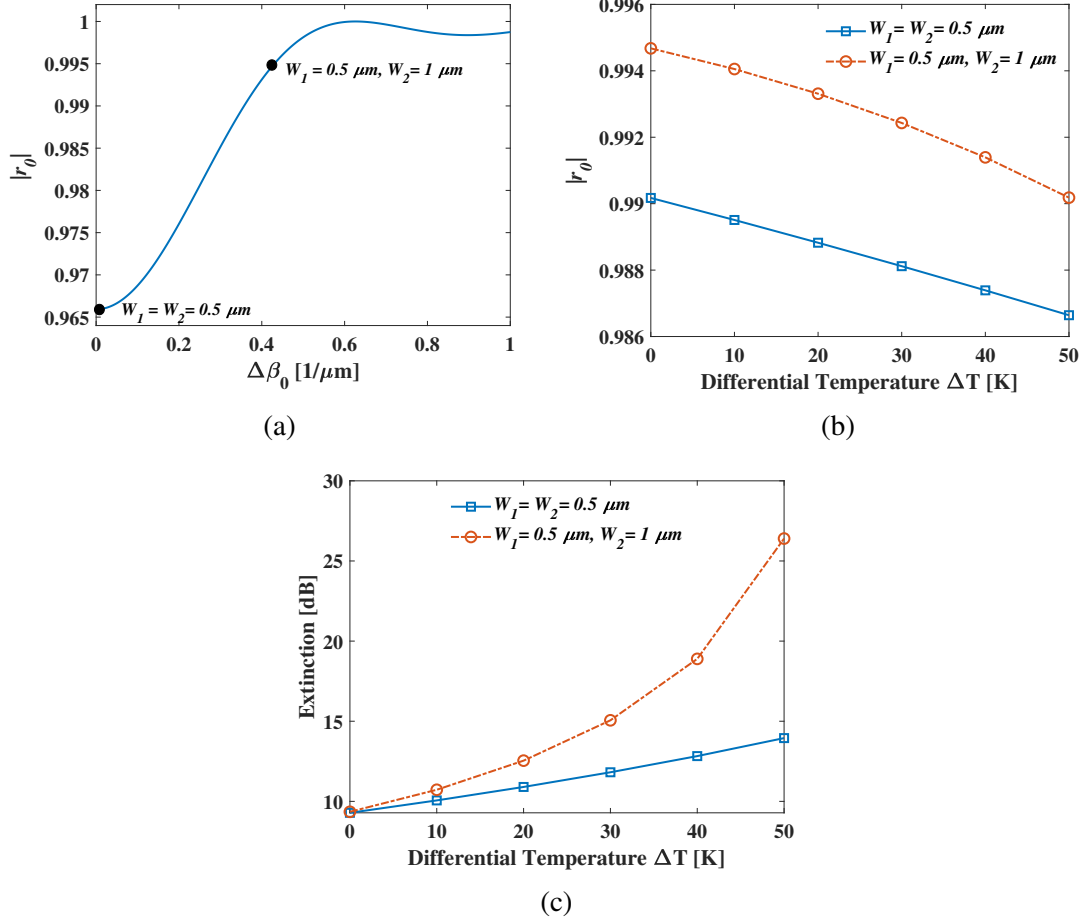


Figure 3.4: Simulation results of a MRRs for the parameter values given in Table 3.1: (a) the self-coupling coefficient  $|r_0|$  as a function of the effective phase mismatch  $\Delta\beta_0$  (between the fundamental modes in bus and ring waveguides): the values corresponding to bus and ring waveguides dimensions  $\{W_1 = W_2 = 0.5 \mu\text{m}\}$  and  $\{W_1 = 0.5 \mu\text{m}, W_2 = 1 \mu\text{m}\}$  are annotated; (b) the self-coupling coefficient  $|r_0|$  as a function of the differential temperature  $\Delta T$  between the bus and ring waveguides in the coupler region for  $\{W_1 = W_2 = 0.5 \mu\text{m}\}$  and  $\{W_1 = 0.5 \mu\text{m}, W_2 = 1 \mu\text{m}\}$ ; (c) the MRR extinction ratio as a function of  $\Delta T$  between the bus and ring waveguides in the coupler region for  $\{W_1 = W_2 = 0.5 \mu\text{m}\}$  and  $\{W_1 = 0.5 \mu\text{m}, W_2 = 1 \mu\text{m}\}$ .

Table 3.1: The calculated values for the directional coupler of effective length  $L = 9.75 \mu\text{m}$  used in MRR design of waveguide bend radius  $R = 100 \mu\text{m}$ ,  $W_1 = 0.5 \mu\text{m}$ ,  $W_2 = 1 \mu\text{m}$ ,  $g = 250 \text{ nm}$ .

Fundamental Mode		First-order Mode	
Parameter	Value	Parameter	Value
$\Delta\beta_0$	0.43 [ $1/\mu\text{m}$ ]	$\Delta\beta_1$	0.29 [ $1/\mu\text{m}$ ]
$\kappa_0$	0.26 [ $1/\mu\text{m}$ ]	$\kappa_1$	0.15 [ $1/\mu\text{m}$ ]
$a_0$	0.99	$a_1$	0.88

our proposed OSP design the best performance can be achieved when Q-value and the extinctions are matched for both the resonances.

Fig. 3.4b and Fig. 3.4c shows the comparison of the self-coupling coefficients ( $|r_0|$ ) and the corresponding extinction ratio (Eq. (3.2)) between the symmetrical directional coupler ( $W_1 = W_2 = 0.5 \mu\text{m}$ ) and the asymmetrical directional coupler ( $W_1 = 0.5 \mu\text{m}$ ,  $W_2 = 1 \mu\text{m}$ ) with the differential temperature  $\Delta T$  (between the bus and ring waveguide in the coupler region). From the calculated results shown in the figures it is evident that the proposed waveguide design  $\{W_1 = 0.5 \mu\text{m}, W_2 = 1 \mu\text{m}\}$  is more efficient for the thermo-optic tuning of the Q-value and the extinction ratio, than those for standard design with symmetric coupler  $\{W_1 = W_2 = 0.5 \mu\text{m}\}$ . In addition to the improved tuning efficiency of the coupling coefficient, the proposed design also provides an additional advantage of the reduced mode interaction with sidewall roughness inside the ring (higher waveguide width), and thus improving the Q-value of the MRRs to be fabricated. In summary, the two-fold advantage of the reduced waveguide loss and the improved thermo-optic tuning of the coupling coefficient, the proposed MRR design is superior for the realization of a RF bandpass filters with tunable bandwidth and large tuning range of center frequency up to 60 GHz, which is limited by the FSR of the microring resonators. We have restricted our ring waveguide width to  $1 \mu\text{m}$  supporting two guided modes; to avoid additional resonances which would limit the tuning range of RF bandpass filter operation.

Table 3.2: Simulation parameter values for calculating RF filter output of the proposed OSP described in Fig. 3.1a.

Component	Parameter		
	Description	Parameter	Values
Laser source	Input power	$p_{in}$	13 dBm
	Carrier wavelength	$\lambda_0$	$\sim 1550$ nm
	Carrier frequency	$\nu_0$	$\sim 193.458$ THz
Phase Modulator (Lithium Niobate)	Optical insertion loss	$\alpha_m$	4 dB
	Input RF signal	—	sinusoidal
	Modulation index	$\delta = V_{in}/V_\pi$	0.014
	RF frequency band	$f_m$	1 - 20 GHz
	RF band step size	—	100 MHz
Optical signal processor	Fiber-to-chip coupling loss	$\eta_L$	8 dB/coupler
	Bend radius	$R$	100 $\mu$ m
	Waveguide loss	—	1.4 dB/cm
	Power cross-coupling coefficient	$ t_0 ^2$	2.7%
	Estimated Q-value	$Q$	$3 \times 10^5$
	Extinction	—	10 dB
	FWHM	—	5 pm ( $\sim 600$ MHz)
Photodetector	Responsivity	$R_d$	0.45 A/W
	Matched load	$R_L$	50 $\Omega$

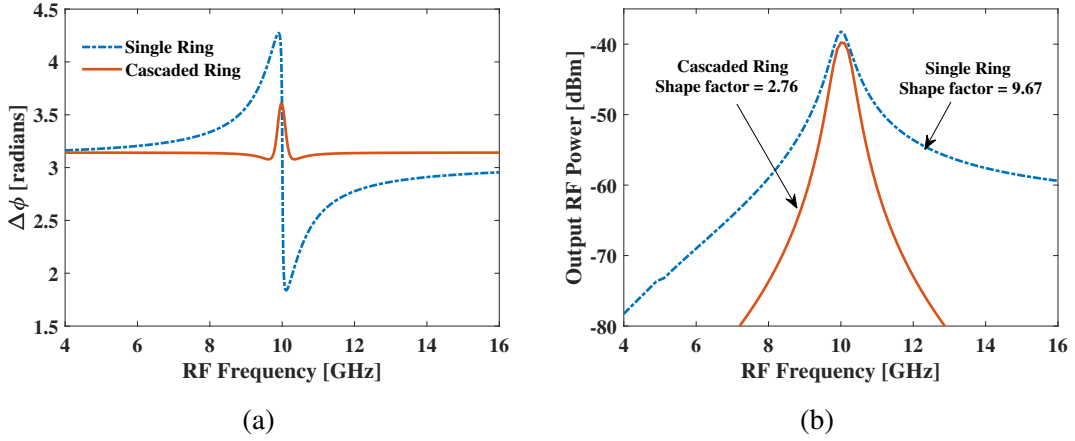


Figure 3.5: Phase and amplitude spectrum for single MRR and cascaded double MRRs: (a) Calculated phase difference (deviation from  $\pi$ ) between the LSB and USB beat signals at the photodetector as function of frequency; and (b) the simulated RF filter response for single ring and cascaded ring configuration with 600 MHz bandwidth. Calculations are carried out for  $f = 10$  GHz (laser wavelength position with respect to a resonant frequency of the MRR) for the single ring and  $f_1 = 9.9375$  GHz,  $f_2 = 10.0625$  GHz for cascaded ring.



Following the OSP device design, the RF filter response was simulated using the theoretical equations discussed in Appendix A, and the simulation parameter values listed in Table. 3.1 and Table. 3.2 for the proposed link given in Fig. 3.1a. In this case, as the cascaded microring resonators are the configured OSP structure in the simulations, the OSP transfer function  $H(\omega)$  is replaced by the product of the individual transfer functions of MRR1 and MRR2, i.e.,  $H(\omega) = T_{R1}(\omega)T_{R2}(\omega)$  (see Eq. (3.3)). Also, the simulation parameters of the OSP listed in Table. 3.1 are considered as per the experimental observations of the in-house fabricated devices. The calculated phase and amplitude spectra are shown in Fig. 3.5, for single MRR and the proposed cascaded two MRRs OSP chip. In case of single MRR we have positioned the laser wavelength with 10 GHz offset from the resonant wavelength of interest, whereas for the proposed OSP chip we have used  $f_1 = 9.9375$  GHz,  $f_2 = 10.0625$  GHz. Thus we obtained bandpass filter response centering around 10 GHz with a 3-dB bandwidth of 600 MHz. As expected, in case of single MRR the filter response (Fig. 3.5b) exhibits asymmetric out-of-band rejection, which is directly related to the asymmetric phase spectrum obtained in Fig. 3.5a. However, our proposed design architecture of the OSP chip comprised of two cascaded MRRs exhibits well-defined symmetric out-of-band rejections. The shape factor, defined as the ratio of 20-dB bandwidth to the 3-dB bandwidth, has reduced from 11.71 (single MRR) to 3.67 (cascaded MRRs).

The bandwidth of the RF filter response can be tuned by tuning the relative position of the microring resonances ( $f_1, f_2$ ) with respect to the laser carrier frequency  $\nu_0$ . We have plotted RF filter responses as a function of  $\Delta f = |f_2 - f_1|$  in Fig. 3.6a. However, it is evident from our simulation results as  $\Delta f$  approaches to 500 MHz, the RF filter passband starts splitting (see the inset of Fig. 3.6a). It is also important to note that the RF link gain drops for narrower RF filter bandwidth. For  $\Delta f \rightarrow 0$  the reduction in link gain is expected as the phase induced by the identical MRRs tends to perfectly cancel each other. However, the change in link gain to realize the RF filter response with bandwidth  $\sim$  MRR FWHM is in the tolerable range ( $< 1.5$  dB). Hence, in the current MRRs configuration

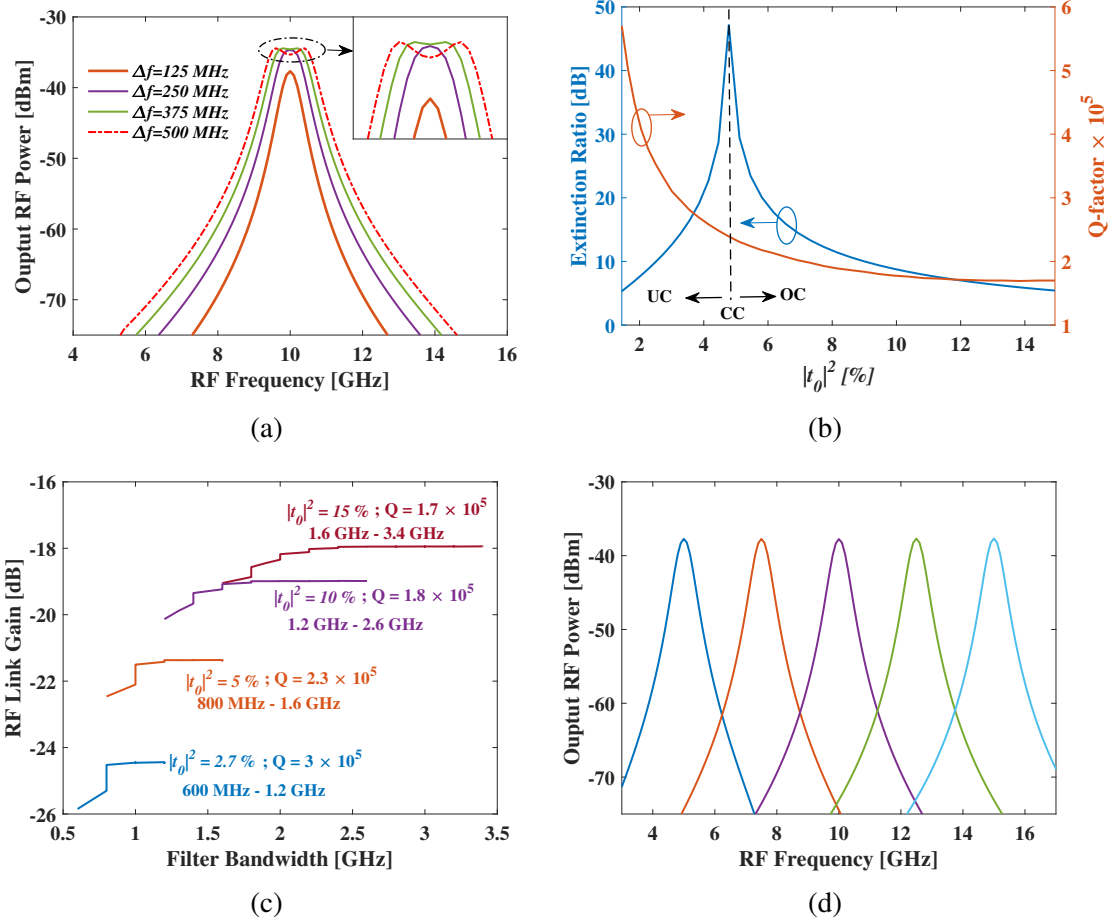


Figure 3.6: (a) The RF filter response with tunable bandwidth by detuning  $\Delta f = |f_2 - f_1|$ , (b) the change in MRR Q-factor and extinction ratio with the coupling coefficient  $|t_0|^2$  with under-coupled (UC), over-coupled (OC) and critically coupled (CC) regions marked, (c) the plot of change in tunable bandwidth range of the RF filter and the corresponding change in RF link gain for different coupling coefficients (Q-factor) of the MRR, and (d) the tuning of RF central frequency by detuning the resonance spacing  $f_1 + f_2$  and maintaining constant  $\Delta f = |f_2 - f_1| = 125$  MHz and MRR coupling coefficient  $|t_0|^2 = 2.7\%$ .

( $|t_0|^2=2.7\%$ ), considering the maximum allowable ripples in the passband as 0.5 dB, we have achieved the filter bandwidth tuning range of 600 MHz to 1200 MHz. However, tuning the FWHM (or Q-factor) of the MRR can change the filter bandwidth and its tuning range.

Since the proposed OSP design can be programmed in terms of Q-value and extinction ratio of the individual MRRs by means of integrated micro-heaters ( $PS_{\kappa 1}$  and  $PS_{\kappa 2}$ ) as shown in Fig. 3.6b, the RF filter bandwidth can be programmed as desired within a specified range. The operating condition of the MRR moves from the under-coupled (UC) state to the over-coupled (OC) with the increase in the power coupling coefficient  $|t_0|^2$ , and the maximum extinction point is denoted as the critically coupled (CC) state. As the phase response of the MRR depends on the state of the coupling condition, the change in bandwidth tuning range (by tuning  $|t_0|^2$ ) is accompanied by the change in the link gain of the RF filter [66]. Fig. 3.6c shows the change in the filter tunable bandwidth range for different coupling conditions for which the link gain variation with the bandwidth is less than 1.5 dB. As expected, the filter bandwidth and tuning range increase due to the increase of the MRR FWHM (by tuning  $|t_0|^2$ ). The link gain shows similar behavior for all the coupling coefficients as shown in Fig. 3.6a.

Likewise the passband width, the center frequency can be detuned but in this case both the microring resonators resonances ( $f_1, f_2$ ) have to be equally tuned towards/away from the carrier frequency  $\nu_0$ , using the thermo-optic phase shifter ( $PS_{\lambda 1}$  and  $PS_{\lambda 2}$ ). Fig. 3.6d shows the RF filter tuning response for a given bandwidth 600 MHz (corresponding to a fixed  $\Delta f = 125$  MHz). It is worth to mention here that the estimated link gain of the -27.7 dB ( $= P_{RF,out}/P_{RF,in}$ ) and it can be improved by increasing input laser power and decreasing optical losses. The detector responsivity  $R_d$  and modulator half-wave voltage  $V_\pi$  also play roles in the RF insertion loss. From Fig. 3.6a and Fig. 3.6d, the theoretical model predicts an out-of-band rejection greater than 40 dB for the entire tuning range of the central frequency and the filter bandwidth.

Table 3.3: Design parameters chosen for the fabrication of the OSP.

Description	Symbol	Value
Device layer thickness	$H$	220 nm
Slab height	$h$	150 nm
Ring radius	$R$	100 $\mu\text{m}$
Directional coupler gap	$g$	250 nm
Bus waveguide width	$W_1$	0.5 $\mu\text{m}$
Ring waveguide width	$W_2$	1 $\mu\text{m}$
Directional coupler length	$L_{dc}$	10 $\mu\text{m}$
Heater width	$W_H$	2 $\mu\text{m}$
Heater thickness	$t_H$	100 nm
Waveguide to heater gap	$g_H$	2 $\mu\text{m}$

### 3.3 FABRICATION AND CHARACTERIZATION

We have fabricated the proposed design of cascaded MRR based optical signal processor in a SOI substrate with 220 nm device layer thickness using our in-house facilities available at the Centre for NEMS and Nanophotonics (CNNP), IIT Madras. The various design parameter values chosen for fabrication are based on the theoretical discussion in the previous section and they are listed in Table 3.3. The mask layout comprising of two cascaded OSP MRRs (D1 and D2), reference asymmetric directional coupler (D3) and reference single microring resonator (D4) along with the required metal routing, contact pads and test heater elements is given in Fig. 3.7a. The input/output waveguides are terminated with grating couplers for fiber-chip-fiber coupling (see Fig. 3.7b). The Titanium micro-heaters are integrated on the silicon slab within a close proximity of the rib waveguide structures as per requirements of the thermo-optic phase detuning (see Fig. 3.7c). The micro-heater design parameters (width  $W_H = 2 \mu\text{m}$ , thickness  $t_H = 100 \text{ nm}$ , distance from the waveguide  $g_H = 2 \mu\text{m}$ ) were chosen based on the previously studied experimental results [89]. Since all the microheaters may need to be functional simultaneously, we have routed the heater connections using Aluminium interconnects to the contact pads ( $100 \mu\text{m} \times 100 \mu\text{m}$ ) in a row with a pitch of  $150 \mu\text{m}$  (see Fig. 3.7d) such that they can be probed simultaneously using a DC probe card. As the rib waveguide with air cladding is chosen device configuration, the Aluminium metal lines has to be

routed a long distance maintaining sufficient safe distance from the optical waveguides and grating couplers, thus increasing the required space for the design ( $3 \text{ mm} \times 5.6 \text{ mm}$ ).

The optimized recipes and the process flow followed for the fabrication of the prepared mask layout are given in Appendix B. The microscope images of the fabricated microring resonator (OSP MRR: D2) at different stages of the thermo-optic phase shifter integration are given in Fig. 3.8a - Fig. 3.8d, showing the near-perfect translation of the designed layout on to the silicon chip. For the structures with smaller feature sizes, we have performed the scanning electron microscope (SEM) imaging in an E-beam lithography system, and the images are given in Fig. 3.9. The grating coupler, along with the zoomed image of the gratings (with a duty cycle of 49.5 %), are shown in Fig. 3.9a and Fig. 3.9b, respectively. Next, the zoomed-in section of the asymmetric directional coupler of the ring resonator (for device D2) integrated with the phase shifter  $\text{PS}_{\kappa 2}$  indicating all the necessary dimensions are shown in Fig. 3.9c. In addition, the SEM image of the ring waveguide and the phase shifter  $\text{PS}_{\lambda 2}$  is also given in Fig. 3.9d.

Finally, the microscope image of the fabricated structure is shown in Fig. 3.10a, in which a reference directional coupler, a reference MRR and test heater structures have been included. In addition to the OSP structure with an asymmetric directional coupler (design #1), we have followed the same process to fabricate the OSP structure with MZI as the tunable coupler (design #2) to highlight the enhancement in the filter responses with the proposed structure. The corresponding microscope image of the entire fabricated structure is shown in Fig. 3.10b. The characterization results corresponding to the OSP design #1 are discussed in the following section of this chapter. Whereas, the characterization results corresponding to the OSP design #2 are given in Appendix C. The RF filter responses for both the structures are given in Section 3.4

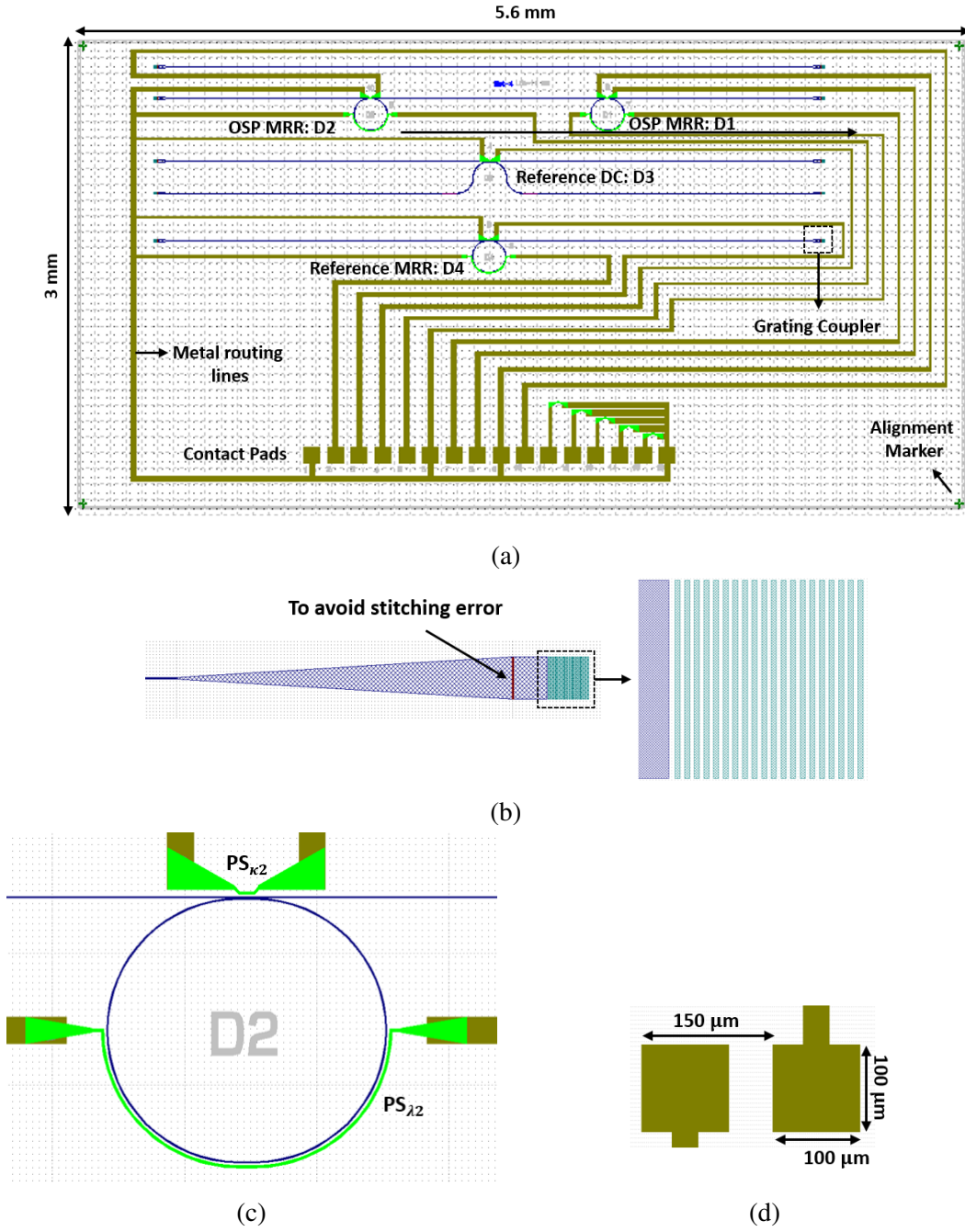


Figure 3.7: (a) Mask layout of the fabricated structure comprising of two cascaded OSP MRRs (D1 and D2), reference asymmetric directional coupler (D3), reference single microring resonator (D4) along with grating couplers, metal routing, contact pads and test heater elements, (b) zoomed-in mask layout indicating the grating coupler and an extra polygon added to avoid to the stitching error in e-beam lithography, (c) mask layout of the rib waveguide based OSP MRR (D2) along with the phase shifters and (d) contact pads for the probing of the fabricated structures along with its dimensions.

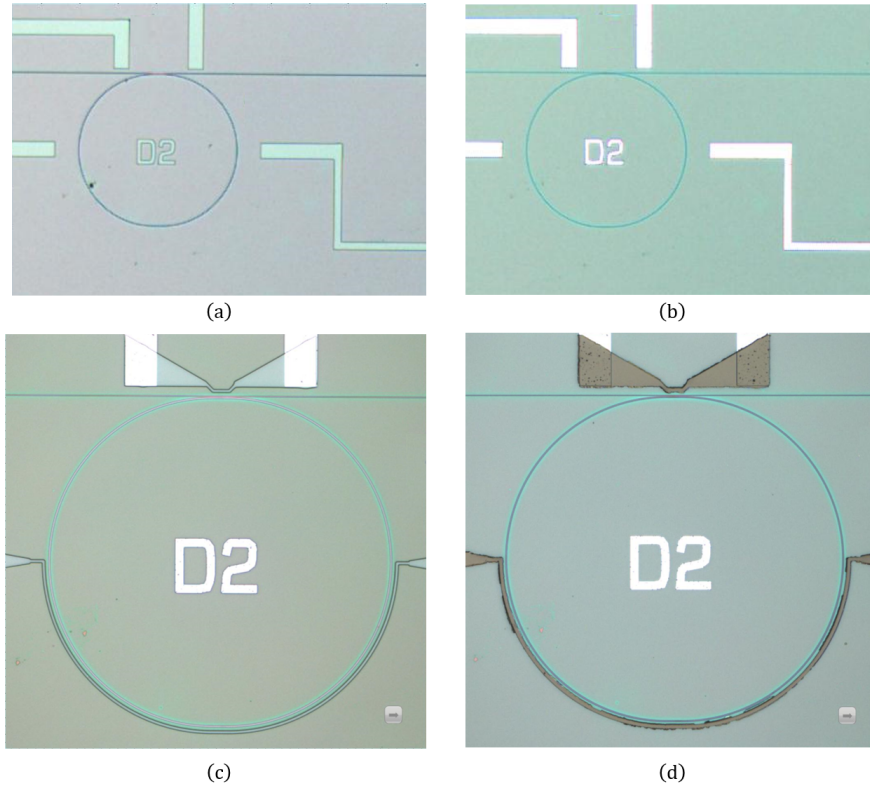


Figure 3.8: Microscope images of the fabricated structures during different stages of the active fabrication process: (a) after the contact patterning and development, (b) post Aluminium metal deposition and lift-off, (c) after microheater patterning and development, and (d) post Titanium deposition and lift-off.



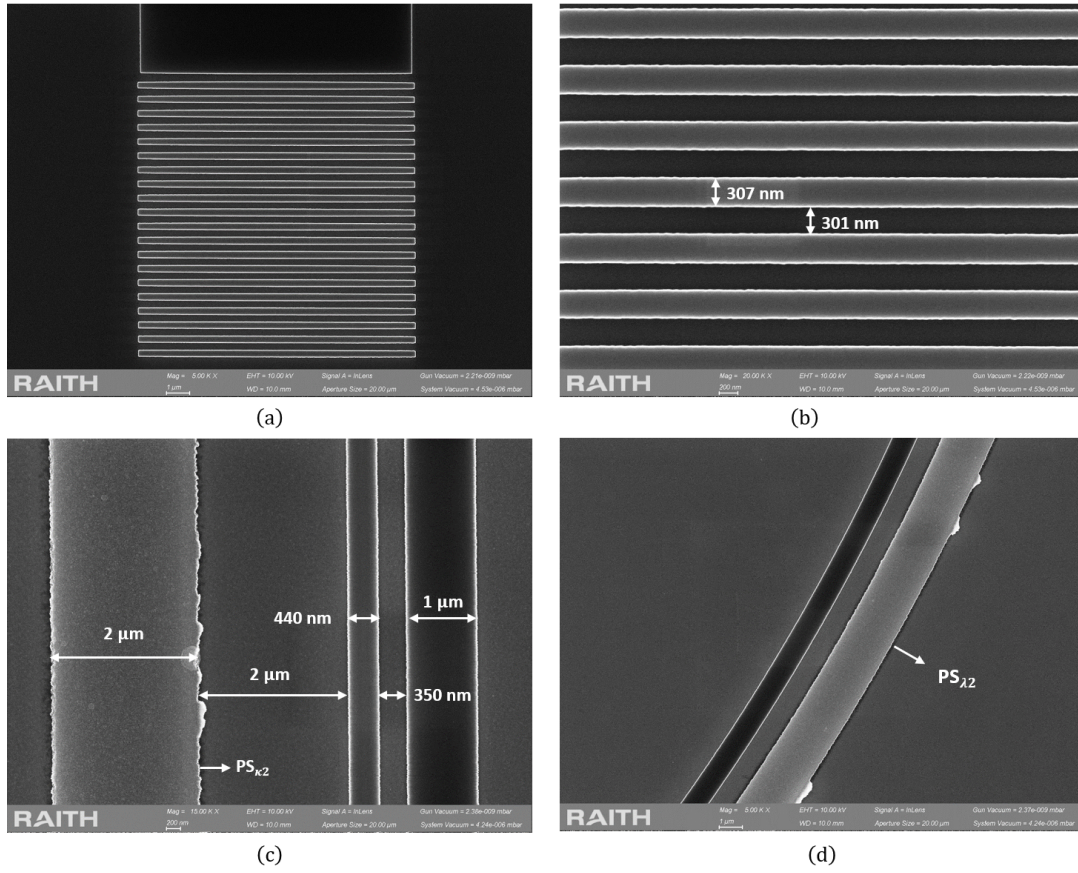


Figure 3.9: Scanning electron microscope (SEM) images of the fabricated structures: (a) grating coupler, (b) zoomed image of the grating coupler with 49.5 % duty cycle, (c) asymmetric directional coupler of the fabricated ring (device D2) indicating the integrated microheater  $PS_{\kappa 2}$  and the device dimensions, and (d) ring waveguide integrated microheater  $PS_{\lambda 2}$ .



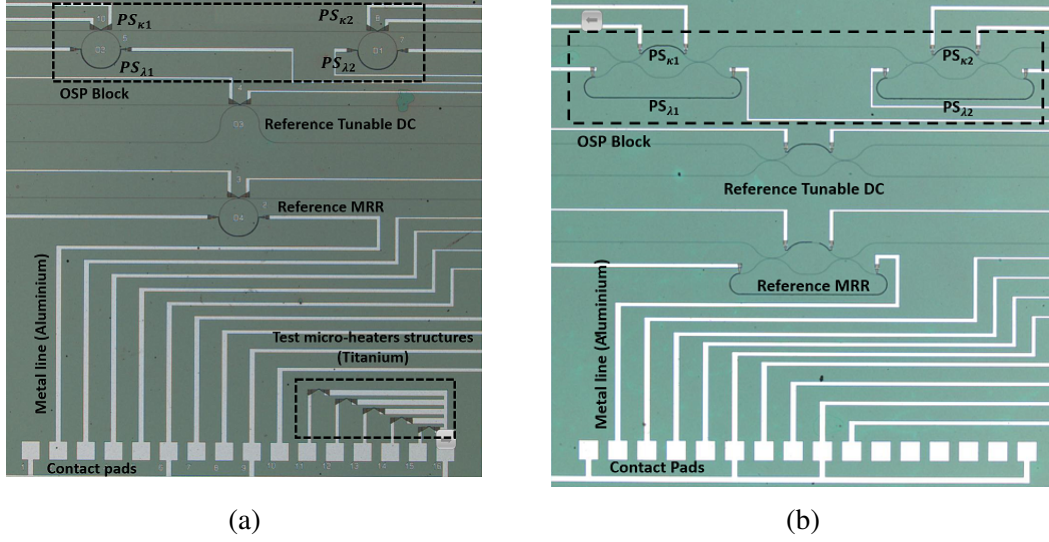


Figure 3.10: Microscope image of the fabricated OSP (a) with asymmetric DC as the tunable coupler (design #1), and (b) with MZI as the tunable coupler (design #2), along with a reference tunable coupler, a reference MRR and test microheater structures.

### 3.3.1 Passive Transmission Characteristics

After the fabrication of the desired structures, we have carried out the passive and thermo-optic characterization of the ring resonators, using the same setup shown in Fig. 2.17 of the previous chapter. The devices were characterized for  $1520 \text{ nm} \leq \lambda \leq 1620 \text{ nm}$ . The transmission characteristics of the single MRR and cascaded MRR are given in Fig. 3.11a and Fig. 3.11b, respectively; the results are shown only around  $\lambda \sim 1540 \text{ nm}$ , as the grating coupler efficiency (loss  $\sim 8 \text{ dB/facet}$ ) is found to be maximum around this wavelength range. As expected, resonances corresponding to the fundamental ( $\text{TE}_0$ ) and first-order ( $\text{TE}_1$ ) guided modes are present in both the devices. The resonances corresponding to the  $\text{TE}_0$  are found to have higher Q-values ( $\sim 10^5$ ) than those for  $\text{TE}_1$  ( $\sim 10^4$ ). The extinction ratio (ER), free spectral range (FSR) and the corresponding group indices ( $n_g$ ) could be directly estimated from the transmission characteristics ( $\text{FSR} = \frac{c}{n_g L_r}$ ). The other parameters such as self-coupling coefficient  $r$ , round trip loss factor  $a$ , waveguide loss  $\alpha$  and Q-values were extracted by modeling individual resonance and are listed in Table 3.4. The group index of the  $\text{TE}_1$  mode is found to be slightly

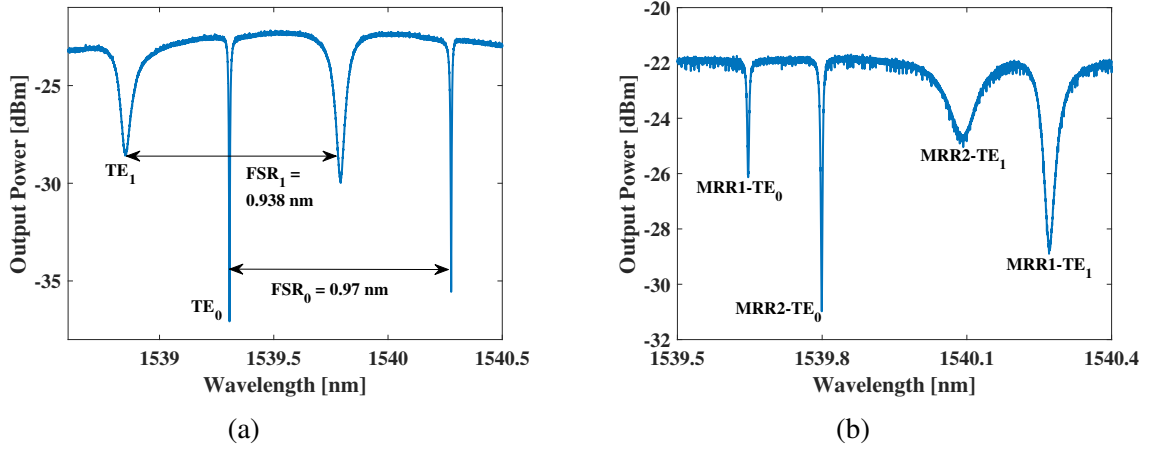


Figure 3.11: Transmission characteristics of the fabricated (a) single MRR; and (b) cascaded MRR devices around  $\lambda \sim 1540$  nm.

higher ( $\sim 3.87$ ) than that of the  $TE_0$  mode ( $\sim 3.81$ ). Similarly, the minimum losses corresponding to the  $TE_0$  guided mode is extracted to be lower ( $\sim 1.4$  dB/cm) than that of the  $TE_1$  mode ( $\sim 8$  dB/cm). These results are in accordance with the theoretical prediction as discussed in the previous section. It must be noted that the extracted waveguide loss corresponding to the guided  $TE_0$  mode in a single-mode waveguide (using design #2), reported in Appendix C, is almost three times higher (4 dB/cm), and the corresponding Q-value was about 5 times lower ( $\sim 0.58 \times 10^5$ ; see Appendix C). Therefore, the proposed OSP chip designed with multi-mode waveguide ring resonator is expected to perform better in terms of RF photonic bandpass filter function, which would be discussed in the following section.

### 3.3.2 Thermo-Optic Characteristics

To realize an efficient RF photonic bandpass filter functions with symmetric out-of-band rejection, the resonances of MRR1 and MRR2 corresponding to the  $TE_0$  mode should be positioned with a desired spacing (decides the central frequency of the RF passband) and the identical extinction ratio; and also the resonances corresponding to  $TE_1$  modes do not intrude within the RF frequency band of interest. Therefore, the thermo-optic tuning of four integrated phase-shifters (see Fig. 3.8e) play crucial roles; they need to

Table 3.4: Extracted coefficients of the fabricated devices. FSR: free spectral range,  $\lambda_r$ : resonant wavelength,  $n_g$ : group index,  $r$ : self-coupling coefficient,  $a$ : round trip loss factor,  $Q$ : quality factor  $\alpha$ : waveguide loss and ER: extinction ratio

	TE <sub>0</sub>		TE <sub>1</sub>	
	Parameter	Value	Parameter	Value
Single ring	FSR <sub>0</sub>	0.97 nm	FSR <sub>1</sub>	0.938 nm
	$\lambda_{r0}$	1539.3 nm	$\lambda_{r1}$	1539.8 nm
	$n_{g0}$	3.81	$n_{g1}$	3.94
	$r_0$	0.99	$r_1$	0.954
	$a_0$	0.985	$a_1$	0.893
	$Q_0$	$2 \times 10^5$	$Q_1$	$3 \times 10^4$
	$\alpha_0$	1.9 dB/cm	$\alpha_1$	15 dB/cm
	ER <sub>0</sub>	14.46 dB	ER <sub>1</sub>	6.84 dB
Cascaded ring (MRR1)	FSR <sub>0</sub>	0.97 nm	FSR <sub>1</sub>	0.95 nm
	$\lambda_{r0}$	1539.65 nm	$\lambda_{r1}$	1539.27 nm
	$n_{g0}$	3.81	$n_{g1}$	3.89
	$r_0$	0.997	$r_1$	0.978
	$a_0$	0.988	$a_1$	0.942
	$Q_0$	$3.6 \times 10^5$	$Q_1$	$6 \times 10^4$
	$\alpha_0$	1.5 dB/cm	$\alpha_1$	8 dB/cm
	ER <sub>0</sub>	4 dB	ER <sub>1</sub>	6.65 dB
Cascaded ring (MRR2)	FSR <sub>0</sub>	0.971 nm	FSR <sub>1</sub>	0.958 nm
	$\lambda_{r0}$	1539.8 nm	$\lambda_{r1}$	1540.1 nm
	$n_{g0}$	3.81	$n_{g1}$	3.86
	$r_0$	0.994	$r_1$	0.98
	$a_0$	0.989	$a_1$	0.882
	$Q_0$	$3 \times 10^5$	$Q_1$	$3.5 \times 10^4$
	$\alpha_0$	1.4 dB/cm	$\alpha_1$	16 dB/cm
	ER <sub>0</sub>	8.87 dB	ER <sub>1</sub>	2.76 dB

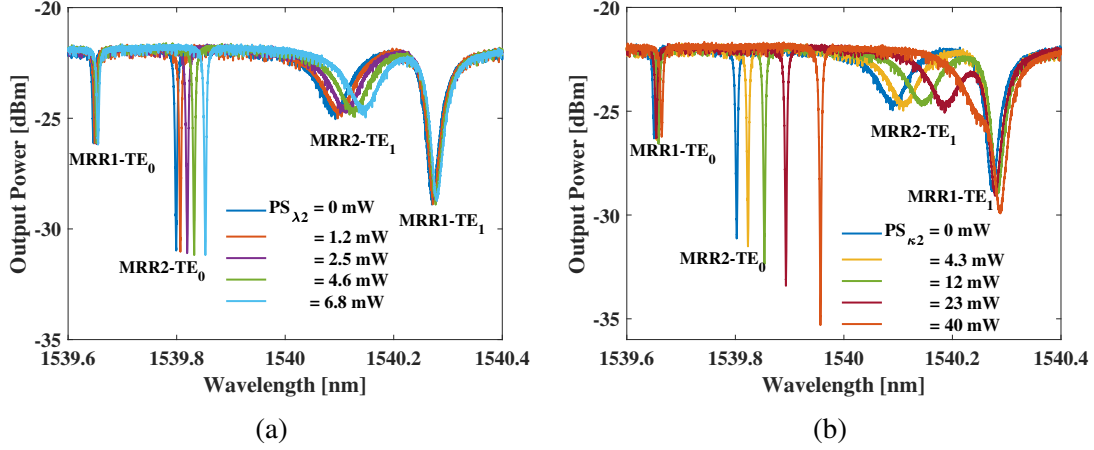


Figure 3.12: The thermo-optic tuning characteristics of: (a) resonance wavelength; and (b) extinction ratio of MRR2 using the phase shifters  $PS_{\lambda 2}$  and  $PS_{\kappa 2}$ , respectively, for the different settings of the thermal power level  $P_{th}$ .

be individually reconfigured or programmed. Fig. 3.12a and Fig. 3.12b present the thermo-optic detuning of resonance wavelengths and coupling coefficient for the MRR2 by using the phase-shifters  $PS_{\lambda 2}$  and  $PS_{\kappa 2}$ , respectively. By tuning  $PS_{\lambda 2}$ , we observed the tuning efficiency of  $\sim 8$  pm/mW for both  $TE_0$  mode and  $TE_1$  mode resonances. It must be noted that this tuning efficiency is directly related to the FSR of the MRR; higher the FSR, higher is the tuning efficiency. In the process, there is a thermal crosstalk observed in MRR1 while the active tuning of MRR2 using  $PS_{\lambda 2}$ ; we noted thermal crosstalk induced tuning of MRR1 resonances is nearly about 8 times lower ( $\sim 1$  pm/mW) than that of active MRR2 resonance tuning. This thermal crosstalk can be mitigated by suitable programming of all the phase shifters simultaneously. However, the thermal crosstalk can be eliminated to a large extent by adding trenches (up to the BOX layer of the SOI substrate) between the phase shifters.

As we intend to have identical extinction for  $TE_0$  resonances for both the MRRs, we carried out thermo-optic tuning of the  $PS_{\kappa 2}$  and the results are shown in Fig. 3.12b. We could achieve change in extinction from 9.3 dB to 13.2 dB for a thermal power consumption of  $P_{th} = 40$  mW. However, we also observed wavelength tuning with a slope

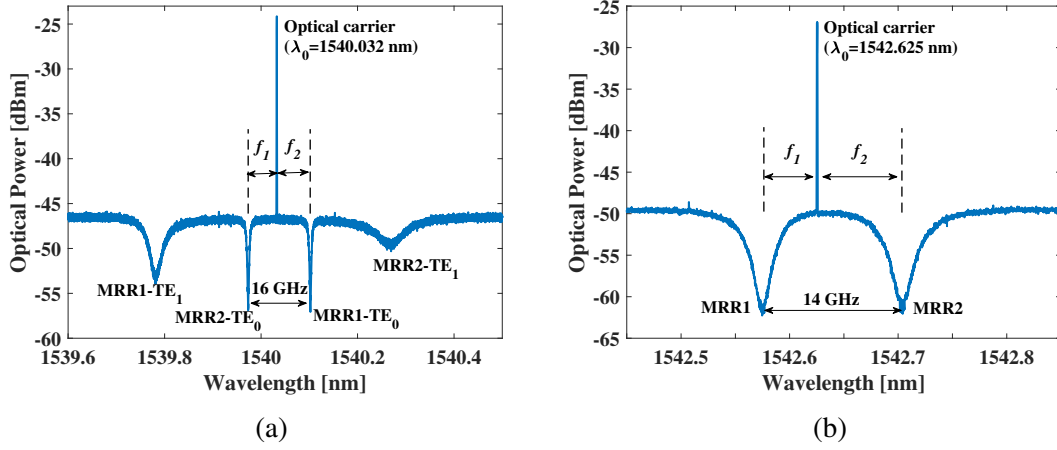


Figure 3.13: The transmission characteristics of the fabricated OSP designs (1 % tapped from FOC<sub>2</sub> shown in Fig. 2.23) for a programmed setting of thermo-optic phase shifters, along with the launched optical carrier for a RF photonic bandpass filter with symmetric out-of-band rejection: (a) for OSP design #1,  $\lambda_0 = 1540.032$  nm,  $PS_{\kappa 1} - 83.7$  mW,  $PS_{\lambda 1} - 10.8$  mW,  $PS_{\kappa 2} - 0$  mW,  $PS_{\lambda 2} - 0$  mW, central frequency  $\sim 8$  GHz, and (b) for OSP design #2,  $\lambda_0 = 1542.625$  nm,  $PS_{\kappa 1} - 0$  mW,  $PS_{\lambda 1} - 0$  mW,  $PS_{\kappa 2} - 21.8$  mW,  $PS_{\lambda 2} - 0$  mW, central frequency  $\sim 7$  GHz.

of  $\sim 2.32$  pm/mW. A similar exercise was carried out for the OSP design #2, and the corresponding thermo-optic tuning characteristics are given in Fig. C.2 of Appendix C. Again, the desired extinction and resonance wavelength settings can be obtained by configuring the four phase shifters simultaneously. For example, we achieved one set of desired operating condition for design #1 (shown in Fig. 3.13a) by following set of thermal power consumption at the phase shifters:  $PS_{\kappa 1} - 83.7$  mW,  $PS_{\lambda 1} - 10.8$  mW,  $PS_{\kappa 2} - 0$  mW,  $PS_{\lambda 2} - 0$  mW (expected  $f_c - 8$  GHz). Similarly, we achieved the desired operating condition for design #2 (shown in Fig. 3.13b) by following set of thermal power consumption at the phase shifters:  $PS_{\kappa 1} - 0$  mW,  $PS_{\lambda 1} - 0$  mW,  $PS_{\kappa 2} - 21.8$  mW,  $PS_{\lambda 2} - 0$  mW (expected  $f_c - 7$  GHz).

### 3.4 RF FILTER EXPERIMENTS

To demonstrate the RF photonic bandpass filter function with the symmetric rejection, we have used the same experimental setup shown in Fig. 2.23. The OSP (design #1) was

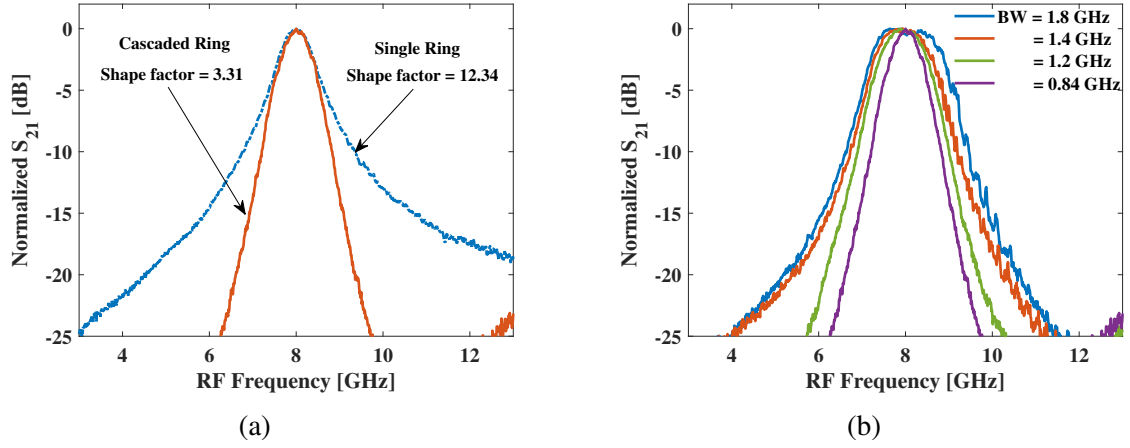


Figure 3.14: (a) Measured RF filter response with single ring and cascaded ring configuration, and (b) measured RF filter response at 8 GHz central frequency with tunable bandwidth of 0.84 GHz - 1.8 GHz. The given results correspond to OSP design #1.

configured to its operating condition, as shown in Fig. 3.13a, such that  $f_1 = 7.78$  GHz,  $f_2 = 8.22$  GHz and subsequently the observed RF filter function in LCA has been shown in Fig. 3.14a. To distinguish the performance of our proposed OSP with double ring configuration, we have also shown the performance of a RF filter function with single MRR design. It is clearly evident that the asymmetric out-of-band rejection is observed in case of single MRR and symmetric out-of-band rejection in case of cascaded MRRs, as predicted in our theoretical simulations shown earlier in Fig. 3.5b. The observed 3-dB bandwidth of the OSP RF filter function is 0.84 GHz and the out-of-band rejection is greater than 20 dB (limited by the noise floor of the RF link). As expected, the shape factor of the filter response has improved from 12.34 (in case of single MRR) to 3.31 (for cascaded MRRs). The center frequency of the RF photonic bandpass filter is 8 GHz, which is matching to the expected value of  $f_{c,RF} = \frac{1}{2}(f_1 + f_2)$ . For a fixed optical carrier wavelength ( $\lambda_0 = 1540.032$  nm) and the fixed  $f_{c,RF} = 8$  GHz, the values of  $f_1$  and  $f_2$  were adjusted by thermo-optically detuning the resonance wavelengths (MRR1-TE<sub>0</sub> and MRR2-TE<sub>0</sub>), to obtain the bandwidth detuning from 0.84 GHz to 1.8 GHz of RF photonic bandpass filter function, as shown in Fig. 3.14b.

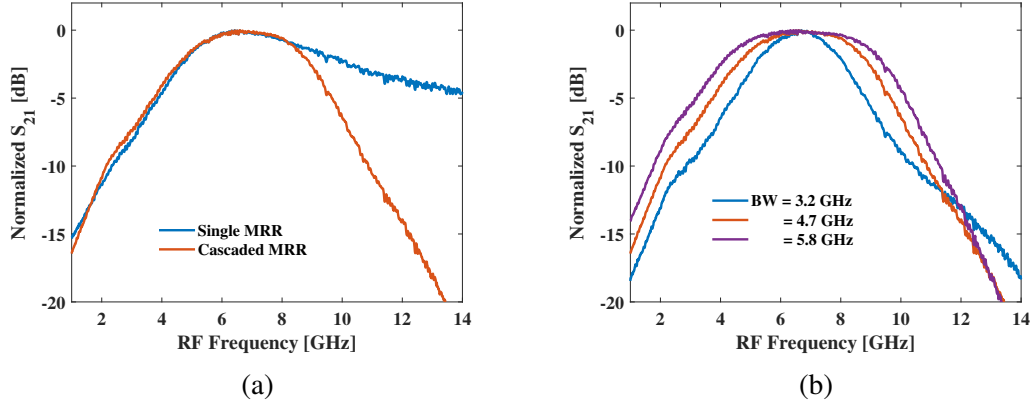


Figure 3.15: (a) Measured RF filter response with single ring and cascaded ring configuration, and (b) measured RF filter response with tunable bandwidth of 3.2 GHz - 5.8 GHz. The given results correspond to OSP design #2.

Next, Fig. 3.15a shows the filter responses corresponding to OSP design #2 (see Fig. 3.10b) with single ring and cascaded ring for the central frequency  $\sim 7$  GHz. As expected, the asymmetric out-of-band rejection (with 3-dB BW = 6.1 GHz) is observed in the case of single MRR, and symmetric out-of-band rejection (with 3-dB BW = 4.7 GHz) in the case of cascaded MRRs, but with increased values of 3-dB bandwidths when compared with design #1. For the measured results, we were unable to calculate the shape factors as the 20-dB bandwidth values for the responses are greater than the range of operating frequencies. Next, for the fixed value of the resonance spacing, i.e.,  $(f_1 + f_2)/2 = 7$  GHz, their difference  $|f_1 - f_2|$  was adjusted by detuning the optical carrier wavelength to obtain the bandwidth detuning from 3.2 GHz to 5.8 GHz of RF photonic bandpass filter function, as shown in Fig. 3.15b. The comparison of the measured filter responses given in Fig. 3.14 (with the OSP design #1) and Fig. 3.15 (with the OSP design #2), establishes the enhancement in filter characteristics (improved roll-off with narrowband response) using the proposed asymmetric DC based tunable coupler.

Fig. 3.16a shows the tuning characteristics of the RF photonic bandpass filter function for OSP design #1 by tuning the value of  $f_{c,RF}$  (2 GHz to 8 GHz) through thermo-optic detuning of  $f_1$  and  $f_2$ , maintaining the value of  $|f_1 - f_2|$  constant. Our tuning

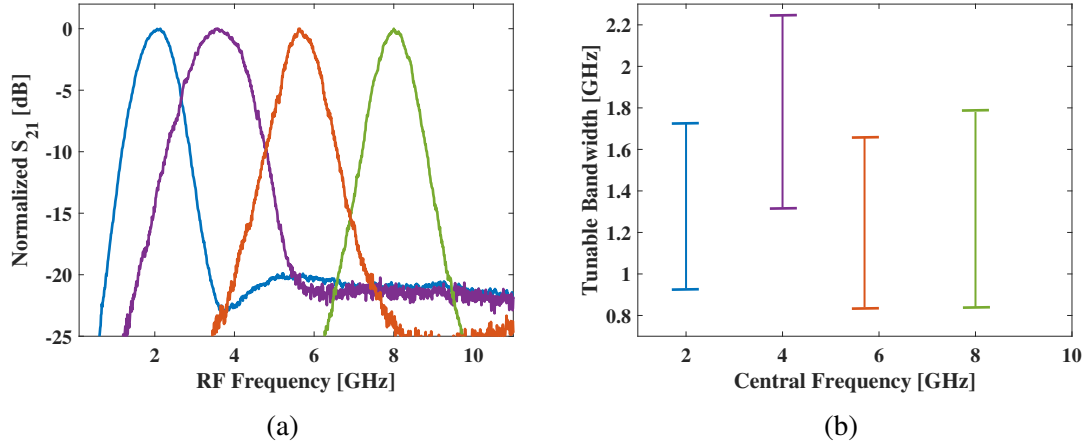


Figure 3.16: (a) Measured RF filter response with central frequency tuned from 2 GHz - 8 GHz and fixed 3-dB bandwidth close to 1 GHz, and (b) the 3-dB bandwidths of the measured filter responses at different central frequencies.

characteristics was limited up to 8 GHz, due to the limitation of microheater operation. An improved design of microheater would facilitate the RF photonic filter function up to 60 GHz ( $\sim \text{FSR}_0/2$ ). In the results given in Fig. 3.14b and Fig. 3.16a, the individual filter responses were normalized with their corresponding peak transmissions. Next, for each value of  $f_{c,RF} = 2$  GHz, 4 GHz, 6 GHz and 8 GHz, the bandwidth of the RF photonic filter function could be detuned and there values are shown in Fig. 3.16b. The bandwidth detuning was obtained without maintaining the overall operating temperature of the OSP chip and therefore we observed a bit of randomness in the observed bandwidth values.

The comparison of the measured RF filter response with the state-of-the-art demonstrations is listed in Table. 3.5. The comparison shows that the frequency and bandwidth tuning range limits any attempt to realize a single MRR-based narrow-band filter response with improved value rejection despite the asymmetry. Even though the other filter demonstrations with symmetric rejection are promising, these are again limited by the frequency tuning range. The proposed OSP design is superior among the other works as it offers a wide frequency range of operation with symmetric out-of-band rejection. Even though the value of rejection reported here is  $\sim 20$  dB, it can be improved with the



Table 3.5: Comparison of the measured RF filter responses with the proposed OSP and the state-of-the-art demonstrations.

Ref.	Platform	OSP	Modulator and Photodetector	Rejection	Frequency Tuning [GHz]	Bandwidth Tuning [GHz]
[66]	SiN	Single MRR with MZI as tunable coupler	off-chip	Asymmetric & > 20 dB	1 - 11 (FSR limited)	0.26
[68]	SiN	Single MRR with asymmetric coupler	off-chip	Asymmetric & 27 dB	2 - 18 (FSR limited)	0.18
[44]	SOI	Single MRR with tapered width of ring waveguide	on-chip	Asymmetric & > 10 dB	3 - 21 (FSR limited)	0.36 - 0.47
[70]	SOI	Single MRR with tapered width of ring waveguide	off-chip	Asymmetric & 26.5 dB	2 - 18.4 (FSR limited)	0.17
[65]	SiN	Single MRR with dual carrier	off-chip	Symmetric & 31.5 dB	2 - 14 (FSR limited)	0.67 - 2.8
[71]	SOI	Cascaded MRR on two chips	off-chip	Symmetric & 20 dB	6 - 17 (FSR limited)	1.65
[73]	SiN	Cascaded MRR with MZI as tunable coupler	off-chip	Symmetric & 34 dB	4 - 21.5 (FSR limited)	0.4 - 15.8
[94]	SOI	Single MRR with doped ring waveguide	off-chip	Asymmetric & 23 dB	3 - 51 (FSR limited)	1.3 - 4.5
This work	SOI	Cascaded MRR with asymmetric coupler	off-chip	Symmetric & > 20 dB	2 - 8 (extendable to 60 GHz)	0.84 - 1.8

on-chip integration of the modulator and detector.

### 3.5 SUMMARY

In this chapter, a novel integrated OSP design, comprised of two identical microring resonators (MRRs) cascaded in series and integrated with four thermo-optic phase shifters, has been proposed to realize an RF photonic bandpass filter with symmetric rejection. The design concept has been implemented in CMOS-compatible silicon photonics platform along with theoretical modeling and experimental demonstration. The design parameters for the ring and bus waveguides were chosen such that the Q-values could be maximized even using standard fabrication process available in our labs. It has been shown theoretically that the proposed OSP design can offer a symmetric out-of-band rejection, and can be programmed to independently tune the central frequency and the bandwidth of the RF photonic bandpass filter response. In the theoretical analysis,

we have also shown that the tuning range of the filter bandwidth can be changed by controlling the coupling coefficients (or Q-factor) of the individual MRRs of the OSP and also studied the corresponding change in the link gain of the RF filter.

For the experimental validation, in addition to the proposed OSP design with asymmetric waveguides as the tunable coupler (design #1), we have fabricated OSP design with conventional MZI as the tunable coupler (design #2). We have shown experimentally that the MRRs of the fabricated OSP (design #1) have waveguide loss of 1.4 dB/cm, Q-values  $\sim 3 \times 10^5$  and FWHM  $\sim 5$  pm ( $\sim 0.6$  GHz). The OSP could be programmed to experimentally demonstrate the RF photonic filter functions to be tuned from 2 GHz to 8 GHz with the 3-dB bandwidth tunability from 0.84 GHz to 1.8 GHz. The experimentally observed symmetric out-of-band rejection was found to be  $> 20$  dB and the shape factor is  $\sim 3.3$ , which are in accordance with our theoretical prediction. The comparison of the measured filter responses with OSP design #2 (waveguide loss: 4 dB/cm, Q-factor:  $0.6 \times 10^5$ , 3-dB bandwidth tuning range: 3.2 GHz to 5.8 GHz, shape factor: NA) validate the enhancement in the filter responses using the proposed OSP design #1.

The tuning range of the RF photonic filter in experiments was limited by the phase modulator bandwidth available to us and partly due to the limited performance of thermo-optic phase shifter; the optimized design of the phase shifters has not been considered for this experimental demonstration. Also, for the fabricated OSP design #1, the presence of resonances corresponding to  $TE_1$  mode will limit the filter tuning range, which can be mitigated by appropriate design of the directional coupler, to excite the resonances corresponding to  $TE_0$  mode only. Nevertheless, we have shown the proof-of-concept of a novel design of the OSP for widely tunable RF photonic filter functions, the performance of which can be improved further.



## CHAPTER 4

# OSP WITH PROGRAMMABLE MESH ARCHITECTURE

In the previous two chapters, we have seen the influence of tuning of MRRs coupling coefficient and its resonant wavelength on the microwave photonic filter response through simulations and experimental demonstrations. However, tuning one of the MRR's critical figures of merit, free spectral range (FSR), and its effect on the microwave filter response has yet to be explored to a large extent in the literature. In this chapter, we are going to discuss a programmable mesh architecture (PMA) design based on tunable Mach-Zehnder interferometer (MZI) in SOI platform which could be configured into microring resonators with desired FSRs in all-pass configurations. We have programmed the PMA into a necessary OSP function for a desired multiband microwave photonic filter response. Finally, we present a proof-of-concept study of the PMA-based microwave bandpass filter application in a radio over fiber receiver link.

### 4.1 DESIGN AND WORKING PRINCIPLE

Fig. 4.1a shows the schematic of the PMA with four inputs (I1, I2, I3 and I4), four outputs (O1, O2, O3 and O4) and 14 tunable basic units (TBU) arranged in square configuration. Each TBU is a balanced Mach-Zehnder interferometer (MZI) with  $2 \times 2$  multi-mode interferometer (MMI) as the 3-dB coupler and two phase shifters  $PS_{mX}$  and  $PS_{mY}$  integrated on both the arms, as shown in Fig. 4.1b. The subscripts  $mX$  and  $mY$  indicate the phase shifters integrated to the  $m$ -th TBU, respectively, where  $\{X, Y\} = \{L, R\}$  (left and right) for the vertical TBUs (3, 6, 9 and 12), and  $\{X, Y\} = \{T, B\}$  (top and bottom) for the remaining horizontal TBUs. For the TBU, we have considered a strip waveguide (width = 450 nm) owing to its high modal confinement, low bend loss, and, thus, low

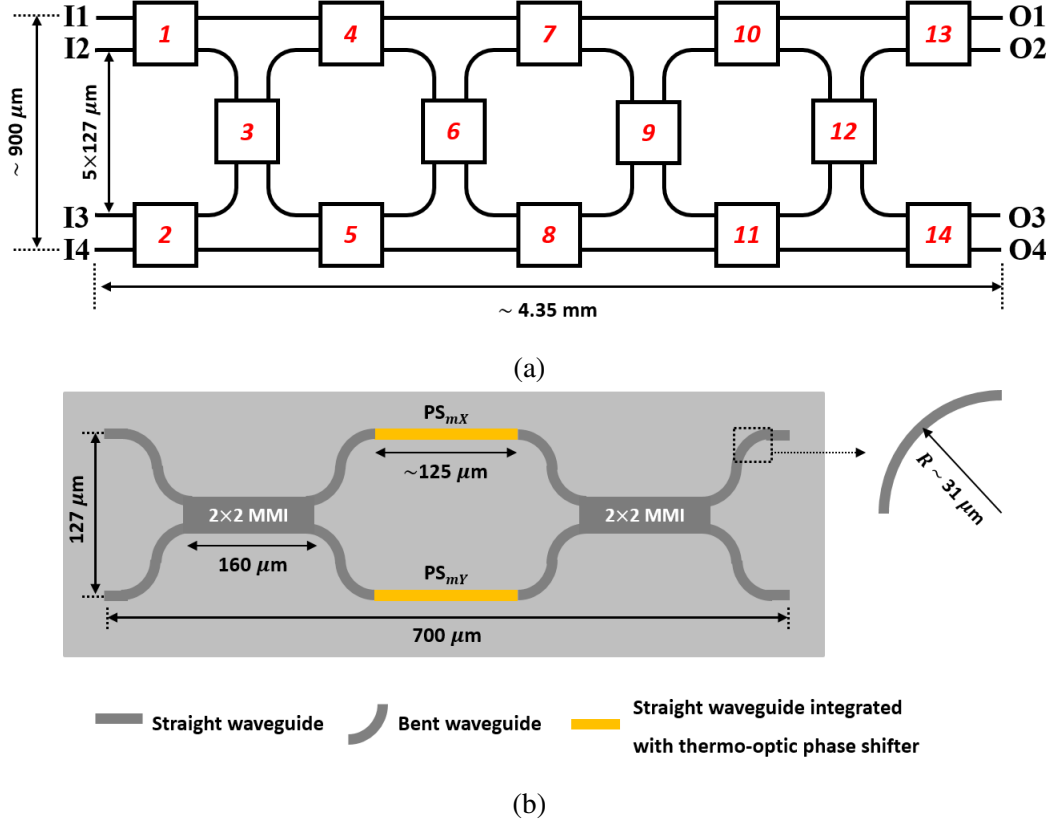


Figure 4.1: (a) Schematic representation of the PMA design based on 14 thermo-optically tunable MZIs with four input ports (I1, I2, I3 and I4) and four output ports (O1, O2, O3 and O4); and (b) schematic top view of an MZI used as the tunable basic unit (TBU) in the mesh architecture annotated with its physical design parameters and their values: two phase shifters ( $PS_{mX}$ ,  $PS_{mY}$ ) on both the arms and indicating the dimensions of the individual components of the TBU. MMI: multimode interferometers,  $PS_{mX}$ ,  $PS_{mY}$  corresponds to the integrated phase shifter to both the arms of the  $m$ -th TBU, where  $\{X, Y\} = \{L, R\}$  (left and right) for the vertical TBUs (3, 6, 9 and 12),  $\{X, Y\} = \{T, B\}$  (top and bottom) for the remaining horizontal TBUs and  $R$  is the waveguide bend radius.

Table 4.1: A set of programming schemes for the 14 TBUs to reconfigure the PMA into three different MRRs in all-pass configurations.

Metrics	configuration-1	configuration-2	configuration-3
No. of Cross state TBUs	2	3	7
No. of Bar state TBUs	5	6	4
No. of Tunable coupler TBUs	1	1	1
Total No. of active TBUs	8	10	12
Bus waveguide TBUs	1 → 4 → 7 → 10 → 13		
MRR Cavity TBUs	4 → 6 → 5 → 3 → 4	4 → 6 → 8 → 9 → 7 → 6 → 5 → 3 → 4	4 → 6 → 8 → 11 → 12 → 10 → 9 → 8 → 5 → 3 → 4
Cavity length [mm]	3	6	8
Estimated FSR [GHz]	22.3	12.7	9.9

footprint. The MMI design with a footprint of  $\sim 20 \times 160 \mu\text{m}^2$  was taken from the process design kit (PDK) library of the IMEC foundry. Considering the packaging design rules for fiber attachment and MMI footprint, the waveguide bend radius  $R$  and MZI arm length were carefully calculated as  $31.05 \mu\text{m}$  and  $124.28 \mu\text{m}$ , respectively, to maintain the vertical spacing between the successive input ports of the TBU and the PMA as a multiple of  $127 \mu\text{m}$ . The thermo-optic phase shifter (width =  $600 \text{ nm}$ , thickness =  $300 \text{ nm}$ , vertical distance from the waveguide =  $1 \mu\text{m}$ , material: Tungsten) is also considered as per the design rules of the IMEC PDK and is placed exactly on top of the waveguide without any lateral shift. With all the considered metrics, the footprint of the designed TBU and the PMA is  $\sim 127 \times 700 \mu\text{m}^2$  and  $\sim 0.9 \times 4.35 \text{ mm}^2$  (excluding the bond pads), respectively. As evident, the MMI consumes almost half the space in the designed TBU, which can be optimized further (without compromising the MMI imbalance and the insertion loss) to realize a TBU with a reduced footprint.

By appropriate programming of 14 TBUs, three individual MRRs in all-pass configurations are targeted as shown in Fig. 4.2. In all three MRR configurations, the input port I2 and output port O2 of the PMA are shown to be acting as input and output of the bus waveguides. For all the cases, the TBU-4 is used to tune the coupling strengths between the bus waveguide and the MRR, and the TBU-3 is used to tune the resonance wavelengths while maintaining its bar-state switching operations. As an

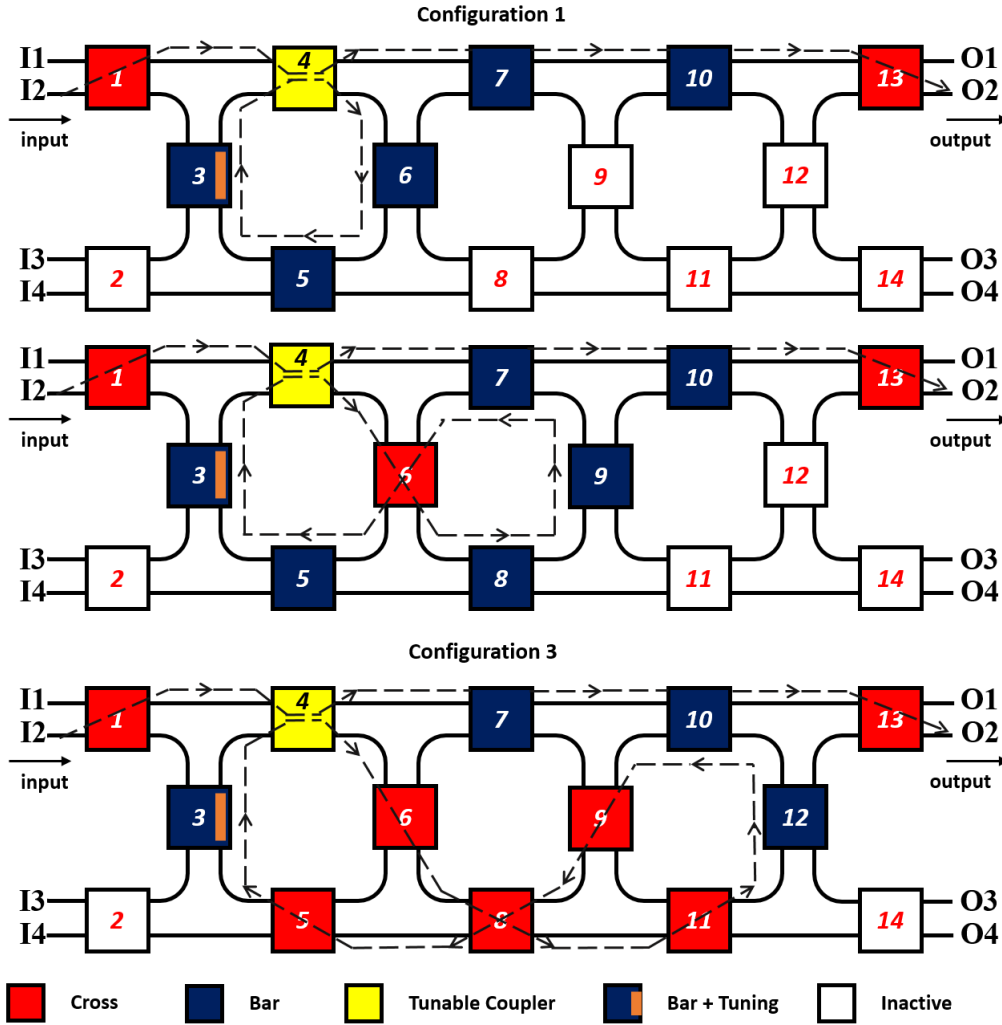


Figure 4.2: Schematic representation of the PMA to operate in three different MRRs in all-pass configurations with 3-mm (configuration-1), 6-mm (configuration-2), and 8-mm (configuration-3) cavity lengths, respectively. Inset: color-codes to indicate functions of TBUs.

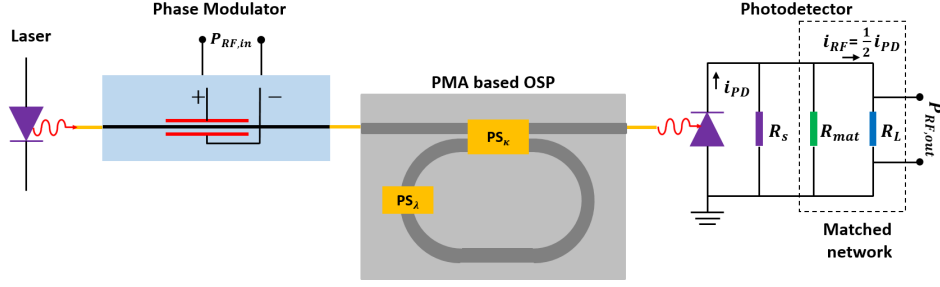


Figure 4.3: Component level schematic representation for the realization of microwave photonic bandpass filter using PMA-based OSP:  $P_{RF,in}$ : input RF signal power (frequency tunable),  $PS_\kappa$ : MZI based tunable phase shifter to tune the MRR coupling coefficient,  $PS_\lambda$ : MZI based tunable phase shifter to tune the MRR resonant wavelength,  $i_{PD}$ : photocurrent generated at the detector,  $R_s$ : internal resistance of the detector,  $R_L$ : load resistor,  $R_{mat}$ : resistor to match the detector and the load such that  $R_s || R_{mat} = R_L$ ,  $i_{RF}$ : photocurrent through the load resistor,  $P_{RF,out}$ : average output RF power.

example, the programming schemes for the 14 TBUs are summarized in Table 4.1.

It is evident from the above description that MRRs with certain set of figure of merits (such as FSR, resonance wavelength and Q-value, etc.) can be configured by designing an appropriate PMA. Our objective here is now to prove how an MRR derivable from the PMA in all-pass configuration can be used for the demonstration of multiband microwave photonic filters with symmetric out-of-band rejections. The operating scheme of an on-chip MRR based OSP (derived out of the PMA in this case) in all-pass configuration has been shown in Fig. 4.3; where a laser source (for optical carrier frequency  $\nu_0$ ), a phase modulator (for RF to optical up conversion), and a photodetector (for optical to RF down conversion) with matched network for maximum power transfer are shown to be externally connected for the demonstration of a microwave photonic filter functions with desired specifications. The derivation of foundational analytical equations used for simulating microwave photonic filter circuit shown in Fig. 4.2 are given in Appendix A. For the OSP, we have just used the frequency domain transfer function of the MRR given by Eq. (2.3). The parameter values used for simulating the microwave photonics filter system (see Fig. 4.3) performances are given in Table. 4.2.



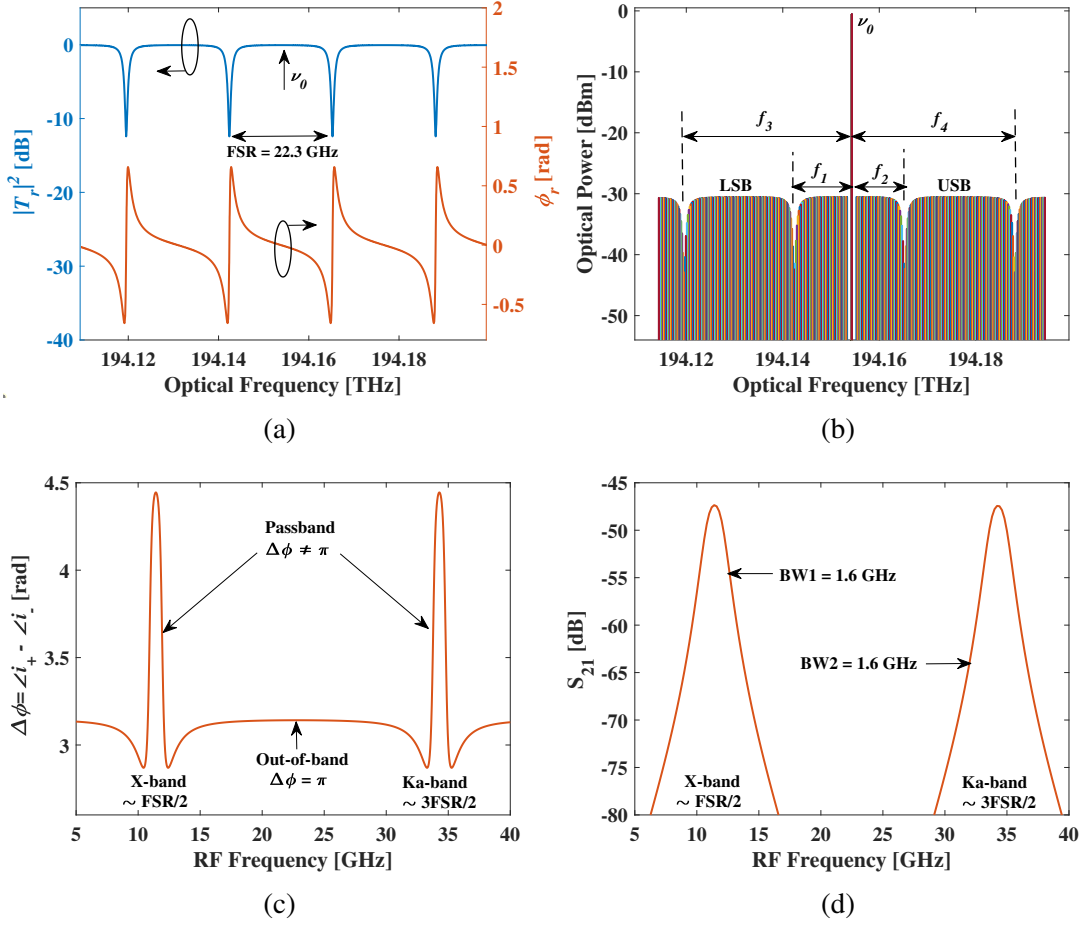


Figure 4.4: Theoretical demonstration of multiband microwave photonic filter using PMA based OSP: (a) Normalized optical power transmission and phase associated with its electric field of the MRR in configuration-1 around the carrier frequency  $\nu_0$  ( $\pm 45$  GHz); (b) optical power transmission characteristics of the modulated laser light aligned with the four resonances of the equivalent MRR, indicating the resonance positions at  $f_1, f_2, f_3, f_4$  with respect to the laser carrier frequency  $\nu_0$ , such that  $f_1 + f_2 = \text{FSR}$  and  $f_3 + f_4 = 3\text{FSR}$ ; (c) the difference in phase of the detected ac beat signals corresponding to optical carrier and USB ( $i_+$ ), and the optical carrier and LSB ( $i_-$ ); and (d) calculated  $S_{21}$  ( $= P_{RF,out}/P_{RF,in}$ ) exhibiting pass-bands around microwave X- and Ka-bands: The simulation results are for the parameter values given in Table. 4.2 and  $\Delta f_{12} = \Delta f_{34} = 1$  GHz.

Table 4.2: The parameters for the laser source, modulator, PMA based MRR configuration-1, and detection circuit used for simulation results shown in Fig. 4.4.

Component	Parameter		
	Description	Symbol	Value
Laser source	Input power	$p_{in}$	13.5 dBm
	Carrier frequency	$\nu_0$	194.154 THz
	Carrier wavelength	$\lambda_0$	$\sim 1545.165$ nm
Phase modulator (Lithium Niobate)	Optical insertion loss	$\alpha_m$	4 dB
	Input RF signal	–	sinusoidal
	Modulation index	$\delta = V_{in}/V_\pi$	0.014
	RF frequency band	$f_{rf}$	1 - 40 GHz
	RF band step size	–	200 MHz
PMA based MRR (configuration-1)	Fiber-to-chip coupling loss	$\eta_L$	5 dB/coupler
	Cavity length	$L$	3 mm
	Self-coupling coefficient	$r$	0.92
	Loss factor	$a$	0.88
	Free spectral range around $\nu_0$	FSR	22.3 GHz
Photodetector	Responsivity	$R_d$	0.45 A/W
	Matched load	$R_L$	50 $\Omega$

Fig. 4.4a shows the normalized optical power transmission ( $|T_r|^2$ ) and the phase of its transmitted electric field amplitude ( $\phi_r = \angle T_r$ ) at the output of the PMA based MRR in configuration-1 (see Fig. 4.2) as a function of optical frequency around the carrier ( $\nu_0 = 194.154$  THz); there are four resonances observed with FSR  $\sim 22.3$  GHz over an optical frequency range of 90 GHz. The values of  $r = 0.92$  and  $a = 0.88$  were chosen from the prior experimental results (assumed constant over the chosen frequency range). A broadband RF modulated optical carrier at  $\nu_0$  transmitted through the MRR and received at the detector has been simulated and is shown in Fig. 4.4b. In the simulations, the RF frequency band is visualized by sweeping the frequency of the input sinusoidal RF signal to the modulator (1 - 40 GHz), in the steps of 200 MHz. The signature of four MRR resonances around  $\nu_0$  are clearly visible in this transmission characteristics; two in the upper sideband (USB) and and other two in the lower sideband (LSB). It must be noted that the carrier frequency  $\nu_0$  has been selected such that resonances are positioned at

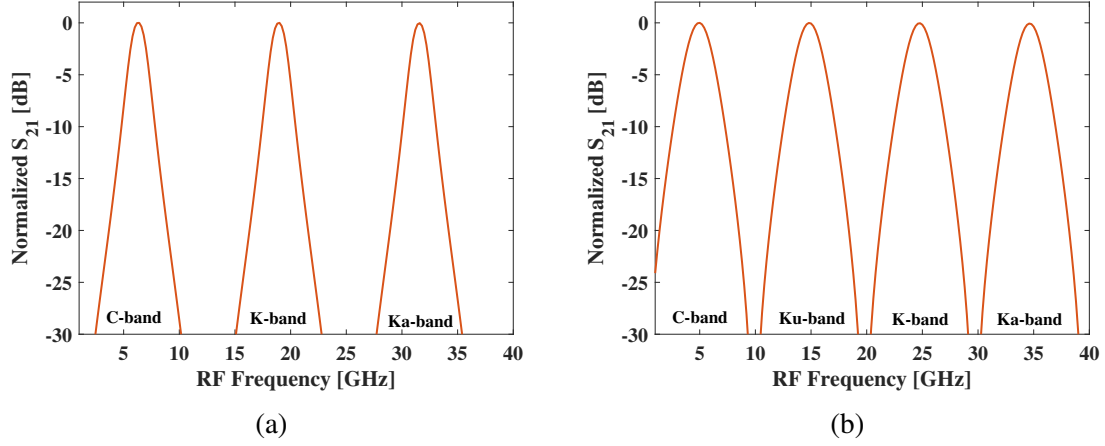


Figure 4.5: Simulation of  $S_{21} = P_{RF,out}/P_{RF,in}$  exhibiting multi-band microwave photonic filter using PMA based OSP and the parameter values given in Table-2: (a) PMA configuration-2 (see Fig. 4.2) gives simultaneous bandpass filter response around C-, K- and Ka-bands by setting  $r = 0.83$ ,  $a = 0.75$ ; and (b) PMA configuration-3 (see Fig. 4.2) gives simultaneous bandpass filter response around C-, Ku-, K- and Ka-bands by setting  $r = 0.49$ ,  $a = 0.54$ .

$f_1, f_2, f_3$ , and  $f_4$ , with respect to the carrier frequency, such that:

$$f_1 + f_2 = \text{FSR}; f_3 + f_4 = 3\text{FSR}$$

$$0 < \Delta f_{12} = |f_2 - f_1| < \Delta\nu_{\text{FWHM}}$$

$$0 < \Delta f_{34} = |f_4 - f_3| < \Delta\nu_{\text{FWHM}} \quad (4.1)$$

where  $\Delta\nu_{\text{FWHM}}$  is the full-width at half maxima of the resonances which is  $\sim 1.6$  GHz (at  $\lambda_0 \sim 1545$  nm) for the chosen values of  $r$  and  $a$ , as given in Table. 4.2.

The ac component of the output photocurrent  $i_{RF}$  across the matched load  $R_L$ , is the result of superposition between two beat signals. We have defined the beat current component between the carrier and the USB as  $i_+$ , and between the carrier and LSB as  $i_-$ . In the case of phase modulated optical carrier directly transmitted into the photodetector (in the absence of OSP), the phase difference between the beat components  $\Delta\phi = \angle i_+ - \angle i_- = \pi$  for all the frequencies, and thus resulting in the destructive interference of the beat

signals for the entire frequency band and no RF signal detected at the photodetector output. However, in the presence of OSP, the MRR resonances are aligned with the sidebands (as shown in Fig. 4.4b) and the phase difference between the beat components  $\Delta\phi \neq \pi$  (see Fig. 4.4c) for the frequencies around  $f_{c1} = (f_1 + f_2)/2$  and  $f_{c2} = (f_3 + f_4)/2$  within the simulation frequency window results into non-zero  $i_{RF}$ . Accordingly, the simulations result for  $S_{21}$  ( $= P_{RF,out}/P_{RF,in}$ ) shown in Fig. 4.4d exhibits desired bandpass filter response centering at X-band ( $\sim 11.2$  GHz) and Ka-band ( $\sim 33.5$  GHz), using the parameter values given in Table 2. The link gain and 3-dB bandwidth for both the pass-bands are  $\sim -47$  dB and  $\sim 1.6$  GHz, respectively. Similarly, the bandwidth can be detuned by controlling the resonances spacing with the carrier ( $\Delta f_{12}$  and  $\Delta f_{34}$ ) without affecting the MRR extinction and Q-value by using the phase shifter  $PS_\lambda$  alone. In principle, there are several passbands present in the  $S_{21}$  spectrum, with a periodicity exactly equals to the free spectral range of the MRR. However, the observed number of bands are limited by the bandwidths of modulator and detection circuit. The poor link gain in the simulations ( $\sim -47$  dB) can be majorly attributed to the efficiency of the modulators and detectors, and considered fiber-to-chip coupling losses, which can be improved with the optical amplification and design optimization of modulator, detector and on-chip couplers.

We can also easily extend the same working principle to increase the number of realizable passbands by reconfiguring the PMA to configuration-2 and 3 of the equivalent MRR with increased cavity length. In such cases, the central frequency of the RF bands is given by:

$$f_{cn} = \left( \frac{2n-1}{2} \right) \times \text{FSR} ; n = 1, 2 \dots p \quad (4.2)$$

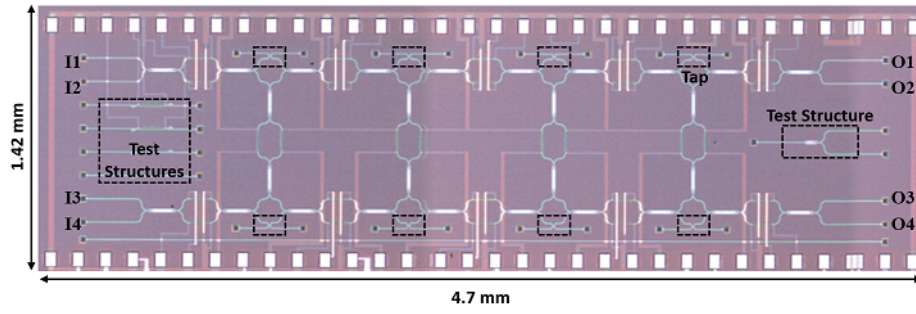
where  $p$  is the number of filter passbands at the output and  $2p$  is the number of MRR resonances aligned with the modulated optical spectrum. Fig. 4.5a and Fig. 4.5b, show the calculated  $S_{21}$  (normalized with the peak power) for the three-band (C-, K- and Ka-band) and four-band (C-, Ku-, K- and Ka-band) filter response, with  $\{r, a\} =$

$\{0.83, 0.75\}$  and  $\{0.49, 0.54\}$ , respectively, at the desired passband frequencies within the modulator bandwidth. For both the results  $\Delta f_{12} = \Delta f_{34} = 1$  GHz.

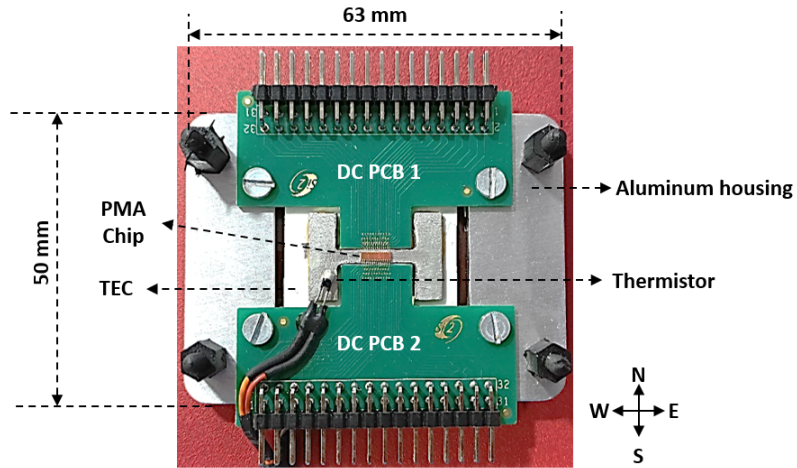
## 4.2 FABRICATION AND TESTING

The proposed PMA design with 14 TBUs was fabricated on a 220 nm silicon-on-insulator (SOI) platform using iSiPP50G process of IMEC multi-project-wafer (MPW) run. The microscope image of the fabricated structure along with the test structures is shown in Fig. 4.6a. The footprint of a single TBU is  $127 \times 700 \mu\text{m}^2$ , and the PMA covers an area of  $1.42 \times 4.7 \text{ mm}^2$  including the bond pads used for interfacing a multi-channel DC power supply for thermo-optic phase detuning. In the design, we have placed eight taps, with the bar port fed to the subsequent TBUs, for any necessary calibration of the mesh architecture. In the fabricated structures, we have estimated the tap percentage of the cross port as 5% at 1550 nm wavelength. However, we did not have to use them for experimental demonstrations. The fabricated chip was mounted on a Aluminum housing ( $50 \times 63 \text{ mm}^2$ ) and was electrically packaged with the necessary DC printed circuit boards (PCBs) in the north and south directions, as shown in Fig. 4.6b. The coupling of optical light in and out of the chip was carried out in the east and west directions through the input and output grating couplers. In addition, the package was integrated with a thermistor and thermo-electric cooler (TEC) to stabilize the die temperature (accuracy  $\pm 0.002^\circ\text{C}$ ) actively during the experiments.

To demonstrate the multiband microwave photonic bandpass filter using the programmable photonic integrated circuit package, we have used the setup shown in Fig. 4.7. The carrier laser light source (Thorlabs MX40C,  $p_{in} = 13.5 \text{ dBm}$ ) was launched into the phase modulator (Thorlabs LN6118,  $V_\pi = 7 \text{ V}$  at 1 GHz, 3-dB BW = 40 GHz, insertion loss = 4 dB) through a polarization maintaining fiber. The Lightwave Component Analyzer (LCA, Keysight N4373E) was used to drive the phase modulator, and the sinusoidal RF signals were swept from 1 GHz to 40 GHz, with a frequency steps of 10 MHz ( $P_{in,RF}$



(a)



(b)

Figure 4.6: (a) Microscope image of the fabricated PMA structure along with a few test structures; and (b) PMA mounted on a Aluminum housing and electrically packaged with necessary DC printed circuit boards (PCB), thermistor and thermo-electric cooler (TEC).

= -10 dBm). The erbium-doped fiber amplifier (EDFA, Pritel PMFA-33) was used to amplify the modulated laser light up to 23 dBm and subsequently launched into the input grating coupler of the PMA via 50:50 fiber-optic coupler (FOC<sub>1</sub>) and polarization controller (PC<sub>2</sub>). The output from the square mesh is collected through the grating coupler, and 10% of it was tapped into the optical source/spectrum analyzer, and the remaining 90% was fed into the LCA using FOC<sub>2</sub>. The RF measurements were carried out in the LCA with a resolution bandwidth of 500 Hz. For thermo-optic tuning of the PMA, a 16-channel programmable DC power supply was used to drive the phase shifters through the PCBs. In the experiments, we set the temperature of the photonic chip to 26 °C and used a PID controller to control the chip temperature actively against ambient temperature variations. The PID controller had an initial settling time of 30 - 40 s with steady state temperature variations in the order of  $\pm 0.002^{\circ}\text{C}$ . The resonant wavelength shift for the temperature variation of  $\pm 0.002^{\circ}\text{C}$  was measured to be less than 2 pm ( $\pm 250$  MHz), which was within the tolerance range of the experiments as the measured frequencies and bandwidth of the microwave filter are at least one order more than 250 MHz.

Prior to the experimental investigations on microwave photonic filter function, the tunable MZI building blocks or TBUs were calibrated to address the fabrication process induced phase errors between the interferometric arms. Two microheaters integrated with each of the MZI arms were tuned strategically to estimate these phase errors. In doing so, the carrier laser light source, modulator, EDFA, LCA, FOC<sub>1</sub>, and FOC<sub>2</sub> in the setup were disconnected from the experimental setup shown in Fig. 4.7 and the input power  $P_{\text{in}}$  (= -5.6 dBm) from the optical source/spectrum analyzer (OSSA) was directly launched into the PMA package through PC<sub>1</sub>, and the laser wavelength of the in-built tunable laser source (TLS) of the OSSA was swept from 1520 nm to 1620 nm. The PMA output power ( $P_{\text{out}}$ ) corresponding to each wavelength was directly transmitted to the OSSA detector, where the measurements were carried out at a resolution of 0.8 pm. We have discussed about the calibration of the tunable MZIs and the characterizations of three

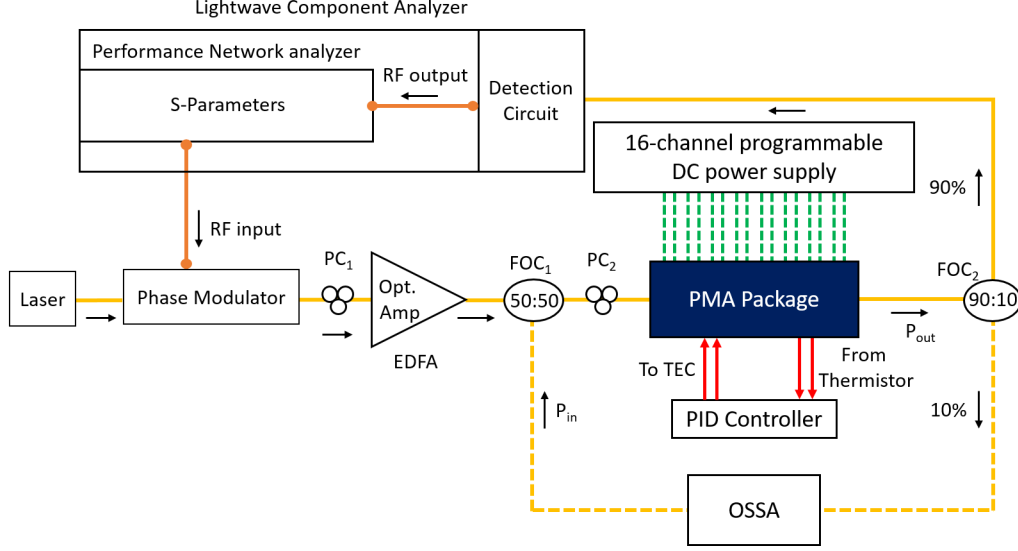


Figure 4.7: Experimental setup for the demonstration of multiband microwave photonic bandpass filter functions: Opt. Amp. - optical amplifier; EDFA - erbium doped fiber amplifier; PC - polarization controller; FOC - fiber-optic coupler; PMA - programmable mesh architecture; TEC - thermo-electric cooler; P<sub>in</sub> - input optical power (= -5.6 dBm) from OSSA; and P<sub>out</sub> - output optical power from PMA package.

MRR configurations in the following two sub-sections.

#### 4.2.1 Calibration of Tunable MZIs (TBUs)

The minimization of fabrication process induced phase imbalance/error between the MZI/TBU arms designed for a PMA is very important but practically unavoidable as the nanometer scale variations in silicon waveguide core can alter the effective refractive index of guided modes significantly ( $10^{-3} - 10^{-4}$ ). Therefore, random distribution of such phase errors amongst the TBUs are expected in any fabricated PMA [95]. We evaluated the phase errors of all the 14 TBUs, in terms of the lowest electrical power required between the thermo-optic phase shifters integrated in two arms of the TBUs, such that the launched optical power in one of the two input ports of a TBU to deliver maximum at its output cross-port. For example, Fig. 4.8a shows an all-cross path in the square mesh from input I1 to output O2 (I1→O2), passing through seven TBUs (1, 3, 5, 8, 9, 10, 13). Without any fabrication errors, we expect the entire power launched at I2



to appear at O2 with some insertion loss and no power detected at other output ports. Crosstalks at other output ports is an important metric used to estimate the functioning of such switching networks, which is infinite for an ideal circuit. However, for the fabricated structure, Fig. 4.8b shows the spectral characteristics measured at all the output ports for a launched power of  $P_{in} = -5.6$  dBm; the results are shown only for  $1550 \pm 5$  nm, for which the grating coupler efficiency is found to be maximum. As expected, the output O2 receives the highest power ( $\sim -20$  dBm), which is limited by input and output grating coupler loss ( $\sim 6$  dB/coupler), power leaked out through the two taps present in the path ( $\sim 0.22$  dB/tap), and the TBU insertion loss ( $\sim 0.3$  dB/TBU). However, the residual powers detected at other output ports limit the cross-talk to 8 dB. These crosstalks are partly due to the random distribution of MMI imbalance and partly due to the phase errors between the arms of TBUs. With the current MMI design, it is hard to fine-tune any imbalances. However, we could correct the phase errors of the TBUs by applying extra power across the thermo-optic phase shifters for the TBUs to operate in the cross-state (initial state for the ideal structure). Though there are a few optimization algorithms are reported in the literature to estimate the thermal power required for the each TBU to correct the phase errors of the mesh architecture [96, 97], we could correct the phase errors in this case step by step accurately without any difficulties. In this section, the extracted thermal switching powers for each TBU and the experimental results after the calibration of the PMA are discussed. However, the detail procedure followed for the calibration of the tunable MZIs of the PMA is explained in Appendix D.

Fig. 4.8c shows the measured optical spectrum at all the output ports after performing the phase error corrections and applying the appropriate thermal power to TBUs in the selected path to operate in the cross state. An additional thermal power of 11.34 mW across the TBUs in the selected path was needed to improve the crosstalk to 21.2 dB. We have carried out the same analysis for two more paths, I3→O4 and I4→O3, to extract the thermal switching powers for the remaining TBUs to operate in the cross and bar state. The obtained crosstalks with and without the phase error corrections for

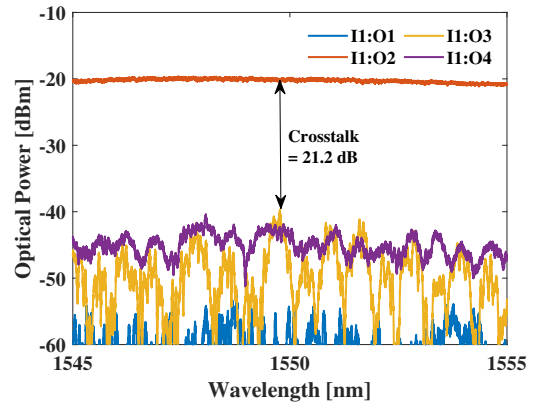
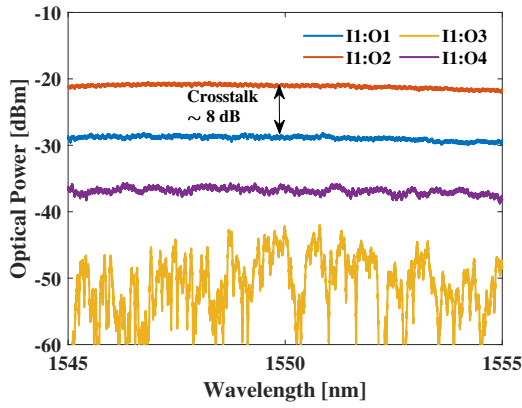
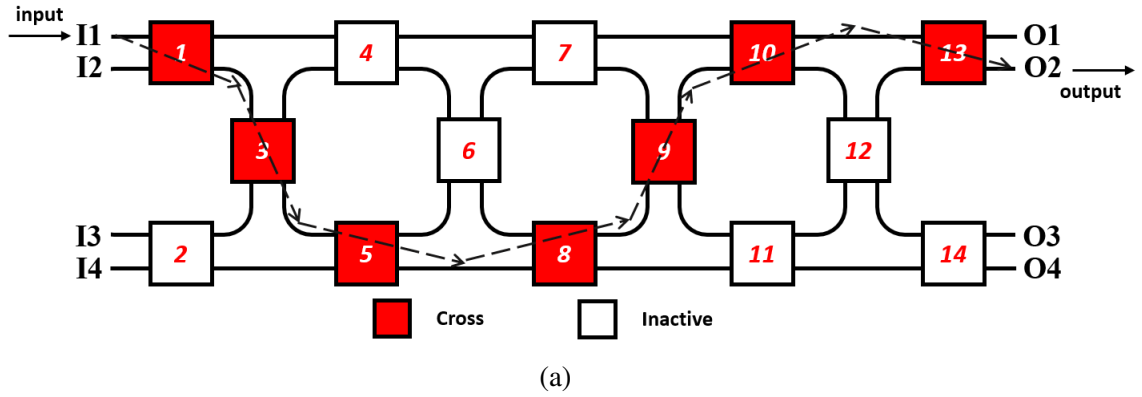


Figure 4.8: (a) Schematic representation of the programmable square mesh indicating an all-cross path from input I1 to output O2 (I1→O2); (b) measured optical power spectrum transmitted at the output ports before phase error corrections, indicating the highest-case crosstalk of 8 dB between O2 and other output ports; and (c) measured optical power spectrum for the selected path at all the output ports after phase error corrections (total thermal power burnt = 11.34 mW) indicating the highest-case crosstalk improved to 21.2 dB between O2 and other output ports.

Table 4.3: The extracted thermal switching powers for each tunable basic unit (TBU) to operate in cross and bar state along with the operated phase shifters, and the cross and bar state extinctions. The phase shifter notation used here is as per the convention given in Fig. 4.1b.  $PS_{mX}$ ,  $PS_{mY}$  corresponds to the integrated phase shifter to both the arms of the  $m$ -th TBU, where  $\{X, Y\} = \{L, R\}$  (left and right) for the vertical TBUs (3, 6, 9 and 12),  $\{X, Y\} = \{T, B\}$  (top and bottom) for the remaining horizontal TBUs.

TBU no.	Cross State Switching (Phase Error Correction)			Bar State Switching		
	Phase Shifter	Thermal Power [mW]	Extinction [dB]	Phase Shifter	Thermal Power [mW]	Extinction [dB]
1	$PS_{1B}$	6.38	21.38	$PS_{1T}$	20.4	26.44
2	$PS_{2T}$	1.26	28.88	$PS_{2B}$	25.27	34.06
3	$PS_{3R}$	1.09	21.51	$PS_{3L}$	23.87	38.38
4	$PS_{4B}$	1.41	31.96	$PS_{4T}$	24.81	33.12
5	$PS_{5T}$	2.72	25.38	$PS_{5B}$	24.66	28.87
6	$PS_{6L}$	1.06	24.23	$PS_{6R}$	25.28	29.9
7	$PS_{7T}$	0.41	32.69	$PS_{7B}$	27.03	29.04
8	$PS_{8B}$	0.01	29.91	$PS_{8T}$	25.8	10.49
9	$PS_{9R}$	0.27	22.8	$PS_{9L}$	26.96	30.51
10	$PS_{10B}$	0.42	25.69	$PS_{10T}$	27.27	31.77
11	$PS_{11B}$	0.53	37.03	$PS_{11T}$	27.43	30.6
12	$PS_{12L}$	0.30	24.5	$PS_{12R}$	25.75	37.25
13	$PS_{13B}$	0.37	38.34	$PS_{13T}$	25.94	30.05
14	$PS_{14T}$	0.13	34.68	$PS_{14B}$	26.91	30.56

the mentioned paths are {15.87 dB, 18.02 dB} and {23.04 dB, 24.23 dB}, respectively. The extracted thermal switching powers for the TBUs to operate in cross and bar states along with the operated phase shifters, and the cross and bar state extinctions are listed in Table. 4.3. The results show that the phase error distribution across the PMA circuit is random, in terms of the amount of phase error (correction power is different) and also its location (the phase shifter required for correction is different). The fabricated square mesh requires dissipation of 16.35 mW of thermal power across the 14 TBUs for the near-ideal operation. In addition, we can note that the difference between the cross state and bar extinction and its variation across the TBUs, indicating the random distribution of MMI imbalances as well.

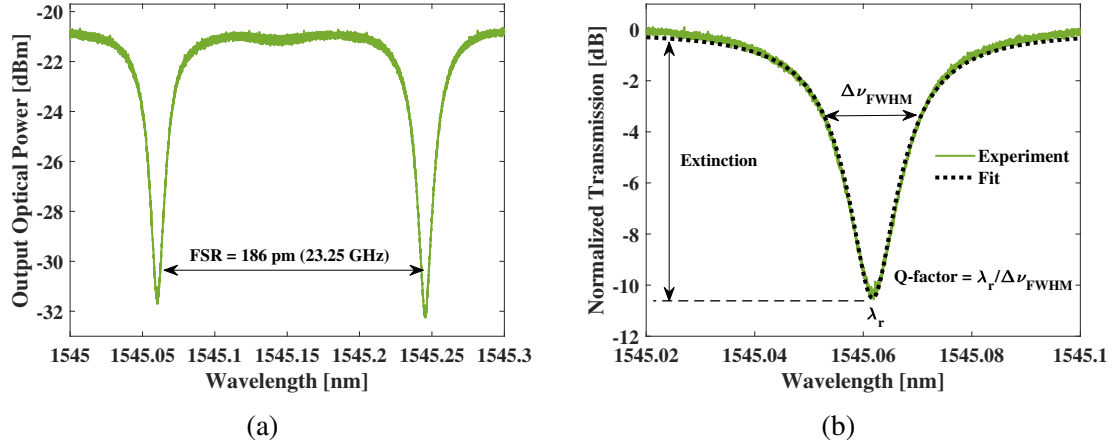


Figure 4.9: (a) Measured MRR response by programming the mesh network to configuration-1 (see Fig. 4.2) exhibiting two resonances around  $\lambda = 1550$  nm with an FSR = 186 pm (23.25 GHz); and (b) the least square fit of the measured data (first resonance in Fig. 4.9a around 1545.06 nm) using Eq. (2.3) to extract coupling coefficient  $r$  and loss factor  $a$ .

#### 4.2.2 Characterizations of Programmable Ring Resonators

Following the phase error corrections and creating look-up Table 4.3 for individual phase-shifter performances, we could successfully program the PMA into three different ring reconfigurable resonators as described in Fig. 4.2 and subsequently their individual figure of merits were experimentally extracted. As already mentioned earlier in Section. 4.1, we configured TBU-3 as phase detuning element ( $PS_\lambda$ ) and TBU-4 to operate as a tunable coupler ( $PS_\kappa$ ) as annotated in Fig. 4.3 for all three ring resonator configurations. Fig. 4.9a shows the transmission characteristics of configuration-1 exhibiting two resonances around  $\lambda \sim 1545$  nm, when the electrical power delivered to  $PS_\kappa$  for thermo-optic coupling was 18.15 mW. We observe the measured FSR = 23.25 GHz closely matching to its theoretical prediction of 22.3 GHz. The corresponding resonance extinction of  $\sim 10$  dB and loaded Q-value of  $\sim 10^5$  were evaluated from the same experimental transmission characteristics by a theoretical fit using Eq. (2.3) (see Fig. 4.9b).

To enhance the programmability of the PMA for a multiband microwave bandpass filter, independent tuning of the MRR resonance position (with respect to the optical carrier

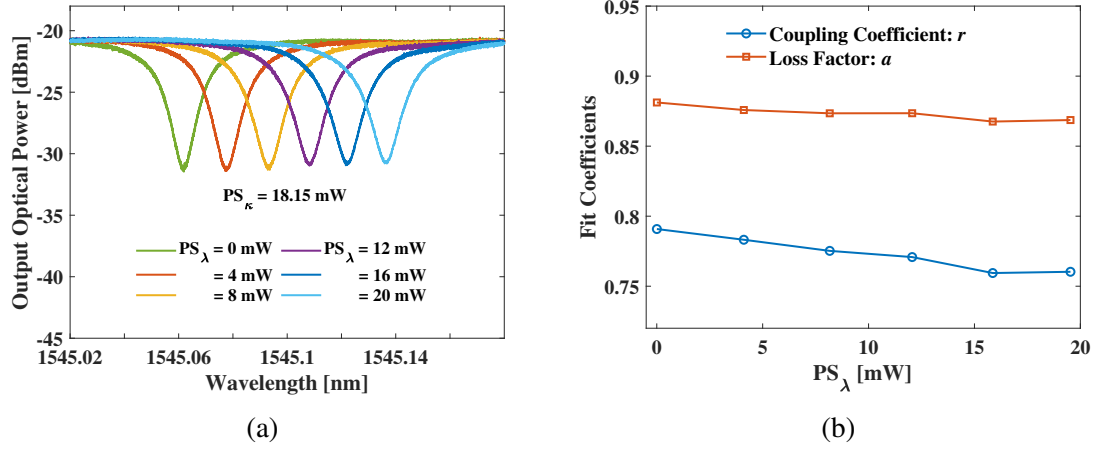


Figure 4.10: Thermo-optic resonance tuning of MRR in configuration-1 for a given coupling condition ( $PS_{\kappa} = 18.15$  mW): (a) Wavelength dependent transmission characteristics for different micro-heater power delivered by  $PS_{\lambda}$ ; (b) extracted values of  $r$  and  $a$  for the ring responses as a function of microheater power delivered by  $PS_{\lambda}$ .

wavelength) as well as its Q-value are essential. To tune the resonance wavelength, an equal amount of thermo-optic power was tuned to both the arms of the TBU-3 ( $PS_{\lambda}$ ) in the range of 0 to 20 mW, for a fixed value of coupling coefficient ( $PS_{\kappa} = 18.15$  mW), without affecting its desired bar operation. The measured results are shown in Fig. 4.10a, following which we have extracted the coupling coefficient  $r$  and the cavity loss factor  $a$  from the measured results using the least square fit method with Eq. (2.3). The values of  $r$  and  $a$  extracted from the ring responses for different thermal powers  $PS_{\lambda}$  are shown in Fig. 4.10b. With  $PS_{\lambda}$ , the values of  $r$  ( $\sim 0.78$ ) and  $a$  ( $\sim 0.88$ ) are nearly invariant, which is expected as  $PS_{\kappa}$  is not changing in the measurements. Next, to tune the coupling coefficient of the ring, the thermal power applied to the TBU-4 ( $PS_{\kappa}$ ) was varied in the range of 18.15 - 23.46 mW, and the corresponding coupling coefficient  $r$  and the cavity loss factor  $a$  are extracted, and the results are given in Fig. 4.11a and Fig. 4.11b, respectively. As expected with  $PS_{\kappa}$ , the coupling coefficient  $r$  (0.73 - 0.93) is tuned around the loss factor  $a$  ( $\sim 0.88$ ) to realize MRR resonances corresponding to the over-coupled (OC,  $r < a$ ), critically coupled (CC,  $r = a$ ) and the under-coupled (UC,  $r > a$ ) regimes of operation. The slight changes in the values of  $r$  with  $PS_{\lambda}$  (0.76 -

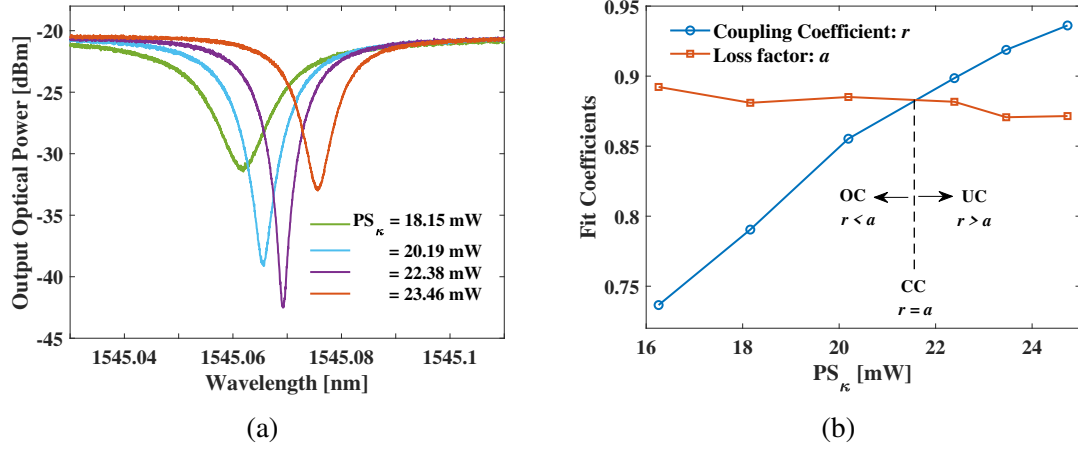


Figure 4.11: (a) Measured characteristics of the PMA programmed to MRR in configuration-1 by tuning  $PS_k$  in the range of 18.15 - 23.46 mW; and (b) extracted values of  $r$  and  $a$  for the ring responses at different  $PS_k$ .

0.79), and  $a$  with  $PS_k$  and  $PS_\lambda$  (0.86 - 0.88) can be associated with the dispersion of the directional coupler and slight asymmetric heating of both phase shifters in TBU-3 and thermal cross-talk in the experiments.

Similar to the characterizations of configuration-1 discussed above, the configurations 2 and 3 of the PMA were investigated. Important observations and figure of merits for all three configurations are given in Table 4.4; the relative trends for all these values in three configurations are consistent with the design and theoretical evaluations.

It is important to note that the MRR with configuration-3 is realized with more TBUs operating in cross-state (when compared with the other configurations), thus reducing the total thermal power dissipated across the PMA. Also, for the measured ring responses due to the increase in the cavity loss (and correspondingly FWHM) with the cavity length, the finesse defined as  $FSR/\Delta\nu_{FWHM}$  also degrades, which we will see in Section. 4.3 also deteriorate the filter responses. Finally, Fig. 4.12a and Fig. 4.12b shows the calculated extinction ratio and the Q-factor for the tuned range of  $r$  (with  $PS_k$ ; around  $a$ ), to realize MRR responses corresponding to OC, CC and UC, for the all three configurations. These results help us understand the required value of  $r$  (and  $PS_k$ ) to set the MRR response in

Table 4.4: Experimentally observed important figure of merits of three configurations of the PMA (given in Fig. 4.2).

Metrics	Configuration-1	Configuration-2	Configuration-3
FSR ( $\lambda \sim 1545$ nm)	186 pm (23.25 GHz)	94 pm (11.75 GHz)	70 pm (8.75 GHz)
Finesse ( $\lambda \sim 1545$ nm)	13.6	5.8	3.2
Round-trip loss factor $a$	0.88	0.75	0.54
Q-value (at critical coupling)	$1.12 \times 10^5$	$0.96 \times 10^5$	$0.7 \times 10^5$
Operating Thermal Power	157.24 mW	179.9 mW	133.7 mW

the desired operation while performing microwave filter experiments.

### 4.3 DEMONSTRATION OF MULTI-BAND FILTERS

After the calibration of the fabricated TBUs and obtaining the required settings to operate the PMA as MRRs in the three configurations, we have activated the laser source, modulator, optical amplifier, FOC<sub>1</sub> and FOC<sub>2</sub> in the setup shown in Fig. 4.7, to perform multiband microwave filter measurements. For the RF measurements, the in-built laser source of OSSA along with FOC<sub>1</sub> and FOC<sub>2</sub> was used as the probe laser for in-situ tracking of the MRR characteristics with a compromise of additional insertion loss added into the link. First, we have configured the PMA to realize equivalent MRR in configuration-1 (see Fig. 4.2) with a free spectral range of 186 pm ( $\sim 23.25$  GHz). The  $PS_\kappa$  of the MRR was tuned for the ring to operate in the under-coupled regime with an extinction of 10 dB. As mentioned in Section 4.1 in the current MRR configuration, we expect to realize a two-band microwave filter (within the modulator bandwidth). Therefore, we have chosen the carrier wavelength  $\lambda_0$  ( $= 1545.625$  nm) around the four resonances exhibiting the same extinction (and nearly same Q-values).

Fig. 4.13a shows the optical spectrum of the laser carrier aligned with four identical resonances of the MRR, such that  $f_1 = 11.4$  GHz,  $f_2 = 12.2$  GHz,  $f_3 = 34.5$  GHz,  $f_4$

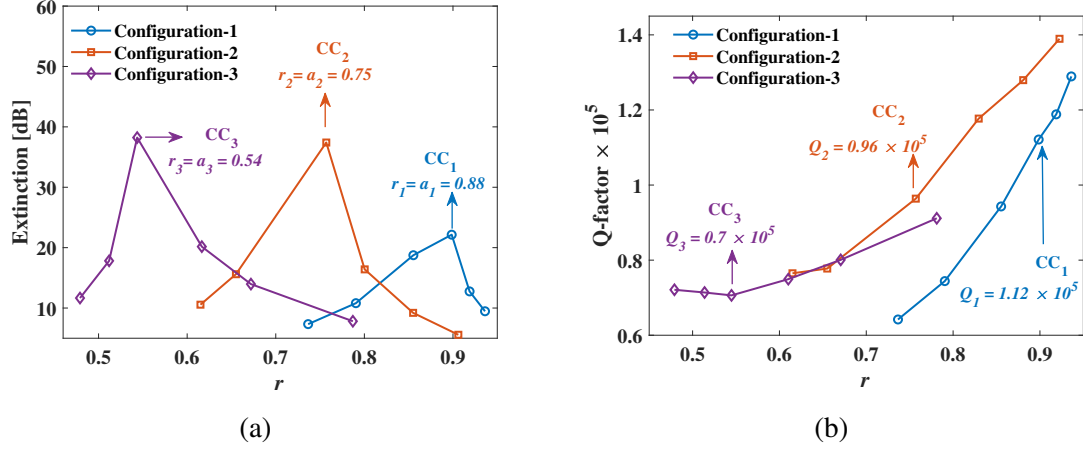


Figure 4.12: Experimental observation of resonance extinction and Q-values as a function of through-put coupling coefficient  $r$  (obtained by powering  $PS_k$ ) for the three configurations of the electrically packaged PMA: (a) extinction ratio; and (b) the Q-value. The subscripts 1, 2 and 3 indicated in the figure for CC,  $r$ ,  $a$  and  $Q$  correspond to the MRR configuration.

= 35.6 GHz. The calculated Q-factor for all four resonances of interest is  $\sim 1.3 \times 10^5$ . Fig. 4.13b shows the corresponding measured filter response and its comparison with the simulated response. For the simulation data shown here, we have adjusted to optical power in the link to match with the link gain obtained in the experiments. As expected, we obtain a two-band microwave filter response with central frequencies at 11.8 GHz ( $\sim \text{FSR}/2$ ) and 35 GHz ( $\sim 3\text{FSR}/2$ ), corresponding to X-band and Ka-band. The observed 3-dB bandwidth, out-of-band rejection, link gain, and shape factor ( $= 10\text{-dB bandwidth}/3\text{-dB bandwidth}$ ) of the two bands are  $\{2.06, 1.95\}$  GHz,  $\{-32.87, -33.16\}$  dB,  $\{17.81, 16.97\}$  dB, and  $\{1.74, 1.63\}$  respectively. The realized filter has identical metrics for both passbands, which confirms the minimal change in free spectral range over the chosen four resonances of interest.

For the simultaneous tuning of the filter bandwidth of both the bands, we detuned the resonance position from the carrier ( $\Delta f_{12}, \Delta f_{34}$ ) without affecting the MRR coupling condition by applying differential thermal power  $PS_\lambda$  to TBU-3. Fig. 4.14a shows the filter responses with different bandwidths labeled #1, #2, #3, #4 and Table. 4.5 shows the



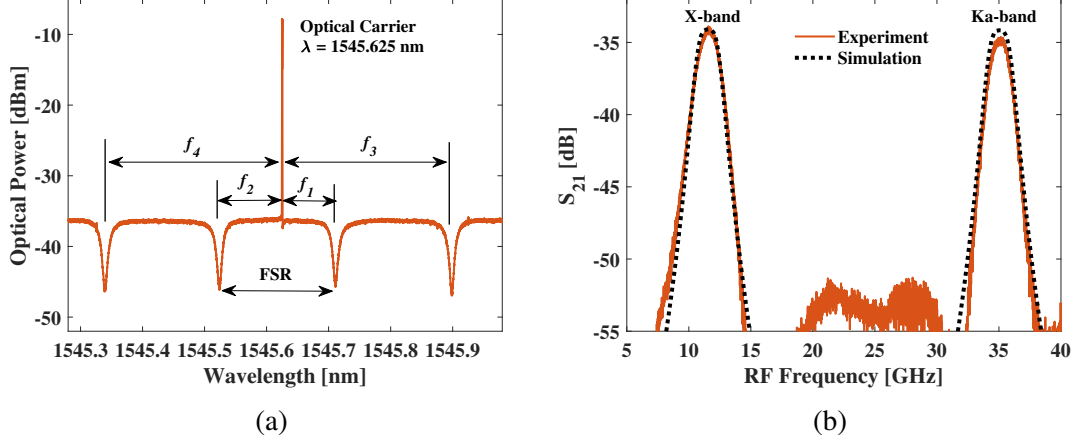


Figure 4.13: Demonstration of X- and Ka-band filter using the MRR configuration-1 of the PMA: (a) The transmission characteristics of the MRR along with the positioning of optical carrier ( $\lambda_0 = 1545.625$  nm) indicating the operating condition to realize a two-band microwave photonic filter, with a band spacing of  $\sim 23.25$  GHz; and (b) Experimental RF filter response exhibiting passbands around X-band and Ka-band closely matching with simulation results. The MRR configuration-1 was tuned such that the resonance extinction = 10 dB, Q-value =  $1.2 \times 10^5$  with  $f_1 = 11.37$  GHz,  $f_2 = 12.19$  GHz,  $f_3 = 34.47$  GHz,  $f_4 = 35.59$  GHz

extracted figure of merits for the corresponding filter responses for both the passbands. The filter bandwidth and link gain for both the bands in all configurations are similar. Here, the maximum achievable bandwidth is limited by the split in the passband induced under the condition,  $\Delta f_{12}, \Delta f_{34} > \text{MRR FWHM}$ . The drop in link gain for narrow filter bandwidth response, as shown in Fig. 4.14b, limits the minimum achievable bandwidth. For a narrowband filter  $\Delta f_{12}, \Delta f_{34} \rightarrow 0$ , which tends to the symmetric spacing of the identical resonances around the carrier and a near-perfect cancellation of the MRR-induced phase for all the RF frequencies (as already discussed in Chapter 3). The drop in the link gain also degrades the filter rejection for narrowband response. Considering the allowable bandpass split to be less than 1 dB and the filter to have a minimum rejection of 15 dB, in our experiments for the current MRR configuration, we could tune the filter bandwidth in the range of 1.66 GHz to 4.45 GHz for X-band response and 1.59 GHz to 4.14 GHz for Ka-band response. The maximum rejection

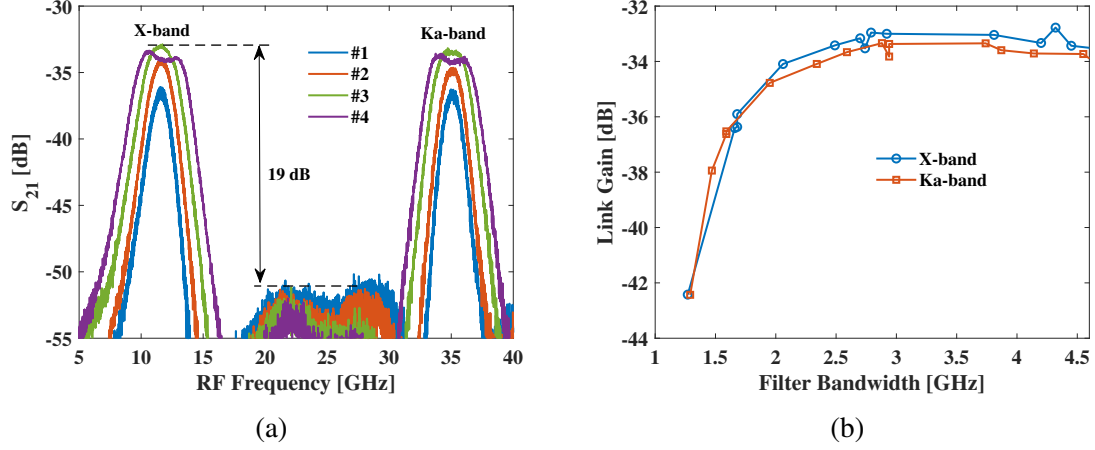


Figure 4.14: (a) Measured two-band microwave filter response with tunable bandwidth for 3-mm cavity length MRR configured in under-coupled region with extinction = 10 dB,  $Q = 1.2 \times 10^5$ ; and (b) the corresponding variation of the RF link gain with the filter bandwidth.

Table 4.5: Extracted figure of merits of the measured filter responses marked as #1, #2, #3 and #4 in Fig. 4.14a. Shape Factor = (10-dB bandwidth)/(3-dB bandwidth)

	X-Band				Ka-Band			
	#1	#2	#3	#4	#1	#2	#3	#4
Bandwidth [GHz]	1.66	2.06	2.92	4.45	1.59	1.95	2.94	4.14
Link Gain [dB]	-36.11	-33.88	-32.87	-33.35	-36.26	-34.63	-33.16	-33.58
Rejection [dB]	16.60	17.81	19.48	19.88	14.82	16.97	19.19	19.20
Shape Factor	2.07	1.91	1.74	1.49	1.96	1.81	1.63	1.47

realized is around 19 dB. The other key metric of the filter, the shape factor, decreases with bandwidth and approaches one for higher bandwidth response indicating a sharp roll-off.

Since the PMA can be easily programmed to tune the MRRs extinction and Q-factor with  $PS_K$ , we have adjusted the MRR to operate with the same 10 dB extinction, but in the over-coupled state with a Q-factor of  $0.75 \times 10^5$ . Following the same procedure of tuning  $PS_\lambda$  to shift the resonance spacing with the carrier, we again realized a tunable bandwidth filter response for the new configuration. Fig. 4.15a shows the corresponding filter response with the bandwidth tuned from 2.8 GHz to 8.1 GHz (shape factor: 2.1 to

1.4). As mentioned earlier, the filter bandwidths of both X-band and Ka-band responses are very close, hence in the subsequent results we have only given the bandwidth values corresponding to the first band at  $\sim \text{FSR}/2$  (X-band in this case). Here, we observe the increase in bandwidth tuning range, with a compromise on the minimum achievable bandwidth. The reason for both is the drop in the Q-factor of the MRR in the over-coupled state, thus increasing the MRR FWHM. However, it is critical to note the increase in the link gain and, correspondingly, the rejection of the filter response to  $\sim -30$  dB and 24 dB, respectively. The improvement is because of the change in the MRR coupling condition from UC to OC and its corresponding phase response. For an over-coupled ring, the phase difference between the two beat signals  $\Delta\phi$  in the passbands tends more towards  $2\pi$  or 0 when compared with the under-coupled ring, as shown in Fig. 4.15b; hence the improved link gain and rejection. To validate the explanation, we have further configured the MRR to operate in the deep OC region with 5 dB extinction and a Q-factor of  $\sim 0.6 \times 10^5$  and the filter response is shown in Fig. 4.15c. As expected, we see further improvement in the tuning bandwidth range (3.8 GHz to 12.7 GHz), link gain ( $\sim -25$  dB), shape factor (2.1 to 1.4) and rejection (33 dB) with a compromise in the minimum achievable bandwidth.

As mentioned earlier, the critical advantage of a mesh architecture is the structure's versatility in tuning not only the MRRs extinction and Q-factor but also its free spectral range, which is not trivial using any conventional structures. The scope of FSR tuning enables reconfiguring the number of bands in the microwave filter using the proposed operation scheme. To reconfigure the obtained two-band response to a three-band response, we have tuned the square mesh to operate in configuration-2 of the MRR with 6-mm cavity length (see Fig. 4.2). Here, we have again performed the filter measurements for the under-coupled resonance with 10 dB extinction ( $Q = 1.2 \times 10^5$ ). Fig. 4.16a, shows the three-band filter response at 5.85 GHz ( $\sim \text{FSR}/2$ , C-band), 17.4 GHz ( $\sim 3 \times \text{FSR}/2$ , Ku-band) and 29.3 GHz ( $\sim 5 \times \text{FSR}/2$ , Ka-band) with tunable bandwidth. In the figure, the responses are normalized with their respective peak powers. Here, the

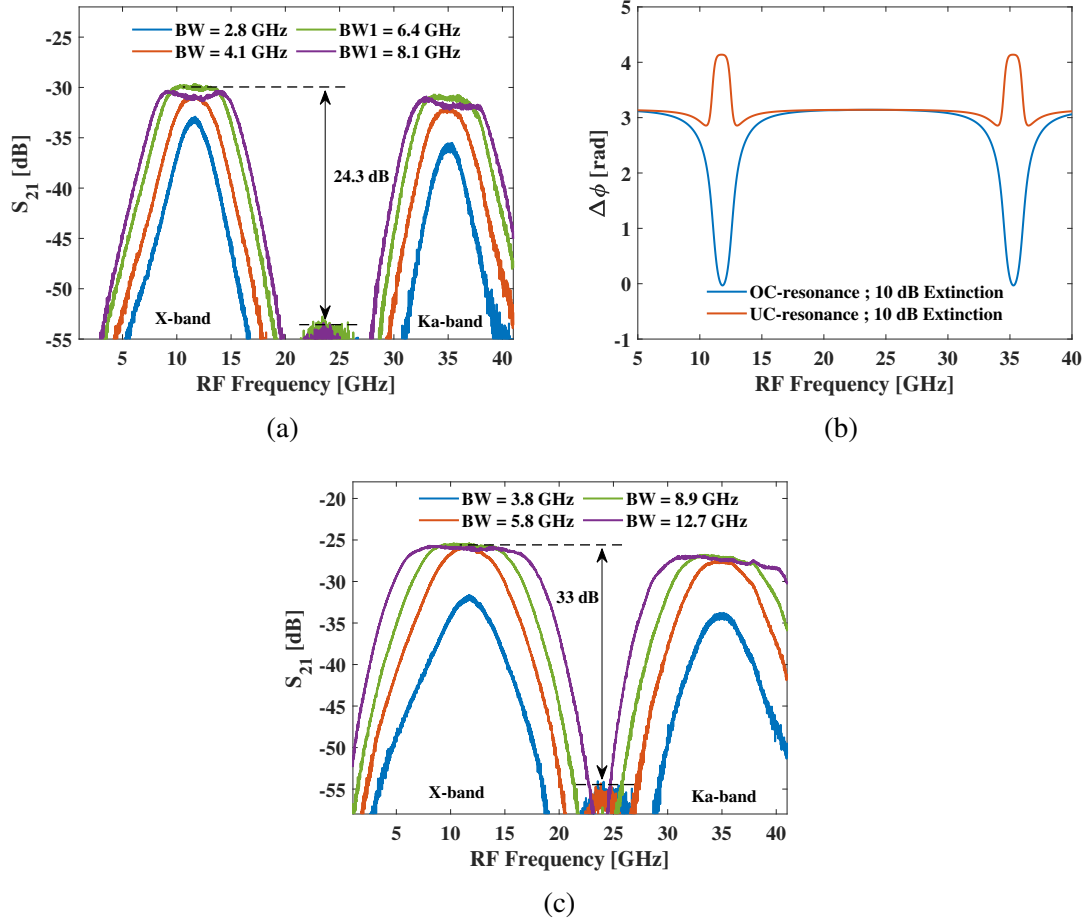


Figure 4.15: (a) Measured two-band microwave filter response with tunable bandwidth using configuration-1 MRR programmed to operate in over-coupled region with extinction = 10 dB,  $Q = 0.75 \times 10^5$ ; (b) calculated  $\Delta\phi$  variation of two-band microwave filter for MRR operating in over-coupled (OC) and under-coupled (UC) region with 10 dB extinction and (c) measured two-band microwave filter response with tunable bandwidth using configuration-1 MRR programmed to operate in over-coupled region with extinction = 5 dB,  $Q = 0.6 \times 10^5$ .

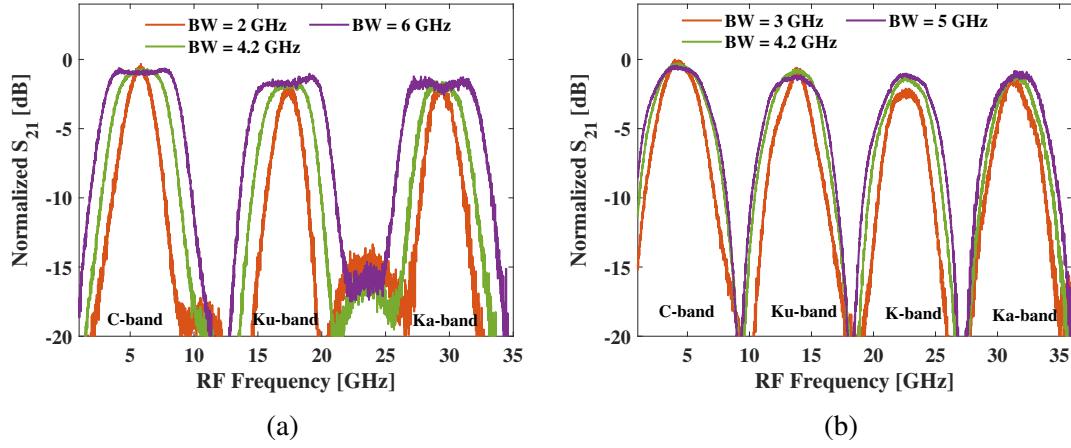


Figure 4.16: (a) Measured three-band microwave filter response with tunable bandwidth (2 GHz - 6 GHz) using configuration-2 MRR operating in under-coupled region with extinction = 10 dB,  $Q = 1.2 \times 10^5$ , and (b) Measured four-band microwave filter response with tunable bandwidth using configuration-3 MRR operating in under-coupled region with extinction = 10 dB,  $Q = 0.8 \times 10^5$ .

bandwidth tuning range over the two MRR configurations is limited to 2 GHz to 6 GHz. As in the previous case, MRRs FWHM limits the minimum achievable bandwidth and the passband ripples limit the maximum achievable bandwidth. To further extend the idea, we have programmed the square mesh to configuration-3 of the MRR with 8-mm cavity length (see Fig. 4.2) operating in the under-coupled regime with 10 dB extinction ( $Q = 0.8 \times 10^5$ ). Fig. 4.16b shows the four-band filter response at 4.2 GHz ( $\sim \text{FSR}/2$ , C-band), 13.9 GHz ( $\sim 3 \times \text{FSR}/2$ , Ku-band), 22.7 GHz ( $\sim 5 \times \text{FSR}/2$ , K-band) and 31.5 GHz ( $\sim 7 \times \text{FSR}/2$ , Ka-band), with tunable bandwidth. As expected, both minimum (limited by FWHM) and maximum (limited by the finesse) achievable bandwidth further degrades, and the realized bandwidth tuning range is 3 - 5 GHz.

The comparison of the measured multi-band RF filter responses with the state-of-the-art demonstrations is listed in Table. 4.6. The comparison establishes the superiority of the measured filter results in the ability to reconfigure the number of filter passbands and the symmetricity of the out-of-band rejection. Even though the bandwidth tuning range for three-band and four-band filter responses, it can be improved by finesse of the realized

Table 4.6: Comparison of the measured multi-band RF filter responses with the programmable square mesh and the state-of-the-art demonstrations.

Ref.	Platform	OSP	Modulator and Photodetector	Rejection	No. of Passbands	Frequency Tuning [GHz]	Bandwidth Tuning [GHz]
[66]	SiN	Two MRRs with MZI as tunable coupler	off-chip	Asymmetric > 20 dB	2	3 - 9 & 5 - 11	0.26 (for both the bands)
[68]	SiN	Single MRR with asymmetric coupler	off-chip	Asymmetric & 27 dB	2	5 & 16	0.12 & 0.32
[78]	SiO <sub>2</sub>	Single MRR with large cavity length	off-chip	Symmetric & > 25 dB	3	3.5 & 5 & 8	0.73 - 2.73 (for all the bands)
This work	SOI	Programmable Square Mesh	off-chip	Symmetric & > 25 dB	2	11.8 & 35	1.6 - 12.7 (for both the bands)
				Symmetric & > 15 dB	3	5.8 & 17.4 & 29.3	2 - 6 (for all the bands)
				Symmetric & > 15 dB	4	4.2 & 13.9 & 22.7 & 31.5	3 - 5 (for all the bands)

ring responses by reducing insertion loss of the TBU.

#### 4.4 LINK PERFORMANCE EVALUATION

After realizing the multiband filter functionalities, we carried out two-tone modulation experiment to evaluate the RF link performance metrics in terms of intermodulation distortions, noise figures and spurious free dynamic range (SFDR). Following that, we evaluated the performance of the filter module by establishing radio over fiber (RoF) receiver link as a proof-of-concept validation of the proposed multiband microwave photonic filter applications in wireless communication systems. However, because of hardware resource limitation, we focused on X-band link only rather than on all other passbands, which is obvious.

For the two-tone test experiment, we sourced the modulator with two frequency X-band tones at  $f_{rf1} = 11.0$  GHz and  $f_{rf2} = 11.1$  GHz falling around the center frequency of the first passband (see Fig. 4.15a), from two different output channels of a performance network analyzer (PNA, Keysight N5222B) operates up to 26.5 GHz. The tones were multiplexed through a 50:50 coupler (Mini-Circuits, ZC2PD-K0144+, 3-dB bandwidth =

40 GHz). The output of the detector consisting of all possible spurious tones within its bandwidth limit, is fed to the PNA's in-built electrical spectrum analyzer. The PMA was pre-programmed to realize an equivalent MRR in configuration-1 with a set  $PS_k$  value to operate the MRR in an under-coupled resonance condition (resonance extinction of 10 dB and Q-value of about  $1.3 \times 10^5$  at  $\lambda_r \sim 1545.6$  nm). The input RF power corresponding to the frequency tones used for the electro-optic phase modulation were set identical and swept from -2 dBm to +4 dBm. The corresponding output RF powers for the fundamental tones at  $f_{rf1}$ ,  $f_{rf2}$  and the third-order intermodulation tones (IMD3) at  $2f_{rf1} - f_{rf2}$  and  $2f_{rf2} - f_{rf1}$  were measured after optical to electrical down-conversion by the built-in photodetector of the LCA; the corresponding observed experimental results are presented in Fig. 4.17, along with their respective linear fits. During the measurements, we have adjusted the filter response to have a flat-top response ensuring all four tones of interest experience the same link gain from the filter. Using linear fits, we have extracted the third-order input intercept point ( $IIP_3 = 19$  dBm), output intercept point ( $OIP_3 = -14.29$  dBm) and link gain ( $G = -33.04$  dB,  $P_{RF,out}$  for  $P_{RF,in} = 0$  dBm); they are marked the same in Fig. 4.17. The noise figure of 63.5 dB and the spurious free dynamic range ( $SFDR_3$ ) = 86.3 dB.Hz<sup>2/3</sup> of the microwave filter link are extracted from the measured noise floor  $p_{N,out} = -137.3$  dBm/Hz and using the formulas given by [98]:

$$NF \text{ [dBm/Hz]} = p_{N,out} \text{ [dBm/Hz]} - G - p_{N,in} \text{ [dBm/Hz]} \quad (4.3)$$

$$SFDR_3 = \frac{2}{3} [IIP_3 - NF - p_{N,in}] \quad (4.4)$$

where  $p_{N,in}$  is the noise power spectral density at input, which we considered to be contributed only by the thermal noise (= -174 dBm/Hz). The degradation in the SFDR of the reported RF filter link is majorly contributed by the fiber-to-chip grating coupler loss ( $\sim 6$  dB/coupler). An efficient design of the fiber-to-chip grating (or edge) couplers will improve the link gain, noise figure and SFDR of the filter link. However, the measured SFDR of the filter link is comparable with the reported results (MRR-based OSP with off-chip modulator and detector) of 90.7 dB.Hz<sup>2/3</sup> in [72] and 83.6 dB.Hz<sup>2/3</sup> in [99].

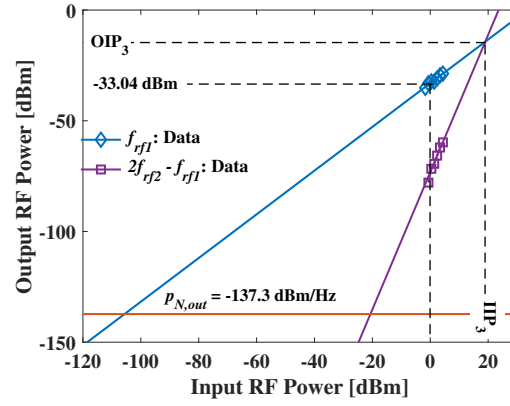


Figure 4.17: Output RF power variation for fundamental tone  $f_{rf1}$  and IMD3 tone  $2f_{rf2} - f_{rf1}$  with the input RF power along with the linear fits and indicating the link gain  $G = (-33.04 \text{ dB} ; P_{RF,out} \text{ for } P_{RF,in} = 0 \text{ dBm})$ , input intercept point  $IIP_3$  and output intercept point  $OIP_3$ . The subscript three correspond to the third order inter-modulation terms and  $p_{N,out}$  - output noise power spectral density.

Table 4.7: Extracted metrics of the two-tone test for the X-band filter responses given in Fig. 4.14a and Fig. 4.15.  $G$  - RF link gain;  $IIP$  - input intercept point;  $OIP$  - output intercept point; SFDR - spurious free dynamic range; NF - noise figure. The subscript three correspond to the third order inter-modulation terms.

Extinction	10 dB (UC)	10 dB (OC)
Q-factor	$1.3 \times 10^5$	$0.75 \times 10^5$
$G$ [dB]	-33.04	-28.9
$IIP_3$ [dBm]	19	18
$OIP_3$ [dBm]	-14.3	-12.1
NF [dB]	63.5	59.4
SFDR <sub>3</sub> [dB.Hz <sup>2/3</sup> ]	86.3	88.5



Next, we also repeated the two-tone experiment by programming the microring resonator to operate in over coupled state (OC-state) with 10 dB resonance extinction, and both the resulting outcomes are summarized in Table 4.7. As expected, the filter response with OC-resonance exhibit improved filter metrics due to the link gain enhancement of the filter response with minimal addition of noise into the filter link (as shown earlier in Fig. 4.15a and Fig. 4.16a). The comparative results given in Table 4.7 further establish the benefits of operating the ring resonator in the OC resonant condition with a compromise in the minimum achievable bandwidth. The SFDR can be improved (towards 120 dB.Hz<sup>2/3</sup>; required for the practical microwave photonic systems [44]) by opting for the linearization techniques as discussed in [66, 100]. Following the decent demonstration of two-tone test experiment as discussed above, we investigated the performance of the demonstrated microwave photonic filter by establishing RoF receiver link. For this purpose, we modified the experimental setup used earlier (see Fig. 4.7) with equivalent remote radio head (RRH) and baseband unit (BBU) sections, as shown in Fig. 4.18.

Here, we have used an arbitrary waveform generator (AWG, Keysight M9505A) to generate non-return to zero (NRZ) pseudo-random binary sequence (PRBS) data with a word length of  $2^7-1$ . The PRBS data is internally upconverted on top of the RF carrier frequency  $f_c$  in AWG (first up-conversion; baseband to GHz). The PRBS data (upconverted to GHz) is then fed into the inbuilt electrical amplifier of Thorlabs modulator bias controller (MX40A, 3-dB BW = 20 GHz) followed by the phase modulator for the second up-conversion of RF signal into the optical domain (GHz to THz). The phase-modulated optical spectrum is launched into the PMA package. As mentioned in the previous section, the internal laser of the OSSA is used to track the resonance position and achieve the desired filter response. A low-noise, high-power EDFA (Pritel LNHP-FA-37-IO-NMA) was used at the output of the PMA package to amplify even the weak optical signal to the power levels close to the detector saturation, and then transmitted to BBU through SMF-28 optical fiber. The received signal at the BBU is fed to the detection circuit for the first down-conversion (THz to GHz). The output

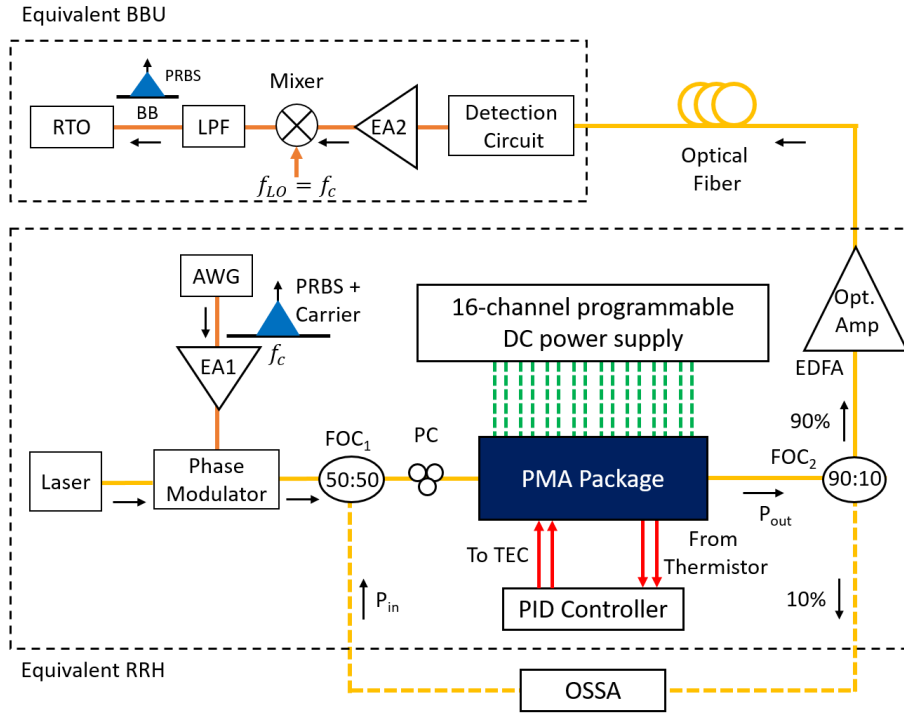


Figure 4.18: Experimental setup for the demonstration of X-band radio over fiber receiver link. BBU - baseband unit; RRH - remote radio head; Opt. Amp. - optical amplifier; EDFA - erbium doped fiber amplifier; PC - polarization controller; FOC - fiber-optic coupler; PMA - programmable mesh architecture; TEC - thermo-electric cooler;  $P_{in}$  - input optical power ( $= -5.6$  dBm) from OSA;  $P_{out}$  - output optical power from PMA package; AWG - arbitrary waveform generator; PRBS - pseudo-random binary sequence; EA - electrical amplifier; LO - local oscillator; LPF - low-pass filter; BB - baseband; ESA - electrical spectrum analyzer; and RTO - real-time oscilloscope.

of the detection circuit is then amplified again through the second electrical amplifier (Mini-Circuits ZVA-443HGX+, 3-dB BW = 43.5 GHz) and subsequently passed into the mixer (Mini-Circuits, ZMDB-44H-K+) and a low-pass filter (Mini-Circuits VLF-575+, 3-dB BW = 5.75 GHz) for the second down-conversion (GHz to baseband). The local oscillator (LO) required for the mixer was provided through the 26.5 GHz PNA (Keysight N5222B), with the frequency set equal to the carrier frequency of the data ( $f_{LO} = f_c$ ), to ensure the direct down-conversion to the baseband. The low-pass filter output was observed by the real-time oscilloscope (RTO, Keysight UXR0502A) for post-processing. The received signal in the RTO is then processed externally in MATLAB to construct the eye diagram (due to a frequency offset of 2 kHz between the RF carrier from AWG and LO signal from PNA) and calculate the bit-error rate (BER). In the first set of experiments to estimate the optimal operating point for the ring resonator, the equivalent RRH and BBU sections are connected back-to-back, which we consider zero fiber length.

While performing the experiment, the PMA is programmed to activate the ring with 10 dB resonance extinction operating in OC-state (owing to the improved filter metrics), with the laser frequency and the resonance positions were adjusted to have the maximum allowed filter bandwidth with a flat-top response. For the mentioned operating state of PMA and a data rate of 100 Mbps, Fig. 4.19a show the eye diagram with the RF carrier  $f_c$  (and  $f_{LO}$ ) set to 11 GHz ( $\sim$  filter central frequency). From the figures, the eye's opening is evident with an eye height of 200 mV for 11 GHz carrier frequency. The result validates the efficient transmission of the PRBS data centered around filter central frequency. From the eye-diagrams of the received data, we have calculated the BER of the receiver link using the standard complimentary error function formula given by [101]:

$$\text{BER} = \frac{1}{2} \text{erfc} \left( \frac{Q_d}{\sqrt{2}} \right) ; Q_d = \frac{\mu_1 - \mu_0}{\sigma_1 + \sigma_0} \quad (4.5)$$

where  $Q_d$  is the quality metric to indicate the signal-to-noise ratio of the transmitted bits,  $\mu_{1,0}$  and  $\sigma_{1,0}$  are the mean and the standard deviation of the output voltages corresponding

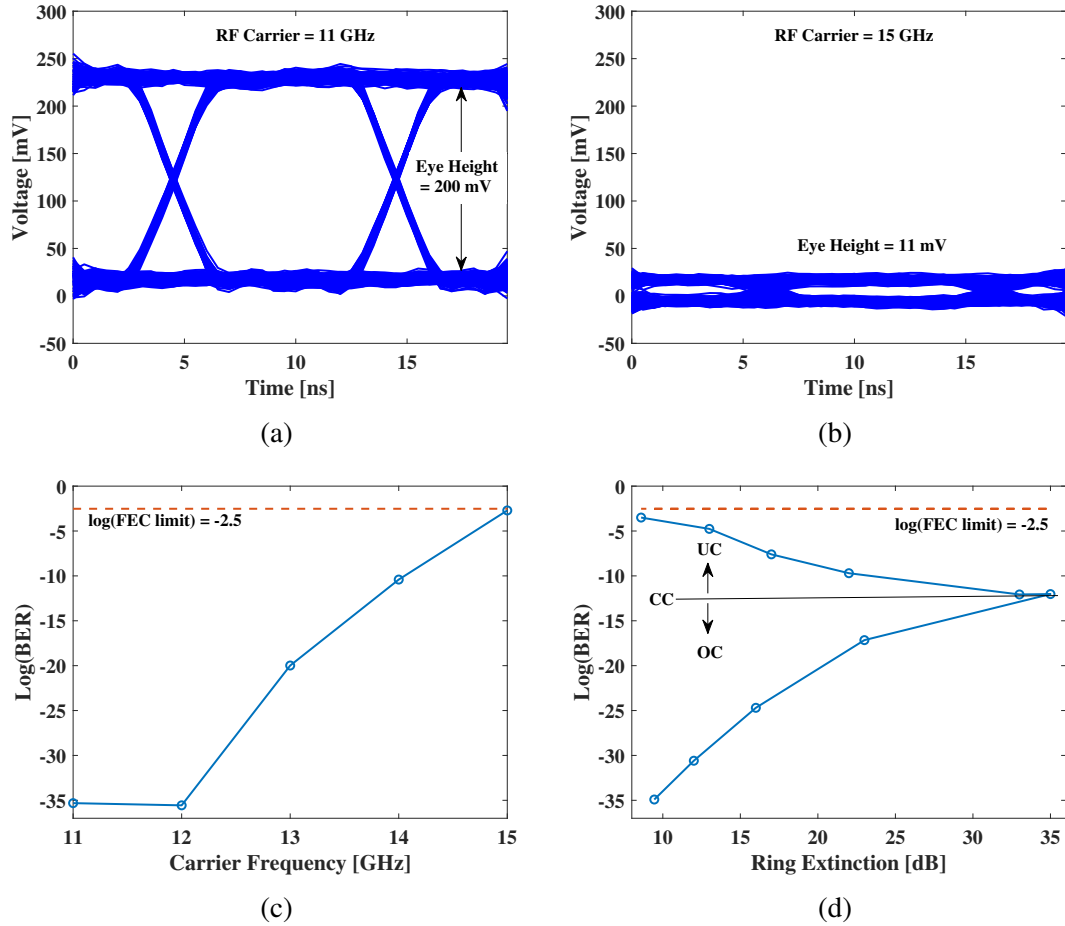


Figure 4.19: Eye diagram of the received PRBS data with the PMA programmed to configuration-1 with 10 dB resonance extinction in over-coupled state and the data transferred with a carrier frequency of (a) 11 GHz; (b) 15 GHz; (c) calculated BER of the receiver link with the carrier frequency of the PRBS data, and (d) Calculated BER of the receiver link with the change in the extinction (coupling condition) of the ring resonator. OC - over-coupled; CC - critically-coupled; and UC - under-coupled.

to bits {1,0}, respectively. For the eye diagram depicted in Fig. 4.19a (transmission at 11 GHz) the BER is estimated about  $10^{-35}$ , indicating an efficient data transmission within the forward error correction (FEC) limit of  $3 \times 10^{-3}$  [102].

A similar exercise was carried out by detuning the carrier frequency of the PRBS data from 11 GHz to 15 GHz, in the steps of 1 GHz. The minimum applicable carrier frequency in this case is limited by the operating frequency of the mixer (10 GHz). The eye diagram for the transmitted data with 15 GHz carrier frequency is shown in Fig. 4.19b, indicating a significant drop in the eye height (and BER) to 11 mV (and  $\sim 2 \times 10^{-3}$ ), due to the roll-off of the filter response. The BER variation with the carrier is shown in Fig. 4.19c, where the BER is similar for 11 GHz and 12 GHz ( $\sim 10^{-35}$ ) due to the flat-top response of the filter. However, the BER degrades as the input RF spectrum aligns with the roll-off of the filter response and is slightly beyond the FEC limit for 15 GHz carrier frequency. The results given in Fig. 4.19 validate the potential of the PMA-based microwave photonic filter for simultaneous data transmission and filtering in RoF receiver link.

Further, we performed the same experiment to assess the optimal operating coupling condition of the ring resonator for efficient link performance. For this purpose, we have programmed the PMA to configuration-1 and calculated the BER for different extinction values of the resonances (by tuning the thermal power  $PS_k$  applied to the TBU 4 of the PMA) such that the ring response is tuned from OC-state to UC-state, and the results are given in Fig. 4.19d. For the given results, fiber length, RF carrier frequency and applied data rate are zero, 11 GHz and 100 Mbps, respectively. Because of the RF link gain dependence on the ring coupling condition (as shown earlier in Fig. 4.15a and Fig. 4.16a.), we see a significant variation in the calculated BER ( $10^{-35}$  to  $10^{-4}$  from OC to UC) despite no change in the received optical power by the detection circuit ( $\sim 4.5$  dBm). In the results, even though the BER is within the forward error correction limit for the entire range of OC to UC-state, we can expect the performance to degrade in the

Table 4.8: Calculated BER for the change in the fiber length between the equivalent RRH and BBU sections (as marked in Fig. 4.18) and the transmitted data rate. Zero fiber length: back-to-back fiber connections between the equivalent RRH and BBU sections.

Data rate = 100 Mbps		Fiber Length = 400 m	
Fiber Length [m]	log(BER)	Data Rate [Mbps]	log(BER)
0	-35.5	100	-19.3
100	-34.2	500	-11.9
200	-29.5	1000	-5.4
300	-26.1	—	—
400	-19.3	—	—

presence of the transmitting optical fibers and increased data rates.

To study the link performance degradation with the distance of data transmission between the equivalent RRH and BBU sections (as depicted in Fig. 4.18), we carried out the BER calculations for different lengths of optical fibers (0 to 400 m, as per the availability in the laboratory), with ring response set to OC resonance with 10 dB extinction. In our experiments, we have used four 100 m optical fiber cables with fiber-optic connectors (insertion loss  $\sim 0.2$  dB/connector) to realize a fiber-optic transmission length of 400 m. Therefore, we interpret the BER degradation with fiber-optic length shown in Table. 4.8 to the connector losses. Similarly, we calculated the BER for the data rates of 100, 500 and 1000 Mbps with a fiber length of 400 m between the equivalent RRH and BBU sections. The corresponding results are listed in the Table. 4.8. From the obtained results, we can conclude the BER is well within the FEC limit for the chosen range of the fiber lengths and data rates; thus confirming the feasibility of the integration of PMA-based microwave photonic filter in the data communication systems. This study can be further extended to filter responses realized with the PMA programmed to operate in configuration-2 and configuration-3, and validate its performance in multi-band communication systems as well.

#### 4.5 SUMMARY

In this chapter, a multiband microwave photonic filter with a tunable bandwidth and a reconfigurable number of passbands has been successfully demonstrated, with programmable mesh architecture (PMA) as the OSP. The PMA was carefully calibrated for the fabrication-induced phase errors and was subsequently programmed to realize MRR responses with independent tuning of the coupling coefficient and the resonant wavelength for the desired three configurations. The FSR, Q-factor at CC, loss factor  $\alpha$  at CC of the measured responses are  $\{23.25 \text{ GHz}, 1.15 \times 10^5, 0.88\}$ ,  $\{11.75 \text{ GHz}, 0.96 \times 10^5, 0.75\}$ , and  $\{8.75 \text{ GHz}, 0.7 \times 10^5, 0.54\}$ . Among the three ring configurations, the two-band filter (at X-band and Ka-band) obtained from configuration-1 was thoroughly investigated to study the effect of MRR coupling coefficient on the filter bandwidth and its tuning range, link gain and rejection. An extensive bandwidth tuning range of 1.6 GHz to 12.7 GHz was obtained for the two-band filter response. However, we observed the bandwidth tuning range of the three-band filter at C-, Ku- and Ka-band (2 GHz - 6 GHz) and the four-band filter at C-, Ku-, K-, and Ka-band (3 GHz - 5 GHz) are limited by the finesse of the ring resonator.

Following the realization of filter responses, we have done a proof-of-concept evaluation of the performance of the PMA-based microwave photonic filter at X-band, in a RoF receiver link with equivalent RRH and BBU. From the experiments, we have established that the OC region is well suited for the ring operation to obtain the improved link gain, SFDR, noise figure and BER  $\{G_{OC}, SFDR_{OC}, NF_{OC}, BER_{OC}\} = \{-29 \text{ dB}, 88.54 \text{ dB.Hz}^{2/3}, 59.44 \text{ dB}, 10^{-35}\}$ , when compared with UC region  $\{G_{UC}, SFDR_{UC}, NF_{UC}, BER_{UC}\} = \{-33 \text{ dB}, 86.28 \text{ dB.Hz}^{2/3}, 63.56 \text{ dB}, 10^{-4}\}$ , with a compromise in the minimum achievable bandwidth. The dependence of filter metrics on MRRs coupling condition is mainly attributed to the link gain enhancement of filter response with over-coupled resonances with minimal addition of noise into the filter link. With the optimized settings of ring resonator, we have achieved a BER of  $\sim 10^{-5}$  for the fiber optic transmission length of 400 m between the equivalent RRH and BBU at the data rate of 1 Gbps.

In the designed PMA, the finesse of the configured MRRs and BER of the transmitted data can be improved by optimizing the unit TBU loss, MMI imbalances, grating coupler losses or opting for an edge coupler altogether. In the current experiments, thermal crosstalk between the two MZI arms has increased the required thermal power (especially for bar port operation) to realize the desired MRR responses, which can be reduced by isolating the two arms with trenches up to the Silicon substrate layer. Nevertheless, this study can be easily taken forward for the development of low-cost and high performance microwave photonic processor chip co-integrated with the lasers, high-speed modulators, photodetectors, and driver electronics using a suitable SOI-based CMOS technology offered by commercial foundries like Tower Semiconductors, Global Foundries, etc.





## CHAPTER 5

### INTEGRATED MICROWAVE PHOTONIC FILTER

In this chapter, we extend the operation scheme discussed in Chapter 3 to realize a integrated microwave photonic filter with an on-chip modulator, OSP and photodetector. The OSP is designed with an MZI-based tunable coupler to realize a two-band filter response with tunable frequency and bandwidth. Following the discussion of the operation scheme, we will discuss the schematic of the fabricated chip and the electrical packaging of the photonic chip for active temperature control and multiple heater operation. Next, we will discuss the individual characteristics of the on-chip modulator, photodetector and OSP structure and the challenges faced with the simultaneous RF probing of the modulator and detector due to the crosstalk between the input-output RF ports. Finally, we present the filter characteristics by individually probing the on-chip modulator and on-chip PD, followed by the tuning characteristics of the filter.

#### 5.1 OPERATION SCHEME AND CHIP LAYOUT

For the chip-scale integration of microwave photonic filter, we have extended the operation scheme discussed in Chapter 3 and realized a two-band filter response with tunable frequency and bandwidth. The spacing between the two filter passbands is dependent on the free spectral range of the MRRs used in the OSP. As mentioned, in this work, the phase modulator, OSP (identical cascaded microring resonators integrated with four thermo-optic phase shifters) and the photodetector were integrated on the same photonic integrated circuit (PIC), as represented in Fig. 5.1a. Similar to the earlier design discussed in Chapter 3, each ring is integrated with two thermo-optic phase shifters  $PS_{\kappa}$  and  $PS_{\lambda}$  to independently tune the ring's coupling coefficient and the resonant wavelength. However, in contrast to the OSP design (with asymmetric directional coupler) discussed in Chapter

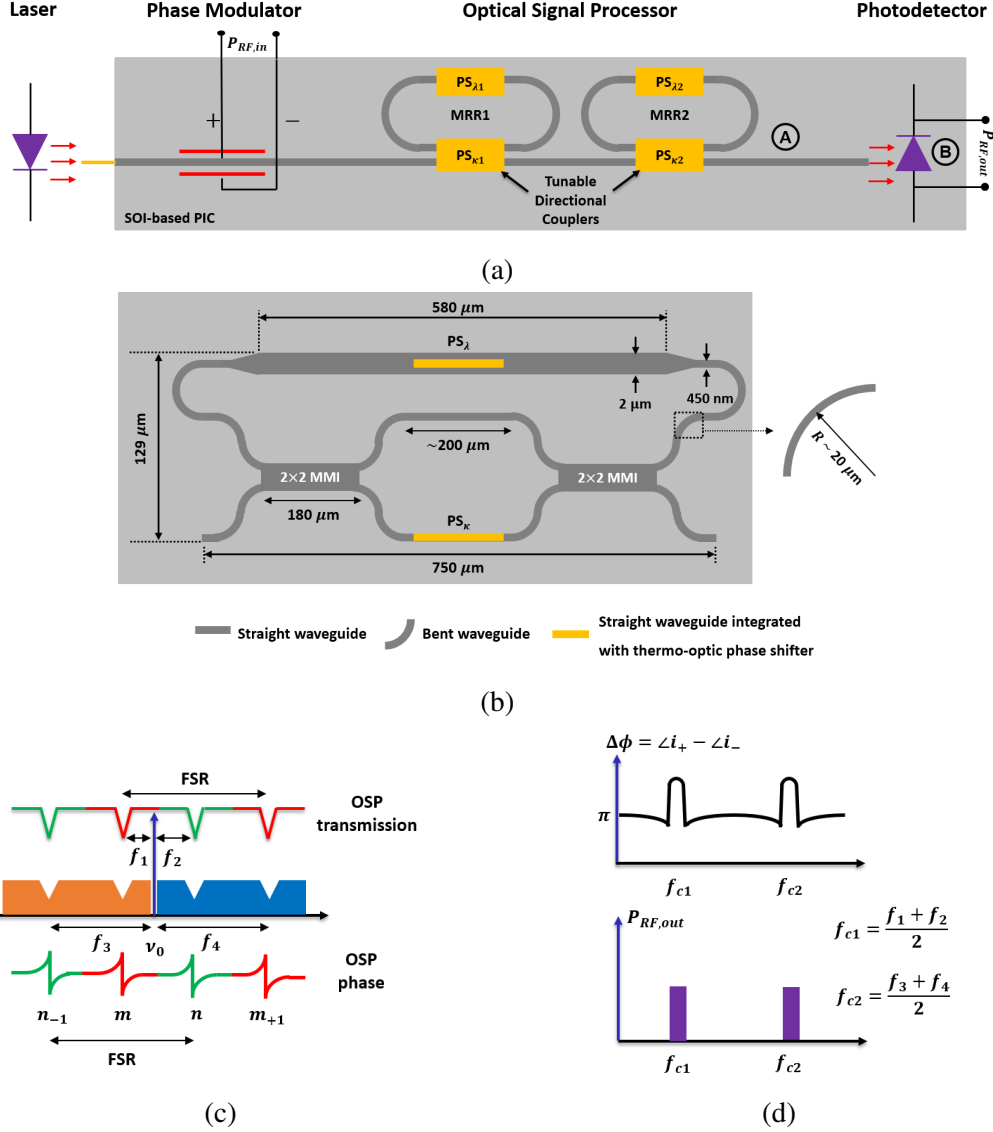


Figure 5.1: (a) The schematic of the proposed OSP chip along with its operational scheme for the RF photonic bandpass filter functions with symmetric out-of-band rejection; (b) schematic representation of the fabricated ring resonator of the OSP indicating the critical dimensions, (c) optical transmission characteristics of the modulated laser light along with the transmission and phase spectrum of the OSP,  $f_1, f_2, f_3, f_4$  correspond to the resonance spacings with respect to the laser carrier frequency  $\nu_0$ , and (d) schematic representation of the phase deviation  $\Delta\phi$  (from  $\pi$ ) between beat photocurrents  $i_+$  and  $i_-$  at the photodetector as a function of RF frequency (top) and microwave filter response corresponding to the superposition of  $i_+$  and  $i_-$  at the photodetector output.

3, we have considered the Mach-Zehnder interferometer (MZI) as a tunable coupler for the ring resonators (shown in Fig. 5.1b), owing to the foundry yield, improved waveguide loss in the foundry process, and the wide tuning range of the coupling coefficient. In the ring ( $129 \times 750 \mu\text{m}^2$ ), the design of  $2 \times 2$  multi-mode interferometer (MMI,  $25.8 \times 180 \mu\text{m}^2$ ) and the thermo-optic phase shifter (width = 600 nm, thickness = 300 nm, vertical distance from the waveguide =  $1 \mu\text{m}$ , material: Tungsten) were considered as per the PDK of the IMEC foundry. In addition, to mitigate the Q-factor degradation with the increase in cavity length [85], we have adiabatically tapered the width of the ring waveguide from 450 nm to  $2 \mu\text{m}$  over the length of  $40 \mu\text{m}$  (and also tapered back), as shown in Fig. 5.1b.

As already mentioned in Chapter 3, the choice of MZI as the tunable coupler is expected to decrease the FSR of the ring and, thus, the tuning range of the microwave photonic filter. However, because of the periodic nature of the microring resonator response, i.e., FSR, any MRR-based microwave filter, in principle, can realize a multiband filter. The number of realizable passbands depends on the FSR value and the microwave filter's operating frequency range. For our experiments, with the operating frequency range of 1 - 50 GHz, we have designed the cavity length of both the MRRs such that the theoretical estimate of the FSR is  $\sim 45$  GHz to realize a two-band filter response. The corresponding operation scheme is explained below.

As we already know, to achieve the filter response with symmetric out-of-band rejection, two identical resonances ( $m$ -th,  $n$ -th) of both the rings (MRR1, MRR2) with equal extinction and Q-factor are placed asymmetrically to the laser carrier with a spacing of  $f_1, f_2$ . However for the designed OSP (FSR  $\sim$  maximum operating frequency),  $m_{+1}$ -th,  $n_{-1}$ -th resonances also gets aligned with the phase modulated optical spectrum with spacings  $f_3, f_4$  with the laser carrier such that  $\text{FSR} = f_1 + f_4 = f_2 + f_3$ , as shown in Fig. 5.1c. The presence of the  $m$ -th and  $n$ -th resonance around the carrier results in the filter response at  $f_{c1} = (f_1 + f_2)/2$ . Also, a second band at  $f_{c2} = (f_3 + f_4)/2 = \text{FSR} - f_{c1}$  due to

the presence of  $m_{+1}$ -th and  $n_{-1}$ -th resonances of two rings. Here, the bandwidth of both the bands can simultaneously be tuned by the slight detuning of  $\Delta f_{12} = |f_1 - f_2|$  (which also results in the detuning of  $\Delta f_{34} = |f_3 - f_4|$ ). In addition, the central frequencies of both bands can also be tuned by adjusting the spacing between the resonances corresponding to both the MRRs, i.e.,  $f_1 + f_2$  and  $f_3 + f_4$ . Even though it is not depicted here, for the mentioned operation scheme there exists a third passband at  $f_{c3} = \text{FSR} + f_{c1}$ , because of  $m_{-1}$  and  $n_{+1}$  resonances of MRR1 and MRR2 of the OSP, respectively. However, in our experiments, the presence of the third passband is limited only to smaller values of  $f_{c1}$  ( $< 5$  GHz). The corresponding results are discussed in Section 5.3.

In our design, the phase modulator is a PN-doped straight waveguide with a slab height of 70 nm (see Fig. 5.2a) operating in reverse bias and thus depleting the charge carrier in the waveguide core region. The input RF signal (applied with a reverse bias offset) modulates the charge carrier depletion in the waveguide and correspondingly the real and imaginary parts of the mode effective index (plasma-dispersion effect) [103]. The change in the real part leads to the phase modulation, and the imaginary part modulation tends to the loss modulation, which is a non-ideal effect (for a phase modulator) that limits the large signal operation of the modulator. Here, we have not depicted the traveling wave electrode associated with the phase modulator in Fig. 5.2a. On the other hand, in the commercial silicon photonic foundry, the photodetector is a vertical PIN diode with epitaxial-grown Germanium acting as the intrinsic region [104]. The typical cross-section of the Ge-photodetector available in the process library of a silicon photonics foundry is depicted in Fig. 5.2b, with the  $n^{++}$ -doped region of Ge completing the PIN diode and as well as establishing the ohmic contact with the via. In our current design, we have opted for the design of the phase modulator, traveling wave electrode and photodetector as per the process design kit (PDK) of the IMEC foundry.

Based on the operation scheme mentioned, we have designed the PIC with an on-chip modulator, OSP and photodetector, shown schematically in Fig. 5.3. The chip

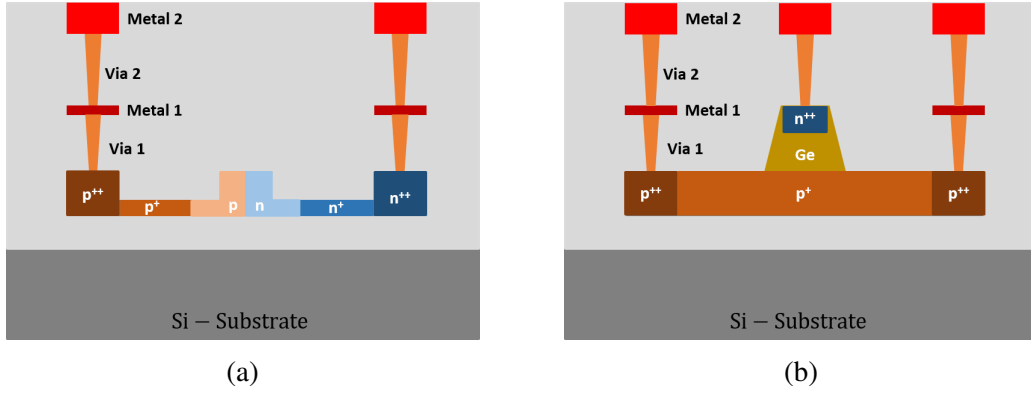


Figure 5.2: (a) Cross-sectional view of the PN doped silicon waveguide for phase modulator, and (b) cross-sectional view of the vertical Ge-PIN photodetector.

comprises three devices, D1, D2 and D3, with laser light coupled in and out of the chip through grating couplers (design as per the process design kit of IMEC foundry, loss: 5 dB/coupler). All three devices are integrated with the phase modulator and the necessary traveling wave electrodes to match optical and applied RF signal group velocity. Among these, device D1 (with an on-chip modulator and the OSP) is designed to test the filter functionality with an off-chip detector; hence, the OSP's output is directly fed to the output grating couplers. Whereas, the devices D2 (with on-chip modulator and single ring resonator) and D3 (with on-chip modulator and the OSP) are designed along with the on-chip photodetectors, with necessary 90:10 taps (90% fed to the on-chip detector and 10% fed to the output grating coupler for coupling maximization and resonance tracking during the experiments), as shown in Fig. 5.3. Among the three on-chip devices, we will focus mainly on devices D1 and D3 for individual component characterization and filter experiments, which will be discussed in the following sections.

The designed PIC was fabricated on a 220 nm silicon-on-insulator (SOI) platform using the iSiPP50G process of IMEC multi-project-wafer (MPW) run. The microscope image of the fabricated structure, along with the zoomed-in images of the grating couplers, ring resonator, multi-mode interferometers, 90:10 tap and the photodetector are shown in Fig. 5.4. In the design, optical inputs and outputs are placed in the west and east direction,

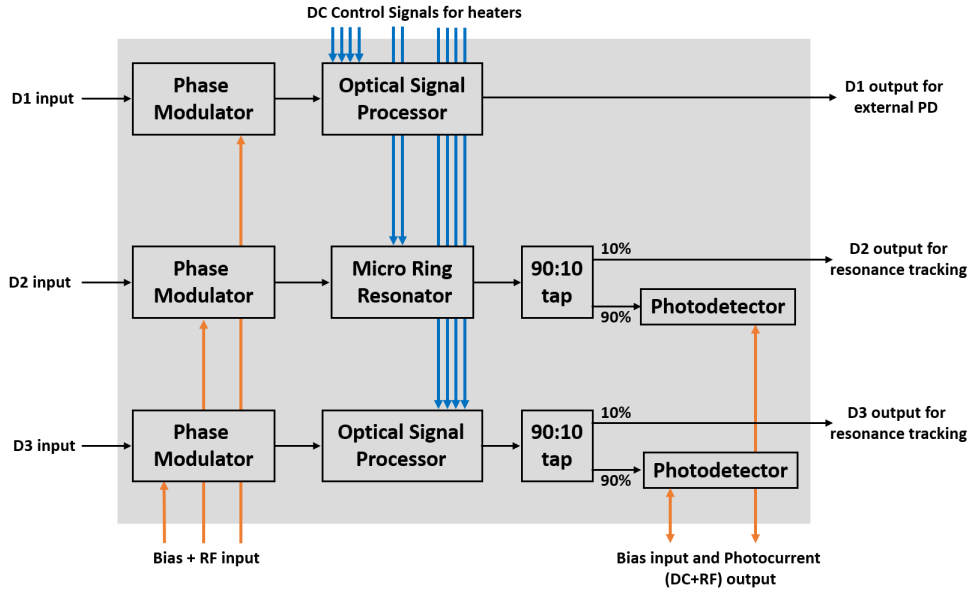


Figure 5.3: Schematic representation of the designed PIC for microwave photonic filter with on-chip modulator, detector and single/cascaded ring resonator along with the necessary 90:10 taps.

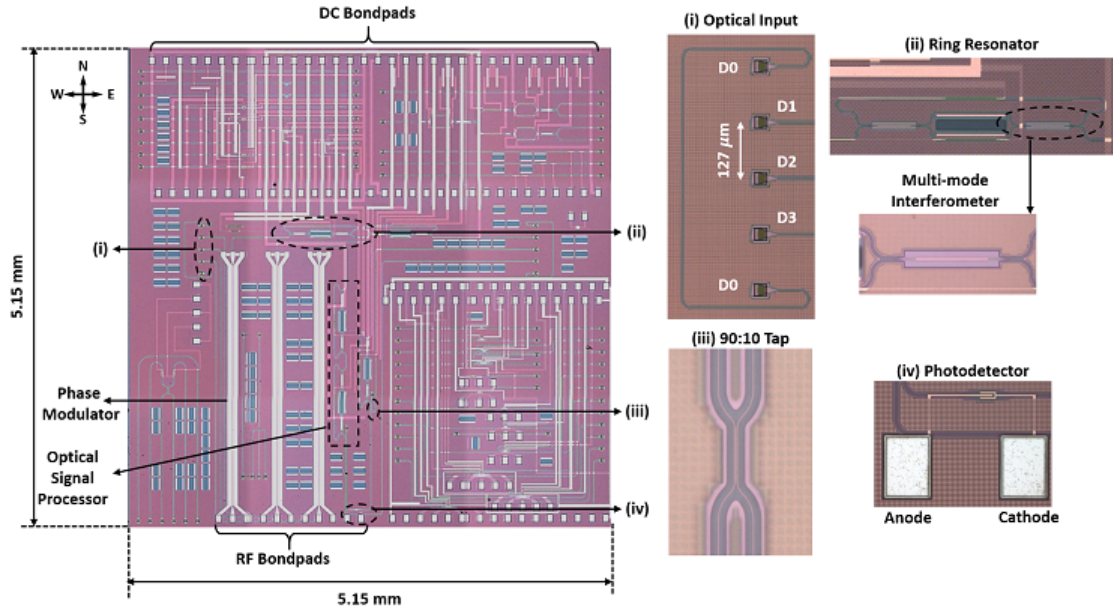


Figure 5.4: Microscope image of the fabricated PIC along with the zoomed images of input grating coupler array, ring resonator, multi-mode interferometer, 90:10 tap and photodetector.

respectively, with a grating coupler spacing of  $127\ \mu\text{m}$  adhering to the packaging design rules for the fiber attachment. Here, an additional device, D0 (shunt waveguide), is also added for the fiber array alignment. In addition, all the thermo-optic phase shifter connections are routed to the DC bond pads placed in the north direction with a pitch of  $150\ \mu\text{m}$ . Finally, the modulators and photodetector, which require RF bond pads, are placed in the south direction with the same pitch of  $150\ \mu\text{m}$ . The total chip area is  $5.15 \times 5.15\ \text{mm}^2$ . The devices in the unspecified regions of the chip are integrated photonic devices unrelated to the microwave photonic filter.

## 5.2 PACKAGING AND COMPONENTS TESTING

The fabricated PIC was mounted on an Aluminum housing ( $50 \times 63\ \text{mm}^2$ ) and was electrically packaged with the necessary DC printed circuit board (PCB) in the north direction, as shown in Fig. 5.5a. The DC bond pads on the north side of the PIC are wire bonded to the PCB bond pads, as shown in Fig. 5.5b, and the PCB trace lines are fanned out to the DC pins for external connections. The package was integrated with a thermistor and thermo-electric cooler (TEC) to actively stabilize the PIC temperature (accuracy  $\pm 0.002^\circ\text{C}$ ) during the experiments. In the current package, the south side is unused for integrating RF PCB, which is required to interface the on-chip modulator and detectors with network analyzers and electronic drivers for biasing. As an alternative, in the current experiments, Form Factor Infinity probes were used to probe the on-chip modulator and detector. After the electrical packaging of the PIC, we have first individually characterized the modulator, photodetector, and ring resonator, and the results are discussed in the following sections. Fig. 5.5c shows the snapshot of the PIC package probed with all the necessary optical and electrical connections (DC and RF) to enable the measurements. In the experiments, a contact substrate and an impedance standard substrate (ISS) card were also placed adjacent to the PIC package (as shown in Fig. 5.5c) for the necessary probe tip planarization and calibrations to de-embed the RF probe (FormFactor Infinity GSG probe, pitch =  $150\ \mu\text{m}$ ) performance from the measurements, respectively.



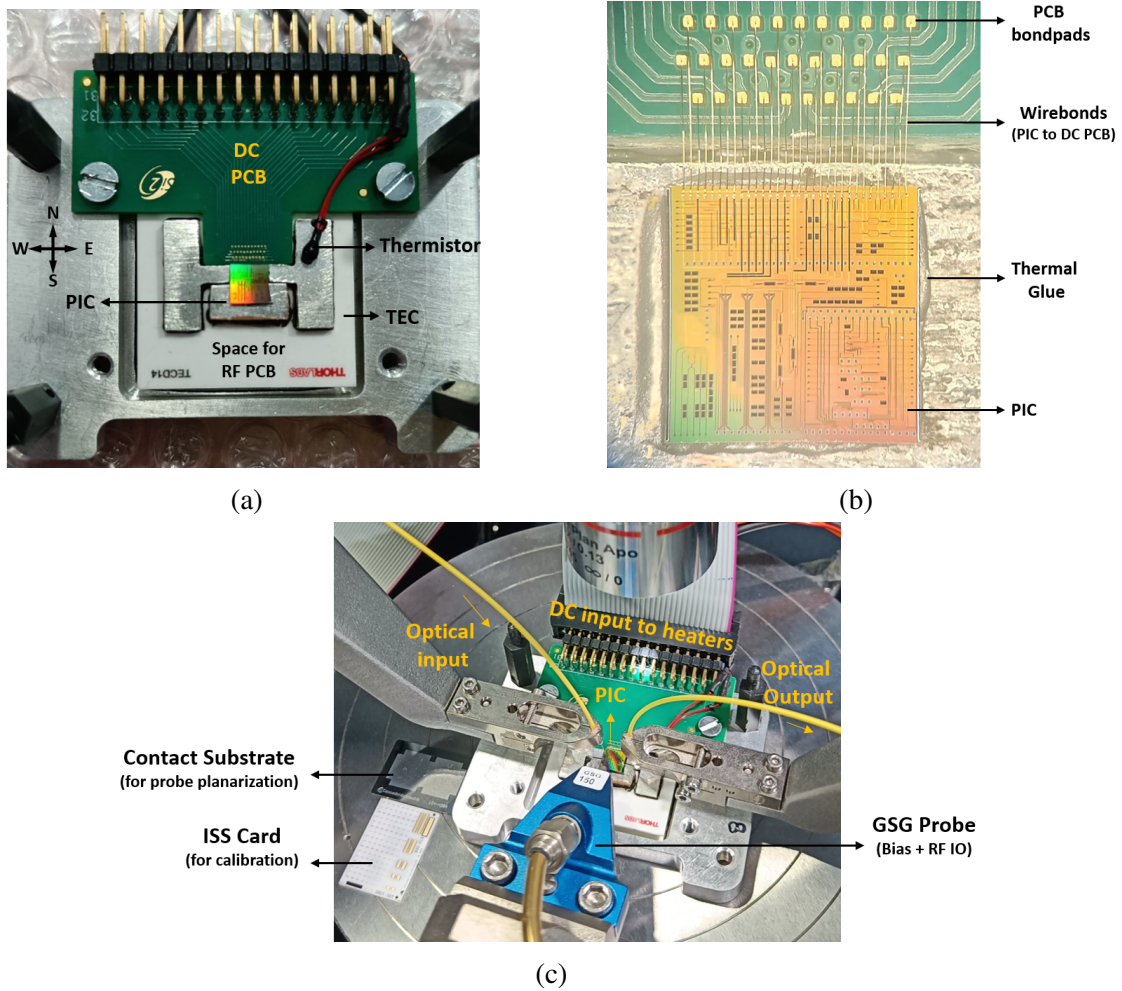


Figure 5.5: (a) Electrically packaged PIC with necessary housing, DC printed circuit boards (PCB), thermistor and thermo-electric cooler (TEC), (b) zoomed-in microscope image of the packaged module showing the wirebonds between the PIC and the DC PCB, and (c) snapshot of the PIC package probed with the necessary optical and electrical connections (DC: wirebonded to PCB, RF: using GSG infinity probe), also indicating the contact substrate and ISS card for planarization and probe calibration.

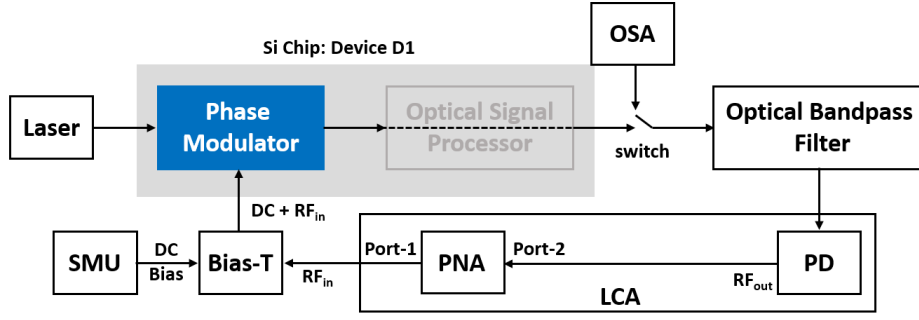


Figure 5.6: Schematic of the experimental setup used to characterize the on-chip phase modulator. OSA: optical spectrum analyzer, PNA: performance network analyzer, PD: photodetector, LCA: lightwave component analyzer, and SMU: source meter unit.

### 5.2.1 Phase Modulator

For the characterization of the phase modulator, we have used the device D1 of the PIC (see Fig. 5.3) and the setup shown in Fig. 5.6. We have not activated the OSP for this experiment, which is hence shown with weak colour in the setup. The laser light is coupled in and out of the chip through the grating couplers. The required DC bias and the RF signal to the phase modulator are provided through a source meter unit (SMU) and the port-1 of the performance network analyzer (PNA, Keysight N5225B), respectively, through a bias-T (Mini-circuits, ZBT-V543-FT+).

The optical output of the PIC is first connected to the optical spectrum analyzer (OSA) to observe the spectrum of the modulated signal. Fig. 5.7a shows the phase-modulated optical spectrum for different RF frequencies applied to the modulator from the PNA (power = 0 dBm), at the reverse bias voltage of -2 V. The carrier wavelength and the corresponding upper and lower side lobes are also marked in the figure, indicating the modulation of the carrier light. However, in the OSA measurements, the RF power delivered to the on-chip modulator for different frequencies is not the same due to the frequency-dependent loss of the RF cables, bias-T and the RF probes used in the experiments. Also, the direct detection of the phase-modulated signal through the PD does not result in an RF signal (due to the  $\pi$  phase difference between the sidelobes).

Hence, to accurately measure the modulator bandwidth, we have launched the PIC optical output to an optical bandpass filter (OBPF) to suppress one side lobe/band and create a single sideband optical spectrum, thus making RF power detection at the PD output possible. The OBPF output was fed to the LCA's internal photodetector, the detector's output port was connected to the port-2 of the PNA, and the  $S_{21}$  of the link was measured. However, the roll-off of the OBPF limits the minimum applicable RF frequency in the experiment to 10 GHz. In the measurements, the effect of all the peripheral RF components (cables and GSG probes), including the internal PD of the LCA, was de-embedded from the device measurements with appropriate calibration (1-port short-open-load (SOL)) using the ISS card and WinCal software of FormFactor and the PNA fixtures.

Fig. 5.7b, shows the measured  $S_{21}$  of the setup link (with necessary calibrations) for reverse bias voltages  $V_{\text{bias}}$ : {0 V, -1 V, -2 V}. Here, for the 3-dB bandwidth calculation, the measured spectrum for the frequency range of 10 GHz to 30 GHz was extrapolated to the unmeasured low-frequency region (10 MHz to 10 GHz), as shown by the dotted lines in Fig. 5.7b. In the same figure, the 3-dB bandwidth of the 39.7 GHz at  $V_{\text{bias}} = -2$  V is also marked. A similar exercise of response extrapolation and the 3-dB bandwidth calculation was carried out for different bias voltages, and the results are given in Fig. 5.7c. Based on the measured responses, extracted values of the modulator bandwidth and expected operating frequency range (1 - 40 GHz), we have biased the modulator at -2 V in the filter experiments.

### 5.2.2 Photodetector

After the modulator characterization, we carried out the on-chip photodetector characterization using the device D3 and the setup shown in Fig. 5.8. In this experiment, no bias and control signals were applied to the modulator and the OSP, thus leaving them deactivated. The PD was biased through the SMU and bias-T, and the DC and RF components of the detected photocurrent were directed to the SMU and port-2 of the

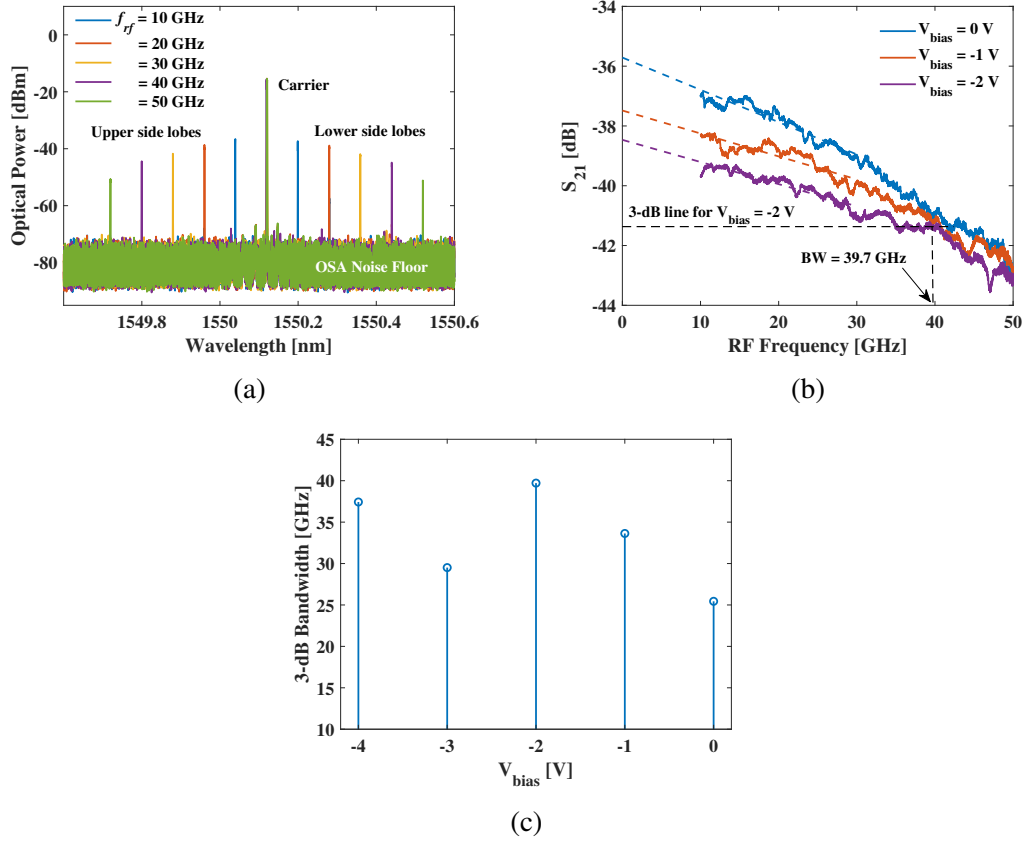


Figure 5.7: (a) Optical spectrum of the phase-modulated optical carrier ( $\lambda_0 \sim 1550$  nm) for different RF frequencies, (b) measured  $S_{21}$  characteristics of the single sideband suppressed on-chip phase modulator for different values of reverse bias voltage, and indicating the 3-dB bandwidth of the measured  $S_{21}$  at -2 V, and (c) extracted 3-dB bandwidth of the on-chip phase modulator for different values of reverse bias voltages.

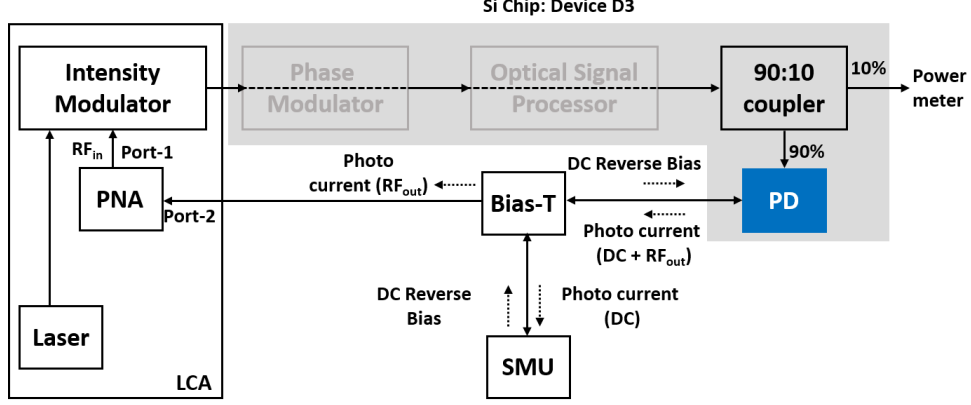


Figure 5.8: Schematic of the experimental setup used to characterize the on-chip photodetector. PNA: performance network analyzer, PD: photodetector, LCA: lightwave component analyzer, and SMU: source meter unit.

PNA, respectively, through the bias-T. Before estimating the RF characteristics of the PD, we first estimated its DC metrics, namely, responsivity and dark current. For this purpose, the intensity modulator and PNA shown in Fig. 5.8 were not activated, and the laser output was directly launched into the chip. The launched light is routed to the PD through the deactivated modulator and the OSP through a 90:10 coupler, with 90% of the light launched into the PD and the remaining 10% is coupled out of the chip to maximize the coupling efficiency.

First, the diode current from the PD is measured using the SMU for different values of the bias voltage, with no laser light incident on the detector (dark current,  $i_{dark}$ ). The measured diode dark currents (in the order of  $\mu A$ ) are given in Fig. 5.9a. The rapid rise in the dark current with bias voltage, especially after -3 V, indicates the small value of diode breakdown voltage. Therefore, in our experiments to estimate the DC metrics of the PD, we have kept the applied voltage within -5 V. Next, the diode photocurrent  $i_{PD}$  was measured by turning on the laser at 1550 nm wavelength and changing the optical power launched from the input laser to the PIC package. For the set values of the laser power, the optical power at the output of the PIC was measured using the power meter and the power launched into the PD,  $P_{in,PD}$ , was calculated by subtracting the effects

of the output grating coupler and 90:10 coupler. The measured diode photocurrents for three different values of  $P_{in,PD}$ , over the chosen range of reverse bias voltages, are given in Fig. 5.9b. As expected, we observe an increase in the photocurrent with the rise in the optical power launched into the PD.

Next, the photocurrent  $i_{PD}$  was measured by sweeping the input laser power from 0 to 10 dBm in the steps of 0.5 dBm for the chosen range of the reverse bias voltages. The measured photocurrents (including the dark current) for different values of estimated  $P_{in,PD}$  for an applied bias voltage of -2 V is shown in Fig. 5.9c. Now for the extraction of the responsivity, the measured data was fit with a linear equation  $i_{PD} = i_{dark} + r_{PD}P_{in,PD}$ , where  $r_{PD}$  is the slope of the linear fit and the responsivity of the photodetector. For the data given in Fig. 5.9c, the extracted responsivity is 0.75 A/W. A similar exercise of responsivity extraction was repeated for different bias voltage values, and the extracted values of the responsivity are given in Fig. 5.9d. Despite the increased responsivity value with reverse bias voltage (especially beyond -3 V), it was preferred not to operate PD in this regime owing to the small breakdown voltage of the PD.

After the DC metrics extraction, we activated the PNA and the in-built intensity modulator of the LCA given in Fig. 5.8 to perform the small-signal AC analysis and estimate the 3-dB bandwidth of the PD. The input RF signal of the intensity modulator was provided from port-1 of the PNA, and the output RF photocurrent from the PD is fed to port-2 of the PNA through a bias-T. Following the connections, the  $S_{21}$  of the link is measured with necessary calibrations (1-port short-open-load (SOL)) with ISS card and WinCal software of FormFactor, and PNA fixtures to de-embed the effects of the cables, bias-T, RF probes and the frequency dependence of the intensity modulator from the measurements. The corresponding results and the extracted 3-dB bandwidth values are shown in Fig. 5.10a and Fig. 5.10b, respectively. From the results, we can conclude that the fabricated PD functions well above 40 GHz for bias voltages beyond -2 V. Hence, taking into account the responsivity, dark current, and the expected operating frequency

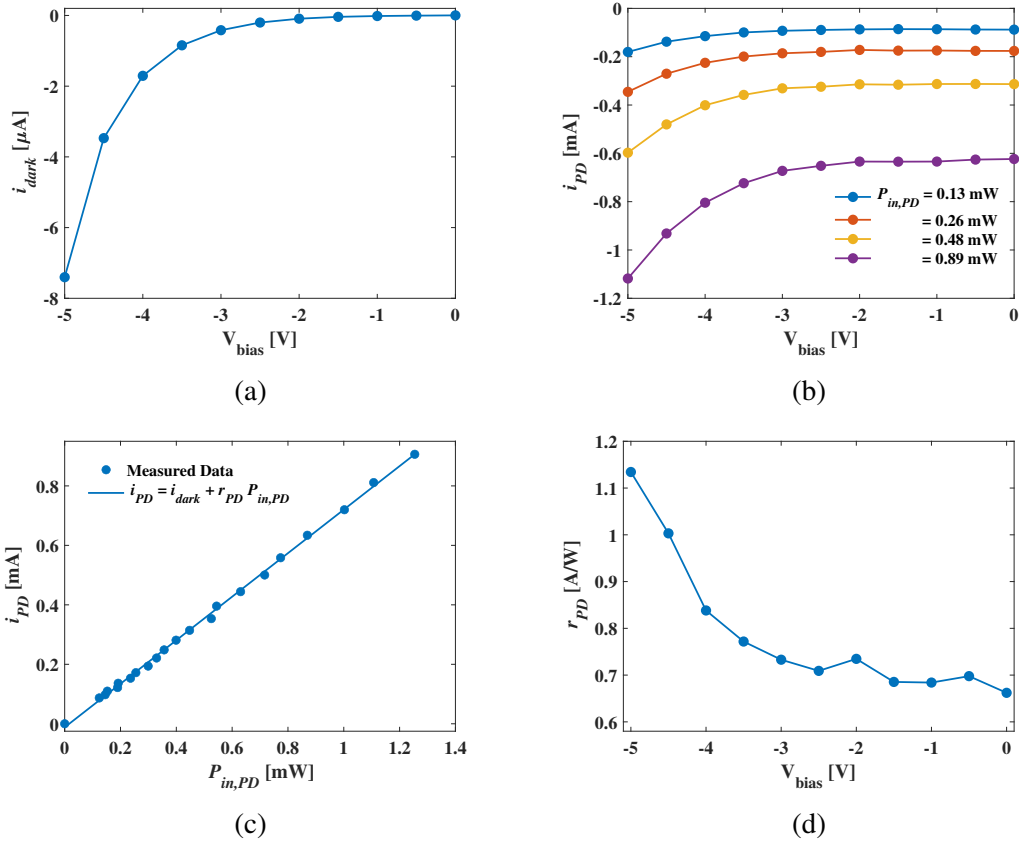


Figure 5.9: (a) Measured dark current of the PD for different values of reverse bias voltage, (b) measured photocurrent of the PD for different values of reverse bias voltage for different optical powers launched on to the PD, (c) measured photocurrent of the PD for different launched optical powers for  $V_{bias}$  of -2 V and the linear fit for responsivity extraction, and (d) extracted responsivity of the PD for different values of applied reverse bias voltage.

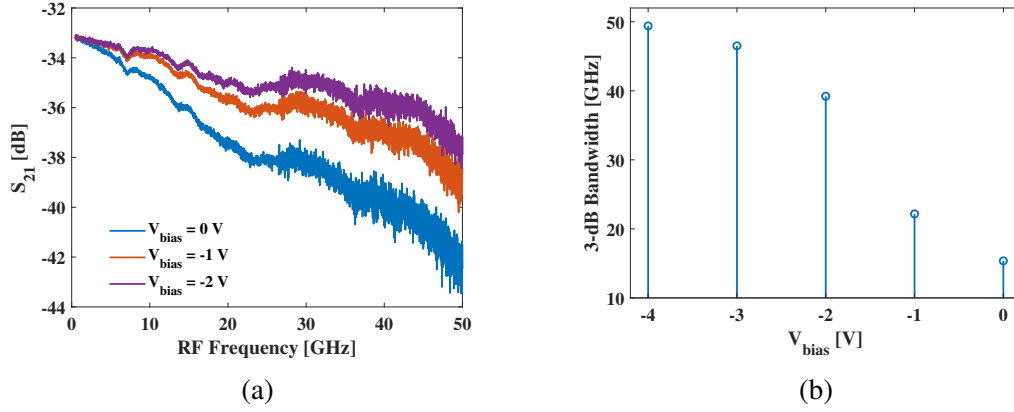


Figure 5.10: (a)  $S_{21}$  characteristics of the photodetector for different values of reverse bias voltage, (b) extracted 3-dB bandwidth of the photodetector for different values of reverse bias voltage.

range, the photodetector bias voltage was set to -2 V in the filter experiments.

### 5.2.3 Optical Signal Processor

Finally, for the OSP characterization, we have used the same setup discussed in the earlier chapters (see Fig. 2.17) and swept the wavelength of the in-built TLS of OSA (APEX 2048A) and measured its corresponding output optical power. We have used an 8-channel programmable supply (XDAC-8MUB-R4G8) to drive the thermo-optic phase shifters. Here, we have given the results corresponding to the MRR1 of device D3 around the wavelength with maximum grating coupler efficiency ( $\sim 1550$  nm). To estimate the fabricated ring's free spectral range, we have set the thermal power  $PS_{\kappa 1}$  as 18.4 mW. The measured spectrum (normalized with the peak power) showing two adjacent over-coupled resonances with a spacing (FSR) of 0.348 nm ( $\sim 43.5$  GHz) is given in Fig. 5.11a. The slight deviation in the value of the experimental FSR from the theoretical prediction of 45 GHz can be associated to the error in the group index estimation of MMI region and the width taper section of the ring resonator. From the measured two resonances, the {Q-factor, FWHM, extinction} are estimated to be identical and the values are  $\{0.77 \times 10^5, 20$  pm, 10 dB $\}$ .



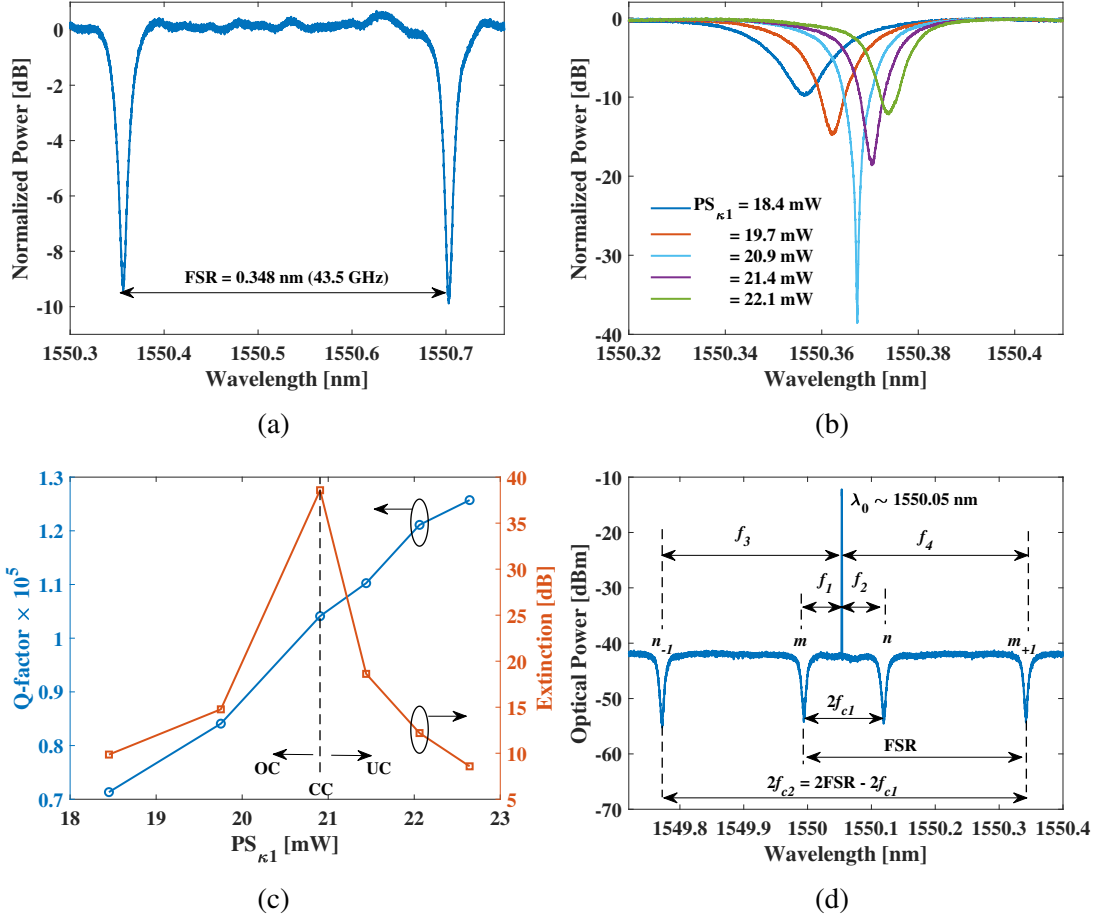


Figure 5.11: (a) Normalized transmission characteristics of MRR1 of device D3 for  $PS_{\kappa 1} = 18.4$  mW, (b) normalized transmission characteristics of MRR1 of device D3 by tuning  $PS_{\kappa 1}$  in the range of 18.4 mW - 22.1 mW, (c) extracted Q-factor and extinction of the ring responses given in Fig. 5.11b, and (d) measured optical spectrum along with the optical carrier for the set values of  $PS_{\kappa 1} = 18.4$  mW,  $PS_{\kappa 2} = 23.2$  mW,  $PS_{\lambda 1} = 5$  mW,  $PS_{\lambda 2} = 0$  mW, such that  $f_{c1} = 8$  GHz and  $f_{c2} = 35.5$  GHz.

Next, to show the tuning of the coupling coefficient, we have tuned the thermal power  $PS_{\kappa 1}$  in the range of 18.4 mW - 22.1 mW, and the measured MRR1 transmission characteristics and the extracted Q-factor and extinction are given in Fig. 5.11b and Fig. 5.11c, respectively. From the results, we can see that for the under-coupled resonances, the Q-factor goes up to  $1.2 \times 10^5$ . However, owing to the knowledge of OC-resonances resulting in the filter responses with improved link gain, discussed in Chapter 3 and 4, we have performed our filter experiments for OC-resonance with 10 dB extinction. Therefore, we have adjusted the thermal power delivered to the four phase shifters to  $PS_{\kappa 1} = 18.4$  mW,  $PS_{\kappa 2} = 23.2$  mW,  $PS_{\lambda 1} = 5$  mW,  $PS_{\lambda 2} = 0$  mW, such that  $f_{c1} = 8$  GHz and  $f_{c2} = 35.5$  GHz (FSR -  $f_{c1}$ ). The obtained spectrum and the optical carrier set around 1550 nm are shown in Fig. 5.11d. Following the adjustment of the thermo-optic phase shifters, we performed the RF filter experiments, which will be discussed in the next section.

### 5.3 MICROWAVE FILTER EXPERIMENT

Following the component characterization and estimating their operating points, we have performed the experiments to realize the integrated microwave photonic filter, using the setup shown in 5.12a. Here, the laser carrier is coupled into the device D3 of the PIC through a 50:50 coupler (the other input port of the coupler is connected to the in-built TLS of the OSA), and the 10% power of the on-chip 90:10 coupler is coupled out of the chip and fed to the OSA for coupling maximization and resonance tracking during experiments. The bias voltages to the modulator and photodetector and control signals to the OSP are provided by SMU (through individual bias-T's) and a programmable power supply using a similar method used during the component characterization. However, for the simultaneous probing of both the modulator and detector, we have used a FormFactor Infinity GSGSG probe with a probe pitch of 150  $\mu$ m in the experiments, as shown in Fig. 5.12b.

After the alignment of the experimental setup and performing the required calibration

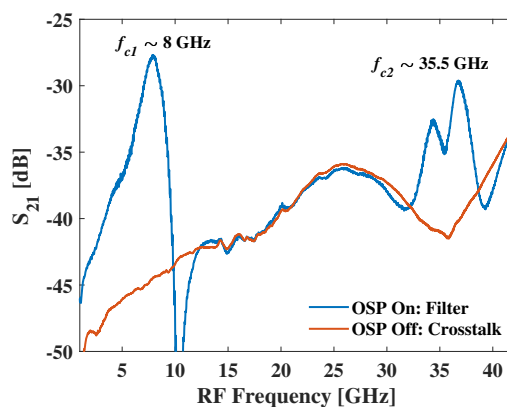
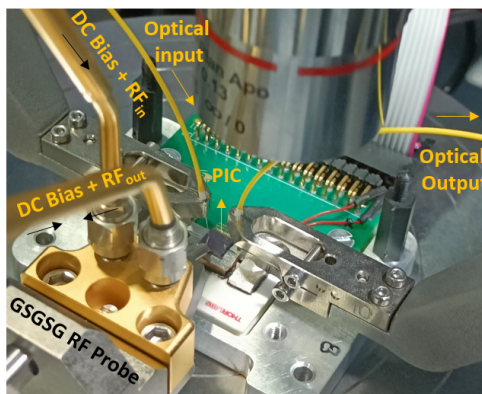
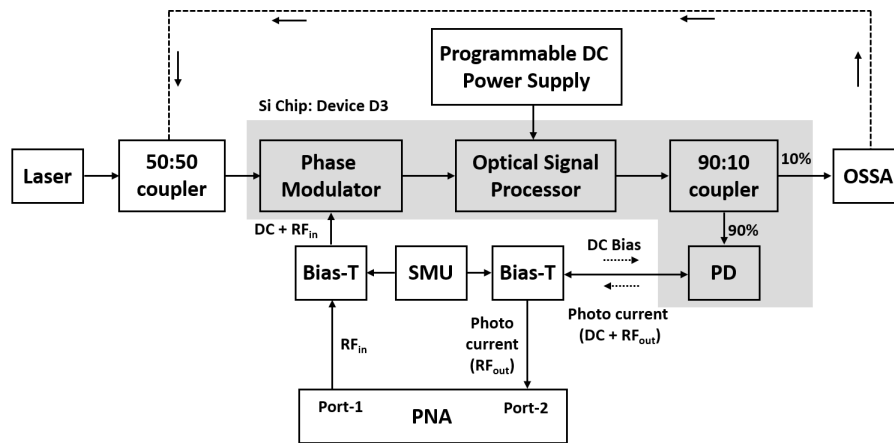


Figure 5.12: (a) Schematic of the experimental setup used to measure the microwave photonic filter response with the on-chip modulator and photodetector, (b) snapshot of the PIC package probed with the necessary optical and electrical connections (DC: wirebonded to PCB, RF: using GSGSG probe), and (c) measured  $S_{21}$  of the microwave photonic link with OSP turned on (filter response) and off (crosstalk between RF IO). PNA: performance network analyzer, PD: photodetector, OSSA: optical source and spectrum analyzer and SMU: source meter unit.

of the RF probes (2-port line-reflect-reflect-match (LRRM)), we have measured the  $S_{21}$  of the microwave photonic link under two conditions: (i) OSP turned On (resonances activated as given in Fig. 5.11d), which correspond to the filter response, and (ii) OSP turned off (no thermal power across the phase shifters), which correspond to the crosstalk between the two signal pads of the modulator and detector. The corresponding two-band filter response  $f_{c1} = 8$  GHz (link gain = -27.8 dB) and  $f_{c2} = 35.5$  GHz are shown in Fig. 5.12c. However, the out-of-band rejection of the filter is affected by the crosstalk between the two RF ports of interest. In addition, we also see the distortion in the filter shape of the second band (at 35.5 GHz) due to the interference of the signal of interest (RF photocurrent from PD) and the crosstalk signal at the output port. Therefore, from these results, we conclude that even though the individual designs of the modulator, OSP and photodetector are working with the desired response, the microwave photonic filter response is distorted due to the proximity of the RF input and output pads. The mentioned crosstalk is expected to reduce by careful wire bonding of the RF bond pads to the RF PCB designed with a proper matching network and also by increasing the on-chip spacing between the signal-to-signal bond pads. To further validate the experimental observation of RF crosstalk deteriorating the filter response, we have performed two sets of experiments: (i) with on-chip modulator (of device D1) and off-chip PD, and (ii) with off-chip modulator and on-chip PD (of device D3), using the experimental setups shown in Fig. 5.13a and Fig. 5.13b, respectively.

In both experiments, we used the FormFactor GSG infinity probe with necessary calibration (1-port SOL) to probe the on-chip RF device of interest (as depicted in Fig. 5.5c). Similar to the previous experiment, we used a 50:50 coupler at the input and a 90:10 coupler at the output to track the resonances. We de-embedded the effects of RF cables with the appropriate PNA fixtures. The microwave photonic filter response under the OSP configuration depicted in Fig. 5.11d and using the setups given in Fig. 5.13a (using on-chip modulator) and Fig. 5.13b (using on-chip photodetector) are given in Fig. 5.13c and Fig. 5.13d, respectively. In both measurements, the laser input power is

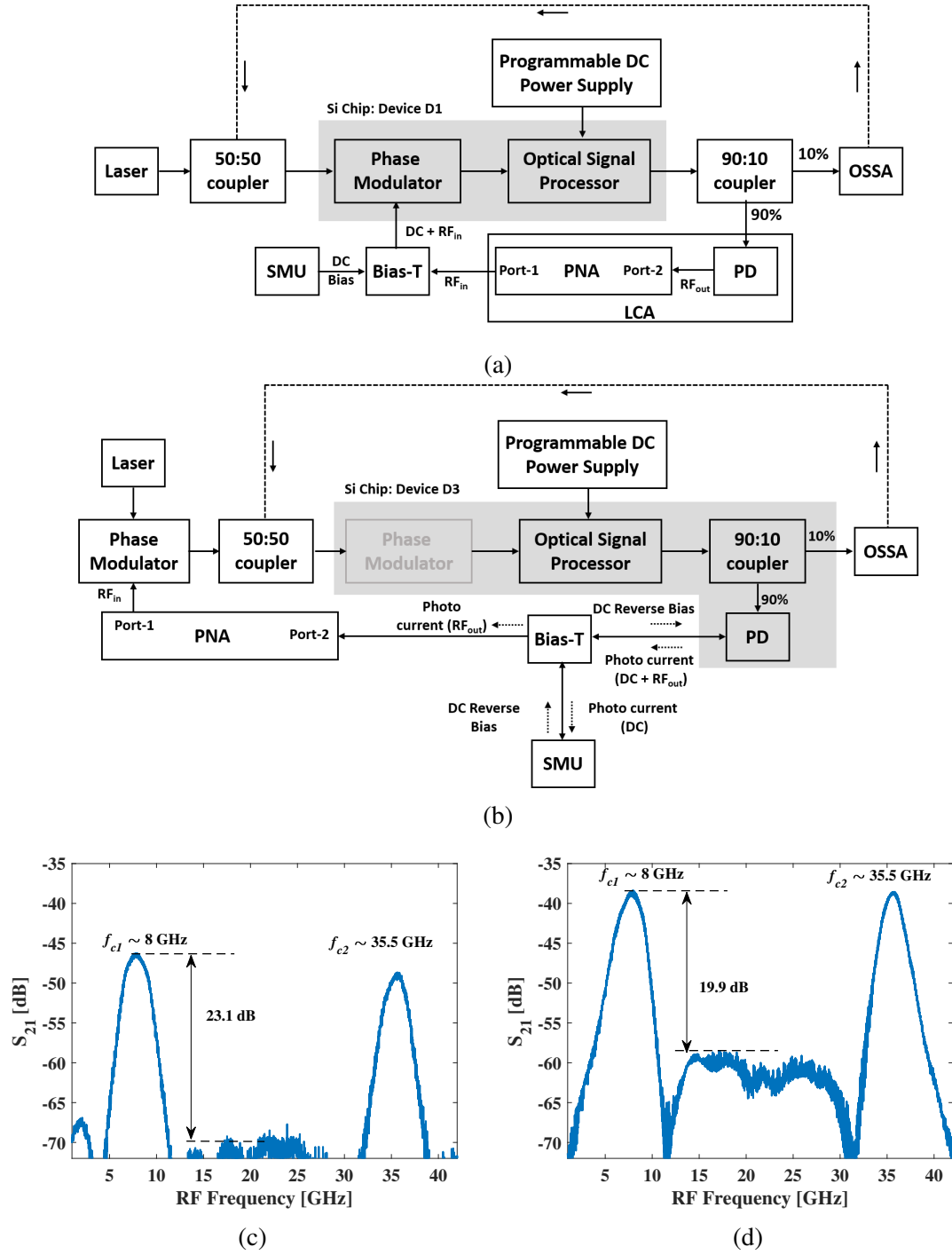


Figure 5.13: (a) Schematic of the experimental setup used to measure the microwave photonic filter response with the on-chip modulator and an external photodetector, (b) schematic of the experimental setup used to measure the microwave photonic filter response with the off-chip modulator and on-chip photodetector, (c) measured two-band microwave photonic filter response with on-chip modulator, and (d) measured two-band microwave photonic filter response with on-chip photodetector.

adjusted such that optical carrier power launched into the PD is  $\sim -5.5$  dBm. From the results, we can observe improved filter shapes in the absence of crosstalk between the input-output RF ports (in comparison with Fig. 5.12c). However, the filter response with an on-chip modulator, in Fig. 5.13c, shows poor link gain performance compared to the filter response with the on-chip photodetector, in Fig. 5.13d. This link gain variation can be accommodated by the lower efficiency of the Si-based phase modulator when compared with the phase modulator on the lithium niobate platform (used in Fig. 5.13b). In addition, the link gain degradation due to the grating coupler loss is double in the experiment using the on-chip modulator as light is coupled both at the input and output of the PIC, in contrast to the case of the experiments with the on-chip detector, where light is coupled only at the input. However, the out-of-band rejection is poor for the on-chip photodetector response, which could be associated with the PD's dark current,  $\sim \mu\text{A}$  (expected dark current for the off-chip PD  $\sim \text{nA}$ ).

From the measured responses, owing to the improved out-of-band rejection, we have opted for the filter configuration with an on-chip modulator to demonstrate the tunable bandwidth and frequency of the filter. Similar to the experiments reported in Chapter 3 and Chapter 4, we have tuned the bandwidth of the filter by detuning the spacing of the carrier with the four resonances of interest, i.e.,  $\Delta f_{12} = |f_1 - f_2|$  and  $\Delta f_{34} = |f_3 - f_4|$  using the thermo-optic phase shifters. The corresponding filter response with the bandwidth tuned from 1.5 - 3.8 GHz, at  $f_{c1} = 8$  GHz and  $f_{c2} = 35.5$  GHz, is shown in Fig. 5.14a. As explained in Chapter 3 and Chapter 4, we see a drop in the link gain for the narrow bandwidth response, because of the near-perfect cancellation of both the MRRs phase response under the condition  $\Delta f_{12}, \Delta f_{34} \rightarrow 0$ .

Next, we have realized the tunable frequency response by controlling the spacing between the resonances ( $f_1 + f_2, f_3 + f_4$ ) for a given value of  $\Delta f_{12}$  and  $\Delta f_{34}$ . The corresponding results are shown in Fig. 5.14b. We were able to tune the filter frequency of the first band from 5 GHz to 18 GHz, for which the second band frequency is tuned from 38.5 GHz to

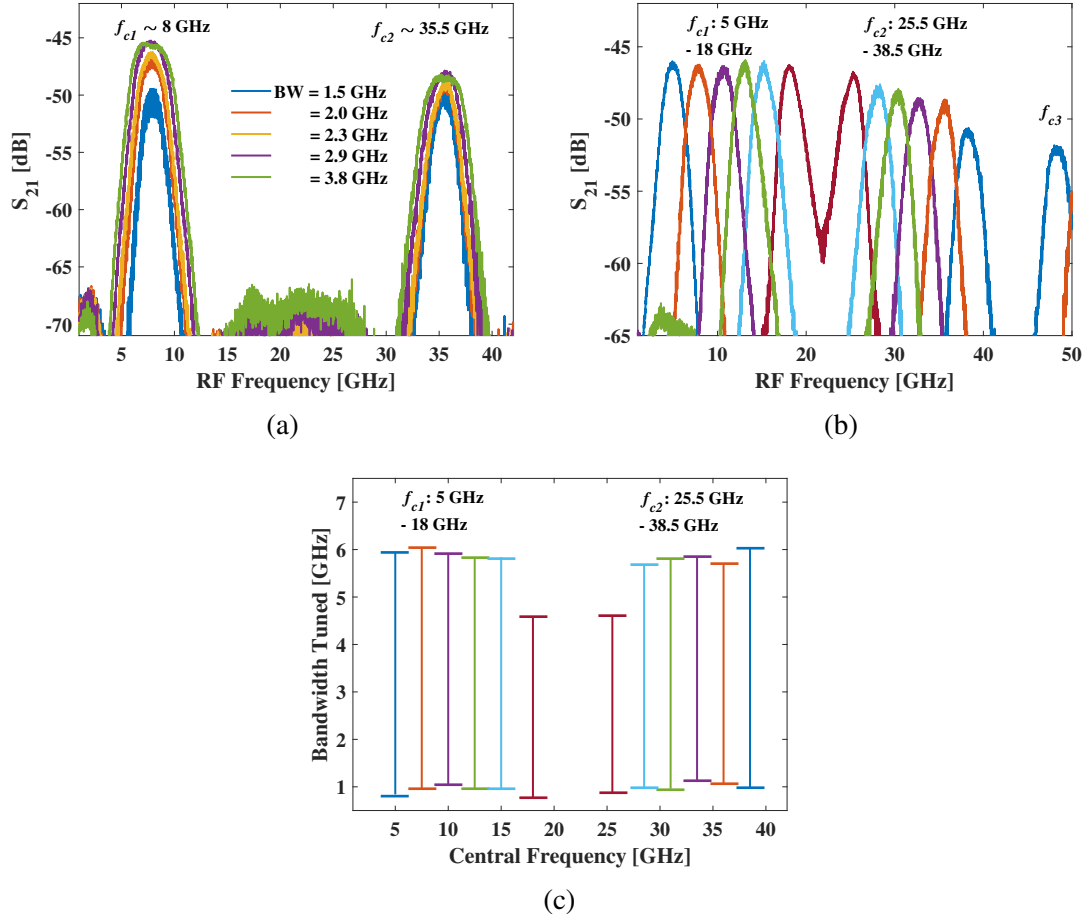


Figure 5.14: (a) Measured two-band microwave photonic filter response with tunable bandwidth (1.5 - 3.8 GHz) at  $f_{c1} = 8$  GHz and  $f_{c2} = 35.5$  GHz, (b) measured two-band microwave photonic filter response with tunable frequency ( $f_{c1}$ : 5 to 18 GHz,  $f_{c2}$ : 38.5 to 25.5 GHz), with a bandwidth of ~ 2 GHz, and (c) the 3-dB bandwidths of the measured filter responses over the range of tuned central frequencies.

25.5 GHz (3-dB bandwidth  $\sim 2$  GHz). From the results, we can see that the roll-off of the first band at 18 GHz is affected by the proximity of the second band at 25.5 GHz, thus limiting the tuning range of the proposed operation scheme. Any further increase in the filter frequency or its 3-dB bandwidth will see heavy degradation of the filter roll-off due to the proximity of both bands. Therefore, the tuning range of the filter with the proposed operation scheme can be given as the difference between FSR/2 and 20-dB bandwidth.

In the same figure, we also see a third passband at  $f_{c3} = 48.5$  GHz ( $\text{FSR} + f_{c1}$ ), corresponding to  $f_{c1} = 5$  GHz, due to  $m_{-1}$  and  $n_{+1}$  resonances of MRR1 and MRR2, respectively. The mentioned third passband is outside the operating frequency range for other values of  $f_{c1}$ . Here, the link gain of the measured filter response at  $f_{c3}$  is limited by the operating bandwidth of the on-chip modulator and photodetector. The measured third filter passband at  $f_{c3}$  establishes the scope of extending the proposed operation scheme and the OSP to realize a multiband microwave photonic filter response with the appropriate design of OSP, modulator and photodetector.

Finally, in 5.14c, we show the range of filter bandwidth tuned at different central frequencies. Overall, we have tuned the bandwidth from 1 to 6 GHz, where the filter responses with bandwidth less than 2 GHz are limited by the drop in the link gain. Whereas, the maximum bandwidth is limited by the ripples in the passband, which occurs under the condition of  $\Delta f_{12}$  and  $\Delta f_{34}$  are greater than the FWHM of the MRRs. The out-of-band rejection ratio is  $> 20$  dB in all the measurements. We see the drop in the bandwidth tuning range for the filter response with  $f_{c1} = 18$  GHz due to the proximity of the second filter band at  $f_{c2} = 25.5$  GHz.

The comparison of the measured two-band RF filter response with the state-of-the-art demonstrations is listed in Table. 5.1. The comparison establishes the superiority of the measured two-band filter results in frequency and bandwidth tuning range, symmetry of the out-of-band rejection and on-chip integration of modulator and detector. Even



Table 5.1: Comparison of the measured multi-band RF filter responses with the proposed OSP and the state-of-the-art demonstrations.

Ref.	Platform	OSP	Modulator and Photodetector	Rejection	No. of Passbands	Frequency Tuning [GHz]	Bandwidth Tuning [GHz]
[66]	SiN	Two MRRs with MZI as tunable coupler	off-chip	Asymmetric > 20 dB	2	3 - 9 & 5 - 11	0.26 (for both the bands)
[68]	SiN	Single MRR with asymmetric coupler	off-chip	Asymmetric & 27 dB	2	5 & 16	0.12 & 0.32
[78]	SiO <sub>2</sub>	Single MRR with large cavity length	off-chip	Symmetric & > 25 dB	3	3.5 & 5 & 8	0.73 - 2.73 (for all the bands)
This work	SOI	Cascaded MRR with MZI as tunable coupler	on-chip	Symmetric & > 20 dB	2	5 - 18 & 38.5 - 25.5	1 - 6 (for both the bands)

though the value of rejection reported here is  $\sim 20$  dB, it can be improved by increasing the physical distance between the on-chip modulator and detector to reduce the crosstalk between the input and output RF ports.

## 5.4 SUMMARY

In this chapter, we demonstrated an integrated microwave photonic filter with an on-chip modulator, OSP (integrated with four thermo-optic phase shifters) and photodetector. We have designed the MRRs of the OSP with a MZI as the tunable coupler, thus increasing the cavity length, to realize a two-band filter response with tunable frequency and bandwidth. We have individually characterized the on-chip modulator (BW  $\sim 39.7$  GHz at -2 V), photodetector (responsivity  $\sim 0.75$  A/W, BW  $\sim 40$  GHz at -2 V), microring resonator (FSR = 43.5 GHz, Q-factor:  $0.77 \times 10^5$ ). The filter responses with simultaneous probing of the modulator and photodetector were limited by the heavy crosstalk between the input-output RF ports, which we expect to reduce by integrating RF PCB into the PIC package. Hence, we performed the filter experiments by individually operating the on-chip modulator and photodetector. We observed that the poor link gain limits the filter response with the on-chip modulator due to the efficiency of the silicon phase modulator, and the filter response with the on-chip detector is limited by the out-of-band rejection due to the detector's dark current. The central frequency of the first filter band centered

at  $f_{c1}$  is tuned over the range of 5 – 18 GHz, correspondingly second filter band centered at  $f_{c2}$  is tuned over the range of 38.5 – 25.5 GHz. We have obtained the bandwidth tuning range of 1 – 6 GHz for the tuned frequency range.

We have also shown that the proposed OSP and the operation scheme has a scope to extend the realizable number of passbands to three, four and so on, by the appropriate design of the MRRs free spectral range, and operating bandwidths of modulator and photodetector.



# CHAPTER 6

## CONCLUSIONS

The primary outcome of the thesis is the study of the silicon MRRs-based OSPs towards the development of microwave photonic filter modules with programmable features for 5G/6G, RADAR and satellite communication systems. The effect of the figures of merits of the ring resonator (Q-factor, extinction, coupling coefficient, resonant wavelength and FSR) on the filter characteristics (central frequency, bandwidth, shape factor, no. of passbands and their spacings) has been studied, and validated by experiments. The preceding five chapters describe the theoretical analysis, design aspects and experimental demonstrations in detail. This chapter gives a comprehensive summary and provides future research directions based on the work carried out for the thesis.

### 6.1 THESIS SUMMARY

The introductory chapter briefly discussed the technological advancements towards developing microwave photonic filter modules. The material platforms explored for such module demonstrations and the challenges in integrating all the required components for different platforms have been discussed briefly. The literature survey on the filter demonstrations with MRR-based OSP highlighted the need to realize the filter response with symmetric out-of-band rejection.

In Chapter 2, the operating principle of the MRR and its characteristics with passive and tunable direction coupler has been studied. The microwave photonic bandpass filter using a single MRR as the OSP has been extensively studied via theoretical simulations to understand the impact of its figures of merit on filter metrics such as bandwidth, link gain, and rejection. The influence of the MRR residual phase on the carrier, resulting in the asymmetric out-of-band rejection and thus limiting the filter performance, has been

observed in simulations for all values of the DC coupling coefficient. The mentioned anomaly of asymmetric out-of-band rejection has been verified in the preliminary experiments using both in-house and foundry fabricated structures.

In Chapter 3, an operation scheme based on a novel OSP design based on cascaded MRR has been proposed to realize the filter response with symmetric out-of-band rejection. The proposed OSP structure and operation scheme are thoroughly investigated in simulations to realize a tunable frequency and bandwidth filter. Next, the OSP was designed using an asymmetric directional coupler on a silicon-on-insulator platform to improve the achievable Q-factor using the in-house fabrication and tune the coupling coefficient within a limited range. The OSP was fabricated using the in-house facilities at IIT Madras, and proof-of-concept experiments using an off-chip modulator and detector were performed to validate the proposed scheme. The filter response with tunable bandwidth (0.84 - 1.8 GHz) and frequency (up to 8 GHz) was realized within the limitations of the experimental setup.

In Chapter 4, the ring resonators FSR dependent multiband microwave photonic filter with tunable bandwidth and filter passbands was discussed. For this purpose, a programmable photonics integrated circuit based on programmable square mesh architecture (PMA) was investigated in experiments. The PMA was carefully calibrated for the fabrication-induced phase errors and was subsequently programmed to realize MRR responses with independent tuning of the coupling coefficient and the resonant wavelength for three configurations with different cavity lengths. Correspondingly, a two-, three- and four-band microwave filter response was realized with simultaneously tunable bandwidth. Among the three MRR configurations, the two-band filter (at X-band and Ka-band) was thoroughly investigated, and an extensive bandwidth tuning range of 1.6 GHz to 12.7 GHz was obtained. Following the realization of filter responses, a proof-of-concept evaluation of the performance of the PMA-based microwave photonic filter at the X-band in a RoF receiver link. With the optimized settings of the ring resonator, we have achieved a BER

of  $\sim 10^{-5}$  for the fiber optic transmission length of 400 m between the equivalent RRH and BBU at the data rate of 1 Gbps.

In Chapter 5, the operation scheme based on the proposed OSP (cascaded MRRs) was extended to realize an integrated microwave filter with tunable frequency, bandwidth and two passbands. In the operation scheme, the passband spacing is FSR-dependent. A PIC chip with an on-chip modulator, OSP and photodetector was designed (at IIT Madras), fabricated (at IMEC Belgium), electrically packaged (at iZMO Microsystems, Bengaluru) and tested (at IIT Madras). The on-chip modulator (BW  $\sim 39.7$  GHz at -2 V), photodetector (responsivity  $\sim 0.75$  A/W, BW  $\sim 40$  GHz at -2 V), microring resonator (FSR = 43.5 GHz, Q-factor:  $0.77 \times 10^5$ ) were individually characterized to understand the desired operating bias voltages for filter experiments. The heavy crosstalk between the input-output RF ports limited the filter responses with simultaneous probing of the modulator and photodetector. Therefore, the filter responses by individually probing the on-chip modulator and detector were measured. The central frequency of the first filter band centered at  $f_{c1}$  is tuned over the range of 5 – 18 GHz, for which the corresponding second filter band centered at  $f_{c2}$  is tuned over the range of 38.5 – 25.5 GHz. The bandwidth tuning range of 1 - 6 GHz was obtained for the entire filter frequency tuning range.

## 6.2 FUTURE OUTLOOK

The extensive study on the MRR-based OSP on the silicon-on-insulator platform has revealed its potential in realizing the microwave photonic filter module. However, the RF PCB must be integrated into the PIC package (shown in Fig. 5.5a), followed by the fiber attachment process to develop the filter module [105]. Apart from the filter functionality, the performance metrics of the filter link need further improvement to compete with its electronic counterparts.

To evaluate the extent of improvements required, we have performed the two-tone test of

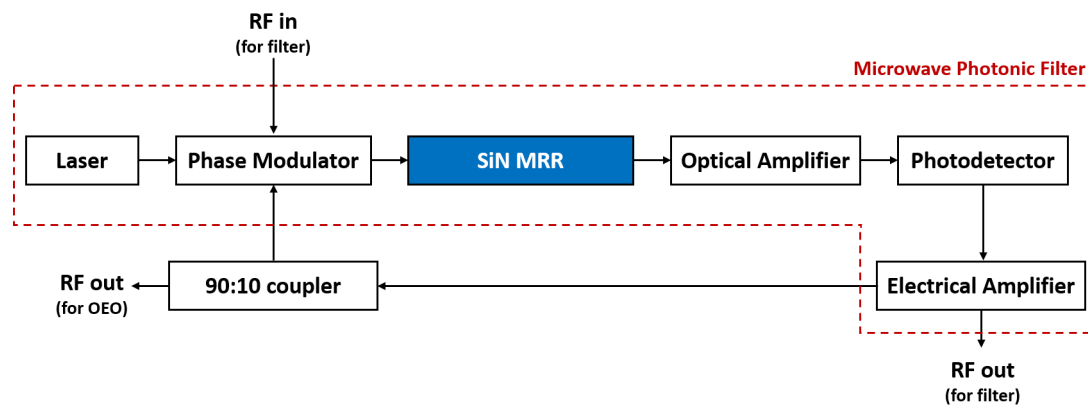
Table 6.1: Extracted metrics of the two-tone test for the filter response at  $f_{c1}$  with on-chip detector given in Fig. 5.13d. G - RF link gain; IIP - input intercept point; OIP - output intercept point; SFDR - spurious free dynamic range; NF - noise figure; OA - optical amplifier (after off-chip modulator, 10 dB gain); EA - electrical amplifier (after on-chip PD, 35 dB gain). The subscript three correspond to the third order inter-modulation terms.

	G [dB]	IIP <sub>3</sub> [dBm]	OIP <sub>3</sub> [dBm]	NF [dB]	SFDR <sub>3</sub> [dB.Hz <sup>2/3</sup> ]
without amplifiers	-41.3	19.7	-22.6	72.3	80.9
with OA	-21.8	19.0	-3.57	52.9	94.3
with OA and EA	14.0	5.5	19.47	31.1	98.9

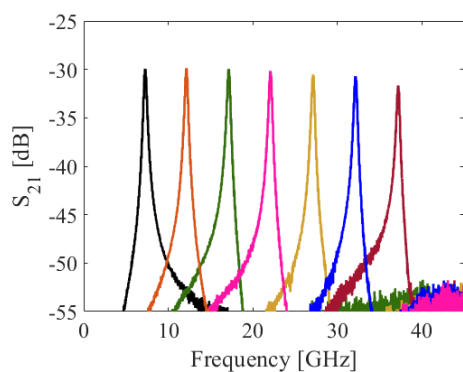
the filter response with the on-chip modulator, given in Fig. 5.13d, at  $f_{c1} = 8$  GHz (such that  $f_{rf1} = 8$  GHz,  $f_{rf2} = 8.1$  GHz). For the experiment, we followed the methodology described in Section 4.4 of Chapter 4 and extracted link gain, input and output intercept point, noise figure and spurious free dynamic range, corresponding to the third order modulation terms at  $2f_{rf2} - f_{rf1}$ ,  $2f_{rf1} - f_{rf2}$ . Table 6.1 shows the improvement in link parameters, with the addition of optical (after the modulator; 10 dB gain) and electrical (after the modulator; 35 dB gain) amplifier, in the setup shown in Fig. 5.13b, establishing the need for the on-chip amplifier integration into the filter module scheme depicted in the first chapter (see Fig. 1.1).

In this regard, there are already some ongoing works towards the hybrid integration of III-V materials on the SOI platform to facilitate on-chip optical amplification [106, 107]. Also, the electrical amplifiers can be co-packaged or co-integrated into the SOI-based filter module [108]. Also, in our experiments, the electrical amplification is performed to highlight the scope for filter metrics enhancement. However, the same can be achieved only using an optical amplifier. For such cases, improved fiber-to-chip coupler designs and modulator efficiencies help reduce the optical amplifier's gain requirements. The coupler efficiency can be improved by grating coupler design modifications [109] or opting for an edge-coupler altogether [110]. Whereas the modulator efficiency can be improved by hybrid integration of efficient electro-optic materials such as Barium Titanate [111, 112], Lithium Niobate [113], Graphene [114], on to the SOI platform.

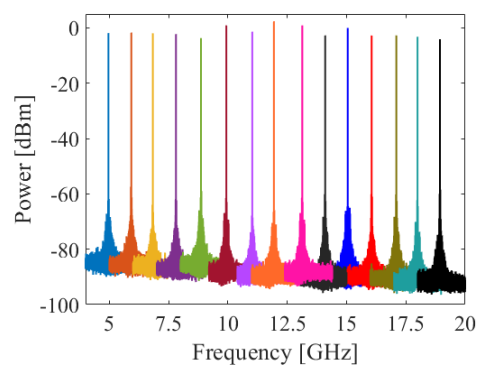
The improvement in the modulator efficiency will also improve the  $IIP_3$  degradation with the amplifier integration shown in the results given in Table 6.1.



(a)



(b)



(c)

Figure 6.1: (a) Schematic representation of the microwave photonic filter looped back to realize an optoelectronic oscillator using SiN-MRR, (b) experimentally measured tunable (up to 40 GHz) narrowband ( $\sim 290$  MHz) filter response using SiN-based high-Q MRR ( $\sim 2.5 \times 10^6$ ), and (c) experimentally measured tunable (up to 20 GHz) optoelectronic oscillator response with side mode suppression ratio  $\geq 60$  dB.

In the literature, it has been shown that the MRR-based OSP for the microwave photonic filters, facilitated with necessary amplifications for link gain enhancement, can be easily extended for the generation of spectrally pure microwave signals [115], also known as optoelectronic oscillators (OEO). Fig. 6.1a shows the schematic representation of the OEO, where the amplified photodetector output of the microwave photonic filter with a single MRR as the OSP (marked with red dashed block) is looped back into the modulator



input to form a cavity. However, in this case, the realization of narrowband filter response to suppress the unwanted cavity modes is very critical, which can be realized using high-Q SiN-based microring resonators [66, 68, 77]. Therefore, we have carefully designed the MRR based on a bi-modal ring waveguide to realize a Q-factor of  $2.5 \times 10^6$ , on the silicon nitride platform using the in-house fabrication facilities [116, 117]. With the fabricated MRR, first, a tunable (up to 40 GHz) narrowband ( $\sim 290$  MHz) microwave filter response was realized. Next, the tunable (up to 20 GHz) optoelectronic oscillator response with side-mode suppression ratio  $> 60$  dB over the entire tuned range was realized as a proof-of-concept demonstration. Such high-Q SiN-based MRR designs can be integrated into the SOI-based PICs using the hybrid integrations processes [118, 50] for the realization of integrated OEO module and improve the oscillator metrics further. The phase-noise, an important metric for oscillators, is measured as  $-74$  dBc/Hz for the realized OEO at 10 GHz, which can also be improved by using the concepts of parity-time symmetry [119] and dual-loop configuration of the OEO [120].

## APPENDIX A

### MICROWAVE PHOTONIC FILTER: THEORETICAL FORMULATION

For the simulations results of the microwave bandpass filter discussed in this thesis, we provide here the detailed derivation of the theoretical formulations. The working principle comprises of the phase modulator, optical signal processor (OSP) and the photodetector, as shown in Fig. A.1. In the simulations discussed in the different chapters of the thesis, the transfer function of the OSP is varied and the filter responses are discussed accordingly.

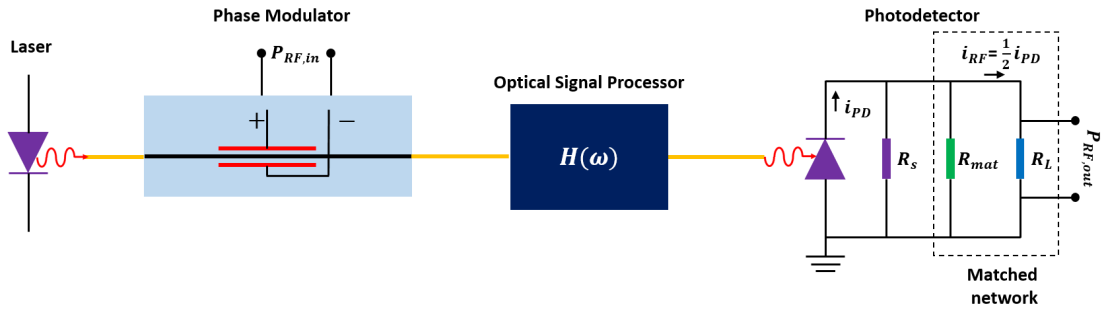


Figure A.1: Component level schematic representation for the realization of microwave photonic bandpass filter in simulations:  $P_{RF,in}$ : input RF signal power (frequency tunable),  $H$  is the transfer function of the optical signal processor,  $i_{PD}$ : photocurrent generated at the detector,  $R_S$ : internal resistance of the detector,  $R_L$ : load resistor,  $R_{mat}$ : resistor to match the detector and the load such that  $R_S || R_{mat} = R_L$ ,  $i_{RF}$ : photocurrent through the load resistor,  $P_{RF,out}$ : average output RF power.

The time-domain electric field amplitude of the laser light phase modulated with a RF frequency band centered at an angular frequency of  $\omega_{rf} (= 2\pi f_{rf})$  and received by the photodetector after passing through the optical signal processor can be analytically expressed as:

$$e(t) = \sqrt{p_{in}\eta_m\eta_g}e^{j\omega_0 t} \left[ H(\omega_0)J_0(\delta) + H(\omega_0 - \omega_{rf})J_1(\delta)e^{-j\omega_{rf}t} - H(\omega_0 + \omega_{rf})J_1(\delta)e^{j\omega_{rf}t} \right] \quad (\text{A.1})$$

where  $p_{in}$  is the optical power launched into the modulator,  $\eta_m$  is the modulator power loss,  $\eta_g$  is the chip coupling loss of the PPIC at input and output,  $\omega_0 (= 2\pi\nu_0)$  is the angular frequency of the laser light,  $H$  is the transfer function of the optical signal processor block,  $J_n$  is the Bessel function of  $n^{th}$  order,  $\delta$  is the modulation index ( $= V_{in}/V_\pi$ ),  $V_{in}$  is the amplitude of the input RF voltage and  $V_\pi$  is the half-wave voltage of the modulator. It is important to note that Eq. (A.1) is valid under small signal approximation, i.e.,  $\delta \ll 1$ . For the electric field intensity given in Eq. (A.1), the photocurrent generated at the detector,  $i_{PD}$ , is given by:

$$i_{PD}(t) = R_d |e(t)|^2 \quad (\text{A.2})$$

where  $R_d$  is the responsivity of the photodetector. For the efficient power transfer the photodetector (with an internal resistance  $R_S$ ) is matched to the load resistor  $R_L$  using a matched resistor  $R_{mat}$ , such that  $R_S || R_{mat} = R_L$ , as shown schematically in Fig. A.1. The output photocurrent through the matched load  $R_L$  is given by:

$$i_{RF}(t) = \frac{1}{2}i_{PD} = \frac{1}{2}R_d |e(t)|^2 \quad (\text{A.3})$$

From equations (A.1) and (A.3), the photocurrent corresponding to the fundamental frequency band can be expanded into:

$$i_{RF}(t) = A[i_+(t) + i_-(t)] \quad (\text{A.4})$$

where,

$$A = \frac{1}{2}\eta_L^2 \alpha_m J_0(\delta) J_1(\delta) |H(\omega_0)|^2$$

$$i_+(t) = R_d p_{in} |H(\omega_0 + \omega_{rf})|^2 \cos(\omega_{rf}t + \phi_+)$$

$$i_-(t) = R_d p_{in} |H(\omega_0 - \omega_{rf})|^2 \cos(\omega_{rf}t + \phi_-) \quad (\text{A.5})$$

where  $i_+$  and  $i_-$  are the photocurrents corresponding to the carrier beat with USB and LSB, respectively, and  $\phi_+$ ,  $\phi_-$  are phases of  $i_+$ ,  $i_-$ , respectively, given by:

$$\begin{aligned} \phi_+ &= \phi_H(\omega_0 + \omega_{rf}) - \phi_H(\omega_0) \\ \phi_- &= \phi_H(\omega_0) - \phi_H(\omega_0 - \omega_{rf}) - \pi \end{aligned} \quad (\text{A.6})$$

where  $\phi_H$  at any given frequency is the phase response of the optical signal processor. The total photocurrent  $i_{RF}(t)$  is dependent on the phase difference  $\Delta\phi$  between  $i_+$  and  $i_-$ , which is given by:

$$\Delta\phi = \angle i_+ - \angle i_- = \phi_H(\omega_0 + \omega_{rf}) + \phi_H(\omega_0 - \omega_{rf}) - 2\phi_H(\omega_0) + \pi. \quad (\text{A.7})$$

In the absence of the optical signal processor ( $|H|=1$  and  $\phi_H=0$ ),  $\Delta\phi=\pi$  and  $i_+ = -i_-$  and hence  $i_{RF}(t) = 0$  and no RF signal is detected at the output. However, in presence of the OSP  $\Delta\phi$  deviates from  $\pi$ , as given by Eq. (A.7), which is again is a function of RF frequency and dependent on the relative position of the resonances with the laser carrier frequency. In such cases, the frequency dependent filter response can be obtained by performing the Fourier transform on the detected photocurrent  $i_{RF}(t)$ , and the average power at a given RF frequency can be expressed by:

$$P_{RF,out} = \langle i_{RF}^2(t) \rangle R_L \quad (\text{A.8})$$



## APPENDIX B

### OPTIMIZED RECIPES AND PROCESS FLOW FOR IN-HOUSE FABRICATED STRUCTURES

#### B.1 SOI WAFER SPECIFICATIONS (SOITEC)

Table B.1: Specifications of silicon-on-insulator wafer used in the fabrication.

Parameter	Device layer	Buried Oxide (BOX)	Handle Layer
Thickness	220 nm	2 $\mu\text{m}$	700 $\mu\text{m}$
Doping type	p-type	–	p-type
Doping concentration	$10^{15} / \text{cm}^3$	–	$10^{15} / \text{cm}^3$
Crystal orientation	(100)	–	(100)
Resistivity	8.5 - 11.5 $\Omega\cdot\text{cm}$	–	750 $\Omega\cdot\text{cm}$

#### B.2 SILICON WAFER CLEANING STEPS

1. **TCE cleaning:** To remove organic contaminants
  - Boil at 60°C for 2 minutes
  - Ultrasonic agitation with TCE for 2 minutes
2. **Acetone Cleaning:** To remove residue formed by TCE
  - Boil at 60°C for 2 minutes
  - Ultrasonic agitation with acetone for 2 minutes
  - Rinse in DI water and blow dry with Nitrogen
3. **RCA-1 Cleaning:** To form metal oxides
  - Boil in the RCA-1 solution (DI water: $\text{NH}_4\text{OH}$ : $\text{H}_2\text{O}_2$  :: 5:1:1) at 80°C for 10 minutes
  - Rinse in DI water and check for hydrophilic surface
  - Blow dry with Nitrogen

4. **RCA-2 Cleaning:** To form metal oxides

- Boil in the RCA-2 solution (DI water:HCl:H<sub>2</sub>O<sub>2</sub> :: 6:1:1) at 80°C for 10 minutes
- Rinse in DI water and check for hydrophilic surface
- Blow dry with Nitrogen

5. **Dilute HF Cleaning:** To remove metal oxides

- Dip in dilute HF (DI water:HF :: 25:1) solution for 45 seconds
- Rinse in DI water and check for hydrophobic surface
- Blow dry with Nitrogen

### B.3 SPIN COATING PROCEDURE

1. Dehydrate the SOI sample over a hot plate at 150°C for 5 minutes. Let the sample cool down to room temperature.
2. Place the sample over the vacuum chuck in the spin coating unit and do a dummy run with the optimized coating parameters for HSQ given in Table. B.2 (for waveguide patterning).

Table B.2: Spin coating parameters for negative tone Hydrogen silsesquioxane (HSQ) resist used for waveguide patterning

Resist	Tone	Speed [RPM]	Acceleration [RPM/sec]	Time [sec]	Thickness [nm]
HSQ	Negative	3000	300	70	100

3. Blow dry the sample with nitrogen air-gun to remove any dust remaining on the sample
4. Pour 3-4 drops of resist on to the sample using a fresh syringe and filter if required.
5. Once the spin coating is over, remove the resist from the corner of the sample using Acetone which is to be clamped on the sample holder. The resist removal process is to ensure proper conductivity between the sample and the clamp.
6. Prebake the HSQ coated sample on a hot-plate at 120°C for 2 minutes (150°C for

PMMA-A8).

## **B.4 ELECTRON-BEAM LITHOGRAPHY: WRITING STRATEGIES**

Raith150-TWO electron-beam lithography system facilitates two patterning techniques:

(a) conventional patterning and (b) fixed beam moving stage (FBMS) patterning.

### **B.4.1 Conventional Patterning**

Here, the patterning area is divided into small squares called write fields and the patterning is carried out in each write field in a sequential order. The stage which holds the sample is positioned such that the electron gun is fixed at the middle of the write field and the electron beam deflects throughout the write field area. After the completion of patterning, the stage then moves to the next write field. The main drawback of the conventional patterning technique is a small misalignment in the stage positioning between adjacent write-fields may cause stitching error between the write fields. Practically, there will always be a positioning error of  $\pm 100$  nm which makes it unsuitable for patterning long structures such as waveguides which have lengths in the order of millimeters. This issue can be overcome using FBMS technique.

### **B.4.2 Fixed Beam Moving Stage**

In FBMS patterning technique, the beam remains fixed and the stage moves continuously as per the mask design. This facilitates stitch-free patterning of longer structures. The width of the FBMS line can be predefined though it cannot be changed within a single component. The photonic waveguides, which span to several millimeters are often defined as FBMS paths since their width remains the same throughout. Aligning the FBMS patterns with the conventional patterns is critical due to the stage positioning error which is inevitable.

The optimized EBL column, patterning and developing parameters for the waveguide patterning on a HSQ coated SOI substrated are given in Table. B.3.



Table B.3: Optimized EBL parameters for patterning and developing the windows for the waveguides

Column Parameters	Patterning Parameters	Developing Solution and Time
Acceleration voltage: 20kV	Area dose: 300 $\mu\text{C}/\text{cm}^2$	MF 319: 1 min 30 s
Aperture: 20 $\mu\text{m}$	Step size: 8 nm	and DI water: 1 min
Working distance: 10 mm	FBMS dose: 500 $\mu\text{C}/\text{cm}^2$	
Write field: 100 $\mu\text{m} \times 100 \mu\text{m}$		

## B.5 DRY ETCHING PARAMETERS

For the in-house fabricated devices reported in the thesis, a Flourine based chemistry using the chemicals  $\text{SF}_6:\text{CHF}_3$  was used for the etching of the Silicon. The optimized recipe is listed in Table. B.4. Here,  $\text{CHF}_3$  gas was used to passivate the sidewalls and obtain verticality, and  $\text{SF}_6$  gas was used to etch silicon. The complete etching process involves two chemical steps of gas phase reaction and surface reaction as given here:

Gas phase reaction:



Surface reaction:



Table B.4: Optimized recipe for the dry etching of silicon using ICP-RIE

Parameter	Value
Chemicals	$\text{SF}_6:\text{CHF}_3$
Flow rate	5:18 sccm
RF power	30 W
ICP power	1000W
Pressure	15 mTorr
Temperature	20°C
Duration	10 s

## B.6 THERMO-OPTIC PHASE SHIFTER PATTERNING

The microheaters were defined in two cycles of metalization followed by lift-off processes: aluminum for the contact pads and the metal routing lines, and titanium for the heaters

[121, 122]. The windows for the contact pads and micro-heaters were defined using EBL. Aluminum was deposited using thermal evaporation technique whereas Titanium was deposited by electron beam evaporation technique. The details of the process steps are given below

### B.6.1 Aluminum Contact Pads and Metal Routing Integration

1. **Resist coating:** For opening the windows for metalization, positive PMMA-A8 resist was spun coat on the SOI substrate which already contained the passive waveguide structures. The spin coating parameters used are given in Table. B.5.

Table B.5: Spin coating parameters for PMMA-A8 resist (positive tone) used for the contact pads and heater (thermo-optic phase shifters) patterning

Resist	Tone	Speed [RPM]	Acceleration [RPM/sec]	Time [sec]	Thickness [nm]
PMMA-A8	Positive	7000	600	45	300

2. **Electron beam lithography:** Windows for the Aluminium contact pads ( $100\ \mu\text{m} \times 100\ \mu\text{m}$ ) and metal routing lines (widths:  $30\ \mu\text{m}$ ,  $20\ \mu\text{m}$  and  $10\ \mu\text{m}$ , based on the device distance from the contact pads) are patterned over the PMMA A-8 resist using Electron beam lithography (Raith150-TWO) and developed using MIBK:IPA developer solution. The optimized patterning and developing parameters are given in Table. B.6

Table B.6: Optimized EBL parameters for patterning and developing the windows for the contact pads and metal routing lines

Column Parameters	Patterning Parameters	Developing Solution and Time
Acceleration voltage: 20kV	Area dose: $300\ \mu\text{C}/\text{cm}^2$	MIBK:IPA (1:3): 30 s
Aperture: $120\ \mu\text{m}$	Step size: 40 nm	and IPA: 30 s
Working distance: 10 mm		
Write field: $250\ \mu\text{m} \times 250\ \mu\text{m}$		

3. **Aluminium deposition:** Aluminium layer of about 100 nm thickness was deposited over the sample using thermal evaporation unit (HPVT-305G).
4. **Lift-off process:** Aluminium is lifted off along with the underlying resist layer from regions outside the windows by ultrasonic agitation in Acetone at  $60^\circ\text{C}$  for 10 minutes followed by cleaning in DI water.

## B.6.2 Titanium Microheater Integration

The resist coating used for patterning Titanium microheater lines are the same as those used for Aluminium contact pads, as detailed in Table. B.5. The optimized patterning parameters for the patterning of Titanium microheaters are detailed in Table. B.7. E-beam evaporation was used to deposit Titanium (Hind Hi Vac BC 300T) of  $\sim 100$  nm thickness. The lift-off process was carried out using ultrasonic agitation in Acetone at  $60^{\circ}\text{C}$  for 2 minutes. Ample care was taken to prevent the re-deposition of Titanium metal flakes over the devices.

Table B.7: Optimized EBL parameters for patterning and developing the windows for the metal heaters

Column Parameters	Patterning Parameters	Developing Solution and Time
Acceleration voltage: 20kV	Area dose: $300 \mu\text{C}/\text{cm}^2$	MIBK:IPA (1:3): 30 s
Aperture: $30 \mu\text{m}$	Step size: 20 nm	and IPA: 30 s
Working distance: 10 mm		
Write field: $100 \mu\text{m} \times 100 \mu\text{m}$		

## B.7 PROCESS FLOW

Fig. B.1a shows the the cross-section of a clean SOI substrate with device layer thickness  $H = 220$  nm. The specifications of the SOI wafer (procured from Soitec) used in the fabrication and its cleaning procedure are given in the sections B.1 and B.2, respectively. The negative tone e-beam resist HSQ was spun coat (thickness: 120 nm) on the clean sample following the procedure explained in Section B.3 (see Fig. B.1b for the cross-section). The coated sample is then patterned and developed to create the window openings for the waveguides, as shown in Fig. B.1c. The patterning was done using the e-beam lithography with the necessary conventional and FBMS structures, as discussed in Section. B.4, based on the optimized parameters given in Table. B.3. After development, the sample was post-baked at the  $300^{\circ}\text{C}$  for 3 minutes, to harden the resist for it to withstand the etching process. The Silicon exposed through the opened windows was etched using ICPRIE with the Fluorine based chemistry discussed in Section. B.5 and the recipe listed in Table. B.4. For the chosen design of the rib waveguide with a slab

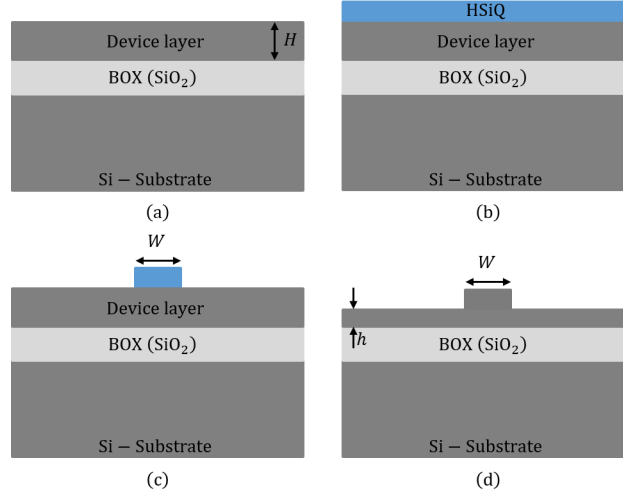


Figure B.1: Schematic cross-section depicting the process steps for the in-house fabrication of SOI waveguides: (a) cleaned SOI substrate, (b) HSQ resist coating on the surface, (c) electron beam lithography for patterning of the rib waveguide, and (d) dry etching (ICPRIE) of the rib waveguide

height  $h = 150$  nm, the etching was carried out for the duration of 10 seconds. Since the e-beam resist HSQ, obtains the properties similar to SiO<sub>2</sub> post e-beam exposure, it was removed using the dilute HF solution. The typical cross-section of the fabricated passive waveguide is shown in Fig. B.1d.

After the fabrication of the passive optical structures, we went ahead for the integration of thermo-optic phase shifters required for the tuning of the device characteristics. The patterning was performed in two cycles of resist coating, e-beam patterning, metal deposition and lift-off, as shown in Fig. B.2. The process parameters are explained in detail in Section. B.6. First, we have spun coat a positive tone e-beam resist PMMA-A8 using the spin coating parameters listed in Table. B.5, for which the expected thickness is  $\sim 300$  nm (see Fig. B.2b). Next, e-beam patterning and resist development was performed for the opening of the windows, required for the contact pads and metal routing lines (see Fig. B.2c). Here, owing to the increased resist thickness and the width of the patterns the e-beam parameters were modified to reduce the exposure time (see Table. B.6). After the development, a conformal deposition of Aluminium was done

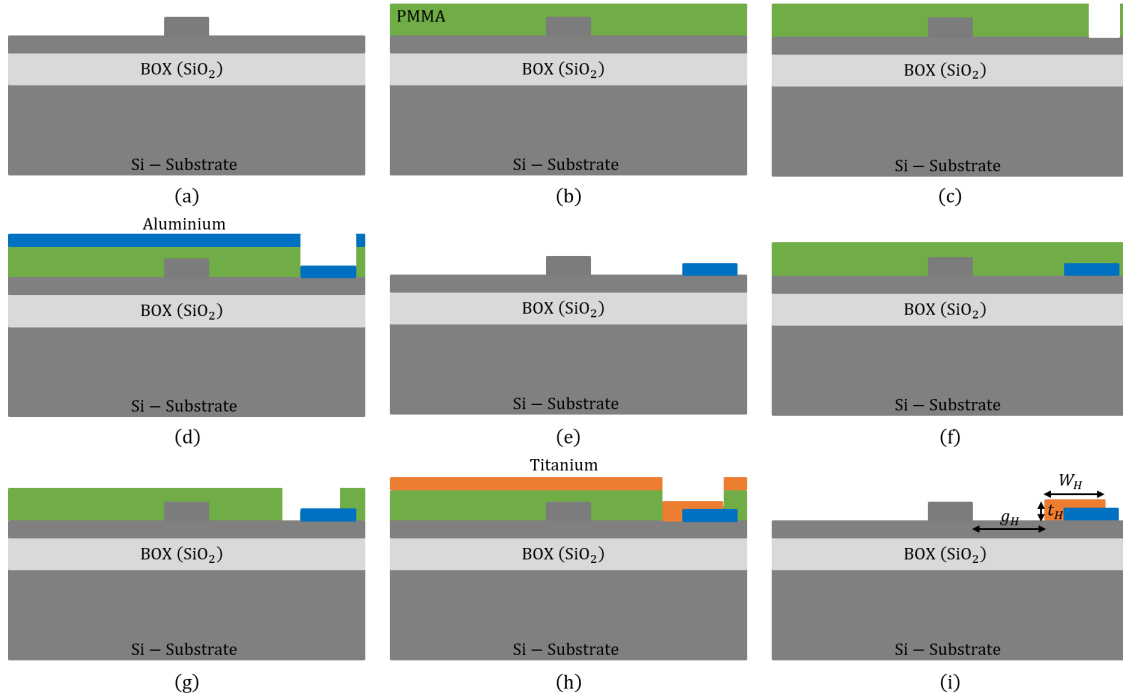


Figure B.2: Schematic cross-section depicting the process steps for the integration of the contact pads, metal routing lines and microheaters, (a) SOI substrate patterned with the rib waveguide, (b) PMMA resist coating on the surface, (c) window opening for Aluminium contact pads and metal routing lines, (d) thermal deposition of Aluminium, (e) Aluminium lift-off using acetone, (f) PMMA resist coating on the surface, (g) window opening for Titanium microheaters, (h) e-beam deposition of the Titanium, (i) Titanium lift-off using acetone.

using the thermal evaporation (see Fig. B.2d). The Aluminium deposition is followed by the lift-off process using acetone, and the cross-section is given in Fig. B.2e.

Next, the same procedure of spin coating (Fig. B.2f), e-beam patterning (Fig. B.2g), metal deposition (Fig. B.2h) and lift-off (Fig. B.2i) was followed for the integration of Titanium microheaters. A couple of notable changes when compared to the contact pads patterning are the e-beam lithography parameters (given in Table. B.7) and the use of e-beam evaporation technique because of the high melting point of Titanium. During the deposition, the chamber temperature was ensured to not exceed 60 °C to avoid the unnecessary hardening of the PMMA-A8 resist and making the lift-off process difficult.



## APPENDIX C

### OSP WITH CASCADED MRR USING MZI AS TUNABLE COUPLER

We provide the measured passive transmission and thermo-optic characteristics for the design #2 of the fabricated OSP structure (cascaded MRRs) with MZI as the tunable coupler (shown in Fig. 3.10b), in this appendix. For the measurements, we have used the same setup shown in Fig. 2.17 and followed the same methodology discussed in Section 2.3.2 of Chapter 2. Here, the device measurements are shown only around  $\lambda \sim 1542$  nm, as the grating coupler efficiency (loss  $\sim 8$  dB/coupler) is maximum around this wavelength range.

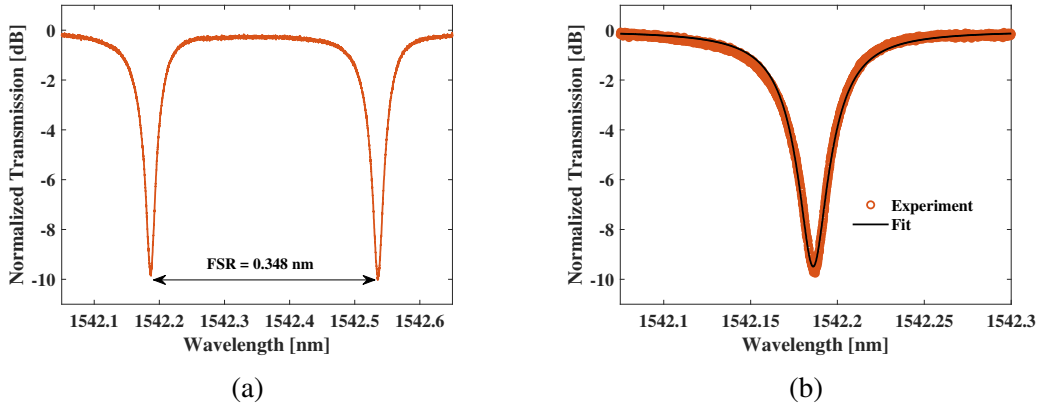


Figure C.1: (a) Normalized transmission characteristics of the in-house fabricated microring resonator with MZI as the tunable coupler indicating its FSR (= 0.348 nm), and (b) the least square fit of the left resonance in Fig. C.1a around 1542.2 nm (using Eq. (2.3)) to extract coupling coefficient  $r$  and loss factor  $a$ .

The normalized transmission characteristics of the cascaded MRR, indicating the free spectral range of 0.348 nm between the two resonances, are given in Fig. C.1a. Here, the resonances of MRR1 are visible in the measured data without any set value of thermal power across the phase shifter  $PS_{\kappa 1}$ , owing to the fabrication-induced phase errors



between the two MZI arms. However, in the case of MRR2, extra thermal power had to be delivered across  $PS_{\kappa 2}$  to measure its resonances, which indicates the randomness of the phase error distribution. Next, the least-square fit of the measured transmission characteristics was performed using the ring transfer function (see Eq. (2.3)) to extract the coupling coefficient  $r$  and loss factor  $a$ . The measured response (first resonance of Fig. C.1a around 1542.2 nm) along with its least-square fit is shown in Fig. C.1b. The coupling coefficient  $r$  and loss factor  $a$  of the device extracted from the fit is  $\{0.85, 0.92\}$ , respectively. Based on the values of  $r$ ,  $a$  and the ring perimeter ( $\sim 1.7$  mm), the Q-factor of the ring and the waveguide loss are calculated to be  $0.58 \times 10^5$  and 4 dB/cm, respectively.

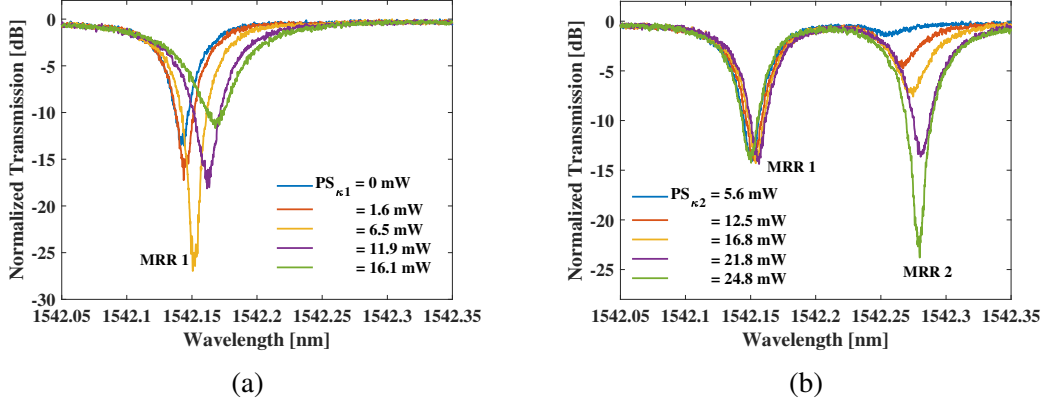


Figure C.2: The thermo-optic tuning characteristics of fabricated OSP shown in Fig. 3.10b: (a) by tuning the phase shifter  $PS_{\kappa 1}$  of MRR1, with  $PS_{\kappa 2}$  set to 0 mW, and (b) by tuning the phase shifter  $PS_{\kappa 2}$  of MRR2, with  $PS_{\kappa 1}$  set to 0 mW.

After measuring the passive transmission characteristics, we have activated the thermo-optic phase shifters. The cascaded MRR transmission characteristics for different values of thermal powers applied to  $PS_{\kappa 1}$  and  $PS_{\kappa 2}$ , individually, are shown in Fig. C.2a and Fig. C.2b, respectively. As mentioned, the resonance corresponding to MRR2 was visible after applying thermal power to the phase shifter  $PS_{\kappa 2}$ . From the measurements, we can observe that the two resonances have equal extinction ( $\sim 13$  dB) and Q-value ( $\sim 0.58 \times 10^5$ ) for  $PS_{\kappa 1} = 0$  mW and  $PS_{\kappa 2} = 21.8$  mW. For the applied thermal powers, the resonance separation is such that the expected central frequency of the filter is  $\sim 7$  GHz.

## APPENDIX D

### CALIBRATION OF PROGRAMMABLE MESH ARCHITECTURE

As already mentioned in Section 4.2.1, the tunable basic units (TBUs) of the designed programmable mesh architecture (PMA) are prone to unavoidable fabrication-induced phase errors, which result in the presence of residual optical power in the undesired output ports, as shown in Fig. 4.8b. In this appendix, we provide the details of the calibration performed on the fabricated PMA (shown in Fig. 4.6a).

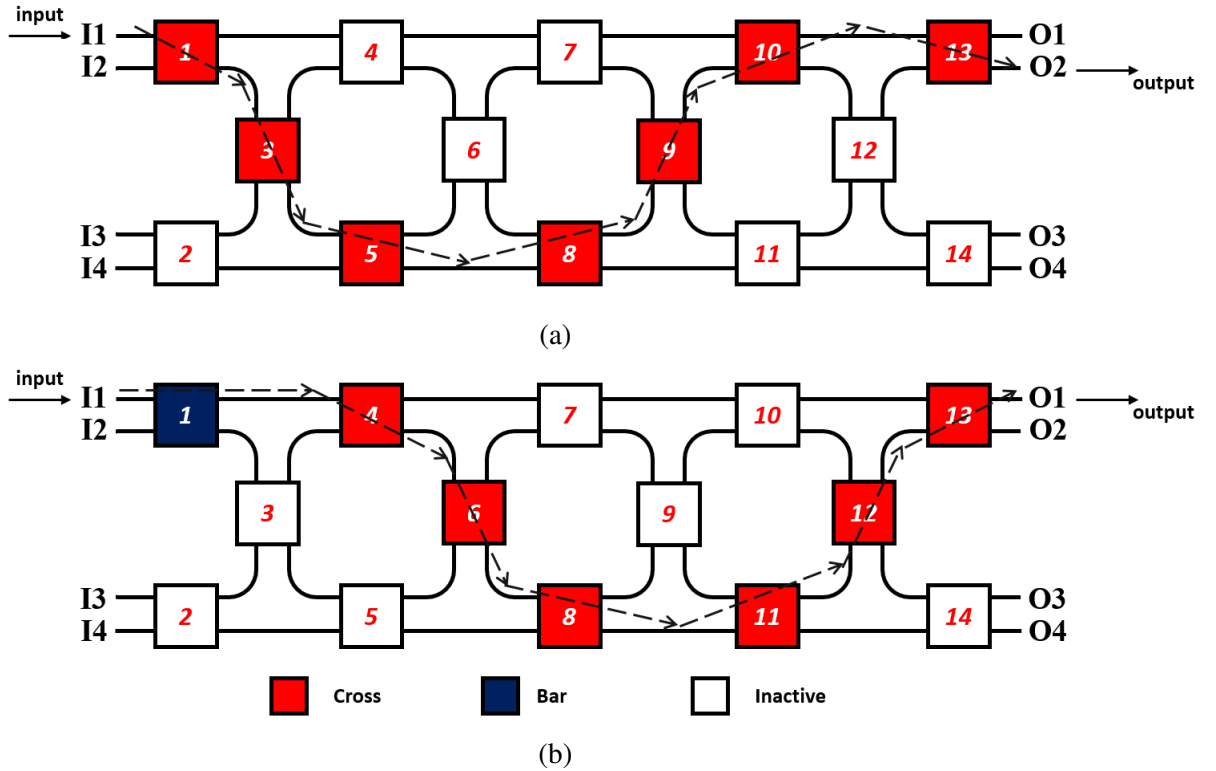


Figure D.1: (a) Schematic representation of the programmable square mesh from input I1 to output O2 with all TBUs in the path operating as a cross-switch, and (b) schematic representation of the programmable square mesh from input I1 to output O1 with TBU 1 operating as a bar-switch and remaining TBUs in the path operating as a cross-switch.

Fig. D.1a shows an all-cross path in the square mesh from input I1 to output O2, passing through 7 TBUs (1, 3, 5, 8, 9, 10 and 13). As we already know, the fabricated TBUs do not necessarily operate in a cross-port configuration because of the phase errors. For the sake of explanation, Fig. D.1b shows an optical path from input I1 to output O1 passing through 7 TBUs (1, 4, 6, 8, 11, 12 and 13) where only TBU 1 is affected with a worst-case phase error of  $\pi$  (i.e., TBU 1 is operating as a bar-switch), and the remaining TBUs operating as perfect cross-switch. From the two schemes of Fig. D.1, we can infer that TBU 1 operating as a perfect cross-switch (and bar-switch) will result in minima (and maxima) at output port O1. From the two schemes given in Fig. D.1, we can also infer that in case of the presence of a phase error between 0 to  $\pi$  to TBU 1, both the paths shown in the schemes get activated with the maximum optical power reaching the desired output port O2 and the residual power at the bar port of the TBU1 reaching output port O1. The statement can be validated from the experimental data shown in Fig. 4.8b. However, it is important to note that some residual optical powers exist for a practical device at output ports O3 and O4 due to phase errors in the other TBUs of the path.

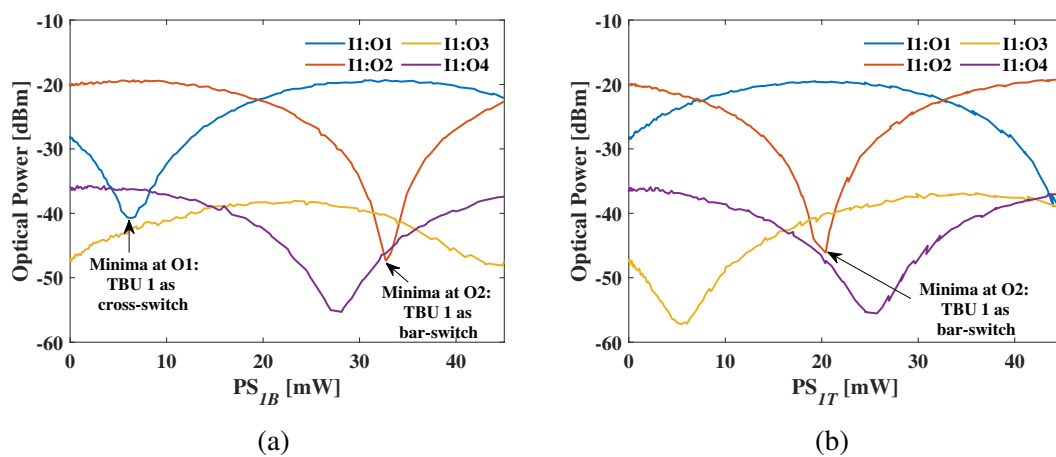


Figure D.2: (a) Measured optical power spectrum transmitted at the output ports by sweeping the thermal power applied to the phase shifter  $PS_{IB}$ , indicating thermal powers for TBU 1 to operate as cross- and bar-switch, and (b) measured optical power spectrum transmitted at the output ports by sweeping the thermal power applied to the phase shifter  $PS_{IT}$ , indicating thermal powers for TBU 1 to operate as bar-switch.

Therefore, to estimate the thermal powers required for the TBU 1 to operate as a bar-switch (i.e., minima at O2 or maxima at O1) and cross-switch (i.e., minima at O1 or maxima at O2), we have launched the optical light at input I1 and swept the voltage applied to phase shifter  $PS_{1B}$  of TBU 1 from 0 to 3 V in the steps of 0.025 V, and measured the optical power at all the output ports. For the fabricated heater configuration (width = 600 nm, thickness = 300 nm, vertical distance from the waveguide = 1  $\mu$ m, material: Tungsten), the corresponding range of the applied thermal power is 0 to 46.5 mW. The corresponding results are given in Fig. D.2a. In the same figure, two operating points of TBU 1 for it to function as a cross-switch and bar-switch are also marked. The extracted thermal power values are 6.38 mW for cross-switch operation and 32.7 mW for bar-switch operation. As the fabricated TBUs are integrated with phase shifters on both arms, we have repeated the same experiment by tuning the phase shifter  $PS_{1T}$ . The corresponding results are given in Fig. D.2b. In the same figure, the operating point of TBU 1 for it to work as a bar-switch is also marked. The extracted thermal power value is 20.4 mW for bar-switch operation. It is important to note that, in this configuration, where the phase shifter  $PS_{1T}$  is activated, the thermal power required for the TBU 1 to operate as a cross-switch would be beyond the applied range of thermal powers ( $> 46$  mW). Hence, in our experiments, the activation of the phase shifters was chosen such that the least power is dissipated across the TBU, i.e., activation of  $PS_{1B}$  for cross-switch operation and activation of  $PS_{1T}$  for bar-switch operation.

Once the operating point of TBU 1 is known, we repeated the same exercise for the next TBUs in the all-cross path (see Fig. D.1a) by setting the preceding TBUs in a cross-switch state. For example, to extract the switching powers of TBU 3, a thermal power of 6.38 mW is delivered to the phase shifter  $PS_{1B}$ . Further, while testing TBU 5, both TBUs 3 and 1 are set to cross-state. Fig. 4.8c shows the optical spectrum at the output ports after calibrating all the TBUs in the path. The results show improved crosstalk between the output ports from 8 to 21 dB. As already mentioned in Section 4.2.1, we have carried out the same calibration method for two more paths, I3 $\rightarrow$ O4 and

I4→O3, to extract the thermal switching powers for the remaining TBUs to operate in the cross and bar state. The corresponding results are summarized in Table 4.3.

## BIBLIOGRAPHY

- [1] K. C. Saraswat and F. Mohammadi, “Effect of scaling of interconnections on the time delay of vlsi circuits,” *IEEE Transactions on Electron Devices*, vol. 29, no. 4, pp. 645–650, 1982.
- [2] S. Bothra, B. Rogers, M. Kellam, and C. M. Osburn, “Analysis of the effects of scaling on interconnect delay in ulsi circuits,” *IEEE Transactions on Electron Devices*, vol. 40, no. 3, pp. 591–597, 1993.
- [3] R. H. Havemann and J. A. Hutchby, “High-performance interconnects: An integration overview,” *Proceedings of the IEEE*, vol. 89, no. 5, pp. 586–601, 2001.
- [4] D. A. Miller, “Optical interconnects to silicon,” *IEEE Journal of Selected Topics in Quantum Electronics*, vol. 6, no. 6, pp. 1312–1317, 2000.
- [5] B. Mukherjee, “Wdm optical communication networks: progress and challenges,” *IEEE Journal on Selected Areas in communications*, vol. 18, no. 10, pp. 1810–1824, 2000.
- [6] M. Lipson, “Guiding, modulating, and emitting light on silicon-challenges and opportunities,” *Journal of Lightwave Technology*, vol. 23, no. 12, pp. 4222–4238, 2005.
- [7] S. Y. Siew, B. Li, F. Gao, H. Y. Zheng, W. Zhang, P. Guo, S. W. Xie, A. Song, B. Dong, L. W. Luo *et al.*, “Review of silicon photonics technology and platform development,” *Journal of Lightwave Technology*, vol. 39, no. 13, pp. 4374–4389, 2021.
- [8] N. Saha, G. Brunetti, A. di Toma, M. N. Armenise, and C. Ciminelli, “Silicon photonic filters: A pathway from basics to applications,” *Advanced Photonics Research*, p. 2300343, 2024.
- [9] R. Maram, S. Kaushal, J. Azaña, and L. R. Chen, “Recent trends and advances of silicon-based integrated microwave photonics,” in *Photonics*, vol. 6, no. 1. MDPI, 2019, p. 13.
- [10] J. W. Silverstone, D. Bonneau, J. L. O’Brien, and M. G. Thompson, “Silicon quantum photonics,” *IEEE Journal of Selected Topics in Quantum Electronics*, vol. 22, no. 6, pp. 390–402, 2016.
- [11] B. Xu, Y. Huang, Y. Fang, Z. Wang, S. Yu, and R. Xu, “Recent progress of neuromorphic computing based on silicon photonics: Electronic–photonic co-design, device, and architecture,” in *Photonics*, vol. 9, no. 10. MDPI, 2022, p. 698.

- [12] C. Dhote, A. Singh, and S. Kumar, “Silicon photonics sensors for biophotonic applications—a review,” *IEEE Sensors Journal*, vol. 22, no. 19, pp. 18 228–18 239, 2022.
- [13] Y. Liu, A. Choudhary, D. Marpaung, and B. J. Eggleton, “Integrated microwave photonic filters,” *Advances in Optics and Photonics*, vol. 12, no. 2, pp. 485–555, 2020.
- [14] C. G. Bottenfield and S. E. Ralph, “High-performance fully integrated silicon photonic microwave mixer subsystems,” *Journal of Lightwave Technology*, vol. 38, no. 19, pp. 5536–5545, 2020.
- [15] A. Khilo, S. J. Spector, M. E. Grein, A. H. Nejadmalayeri, C. W. Holzwarth, M. Y. Sander, M. S. Dahlem, M. Y. Peng, M. W. Geis, N. A. DiLello *et al.*, “Photonic adc: overcoming the bottleneck of electronic jitter,” *Optics express*, vol. 20, no. 4, pp. 4454–4469, 2012.
- [16] B. Gao, F. Zhang, and S. Pan, “Experimental demonstration of arbitrary waveform generation by a 4-bit photonic digital-to-analog converter,” *Optics communications*, vol. 383, pp. 191–196, 2017.
- [17] V. J. Urick, K. J. Williams, and J. D. McKinney, *Fundamentals of microwave photonics*. John Wiley & Sons, 2015.
- [18] D. Marpaung, J. Yao, and J. Capmany, “Integrated microwave photonics,” *Nature photonics*, vol. 13, no. 2, pp. 80–90, 2019.
- [19] G. Zhang, T. Hao, Q. Cen, M. Li, N. Shi, W. Li, X. Xiao, N. Qi, J. Dong, Y. Dai *et al.*, “Hybrid-integrated wideband tunable optoelectronic oscillator,” *Optics Express*, vol. 31, no. 10, pp. 16 929–16 938, 2023.
- [20] Z. Zhu, Y. Liu, M. Merklein, Z. Zhang, D. Marpaung, and B. J. Eggleton, “Si 3 n 4-chip-based versatile photonic rf waveform generator with a wide tuning range of repetition rate,” *Optics letters*, vol. 45, no. 6, pp. 1370–1373, 2020.
- [21] C. Zhu, L. Lu, W. Shan, W. Xu, G. Zhou, L. Zhou, and J. Chen, “Silicon integrated microwave photonic beamformer,” *Optica*, vol. 7, no. 9, pp. 1162–1170, 2020.
- [22] Q. Zhang, J. Ji, Q. Cheng, Y. Duan, J. Zang, J. Yang, H. Yu, and X. Zhang, “Two-dimensional phased-array receiver based on integrated silicon true time delay lines,” *IEEE Transactions on Microwave Theory and Techniques*, vol. 71, no. 3, pp. 1251–1261, 2023.
- [23] R. Cao, Y. He, R. Zheng, Z. He, Y. Zhi, X. Wang, J. Zhang, and J. Yao, “Microwave frequency measurement using a silicon integrated microring resonator,” *Applied Optics*, vol. 61, no. 22, pp. 6671–6676, 2022.

- [24] M. P. Fok and J. Ge, “Tunable multiband microwave photonic filters,” in *Photonics*, vol. 4, no. 4. MDPI, 2017, p. 45.
- [25] L. Li, X. Yi, S. Song, S. X. Chew, R. Minasian, and L. Nguyen, “Microwave photonic signal processing and sensing based on optical filtering,” *Applied Sciences*, vol. 9, no. 1, p. 163, 2019.
- [26] J. Capmany, I. Gasulla, and D. Pérez, “The programmable processor,” *Nature Photonics*, vol. 10, no. 1, pp. 6–8, 2016.
- [27] A. Choudhary, I. Aryanfar, S. Shahnian, B. Morrison, K. Vu, S. Madden, B. Luther-Davies, D. Marpaung, and B. J. Eggleton, “Tailoring of the brillouin gain for on-chip widely tunable and reconfigurable broadband microwave photonic filters,” *Optics Letters*, vol. 41, no. 3, pp. 436–439, 2016.
- [28] Y. Xie, A. Choudhary, Y. Liu, D. Marpaung, K. Vu, P. Ma, D.-Y. Choi, S. Madden, and B. J. Eggleton, “System-level performance of chip-based brillouin microwave photonic bandpass filters,” *Journal of lightwave technology*, vol. 37, no. 20, pp. 5246–5258, 2019.
- [29] Q. Zhang, X. Han, X. Shao, Y. Wang, H. Jiang, W. Dong, and X. Zhang, “Stimulated brillouin scattering-based microwave photonic filter with a narrow and high selective passband,” *IEEE Photonics Journal*, vol. 14, no. 4, pp. 1–7, 2022.
- [30] M. Varun, A. Mishra, and R. Pant, “Microwave photonics applications of stimulated brillouin scattering,” *Journal of Optics*, vol. 24, no. 6, p. 063002, 2022.
- [31] C. Wang, M. Zhang, X. Chen, M. Bertrand, A. Shams-Ansari, S. Chandrasekhar, P. Winzer, and M. Lončar, “Integrated lithium niobate electro-optic modulators operating at cmos-compatible voltages,” *Nature*, vol. 562, no. 7725, pp. 101–104, 2018.
- [32] M. Han, J. Li, C. Wei, and J. Liu, “Ultra-wideband tunable microwave photonic filter based on thin film lithium niobate,” in *Photonics*, vol. 10, no. 10. MDPI, 2023, p. 1080.
- [33] R. Ma, Z. Huang, S. Gao, J. Wang, X. Wang, X. Zhang, P. Hao, X. S. Yao, and X. Cai, “Ka-band thin film lithium niobate photonic integrated optoelectronic oscillator,” *Photonics Research*, vol. 12, no. 6, pp. 1283–1293, 2024.
- [34] H. Feng, T. Ge, X. Guo, B. Wang, Y. Zhang, Z. Chen, S. Zhu, K. Zhang, W. Sun, C. Huang *et al.*, “Integrated lithium niobate microwave photonic processing engine,” *Nature*, vol. 627, no. 8002, pp. 80–87, 2024.
- [35] D. Pérez, I. Gasulla, P. Das Mahapatra, and J. Capmany, “Principles, fundamentals, and applications of programmable integrated photonics,” *Advances in Optics and Photonics*, vol. 12, no. 3, pp. 709–786, 2020.



- [36] J. S. Fandiño, P. Muñoz, D. Doménech, and J. Capmany, “A monolithic integrated photonic microwave filter,” *Nature Photonics*, vol. 11, no. 2, pp. 124–129, 2017.
- [37] H. Zhao, S. Pinna, F. Sang, B. Song, S. T. Š. Brunelli, L. A. Coldren, and J. Klamkin, “High-power indium phosphide photonic integrated circuits,” *IEEE Journal of Selected Topics in Quantum Electronics*, vol. 25, no. 6, pp. 1–10, 2019.
- [38] B. J. Isaac, B. Song, S. Pinna, L. A. Coldren, and J. Klamkin, “Indium phosphide photonic integrated circuit transceiver for fmcw lidar,” *IEEE Journal of Selected Topics in Quantum Electronics*, vol. 25, no. 6, pp. 1–7, 2019.
- [39] M. Smit, K. Williams, and J. Van Der Tol, “Past, present, and future of inp-based photonic integration,” *Apl Photonics*, vol. 4, no. 5, 2019.
- [40] Y. Gao, J.-C. Lo, S. Lee, R. Patel, L. Zhu, J. Nee, D. Tsou, R. Carney, and J. Sun, “High-power, narrow-linewidth, miniaturized silicon photonic tunable laser with accurate frequency control,” *Journal of Lightwave Technology*, vol. 38, no. 2, pp. 265–271, 2020.
- [41] B. Snyder, B. Corbett, and P. O’Brien, “Hybrid integration of the wavelength-tunable laser with a silicon photonic integrated circuit,” *Journal of Lightwave Technology*, vol. 31, no. 24, pp. 3934–3942, 2013.
- [42] G. Roelkens, J. Zhang, L. Bogaert, M. Billet, D. Wang, B. Pan, C. J. Kruckel, E. Soltanian, D. Maes, T. Vanackere *et al.*, “Micro-transfer printing for heterogeneous si photonic integrated circuits,” *IEEE Journal of selected topics in quantum electronics*, vol. 29, no. 3: Photon. Elec. Co-Inte. and Adv. Trans. Print., pp. 1–14, 2023.
- [43] M. R. Billah, M. Blaicher, T. Hoose, P.-I. Dietrich, P. Marin-Palomo, N. Lindenmann, A. Nesic, A. Hofmann, U. Troppenz, M. Moehle *et al.*, “Hybrid integration of silicon photonics circuits and inp lasers by photonic wire bonding,” *Optica*, vol. 5, no. 7, pp. 876–883, 2018.
- [44] Y. Tao, H. Shu, X. Wang, M. Jin, Z. Tao, F. Yang, J. Shi, and J. Qin, “Hybrid-integrated high-performance microwave photonic filter with switchable response,” *Photonics Research*, vol. 9, no. 8, pp. 1569–1580, 2021.
- [45] J. Li, S. Yang, H. Chen, X. Wang, M. Chen, and W. Zou, “Fully integrated hybrid microwave photonic receiver,” *Photonics Research*, vol. 10, no. 6, pp. 1472–1483, 2022.
- [46] R. Heideman, M. Hoekman, and E. Schreuder, “Triplex-based integrated optical ring resonators for lab-on-a-chip and environmental detection,” *IEEE Journal of Selected topics in quantum electronics*, vol. 18, no. 5, pp. 1583–1596, 2012.
- [47] C. G. Roeloffzen, L. Zhuang, C. Taddei, A. Leinse, R. G. Heideman, P. W. van Dijk,

- R. M. Oldenbeuving, D. A. Marpaung, M. Burla, and K.-J. Boller, “Silicon nitride microwave photonic circuits,” *Optics express*, vol. 21, no. 19, pp. 22 937–22 961, 2013.
- [48] X. Ji, R. Ning Wang, Y. Liu, J. Riemensberger, Z. Qiu, and T. J. Kippenberg, “Efficient mass manufacturing of high-density, ultra-low-loss  $\text{Si}_3\text{N}_4$  photonic integrated circuits,” *Optica*, vol. 11, no. 10, pp. 1397–1407, 2024.
- [49] M. H. Pfeiffer, J. Liu, A. S. Raja, T. Morais, B. Ghadiani, and T. J. Kippenberg, “Ultra-smooth silicon nitride waveguides based on the damascene reflow process: fabrication and loss origins,” *Optica*, vol. 5, no. 7, pp. 884–892, 2018.
- [50] C. Xiang, W. Jin, and J. E. Bowers, “Silicon nitride passive and active photonic integrated circuits: trends and prospects,” *Photonics Research*, vol. 10, no. 6, pp. A82–A96, 2022.
- [51] G. T. Reed, G. Mashanovich, F. Y. Gardes, and D. Thomson, “Silicon optical modulators,” *Nature photonics*, vol. 4, no. 8, pp. 518–526, 2010.
- [52] X. Zhou, D. Yi, D. W. U. Chan, and H. K. Tsang, “Silicon photonics for high-speed communications and photonic signal processing,” *npj Nanophotonics*, vol. 1, no. 1, p. 27, 2024.
- [53] Y. Zhang, H. Zhang, J. Zhang, J. Liu, L. Wang, D. Chen, N. Chi, X. Xiao, and S. Yu, “240 gb/s optical transmission based on an ultrafast silicon microring modulator,” *Photonics Research*, vol. 10, no. 4, pp. 1127–1133, 2022.
- [54] D. Benedikovic, L. Viot, G. Aubin, J.-M. Hartmann, F. Amar, X. Le Roux, C. Alonso-Ramos, É. Cassan, D. Marris-Morini, J.-M. Fédéli *et al.*, “Silicon–germanium receivers for short-wave-infrared optoelectronics and communications: High-speed silicon–germanium receivers (invited review),” *Nanophotonics*, vol. 10, no. 3, pp. 1059–1079, 2021.
- [55] L. Vivien, J. Osmond, J.-M. Fédéli, D. Marris-Morini, P. Crozat, J.-F. Damlencourt, E. Cassan, Y. Lecunff, and S. Laval, “42 ghz pin germanium photodetector integrated in a silicon-on-insulator waveguide,” *Optics express*, vol. 17, no. 8, pp. 6252–6257, 2009.
- [56] S. Shekhar, W. Bogaerts, L. Chrostowski, J. E. Bowers, M. Hochberg, R. Soref, and B. J. Shastri, “Roadmapping the next generation of silicon photonics,” *Nature Communications*, vol. 15, no. 1, p. 751, 2024.
- [57] M. Rakowski, C. Meagher, K. Nummy, A. Aboketaf, J. Ayala, Y. Bian, B. Harris, K. Mclean, K. McStay, A. Sahin *et al.*, “45nm cmos-silicon photonics monolithic technology (45clo) for next-generation, low power and high speed optical interconnects,” in *Optical Fiber Communication Conference*. Optica Publishing

Group, 2020, pp. T3H–3.

- [58] R. Baets, J. Van Campenhout, B. Kunert, and G. Roelkens, “4 ways to put lasers on silicon: You can make many things with silicon photonics, but a laser is not one of them,” *IEEE Spectrum*, vol. 60, no. 5, pp. 32–37, 2023.
- [59] X. Xu, M. Tan, J. Wu, T. G. Nguyen, S. T. Chu, B. E. Little, R. Morandotti, A. Mitchell, and D. J. Moss, “High performance rf filters via bandwidth scaling with kerr micro-combs,” *APL Photonics*, vol. 4, no. 2, 2019.
- [60] Y. Long, Y. Zhang, X. Zhang, J. Xia, J. Dong, and J. Wang, “Linear and nonlinear microwave responses of a microwave photonic filter based on a photonic crystal microcavity,” *Journal of Applied Physics*, vol. 121, no. 23, 2017.
- [61] L. Liu and S. Liao, “Low-power active tunable microwave photonic filter using photonic crystal nanocavities,” *IEEE Photonics Technology Letters*, vol. 32, no. 16, pp. 999–1002, 2020.
- [62] C. Porzi, M. Reza, P. Ghelfi, M. Sorel, and A. Bogoni, “Silicon-on-insulator microwave photonic filter with widely tunable and reconfigurable flat-top bandpass functionality,” *Journal of Lightwave Technology*, vol. 40, no. 20, pp. 6666–6675, 2022.
- [63] Y. Cheng, X. Hong, B. Wang, and W. Zhang, “Widely tunable narrowband integrated microwave photonic filter based on an ultra-high-q micro-disk resonator on silicon,” in *2022 27th OptoElectronics and Communications Conference (OECC) and 2022 International Conference on Photonics in Switching and Computing (PSC)*. IEEE, 2022, pp. 1–3.
- [64] W. Zhang and J. Yao, “On-chip silicon photonic integrated frequency-tunable bandpass microwave photonic filter,” *Optics Letters*, vol. 43, no. 15, pp. 3622–3625, 2018.
- [65] J. Li, P. Zheng, G. Hu, R. Zhang, B. Yun, and Y. Cui, “Performance improvements of a tunable bandpass microwave photonic filter based on a notch ring resonator using phase modulation with dual optical carriers,” *Optics Express*, vol. 27, no. 7, pp. 9705–9715, 2019.
- [66] Z. Zhu, Y. Liu, M. Merklein, O. Daulay, D. Marpaung, and B. J. Eggleton, “Positive link gain microwave photonic bandpass filter using si 3 n 4-ring-enabled sideband filtering and carrier suppression,” *Optics express*, vol. 27, no. 22, pp. 31 727–31 740, 2019.
- [67] O. Daulay, R. Botter, and D. Marpaung, “On-chip programmable microwave photonic filter with an integrated optical carrier processor,” *OSA Continuum*, vol. 3, no. 8, pp. 2166–2174, 2020.

- [68] H. Yang, J. Li, G. Hu, B. Yun, and Y. Cui, “Hundred megahertz microwave photonic filter based on a high q silicon nitride multimode microring resonator,” *OSA Continuum*, vol. 3, no. 6, pp. 1445–1455, 2020.
- [69] W. Yang, X. Yi, S. Song, S. X. Chew, L. Li, and L. Nguyen, “Tunable single bandpass microwave photonic filter based on phase compensated silicon-on-insulator microring resonator,” in *2016 21st OptoElectronics and Communications Conference (OECC) held jointly with 2016 International Conference on Photonics in Switching (PS)*. IEEE, 2016, pp. 1–3.
- [70] H. Qiu, F. Zhou, J. Qie, Y. Yao, X. Hu, Y. Zhang, X. Xiao, Y. Yu, J. Dong, and X. Zhang, “A continuously tunable sub-gigahertz microwave photonic bandpass filter based on an ultra-high-q silicon microring resonator,” *Journal of Lightwave Technology*, vol. 36, no. 19, pp. 4312–4318, 2018.
- [71] S. Song, S. X. Chew, X. Yi, L. Nguyen, and R. A. Minasian, “Tunable single-passband microwave photonic filter based on integrated optical double notch filter,” *Journal of Lightwave Technology*, vol. 36, no. 19, pp. 4557–4564, 2018.
- [72] Y. Liu, Y. Chen, L. Wang, Y. Yu, Y. Yu, and X. Zhang, “Tunable and reconfigurable microwave photonic bandpass filter based on cascaded silicon microring resonators,” *Journal of Lightwave Technology*, vol. 40, no. 14, pp. 4655–4662, 2022.
- [73] W. Cheng, D. Lin, P. Wang, S. Shi, M. Lu, J. Wang, C. Guo, Y. Chen, Z. Cang, Z. Tian *et al.*, “Tunable bandpass microwave photonic filter with largely reconfigurable bandwidth and steep shape factor based on cascaded silicon nitride micro-ring resonators,” *Optics Express*, vol. 31, no. 16, pp. 25 648–25 661, 2023.
- [74] C. Taddei, L. Zhuang, C. G. Roeloffzen, M. Hoekman, and K.-J. Boller, “High-selectivity on-chip optical bandpass filter with sub-100-mhz flat-top and under-2 shape factor,” *IEEE Photonics Technology Letters*, vol. 31, no. 6, pp. 455–458, 2019.
- [75] L. Xu, J. Hou, H. Tang, Y. Yu, Y. Yu, X. Shu, and X. Zhang, “Silicon-on-insulator-based microwave photonic filter with widely adjustable bandwidth,” *Photonics Research*, vol. 7, no. 2, pp. 110–115, 2019.
- [76] Y. Liu, Y. Yu, L. Wang, Y. Yu, and X. Zhang, “Reconfigurable microwave photonic bandpass filter based on crow,” *Journal of Lightwave Technology*, vol. 42, no. 5, pp. 1597–1604, 2024.
- [77] P. Wang, W. Cheng, M. Lu, G. Hu, and B. Yun, “Investigating mode characteristics of an ultra-high q silicon nitride micro-disk resonator and high resolution microwave photonic filtering,” *Journal of Lightwave Technology*, 2024.

- [78] Y. Chen, Z. Fan, Y. Lin, D. Jiang, X. Li, and Q. Qiu, “A multiband microwave photonic filter based on a strongly coupled microring resonator with adjustable bandwidth,” *IEEE Photonics Journal*, vol. 15, no. 1, pp. 1–6, 2023.
- [79] L. Zhuang, C. G. Roeloffzen, M. Hoekman, K.-J. Boller, and A. J. Lowery, “Programmable photonic signal processor chip for radiofrequency applications,” *Optica*, vol. 2, no. 10, pp. 854–859, 2015.
- [80] D. Pérez, I. Gasulla, and J. Capmany, “Toward programmable microwave photonics processors,” *Journal of Lightwave Technology*, vol. 36, no. 2, pp. 519–532, 2018.
- [81] D. Pérez-López, A. López, P. DasMahapatra, and J. Capmany, “Multipurpose self-configuration of programmable photonic circuits,” *Nature communications*, vol. 11, no. 1, p. 6359, 2020.
- [82] D. Pérez-López, A. Gutierrez, D. Sánchez, A. López-Hernández, M. Gutierrez, E. Sánchez-Gomáriz, J. Fernández, A. Cruz, A. Quirós, Z. Xie *et al.*, “General-purpose programmable photonic processor for advanced radiofrequency applications,” *Nature Communications*, vol. 15, no. 1, p. 1563, 2024.
- [83] M. Garrett, Y. Liu, M. Merklein, D.-Y. Choi, K. Yan, S. J. Madden, and B. J. Eggleton, “Multi-band and frequency-agile chip-based rf photonic filter for ultra-deep interference rejection,” *Journal of Lightwave Technology*, vol. 40, no. 6, pp. 1672–1680, 2022.
- [84] Z. Tao, Y. Tao, M. Jin, J. Qin, R. Chen, B. Shen, Y. Wu, H. Shu, S. Yu, and X. Wang, “Highly reconfigurable silicon integrated microwave photonic filter towards next-generation wireless communication,” *Photonics Research*, vol. 11, no. 5, pp. 682–694, 2023.
- [85] W. Bogaerts, P. De Heyn, T. Van Vaerenbergh, K. De Vos, S. Kumar Selvaraja, T. Claes, P. Dumon, P. Bienstman, D. Van Thourhout, and R. Baets, “Silicon microring resonators,” *Laser & Photonics Reviews*, vol. 6, no. 1, pp. 47–73, 2012.
- [86] Z. Yao, K. Wu, B. X. Tan, J. Wang, Y. Li, Y. Zhang, and A. W. Poon, “Integrated silicon photonic microresonators: emerging technologies,” *IEEE Journal of Selected Topics in Quantum Electronics*, vol. 24, no. 6, pp. 1–24, 2018.
- [87] A. Yariv and P. Yeh, *Photonics: optical electronics in modern communications*. Oxford university press, 2007.
- [88] S. Chandran, R. K. Gupta, and B. K. Das, “Dispersion enhanced critically coupled ring resonator for wide range refractive index sensing,” *IEEE Journal of Selected Topics in Quantum Electronics*, vol. 23, no. 2, pp. 424–432, 2016.
- [89] R. K. Gupta, S. Chandran, and B. K. Das, “Wavelength-independent directional couplers for integrated silicon photonics,” *Journal of Lightwave Technology*,

vol. 35, no. 22, pp. 4916–4923, 2017.

- [90] V. Scarani, H. Bechmann-Pasquinucci, N. J. Cerf, M. Dušek, N. Lütkenhaus, and M. Peev, “The security of practical quantum key distribution,” *Reviews of modern physics*, vol. 81, no. 3, p. 1301, 2009.
- [91] W. Shan, L. Lu, X. Wang, G. Zhou, Y. Liu, J. Chen, and L. Zhou, “Broadband continuously tunable microwave photonic delay line based on cascaded silicon microrings,” *Optics Express*, vol. 29, no. 3, pp. 3375–3385, 2021.
- [92] H. Sun, Q. Qiao, Q. Guan, and G. Zhou, “Silicon photonic phase shifters and their applications: A review,” *Micromachines*, vol. 13, no. 9, p. 1509, 2022.
- [93] H. Yang, J. Li, P. Zheng, G. Hu, B. Yun, and Y. Cui, “A stopband and passband switchable microwave photonic filter based on integrated dual ring coupled mach–zehnder interferometer,” *IEEE Photonics Journal*, vol. 11, no. 4, pp. 1–8, 2019.
- [94] W. Zhang, Y. Jiang, Y. Liu, and B. Wang, “Fully tunable microwave photonic narrow bandpass filter using an on-chip dual-drive microring resonator,” *Optics Express*, vol. 32, no. 18, pp. 31 043–31 054, 2024.
- [95] I. Zand and W. Bogaerts, “Effects of coupling and phase imperfections in programmable photonic hexagonal waveguide meshes,” *Photonics Research*, vol. 8, no. 2, pp. 211–218, 2020.
- [96] S. Bandyopadhyay, R. Hamerly, and D. Englund, “Hardware error correction for programmable photonics,” *Optica*, vol. 8, no. 10, pp. 1247–1255, 2021.
- [97] X. Xu, G. Ren, T. Feleppa, X. Liu, A. Boes, A. Mitchell, and A. J. Lowery, “Self-calibrating programmable photonic integrated circuits,” *Nature Photonics*, vol. 16, no. 8, pp. 595–602, 2022.
- [98] D. Marpaung, C. Roeloffzen, R. Heideman, A. Leinse, S. Sales, and J. Capmany, “Integrated microwave photonics,” *Laser & Photonics Reviews*, vol. 7, no. 4, pp. 506–538, 2013.
- [99] Z. Lu, J. Li, Y. Wu, H. Chen, S. Yang, and M. Chen, “Reconfigurable rf filter based on cascaded microring resonators,” *IEEE Photonics Journal*, vol. 15, no. 3, pp. 1–6, 2023.
- [100] G. Liu, K. Ye, O. Daulay, Q. Tan, H. Yu, and D. Marpaung, “Linearized integrated microwave photonic circuit for filtering and phase shifting,” *APL Photonics*, vol. 8, no. 5, 2023.
- [101] W. Freude, R. Schmogrow, B. Nebendahl, M. Winter, A. Josten, D. Hillerkuss, S. Koenig, J. Meyer, M. Dreschmann, M. Huebner *et al.*, “Quality metrics

- for optical signals: Eye diagram, q-factor, osnr, evm and ber,” in *2012 14th International Conference on Transparent Optical Networks (ICTON)*. IEEE, 2012, pp. 1–4.
- [102] P. Li, Z. Dai, L. Yan, and J. Yao, “Microwave photonic link to transmit four microwave vector signals on a single optical carrier based on coherent detection and digital signal processing,” *Optics Express*, vol. 30, no. 5, pp. 6690–6699, 2022.
  - [103] R. Soref and B. Bennett, “Electrooptical effects in silicon,” *IEEE journal of quantum electronics*, vol. 23, no. 1, pp. 123–129, 1987.
  - [104] G. Dehlinger, S. Koester, J. Schaub, J. Chu, Q. Ouyang, and A. Grill, “High-speed germanium-on-soi lateral pin photodiodes,” *IEEE Photonics Technology Letters*, vol. 16, no. 11, pp. 2547–2549, 2004.
  - [105] A. Gayen, N. Nallusamy, G. Ezhilarasu, S. Hassan, S. Vinoth, K. Piyush, A. Goswami, and B. Das, “A robust and low-cost fiber-optic array attachment solution for silicon photonics chips with large number of input/output channels,” in *2024 8th IEEE Electron Devices Technology & Manufacturing Conference (EDTM)*. IEEE, 2024, pp. 1–3.
  - [106] W. Shi, C. Zou, Y. Cao, and J. Liu, “The progress and trend of heterogeneous integration silicon/iii-v semiconductor optical amplifiers,” in *Photonics*, vol. 10, no. 2. MDPI, 2023, p. 161.
  - [107] T. Wang, “Semiconductor optical amplifier integrated on silicon photonic chip using photonic wire bonds,” Ph.D. dissertation, University of British Columbia, 2024.
  - [108] W. Bogaerts and L. Chrostowski, “Silicon photonics circuit design: methods, tools and challenges,” *Laser & Photonics Reviews*, vol. 12, no. 4, p. 1700237, 2018.
  - [109] F. V. Laere, G. Roelkens, M. Ayre, J. Schrauwen, D. Taillaert, D. V. Thourhout, T. F. Krauss, and R. Baets, “Compact and highly efficient grating couplers between optical fiber and nanophotonic waveguides,” *J. Lightwave Technol.*, vol. 25, no. 1, pp. 151–156, Jan 2007.
  - [110] X. Mu, S. Wu, L. Cheng, and H. Fu, “Edge couplers in silicon photonic integrated circuits: A review,” *Applied Sciences*, vol. 10, no. 4, 2020.
  - [111] S. Abel, T. Stöferle, C. Marchiori, D. Caimi, L. Czornomaz, M. Stuckelberger, M. Sousa, B. J. Offrein, and J. Fompeyrine, “A hybrid barium titanate–silicon photonics platform for ultraefficient electro-optic tuning,” *Journal of Lightwave Technology*, vol. 34, no. 8, pp. 1688–1693, 2016.
  - [112] Z. Dong, A. Raju, A. B. Posadas, M. Reynaud, A. A. Demkov, and D. M.

- Wasserman, “Monolithic barium titanate modulators on silicon-on-insulator substrates,” *ACS Photonics*, vol. 10, no. 12, pp. 4367–4376, 2023.
- [113] Z. Li, Y. Chen, S. Wang, F. Xu, Q. Xu, J. Zhang, Q. Zhu, W. Yue, X. Ou, Y. Cai *et al.*, “Lithium niobate electro-optical modulator based on ion-cut wafer scale heterogeneous bonding on patterned soi wafers,” *Photonics Research*, vol. 13, no. 1, pp. 106–112, 2024.
- [114] R. Mansoor, S. M. Hameed, and N. A. Mohammed, “Graphene-based silicon-on-insulator optical waveguide electro-optical modulators: pushing the boundaries of light control,” *Journal of Optics*, pp. 1–10, 2024.
- [115] T. Hao, Y. Liu, J. Tang, Q. Cen, W. Li, N. Zhu, Y. Dai, J. Capmany, J. Yao, and M. Li, “Recent advances in optoelectronic oscillators,” *Advanced Photonics*, vol. 2, no. 4, pp. 044 001–044 001, 2020.
- [116] A. Tiwari, A. Velamuri, A. Goswami, D. Venkitesh, E. Bhattacharya, and B. K. Das, “A compact and high-q value sin microring resonator for microwave photonic applications,” in *2024 IEEE Silicon Photonics Conference (SiPhotonics)*. IEEE, 2024, pp. 1–2.
- [117] A. TIWARI, A. Velamuri, R. M. Boyapati, A. Goswami, E. Bhattacharya, and B. K. Das, “High-q microring resonators with bimodal sin waveguides: Microwave photonic applications,” 2024.
- [118] D. Liang, G. Roelkens, R. Baets, and J. E. Bowers, “Hybrid integrated platforms for silicon photonics,” *Materials*, vol. 3, no. 3, pp. 1782–1802, 2010.
- [119] Z. Fan, W. Zhang, Q. Qiu, and J. Yao, “Hybrid frequency-tunable parity-time symmetric optoelectronic oscillator,” *Journal of Lightwave Technology*, vol. 38, no. 8, pp. 2127–2133, 2020.
- [120] J. Yang, Y. Jin-Long, W. Yao-Tian, Z. Li-Tai, and Y. En-Ze, “An optical domain combined dual-loop optoelectronic oscillator,” *IEEE Photonics Technology Letters*, vol. 19, no. 11, pp. 807–809, 2007.
- [121] K. RAMESH, “Broadband silicon photonics devices with wavelength independent directional couplers,” Ph.D. dissertation, INDIAN INSTITUTE OF TECHNOLOGY MADRAS, 2019.
- [122] R. Nandi, “Electrical control of optical bistability in silicon microring resonators,” Ph.D. dissertation, INDIAN INSTITUTE OF TECHNOLOGY MADRAS, 2021.





# CURRICULUM VITAE

**NAME** Ashitosh Velamuri

**DATE OF BIRTH** 03 March 1993

## EDUCATION QUALIFICATIONS

**2014 Bachelor of Technology**

Institution	VNR VJIET, Hyderabad
Specialization	Electronic and Instrumentation

**2019 Master of Science (Research)**

Institution	IIT Kanpur
Specialization	Lasers and Photonics

**Doctor of Philosophy**

Institution	IIT Madras
Specialization	Electrical Engineering
Registration Date	January 2019



# DOCTORAL COMMITTEE

**Chairperson**

Dr. Shanti Bhattacharya  
Professor, Department of Electrical Engineering  
IIT Madras

**Guide(s)**

Dr. Bijoy Krishna Das  
Professor, Department of Electrical Engineering  
IIT Madras

**Member(s)**

Dr. Christopher S  
Professor, Department of Electrical Engineering  
IIT Madras

Dr. Deleep R Nair  
Professor, Department of Electrical Engineering  
IIT Madras

Dr. Madhu Mutyam  
Professor, Department of Computer Science and  
Engineering  
IIT Madras